UNIVERSITÄT
BAYREUTH

Conductive and Radiative Heat Transport: Contributions from Experimental and Theoretical Methods

Dissertation

to be awarded the degree of
Doctor of Natural Sciences (Dr. rer. nat)
at the Faculty of Biology, Chemistry & Earth Sciences

submitted by
Kai Herrmann
born in Oberwesel

Bayreuth, 2022

The work described in this thesis was carried out from September 2018 to May 2022 at the Chair of Physical Chemistry 1 at the University of Bayreuth under the supervision of Prof. Dr. Markus Retsch.

This is a full reprint of the dissertation submitted to obtain the academic degree Doctor of Natural Sciences (Dr. rer. nat.) and approved by the Faculty of Biology, Chemistry & Earth Sciences at the University of Bayreuth.

Thesis submitted:	07.06.2022
Acceptance by the Exam Commission:	15.06.2022
Date of Scientific Colloquium:	14.12.2022

Acting Dean:

Prof. Dr. Benedikt Westermann

Doctoral Commitee:

Prof. Dr. Markus Retsch	(Reviewer)
Prof. Dr. Mukundan Thelakkat	(Reviewer)
Prof. Dr. Jürgen Senker	(Chairman)
Prof. Dr. Hans-Werner Schmidt	

List of Publications

This thesis is written as a cumulative dissertation. The thesis is based on the following publications in peer-reviewed journals:

[1] Patrick Hummel, Anna M. Lechner, Kai Herrmann, Philip Biehl, Carsten Rössel, Lisa Wiedenhöft, Felix H. Schacher, and Markus Retsch, „Thermal Transport in Ampholytic Polymers: The Role of Hydrogen Bonding and Water Uptake“, *Macromolecules*, **2020**, *53*, 5528-5537.

[2] Kai Herrmann, Nelson W. Pech-May, and Markus Retsch, „Photoacoustic Thermal Characterization of Low Thermal Diffusivity Thin Films“, *Photoacoustics*, **2021**, *22*, 100246.

[3] Kai Herrmann,* Tobias Lauster,* Qimeng Song, and Markus Retsch, „Homogeneous Polymer Films for Passive Daytime Cooling: Optimized Thickness for Maximized Cooling Performance“, *Advanced Energy and Sustainability Research*, **2022**, *3*, 2100166.
* *These authors contributed equally to the work.*

[4] Anna M. Neuhöfer, Kai Herrmann, Flora Lebeda, Tobias Lauster, Christoph Kathmann, Svend-Age Biehs, and Markus Retsch, „High-Temperature Thermal Transport in Porous Silica Materials: Direct Observation of a Switch from Conduction to Radiation“, *Advanced Functional Materials*, **2022**, *32*, 2108370.

[5] Theresa Dörres,* Malgorzata Bartkiewicz,* Kai Herrmann,* Marius Schöttle, Daniel Wagner, Zuyuan Wang, Olli Ikkala, Markus Retsch, George Fytas, and Josef Breu, „Nanoscale-Structured Hybrid Bragg Stacks with Orientation- and Composition-Dependent Mechanical and Thermal Transport Properties: Implications for Nacre Mimetics and Heat Management Applications“, *ACS Applied Nano Materials*, **2022**, *5*, 4119–4129.
* *These authors contributed equally to the work.*

[6] Qimeng Song,* Thomas Tran,* Kai Herrmann, Tobias Lauster, Maximilian Breitenbach, and Markus Retsch, „A Tailored Indoor Setup for Reproducible Passive Daytime Cooling Characterization“, *Cell Reports Physical Science*, **2022**, *3*, 100986.
* *These authors contributed equally to the work.*

[7] Kai Herrmann, Simon Freund, Fabian Eller, Tamino Rößler, Georg Papastavrou, Eva M. Herzig, and Markus Retsch, „Microstructural and Thermal Transport Properties of Regioregular Poly(3-hexylthiophene-2,5-diyl) Thin Films“, *Materials*, **2022**, *15*, 7700.

The thesis also includes the following manuscript:

[8] Raisa-Ioana Biega, Kai Herrmann, John Mohanraj, Dominik Skrybeck, Menno Bokdam, Mukundan Thelakkat, Markus Retsch, and Linn Leppert, „Composite Metal-Halide and Molecular Contributions Govern the Electronic Structure and Thermal Transport Properties of 2D Lead-Halide Perovskites“.

The thesis does not include results from the following manuscripts:

[9] Tobias Lauster, Anika Mauel, Kai Herrmann, Viktoria Veitengruber, Qimeng Song, Jürgen Senker, and Markus Retsch, „From Chitosan to Chitin: Bio-inspired Thin Films for Passive Daytime Radiative Cooling“.

[10] Qimeng Song, Thomas Tran, Kai Herrmann, Holger Schmalz, and Markus Retsch, „Reuse of Aluminum-Plastic Laminate Waste in Sustainable and Scalable Passive Daytime Radiative Cooling“.

Abstract

This thesis is dedicated to mainly two aspects of heat transport in current research materials. The first aspect is conductive heat transport which, in the investigated non-metals, mostly takes place through vibrations. The second aspect is radiative heat transport which is of particular interest at high temperatures or special applications like passive radiative cooling.
First, the photoacoustic technique was theoretically optimized and verified experimentally for the cross-plane conductive thermal characterization of polymeric thin films. With this measurement method, a temperature oscillation is optically excited, which can be measured with a microphone utilizing a resulting pressure oscillation. Depending on the sample's thermal properties, the pressure signal contains information about the surface temperature, which has a characteristic phase shift and amplitude relative to the excitation. Non-linear data analysis can, therefore, be used to determine the properties of the sample by fitting the measurement data to an appropriate multi-layer model.
The optimized measurement setup could subsequently be used for the thermal characterization of current research materials in addition to the general proof of applicability.
The first systems were P3HT thin films with different molecular weights, prepared from three different solvents, where possible relations between the microstructural optoelectronic properties extracted from deconvolution of absorption spectra and the thermal conductivity were explored. A variation of the optoelectronic properties, mainly regarding molecular weight, was apparent, while no direct influence of the solvent was discernible. In contrast, the thermal conductivities of all examined films demonstrated an insignificant variability. We, therefore, concluded that mainly the amorphous phase determines the thermal transport properties in these semi-crystalline thin films, as these represent a bottleneck for thermal transport.
The second systems were fully amorphous ampholytic polymers that exhibited different donor and acceptor groups to form hydrogen bonds. In addition to measurements depending on the humidity and/or water absorption of the polymers, a correlation between the strength of the hydrogen bonds and the thermal conductivity was observed. The strength of the hydrogen bonds was determined by deconvolution of

the characteristic carbonyl peak of the IR absorption. A direct correlation between the hydrogen bond strength and the thermal conductivity was observed for the thin films investigated.
Thirdly, anisotropic hybrid Bragg stacks of highly ordered fluorohectorite clay layers that alternate with one or two poly(ethylene glycol) layers were explored. For in-plane thermal characterization, lock-in thermography was used to investigate the anisotropy. The mechanical properties were examined using Brillouin light spectroscopy, indicating an almost ideal reinforcement of the hybrid material and exceptionally high Young's moduli.
Furthermore, 2D hybrid perovskites were studied compared to the widely used 3D methylammonium lead iodide. The influence of the organic cations on the thermal and electronic properties was investigated using light flash analysis, first-principles and molecular dynamics calculations, ultraviolet photoelectron spectroscopy and Raman measurements. As a result, an atomistic understanding of the effects of dimensional reduction on properties relevant to electronic and thermal transport was developed.
While conduction is the dominant transport mechanism in the materials outlined above, radiative transport is the second subject to be investigated.
Particulate silica materials are an exciting and at ambient thermally highly insulating material class that was investigated up to 925 °C by light flash analysis. Performing multibody optical simulations and a newly developed model, a transition of the main transport channel from conduction at ambient to radiation at high temperatures was unraveled. Therefore, the materials partially lose their extraordinary insulating properties at high temperatures.
The final subject area, passive cooling, is a unique application of radiative heat transport. Although thermal radiation is relatively weak at ambient temperatures, outer space can be used as an ultimate heat sink when carefully designing the emitter material to take advantage of the atmospheric transparency window. First, an approach was developed to determine the optimum emitter thickness to maximize the cooling power at ambient conditions or reach the lowest equilibrium temperature. Furthermore, an in-house setup was designed, which allows reproducible cooling power measurements and the variation of several environmental parameters in contrast to rooftop measurements.
In summary, the conductive heat transport in thin films and free-standing samples was investigated in addition to the methodological development. Various structure-property relationships were elucidated, which improved the understanding of thermal transport on small length scales and provides guidance for future material development. Furthermore, through the analysis of radiative heat transport, it could be shown that particulate silica materials, which are highly insulating at room temperature, lose part of their insulating properties at high temperatures. Finally, in the field of passive radiative cooling, it was possible to show how the emitter thickness

can be optimized, and a highly reproducible and variable in-house measurement setup was developed.

Zusammenfassung

Diese Arbeit widmet sich hauptsächlich zwei Aspekten des Wärmetransports in aktuellen Forschungsmaterialien. Der erste Aspekt ist der konduktive Wärmetransport, der in den untersuchten Nicht-Metallen meist durch Schwingungen erfolgt. Der zweite Aspekt ist der strahlende Wärmetransport, der vor allem bei hohen Temperaturen oder speziellen Anwendungen wie der passiven Strahlungskühlung von Interesse ist.

Zunächst wird die photoakustische Technik theoretisch optimiert und experimentell für die flächenübergreifende leitfähige thermische Charakterisierung von polymeren Dünnschichten verifiziert. Bei dieser Messmethode wird eine Temperaturschwingung optisch angeregt, die mit einem Mikrofon unter Ausnutzung einer resultierenden Druckschwingung gemessen werden kann. Abhängig von den Eigenschaften der Probe enthält das Drucksignal Informationen über die Oberflächentemperatur, die eine charakteristische Phasenverschiebung und Amplitude relativ zur Anregung aufweist. Mit Hilfe der nichtlinearen Datenanalyse lassen sich daher die Eigenschaften der Probe bestimmen, indem die Messdaten an ein geeignetes Mehrschichtmodell angepasst werden. Der optimierte Messaufbau könnte anschließend neben dem allgemeinen Nachweis der Anwendbarkeit auch für die thermische Charakterisierung aktueller Forschungsmaterialien verwendet werden.

Bei den ersten Systemen handelte es sich um P3HT-Dünnschichten mit unterschiedlichen Molekulargewichten, die aus drei verschiedenen Lösungsmitteln hergestellt wurden, wobei mögliche Beziehungen zwischen den mikrostrukturellen optoelektronischen Eigenschaften, die aus der Entfaltung der Absorptionsspektren gewonnen wurden, und der Wärmeleitfähigkeit untersucht wurden. Es zeigte sich ein Kontrast zwischen den optoelektronischen Eigenschaften, vor allem in Bezug auf das Molekulargewicht, während kein direkter Einfluss des Lösungsmittels zu erkennen war. Im Gegensatz dazu zeigten die Wärmeleitfähigkeiten aller untersuchten Filme eine unbedeutende Variabilität. Wir kamen daher zu dem Schluss, dass hauptsächlich die amorphen Bereiche die Wärmetransporteigenschaften in diesen teilkristallinen dünnen Filmen bestimmen, da diese einen Engpass für den Wärmetransport darstellen.

Bei den zweiten Systemen handelte es sich um vollständig amorphe ampholytische

Polymere, die unterschiedliche Donor- und Akzeptorgruppen zur Bildung von Wasserstoffbrückenbindungen aufwiesen. Zusätzlich zu den Messungen in Abhängigkeit von der Feuchtigkeit und/oder der Wasseraufnahme der Polymere wurde eine Korrelation zwischen der Stärke der Wasserstoffbrückenbindungen und der Wärmeleitfähigkeit festgestellt. Die Stärke der Wasserstoffbrückenbindungen wurde durch Entfaltung des charakteristischen Carbonylpeaks der IR-Absorption bestimmt. Für die untersuchten Dünnschichten wurde ein direkter Zusammenhang zwischen der Stärke der Wasserstoffbrückenbindungen und der Wärmeleitfähigkeit festgestellt.
Drittens wurden anisotrope hybride Bragg-Stapel untersucht, die aus hoch geordneten Fluorhektorit-Tonschichten bestehen, die sich mit einer oder zwei Poly(ethylenglykol) schichten abwechseln. Zur thermischen Charakterisierung in der Ebene wurde auch hier die Lock-in-Thermografie eingesetzt, um die Anisotropie zu untersuchen. Die mechanischen Eigenschaften wurden mit Hilfe der Brillouin-Lichtspektroskopie untersucht, was auf eine nahezu ideale Verstärkung des Hybridmaterials und außergewöhnlich hohe Elastizitätsmodule hindeutet.
Darüber hinaus wurden 2D-Hybridperowskite im Vergleich zu dem weit verbreiteten 3D-Methylammoniumbleijodid untersucht. Der Einfluss der organischen Kationen auf die thermischen und elektronischen Eigenschaften wurde mit Hilfe von Lichtblitzanalysen, First-Principles-Rechnungen und Ultraviolett-Photoelektronen-Spektroskopie-Messungen untersucht. Als Ergebnis wurde ein atomistisches Verständnis der Auswirkungen der Dimensionsreduktion auf die für den elektronischen und thermischen Transport relevanten Eigenschaften entwickelt.
Während die Leitung der dominierende Transportmechanismus in den oben skizzierten Materialien ist, ist der Strahlungstransport das zweite Thema, das untersucht wird. Partikuläre Siliziumdioxid-Materialien sind eine spannende und bei Raumtemperatur hochisolierende Materialklasse, die bis zu 925 °C mittels Lichtblitzanalyse untersucht wurde. Durch optische Mehrkörpersimulationen und ein neu entwickeltes Modell konnte ein Übergang des Haupttransportkanals von Leitung bei Raumtemperatur zu Strahlung bei hohen Temperaturen entschlüsselt werden. Demnach verlieren die Materialien bei hohen Temperaturen teilweise ihre außergewöhnlichen Isolationseigenschaften.
Der letzte Themenbereich, die passive Kühlung, ist eine einzigartige Anwendung des strahlenden Wärmetransports. Obwohl die Wärmestrahlung bei Umgebungstemperaturen relativ schwach ist, kann der Weltraum als ultimative Wärmesenke genutzt werden, wenn das Strahlungsmaterial sorgfältig entworfen wird, um das atmosphärische Transparenzfenster zu nutzen. Zunächst wurde ein Ansatz entwickelt, um die optimale Strahlerdicke zur Maximierung der Kühlleistung bei Umgebungstemperaturen bzw. zum Erreichen der niedrigsten Gleichgewichtstemperatur zu bestimmen. Darüber hinaus wurde ein hausinterner Aufbau entwickelt, der reproduzierbare Messungen der Kühlleistung und die Variation verschiedener Umgebungsparameter im Gegensatz zu Messungen auf dem Dach ermöglicht.
Zusammenfassend lässt sich sagen, dass der konduktive Wärmetransport in dünnen

Schichten und freistehenden Proben zusätzlich zur methodischen Entwicklung untersucht wurde. Es wurden verschiedene Struktur-Eigenschafts-Beziehungen aufgeklärt, was das Verständnis des Wärmetransports auf kleinen Längenskalen verbessert und Anhaltspunkte für die zukünftige Materialentwicklung liefert. Darüber hinaus konnte durch die Analyse des Strahlungswärmetransports gezeigt werden, dass partikelförmige Silika-Materialien, die bei Raumtemperatur hoch isolierend sind, bei hohen Temperaturen einen Teil ihrer isolierenden Eigenschaften verlieren. Schließlich konnte im Bereich der passiven Strahlungskühlung gezeigt werden, wie die Strahlerdicke optimiert werden kann, und es wurde ein hoch reproduzierbarer und variabler eigener Messaufbau entwickelt.

Preface

General Approach and Objective

This cumulative dissertation consists mainly of two parts. In the first part, the theoretical framework of the addressed topics is developed. The second part contains the publications and manuscripts included in this thesis.
First, in Chapter 1, the theoretical foundations of temperature, heat, and heat transport are established. The basic concepts of microscopic heat transport and the possible transport modes, namely conduction, convection, and radiation, are outlined. After having also dealt with the particularities of low thermal conductivity materials, which represent a substantial part of this thesis, the concept of passive cooling is introduced.
In Chapter 2, the basic principles of the employed methods are presented to ensure a clear understanding of the individual publications and manuscripts. The keystone of the thermal characterization methods used in this work is the solution of the thermal diffusion equation for the respective experimental situation. Therefore, the thermal diffusion equation is derived exemplary for one dimension from the first law of thermodynamics and the Fourier law. Measurements and subsequent data analysis are possible in both the time and frequency domain, which is shown for the cases of Light Flash Analysis for the time domain and the Photoacoustic Technique for the frequency domain. The methods chapter is concluded by treating the numerical methods employed for data analysis and calculations. These are the numerical integration and differentiation for the non-analytic solution of ill-defined functions and non-linear regression for the solution of inverse problems.
In Chapter 3, the larger context of the subjects, a detailed discussion of the individual topics, and a thorough review of my contributions to the publications and manuscripts included in this thesis are provided.
The peer-reviewed publications and manuscripts are presented in the second part. In Chapter 5, the Photoacoustic Technique is elaborated and optimized as a suitable method for the complete thermal characterization of polymeric or other low conductivity thin films. The optimized measuring environment is then applied to re-

gioregular poly(3-hexylthiophene-2,5-diyl) thin films combined with microstructural deconvolution of absorption spectra to explore possible relationships between the thin film microstructure and the thermal conductivity in Chapter 6. Another application of the optimized measurement environment is a set of ampholytic polymers in Chapter 7, revealing the impact of hydrogen bonding on thermal conductivity. In Chapter 8, hybrid Bragg stacks of polyethylene glycol intercalated between sodium hectorites are mechanically and thermally characterized, revealing high anisotropy ratios in both property classes and almost ideal mechanical reinforcement. The transition to the time domain is made in Chapter 9, where 2D hybrid lead halide perovskites are the object of investigation. For thermal characterization, the Light Flash Analysis is used here. In combination with ab initio calculations and ultraviolet photoemission spectroscopy, effects of dimensional reduction on properties relevant for electronic and thermal transport are identified. Also employing Light Flash Analysis, Chapter 10 deals with temperature-dependent thermal transport in particulate silica materials. A gradual transition of the main thermal transport channel from conduction at ambient to radiation at high temperature is revealed here. Thermal radiation is furthermore the main topic in Chapter 11. Here, an optimum thickness for passive cooling materials could be demonstrated both theoretically and practically for the first time. Finally, in Chapter 12, an indoor setup for the reproducible determination of the passive cooling capacity was developed.

In summary, after the theoretical foundations have been established, this thesis addresses current research issues related to conductive heat transport in low thermal conductivity solids and radiative heat transport in particulate silica and for passive cooling applications.

Acknowledgements

The work presented in this thesis would not have been possible without the support of a large number of people, and I want to express my gratitude to them here.
First of all, I would like to thank my supervisor Prof. Dr. Markus Retsch, for providing the necessary funding and giving me the opportunity to do my Ph.D. in his research group. Here I was strongly challenged, which allowed me to grow.
Second, I want to thank Dr. Nelson W. Pech-May, who has been a great source of inspiration and knowledge transfer. Besides excellent expertise, through our collaboration, I learned early on the importance of pursuing academic objectives autonomously with great emphasis. He has strongly affected and reinforced both my way of thinking as well as my expectation attitude.
The time of doctoral studies consists of many single working days, and for their enjoyable arrangement, I would like to thank my colleagues at the chair. Since we are all in somewhat similar situations, we could support each other to face the challenges we encounter and transcend ourselves.
Besides this work support, especially my overall life environment, first made it possible for me to engage in this multiple-year spanning academic project. For this, I want to thank all good friends, mainly from Hunsrück, Hamburg, Siegen, and Bayreuth, for meaningful human interaction and moral support, which can not be underestimated.
The last and most important group of people I would like to thank is my family. You have always been my most substantial support, and I hope this will continue for a long time. Thank you for the opportunity to pursue this privileged education. You have kept me free from the monetary imperatives of modern society for more than half of my higher education, and I am very grateful for that. Only then could I unfold as a person without economic pressure.
Thank you.

Contents

1 Introduction

Energy has always been among the essential resources that endorse human societies' progress, evolution, and prosperity.[1,2] The extensive demand for the large-scale availability of energy has resulted in several adverse secondary effects over the last few centuries. Besides the severe exploitation of natural resources far exceeding rational limits, which alone destroys a multitude of ecosystems, this results in human-made climate change.[3] Starting with the industrial revolution in the 18th century, this dynamic has continuously intensified, accelerated by the imperative of compulsive growth, and is now becoming so dominant that the consequences are becoming abundantly clear.[4]

Besides the critical assessment of which technologies are vital, one approach to tackle these problems is to make the use of energy more efficient.[5] Waste heat represents the main constituent of inefficient energy usage and is estimated to account for up to 80% of the global primary energy consumption.[6,7] A reduction in wasted heat could, therefore, make a direct contribution to sustainability-oriented societies.

To transfer academic research progress into real applications to reduce waste heat for a sustainable future, two approaches are of particular interest. On the one hand, the correct determination of material properties is of particular interest in the context of increasingly complex materials.[8] These properties are fundamentally required for the design of devices. Secondly, in addition to the effective material properties, knowledge of the pathways used to transport heat may also be necessary if the materials are to be further manipulated.[9,10]

The fundamental material property related to waste heat thereby represents the thermal conductivity. The main goals related to thermal conductivity are either dissipating the heat away as efficiently as possible, as with computer processors and solar cells, or maintaining a temperature gradient as in thermal barriers or thermoelectrics.[9] Both properties should therefore be combined in an efficient device to ensure a constant operating temperature while the excess heat is energetically recycled. Excess heat energy recycling is of specific interest for large-scale industrial processes.[11] Large amounts of energy are available here, where even low relative recycling efficiencies can have a high absolute impact.

A significant part of this work revolves around materials with low thermal conductivity. These materials are inherently suitable for effective thermal insulation, i.e., localization of heat in places where it is actually needed or for thermoelectric energy recovery. However, for thermoelectric energy recovery, high electrical conductivity is also required as electricity is supposed to be obtained from a temperature gradi-

ent.[12,13] Another main topic of this work is passive radiative cooling. In contrast to conventional cooling methods, no waste heat is generated during operation, and at the same time, no further energy input is required after the cooler has been manufactured.[14]
After giving a general overview of the basic principles of temperature and heat and their transport required for the publications presented in this thesis, the applied methods will then be addressed. These consist of mainly two methods for the thermal characterization of different specimens and geometries and a short introduction to the numerical methods employed. After highlighting the connections between the various projects and outlining my contributions, the publications and manuscripts are presented.

1.1 Basics of Temperature and Heat

Before thinking about transport phenomena, we need to be clear about what is being transported in the first place. Classical thermodynamics defines temperature as an equilibrium phenomenon, where systems are said to be in thermal equilibrium when there is no net energy change between them.[15] In general, any physical substance is made of atoms and molecules, and their movement is related to temperature.[16] At any temperature above absolute zero, the atoms and molecules are constantly in motion. As any object in motion possesses kinetic energy associated with its mass and velocity, the temperature is a measure of the average kinetic energy. Therefore, the higher the temperature, the higher the kinetic energy of the atoms and molecules or vice versa. There are many scales to quantify temperature, but the Kelvin scale is the scientific standard. Zero on this scale is at absolute zero, which is where all molecular motion stops and it is, therefore, considered an absolute temperature scale.
Based on the definition of temperature, heat is the form of energy that can be transferred from one system to another due to temperature differences.[17,18] Heat transport, therefore, deals with systems that lack thermal equilibrium, and thus it is a non-equilibrium phenomenon.[19] The study of heat transport hence can not be based on thermodynamics alone. However, the laws of thermodynamics build the framework for heat transport. The first law requires that the rate of energy transfer into a system is equal to the rate of increase of the energy of that system. In contrast, the second law requires that heat is transferred in the direction of decreasing temperature.[18] Heat transport will consequently lead to a temperature equilibrium, or equivalently to the disappearance of the temperature gradient.

1.2 Heat Transport

Most transport phenomena are related to a potential gradient, also termed constitutive relations.[20] Flux is, therefore, proportional to a gradient, and the constant of proportionality is a characteristic of the material at a macroscopic scale.[21] For example, diffusion is related to a gradient in concentration, electronic conduction is associated with a gradient in electrostatic potential, and thermal conduction to a gradient in temperature. Consequently, one can state that heat transport occurs if there is a gradient in temperature, as stated above. There can be no net heat transport between two points in space at the same temperature.

1.2.1 Microscopic Heat Transport

A closer look at the microscopic picture of how heat is transported reveals a more complex situation. The most simple case is based on kinetic theory to describe heat transport in a box filled with a monoatomic gas.[22] This situation is depicted in Figure 1.1 and can be used to illustrate the microscopic transport process.

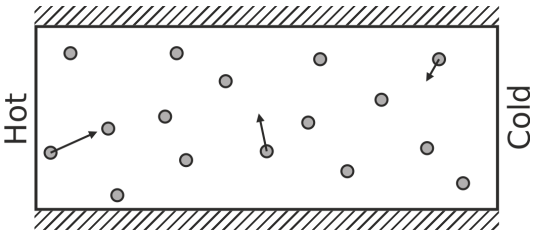

Figure 1.1: Microscopic heat conduction in a monoatomic gas. Arrows indicate the velocity of the random motion.

Heat conduction in this simplification results from the random motion of the gas molecules inside the box. Near the hot wall, gas molecules will often collide with the wall atoms and gain higher kinetic energy, which is directly related to the velocity of their random motion. When moving towards the cold end, they collide with molecules having a smaller random velocity or lower kinetic energy, respectively, and transfer some excess energy. Those collisions trigger a cascade until the cold side is reached. If molecules close to the cold wall have higher kinetic energy than the wall atoms, energy is transferred, causing it to heat up. Therefore, due to the temperature difference between the two sides, a net energy flow is generated, which is transferred by the gas molecules. The net energy flow is only due to the random motion of the molecules, and there is no preferred direction of movement from hot to cold. This simple kinetic theory concept can frequently be effectively applied to heat transport processes in solids.

In dielectric solids, heat is mainly conducted by atomic vibrations.[23] The atoms in solids are bonded to each other by electrostatic interactions, often termed interatomic force interactions.[24] Their interaction is usually described by a Morse potential,[25] which is depicted in Figure 1.2.

When the atoms are close, the interaction is repulsive because the electron orbits or the nuclei begin to overlap.[24] In contrast, when the atoms are far apart, having a large interatomic distance, an attractive force is apparent. The minimum potential defines the equilibrium interatomic distance r_0. Therefore, the motion of each atom is restricted by the interatomic force potential to the respective neighbors.[26]

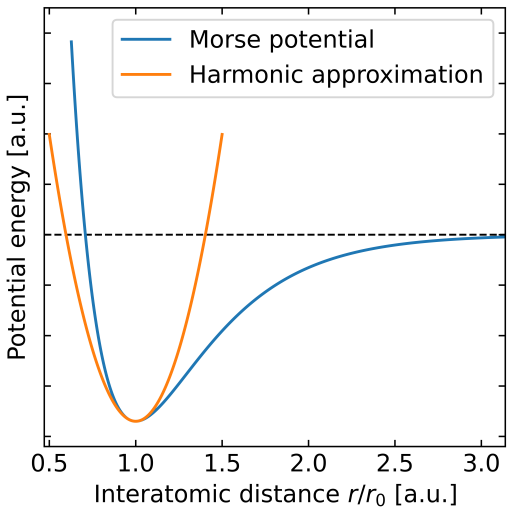

Figure 1.2: Morse potential for atomic interaction with the harmonic approximation, which is valid near the equilibrium distance.

A useful simplification of this situation is the harmonic approximation.[27] Since the thermal energy of the respective atoms is usually minor compared to the depth of potential, their movement is restricted to distances close to the equilibrium distance. Therefore, it is possible to imagine the interatomic interactions as a harmonic spring-mass system, where the atoms in a solid are connected by springs since springs represent a model system for harmonic potentials. The movement of any atom is consequently coupled to the whole system, creating lattice waves. If there are temperature differences in the solid, similar to the situation in Figure 1.1, the atoms near the hot side will have larger vibrational amplitudes, which can propagate to the cold side through lattice waves. Without going into too much detail, those propagating waves can be deduced from quantum mechanical principles, where the minimum energy of a quantized lattice wave is termed a phonon. The superposition of several phonons with multiple frequencies forms wave packets with a narrow spatial extend, which in turn can be considered particles as long as they are much smaller than the crystal.[24] Again, using this particular conception, heat transport in a dielectric solid can be thought of as similar to the heat conduction of the gas molecules in Figure 1.1, resulting in the phonon gas model.[28]

In metallic solids, another transport channel opens up. The phonon picture is also valid in this case, but in contrast to dielectric solids, metals exhibit free electrons.[29] Those free electrons can travel distances much larger than the interatomic distances until they are scattered, leading to the electron gas concept, similar to the phenomena described above.[30] Again, the electronic heat conduction process then can be thought of as similar to the gas in a box with different average velocities due to temperature and, eventually, temperature diffusion due to collisions of the carriers. Since, in most metals, the energy flux carried by electrons is much larger than the one carried by phonons, electrons usually are the dominant heat carriers in metals.[31]

All microscopic descriptions discussed above relate to thermal conduction. In general,

heat can be transferred in three modes. Those are called conduction, convection, and radiation and will be discussed in the following.

1.2.2 Conduction

Heat conduction is the energy transfer process through a medium due to the random motion of heat carriers in a substance.[32] As discussed above, those heat carriers can be molecules, atomic vibrations, phonons, or electrons. Since heat carriers are needed for heat conduction, heat conduction can only take place inside a medium. The macroscopic law describing steady-state heat conduction is named the Fourier law after Joseph Fourier, who expressed it first in his heat transport text in 1822.[33] The law in its one-dimensional form is depicted in Figure 1.3, where the heat flux per unit area Q_{cond} is directly proportional to the temperature gradient. The constant of proportionality is the thermal conductivity k, a material constant at the macroscopic scale.

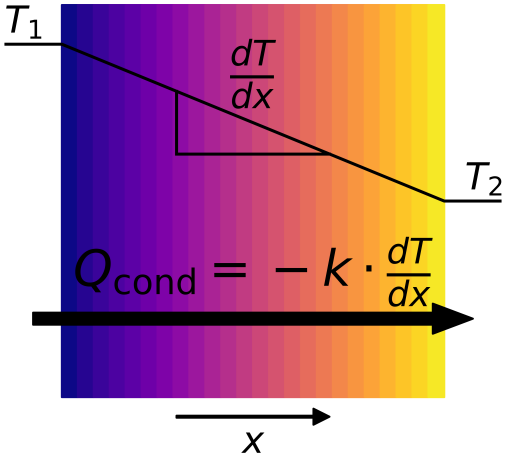

Figure 1.3: Fourier law: Rate of heat conduction through a solid is directly proportional to its thermal conductivity.

The thermal conductivity has units of W m^{-1} K^{-1} and is a measure of the material's ability to conduct heat. A high value for thermal conductivity indicates that the material is a good heat conductor, and a low value indicates that the material is a poor heat conductor or insulator.[18] Value-wise, approximately five orders of magnitude are spanned by natural materials from insulators like gases or foams with 0.01 W m^{-1} K^{-1} to highly conducting materials like diamond with above 1000 W m^{-1} K^{-1} at room temperature.[34–38] In Figure 1.4, the thermal conductivity of some examples of materials is presented.

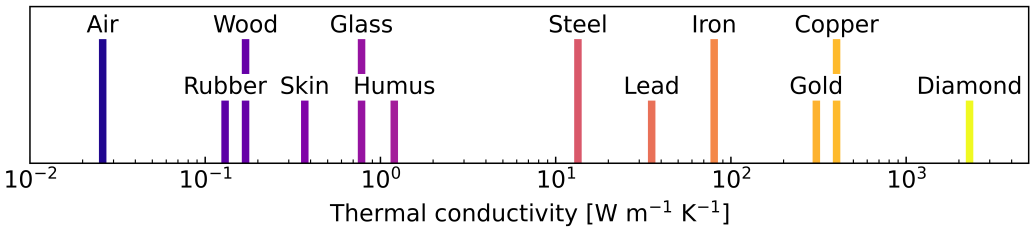

Figure 1.4: Overview of the thermal conductivity of various example materials spanning several orders of magnitude.

1.2.3 Convection

Convection is the mode of energy transfer between a solid surface and the adjacent liquid or gas in motion.[39] It involves the combined effects of conduction and fluid motion.[18] Based on the developed concept of thermal conduction, this can be understood as relatively straightforward. As for conduction, there is a random motion of the heat carriers with an average velocity of zero since they are moving in all directions. For convection, there is a preferred direction of movement and, therefore, a non-zero average velocity. The faster the fluid motion above the solid surface, the higher the convective heat transport. Energy is first transferred from the solid surface to the fluid above by pure conduction. This energy is then transferred away from the surface by convection in the fluid.[18]
Mainly two cases are considered for convection, either forced or natural convection.[40] For forced convection, the fluid is forced to flow over the surface by external means like a fan, pump, or wind.[18] Natural convection, in contrast, is purely buoyancy-driven and therefore related to density differences in the fluid due to temperature. The most commonly used law to describe convective heat transport is Newton's law of cooling, relating the convective heat flux per unit area Q_{conv}, with the temperature difference between solid and liquid $(T_{\mathrm{s}} - T_{\infty})$ and a convective heat transport coefficient h:[41]

$$Q_{\mathrm{conv}} = h \cdot (T_{\mathrm{s}} - T_{\infty}). \tag{1.1}$$

The convection heat transport coefficient h has the unit of W m^{-2} K^{-1}, similar to the thermal conductivity, but in contrast, it is not a property of the fluid. It is an experimentally determined parameter whose value depends on all the variables influencing convection, such as the surface geometry, the nature of fluid motion, the properties of the fluid, and the bulk fluid velocity.[18]

1.2.4 Radiation

Heat transport by thermal radiation is conceptually different from heat transport by conduction or convection. In contrast to (random) movement and consequently collisions between the heat carriers, thermal radiation originates in the movement of charges or energetic transitions of molecules, atoms, and electrons of a substance.[42] Temperature is a measure of the strength of these movements at the microscopic level, and the rate of thermal radiation emission increases with increasing temperature.[18] Similar to radio waves, which are generated by an artificial current, the movement of electrons around nuclei generates thermal radiation. The electrons are a much faster oscillator than the induced current to produce radio waves and, therefore, produce radiation much shorter in wavelength. Consequently, radio waves have wavelengths

in the regime above 1 mm, while thermal radiation at ambient temperature exhibits wavelengths in the regime of several μm. In general, thermal radiation does not require a transport medium, and electromagnetic waves, also termed photons as elementary particles, carry the energy.[24] In contrast to conduction and convection, which are inherently based on collisions of the heat carriers, for radiation, the heat carriers typically travel long distances before interacting with matter.[43] Therefore, analysis of thermal radiation often deals with boundaries and interfaces.

The idealized object that emits the maximum radiation is called a blackbody, and the radiation emitted by a blackbody is called blackbody radiation.[18] The amount of radiation a blackbody emits per unit area and unit solid angle is given by Planck's law:[44]

$$B(\lambda, T) = \frac{2hc^2}{\lambda^5} \frac{1}{\exp(\frac{hc}{\lambda k_b T}) - 1}. \tag{1.2}$$

The spectral radiance of the blackbody B is, therefore, a function of temperature T and wavelength λ.

In Figure 1.5, it can be seen that the maximum spectral radiance shifts to smaller wavelengths with increasing temperature and that the spectral radiance rises with temperature. The shift to lower wavelength, or higher energy, can be explained by the increasing velocity of movement of the electrons at a higher temperature and, therefore, a fast oscillator or a shorter emitter emitted wavelength. The increasing spectral radiance is described by the Stefan-Boltzmann law, stating that the emitted power of a blackbody, equivalent to the area below the curves, scales with T^4.

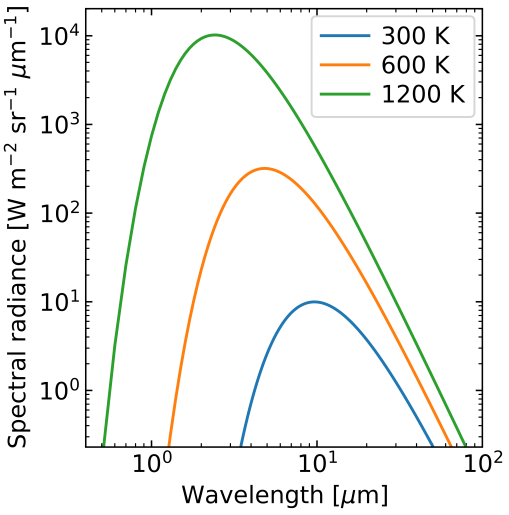

Figure 1.5: Blackbody spectral radiance as a function of temperature.

However, real objects do not resemble an idealized blackbody and emit less thermal radiation. This regard is taken into account by scaling the blackbody spectral radiance with the material's emissivity. The emissivity takes values between zero and one for every wavelength and is a measure of how closely the material resembles a blackbody radiator. The emissivity is equivalent to the absorptivity, as stated by Kirchhoff's law, and can, therefore, be determined experimentally.[45]

In addition to the principles of thermal radiation, the quantification of the heat transport between two objects is also of interest. The simplest case of radiative heat transport are two parallel black walls separated by a vacuum. The radiative

heat flux per unit area Q_{rad} then results from the difference of counter-propagating photons from one wall to the other:

$$Q_{\text{rad}} = \sigma \cdot (T_1^4 - T_2^4). \tag{1.3}$$

Where σ is the Stefan-Boltzmann constant, resulting from the integration of Planck's law over all wavelengths and solid angles corresponding to a hemisphere above the surface, and $T_{1/2}$ the temperatures of the parallel walls. In real situations, emissivities and fields of view have to be considered.

1.3 Low Thermal Conductivity Materials

Most of the materials treated in this thesis possess low thermal conductivities. Therefore, a more detailed picture of the microscopic heat transport in these specific materials will be given.

In Section 1.2.1 a picture of microscopic heat transport in ordered dielectric and metallic solids was presented. However, with low thermally conductive materials, some unique characteristics are to be considered.

The first material class of interest are organic-inorganic halide hybrid perovskites, which attracted considerable attention as promising light absorbers in photovoltaic cells or as emitters in light-emitting diodes due to their outstanding optical properties and solvent processability.[46,47] In general, metal halide perovskites are the first solution-processed semiconductors that can compete in their functionality with conventional semiconductors, such as silicon.[48,49] The most studied example of organic-inorganic halide hybrid perovskites is methylammonium lead triiodide ($MAPbI_3$), whose crystal structure is shown in Figure 1.6.[50]

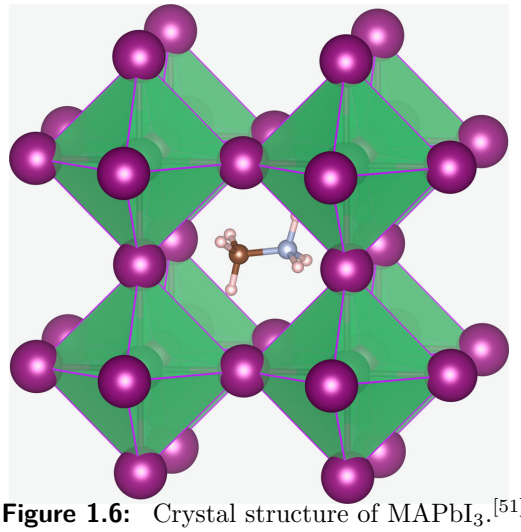

Figure 1.6: Crystal structure of $MAPbI_3$.[51] Reprinted from Springer Nature.

The structure is built from the methylammonium cation, surrounded by corner-sharing PbI_6 octahedra. Even though the inorganic lattice fulfills the criteria for phononic heat transport, namely covalent bonding, and long-range order, this material class exhibits thermal conductivities in the range of $0.3 - 0.5$ W m^{-1} K^{-1}.[52,53] Estimating the thermal conductivity of dielectric solids is based on knowledge about the individual carriers, in this case, phonons. How much energy per carrier do they transport, how many carriers are present, how fast and far they move, and how they interact are issues that need

to be addressed. First-principle calculations can address these questions, which can provide valuable insights into microscopic transport.[54]

Following such calculations, the low thermal conductivity of $MAPbI_3$ is mainly attributed to the rotational motions of the methylammonium cations. The methylammonium cations' translational and rotational movements interact with the lead iodide cages and build couplings between the isolated lattice vibrations, suppressing the overall phonon transport.[55] These findings are most likely applicable to a large portion of organic-inorganic hybrid materials with particular emphasis on the compounds, including complex organic molecules, where more vibrations are reciprocally coupled.[55]

Based on those organic-inorganic halide hybrid perovskites, reducing the dimensionality of the inorganic sublattice by incorporation of large organic molecules such as butylammonium (BA) or phenylethylammonium (PEA), which are too large to fit into a three-dimensional octahedral structure, affords bulk materials that combine many of the outstanding optoelectronic properties of the 3D parent materials, while exhibiting features of quantum and dielectric confinement and improved moisture stability.[56,57] The crystal structures of those 2D perovskites are shown in Figure 1.7. The structures consist of alternating organic and inorganic layers. While in the inorganic layers, energy can be transported via the covalent bonds, in the organic layer, the individual cations are only coupled mostly via van der Waals interactions. These 2D systems now constitute a non-negligible problem if their heat transport properties are to be described by first-principle calculations. As the size of the unit cells expands considerably, the computation time of such calculations increases with the number of particles N by N^3.[58]

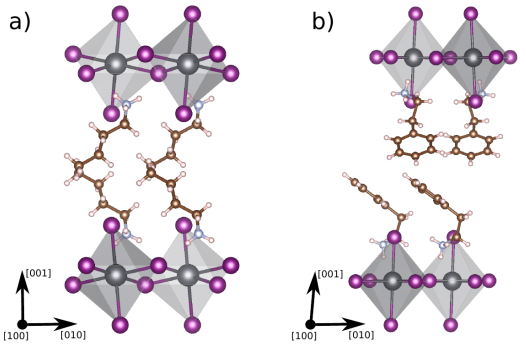

Figure 1.7: Schematic representation of the crystal structures of a) *Pbca* phase of BA_2PbI_4, b) $P\bar{1}$ phase of PEA_2PbI_4.

The thermal properties can therefore only be determined and analyzed experimentally, and structure-property relationships result primarily from the accurate and careful design of the experiments. In contrast to the 3D $MAPbI_3$, the organic component not only couples to the inorganic lattice vibrations, but the inorganic lattice itself is only present in 2D layers. The phonon concept, based on wave packets of lattice vibrations, breaks down perpendicular to the layers. Therefore, the heat transport attenuation is based on the hopping of individual vibrational states from one organic molecule to another perpendicular to the layers instead of wave-like transport.[59] The layered structure leads to a strong directionality of nearly all material properties, termed anisotropy. In general, it is to be expected that transport of all kinds, e.g., electronic or thermal, perpendicular to the layers is significantly reduced compared to transport in or parallel to the layers.

Another low-dimensional system of interest in this thesis are nanosheet polymer stacks, also known as nacre-mimics, composed of synthetic clay sodium fluorohectorite and intercalated polymers.[60] A schematic representation of these systems is shown in Figure 1.8.

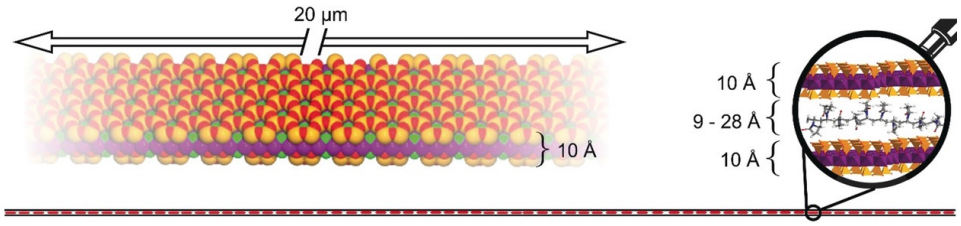

Figure 1.8: Schematic of ultra-anisotropic and extremely confined Hec/PVP Bragg stacks. Space-filling model of one single Hec nanosheet emphasizing the anisotropy of the nanosheet and the corrugation of the clay nanosheet allowing for interdigitation with PVP. True to scale schematic of the pronounced structural anisotropy. The ultra-high-aspect-ratio nanosheets stretch from left to right and have lateral dimensions much larger than the length of the PVP polymer chains. The gallery height is on the order of magnitude of the molecular dimensions.[60] Adapted from John Wiley and Sons.

The hectorite platelets' size is at least in the order of hundreds of nanometers, while their periodicity in the stacking direction is one to three nanometers. These systems, therefore, can be considered two-dimensional and highly anisotropic.[61] Again, while in 2D, a periodic lattice is present, enabling the concepts of wave-like transport, in the perpendicular direction, these concepts break down. In contrast to organic-inorganic halide hybrid perovskites, mainly used for their electronic and optical properties, hectorites especially offer unprecedented potential as highly transparent nanocomposites with superior gas barrier and mechanical properties.[62] The general assumptions of 2D crystallinity of the inorganic component and cross-plane van der Waals interactions between organic component is provided here as well.

Further reducing the order of 2D materials results in amorphous materials. Unlike crystals, amorphous materials lack translational symmetry and periodicity over a long distance.[63] This lack of symmetry and periodicity also is the main reason why the theoretical understanding of heat transport in amorphous materials is considerably less sophisticated compared to their crystalline counterparts.[63] Einstein first proposed a theoretical framework for heat transport in amorphous materials.[64] This theory is based on the assumption of non-correlated vibrations among neighboring atoms or molecules, corresponding to the contrary of extended waves in crystals.[63] Heat transport then results from a random walk of these independent oscillators, similar to the situation described in Figure 1.1. Some example materials are amorphous SiO_2, SiN_x or Al_2O_3.[65–67] Still, the circumstances of lack of symmetry and periodicity can also be encountered in polymers.

The heat transport properties of polymers are very susceptible to the arrangement of the molecules within the material. For example, well-aligned polymeric chains can ex-

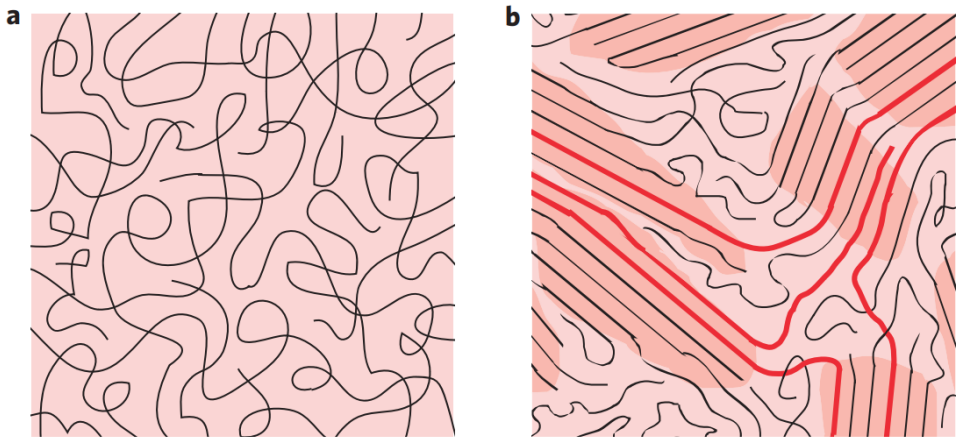

Figure 1.9: a) Schematics of a completely amorphous polymer film and b) the microstructure of a semicrystalline polymer film.[73] Adapted by permission from Springer Nature.

hibit exceptionally high thermal conductivities, i.e., above 100 W m^{-1} K^{-1}.[68,69] In contrast, disordered polymeric chains often exhibit thermal conductivities an order of magnitude smaller than that of silica glass and, therefore, below 1 W m^{-1} K^{-1}.[70,71] In disordered polymeric films, thermal conductivities exhibit temperature dependencies that are typical of amorphous solids, and heat transport is limited by a random walk of localized energy on the time and length scales of atomic vibrations and interatomic spacing, respectively.[70] The general transport scenario is consequently very similar to that in amorphous solids. However, the situation can be even more complicated depending on the polymer. A significant proportion of polymers are not purely amorphous but exhibit a semi-crystalline microstructure.[72] The comparison of amorphous and semi-crystalline microstructures is shown in Figure 1.9.

In an amorphous polymer film, the individual polymer chains are entangled, and there is no long-range order. The chains are, therefore, arranged randomly throughout the material. Some chains form stacks of parallel or folded chains for semi-crystalline polymer films, known as lamellae.[74] These lamellae bring long-range order to polymers, similar to the arrangement of atoms in typical crystals. A variety of free parameters exist in the semi-crystalline microstructure like the overall degree of crystallinity, the paracrystallinity, i.e., fluctuations in lattice spacings, the average size of crystallites, and the connectivity between them, to mention the most important ones. Even though some polymer films exhibit crystalline domains, where transport can be facilitated, the amorphous regions remain the bottleneck to be bridged.[75]

In summary, it can be said that in 3D crystalline materials, low thermal conductivities are mainly present when the properties of the wave-like transport are directly influenced. One example is the introduction of organic cations like methylammonium in $MAPbI_3$, where translational and rotational movements couple to the lattice vibrations, leading to a suppressed heat transport. For 2D materials, like BA_2PbI_4, PEA_2PbI_4 or hectorite/polymer Bragg stacks, the transport perpendicular to the crystalline layers is suppressed as the coupling strength due to van der Waals forces

in the organic layers is significantly decreased compared to the covalent bonds in the inorganic layers. Parallel to the layers, wave-like transport can be present in the inorganic layers, while perpendicular to the layers, the transport is limited by hopping processes in the organic layers. The 2D order, therefore, manifests itself in the phenomena of anisotropic (transport) properties. Further reducing the degree of order to amorphous systems eventually leads to the collapse of wave-like transport. In those systems, heat is transported mostly by hopping of non-correlated vibrations in a random walk fashion.

1.4 Passive Radiative Cooling

The concept of radiative cooling was already discussed in the 1980s but has attracted renewed interest in the last decade.[76–78] As depicted in Figure 1.10, the maximum radiance of a blackbody at ambient temperatures coincides with the major transmittance window of the earth's atmosphere. By exploiting this window between 8 μm and 13 μm, one can cool a body on the earth's surface by radiating its heat away into cold outer space, acting as an ultimate heat sink at 3 K.[77] Because thermal radiation is an inherent material property, as discussed in Section 1.2.4, there is no need for any energy input, making it very interesting from the point of view of energy efficiency. For nighttime operation, a material that approaches the optical properties of a blackbody in the sky window regime as close as possible is well suited. In contrast to this, during daytime operation, where there is the highest demand for cooling applications, special care must be taken to avoid energy uptake due to the absorption of solar radiance.

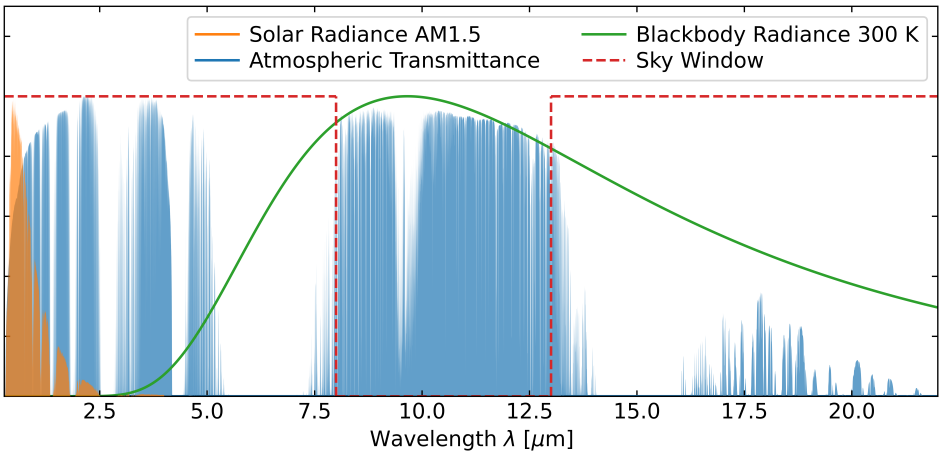

Figure 1.10: Concept of radiative cooling. As the maximum blackbody radiance at ambient falls into the wavelength regime of the sky window, radiation can be emitted into outer space. At the same time, energy uptake due to absorption of solar or atmospheric radiation must be avoided.

The thermal radiance emitted by a present material is defined by the product of the material's emissivity and the blackbody radiation at the respective temperature. Following Kirchhoff's law, stating that the absorptivity α is equal to the emissivity ε at any wavelength, the optical properties of the passive cooler are the essential property.[45] Based on this, the total emitted power, or emittance P is the result of an integration over all wavelengths or energies and over all angles in a hemisphere above the sample. This is conceptually displayed for a fixed angle θ in Figure 1.11. Mathematically the emittance at a fixed angle therefore can be described as $P(T,\theta) = \int_0^\infty B(\lambda,T) \cdot \varepsilon(\lambda,\theta)\, d\lambda$. The total emittance into a hemisphere above then results from performing this for all possible angles, which can also be achieved through integration.

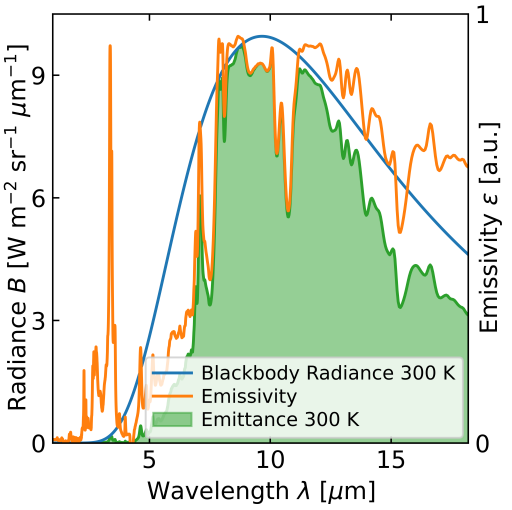

Figure 1.11: Schematic diagram for calculating the thermally radiated power at a fixed angle.

The same concept is valid for absorbed solar or atmospheric radiation, where the total power results from an energetic and for the atmosphere also angular integration over the product of the incoming radiance and the sample's emissivity, or absorptivity, respectively.

One way to optimize this energy balance is to design a material that emits only in the sky window range and does not otherwise interact with electromagnetic radiation.[79]

If the energy equilibrium is to be determined mathematically, the respective radiances, depending on the optical properties, must be integrated over all wavelengths and hemispheric angles to determine the total power. How such an integration can be performed numerically is discussed in Section 2.4.1.

2 Methods

After introducing the theoretical concepts of heat transport, methods for determining the thermal properties can be discussed. In most experimental situations where the thermal properties are determined, convection effects are neglected. While convection severely impacts heat transport in many application-oriented cases, it represents another free parameter for property determination. Therefore, the experimental conditions are usually designed to exclude convective effects. Radiation effects are also neglected in most practical situations at or near room temperature. But as radiative heat transport scales with T^4, for elevated temperatures, it also can have a significant influence on the transport situation. Still, again for property determination, it represents another free parameter that is tried to be excluded. Therefore, the main focus of this chapter is on heat transport through heat conduction.
After discussing the influence of time dependence on thermal measurements, the two primary characterization techniques applied in this work are discussed. These are the light flash analysis and the photoacoustic technique. Finally, the crucial numerical methods used in this thesis will be described.

2.1 Time and Frequency Domain

Measurement methods for characterizing the thermal conductivity (k) of materials can be conceptually divided into steady-state and transient methods. Heat transport in a medium is steady when the temperature does not vary with time and unsteady or transient when a time dependency is present.[18]
Based on Fourier's law, steady-state measurements allow for direct thermal conductivity measurement. The heating power is related to the supplied heat flux for steady-state measurements, while the temperature rise is determined. Fourier's law can thus be used to directly determine the thermal conductivity via the ratio of heat flux and temperature rise. Although conceptually, this sounds relatively simple, the exact determination of the applied heat flux often poses a non-trivial problem.
In contrast, transient measurements are based on the thermal diffusion equation, such that volumetric heat capacity (c_v) and thermal conductivity are coupled via thermal diffusivity (D) or thermal effusivity (ε), depending on the time and length scales of the measurement.[80] The thermal diffusivity is defined by $D = \frac{k}{c_\mathrm{v}}$ and the thermal effusivity by $\varepsilon = \sqrt{k c_\mathrm{v}}$ and the use of this grouping will prove to be very

instructive in the frequency domain.

The thermal diffusion equation is the governing equation for most thermal problems discussed in this thesis. It can be derived from the first law of thermodynamics, namely conservation of energy and the Fourier law. Regardless of whether heat conduction, chemical diffusion, or other diffusion processes are to be described, the diffusion equations governing these diverse physical phenomena are derived using the same methodology.[81] That is, by combining a conservation statement (e.g., conservation of mass or energy) with a constitutive law relating flux to gradients in the conserved potential.[81]

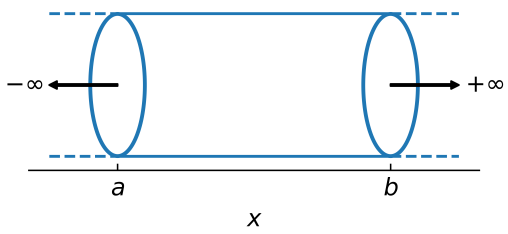

Figure 2.1: Infinite one dimensional rod.

For the most simple 1D case of deriving the thermal diffusion equation, imagine an infinite rod as depicted in Figure 2.1. Taking into account the conservation of energy in the depicted rod, the rate of change in thermal energy ϵ in the section for $a < x < b$ is the net energy flow across the boundaries of this section $Q(a,t)$ and $Q(b,t)$, plus the energy being generated internally $\varphi(x,t)$ in the considered section. This can be expressed as:

$$\frac{\partial}{\partial t}\int_a^b \epsilon(x,t)dx = Q(a,t) - Q(b,t) + \int_a^b \varphi(x,t)dx. \tag{2.1}$$

Assuming that both thermal energy ϵ and energy flow across the boundaries Q have continuous first-order partial derivatives, this leads to:

$$\int_a^b \frac{\partial \epsilon(x,t)}{\partial t}\partial x = -\int_a^b \frac{\partial Q(x,t)}{\partial x}dx + \int_a^b \varphi(x,t)dx, \tag{2.2}$$

which can be rearranged to:

$$\int_a^b \left(\frac{\partial \epsilon(x,t)}{\partial t} + \frac{\partial Q(x,t)}{\partial x} - \varphi(x,t)\right)dx = 0. \tag{2.3}$$

Since this is true for each choice of a and b with $-\infty < a < b < +\infty$, if φ is continuous it follows that:

$$\frac{\partial \epsilon(x,t)}{\partial t} = -\frac{\partial Q(x,t)}{\partial x} + \varphi(x,t). \tag{2.4}$$

By definition, the thermal energy is related to the temperature T and the volumetric heat capacity by:

$$\epsilon(x,t) = c_{\mathrm{v}}(x,t)\cdot T(x,t). \tag{2.5}$$

It is generally assumed that the volumetric heat capacity does not change with time, in which case equation (2.4) simplifies to:

$$c_{\mathrm{v}} \frac{\partial T(x,t)}{\partial t} = -\frac{\partial Q(x,t)}{\partial x} + \varphi(x,t). \tag{2.6}$$

So far there is one equation but two unknown functions $T(x,t)$ and $Q(x,t)$. To solve the mathematical problem, an additional equation is required. This additional equation is phenomenological and is generally called a constitutive relation.[81] For heat flow, the equation is Fourier's law as depicted in Figure 1.3 with $Q = -k \cdot \frac{\partial T}{\partial x}$. Inserting into equation (2.6) leads to:

$$c_{\mathrm{v}} \frac{\partial T(x,t)}{\partial t} = \frac{\partial}{\partial x}\left(k \cdot \frac{\partial T(x,t)}{\partial x}\right) + \varphi(x,t). \tag{2.7}$$

Assuming that the thermal conductivity is homogeneous and not space-dependent, this leads to the final thermal diffusion equation with internal heat generation:

$$\frac{\partial^2 T(x,t)}{\partial x^2} = \frac{1}{D}\frac{\partial T(x,t)}{\partial t} - \frac{1}{k}\varphi(x,t). \tag{2.8}$$

Solving this partial differential equation for the present experimental situation results in the material's thermal properties under investigation. For steady-state conditions, the time dependency of the equation vanishes, while for transient measurements, the entire equation has to be considered.

Typical transient realizations move in either the time or frequency domain. The sample is subjected to a thermal pulse in the time domain while the temporal temperature change is detected following the pulse. The time-dependent excitation and following temperature evolution are conceptually illustrated in Figure 2.2a and b for a Dirac delta excitation.

In the frequency domain, the sample is exposed to a (harmonically) modulated heat source instead of a heat pulse, allowing the amplitude and phase of the oscillating temperature to be determined, as shown in Figure 2.2c and d. Measurements at different frequencies thus yield a characteristic relationship.

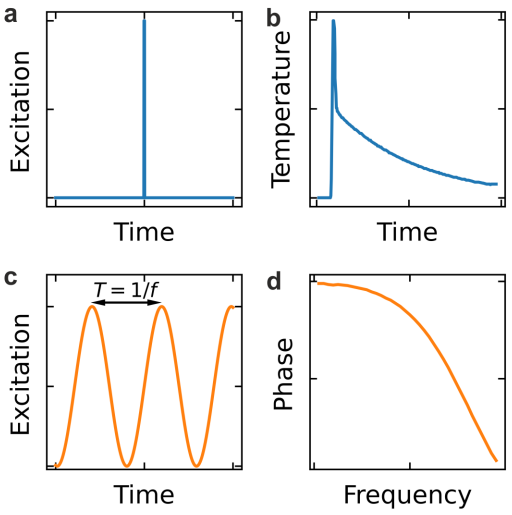

Figure 2.2: a) Thermal excitation in time and c) frequency domain. b) Corresponding thermal response in time and d) frequency domain.

Regardless of the domain used, the measured temperature is fitted to an appropriate model via non-linear regression, whereby the unknown properties are determined.

2.2 Light Flash Analysis

Light flash analysis (LFA), sometimes also referred to as laser or xenon flash analysis, depending on the excitation source, has become a widely used standard technique to measure the thermal diffusivity of bulk materials under various conditions like different gases, atmospheric pressures, and temperatures.[82] The general idea is based on a thermal excitation on one side of the sample, while the temperature increase on the opposite side is detected as a function of time. The characteristic time with which the heat flows through the sample can then be related to the thermal diffusivity. The measurement thus falls into the category of transient measurements. The general measurement geometry for this is shown in Figure 2.3.

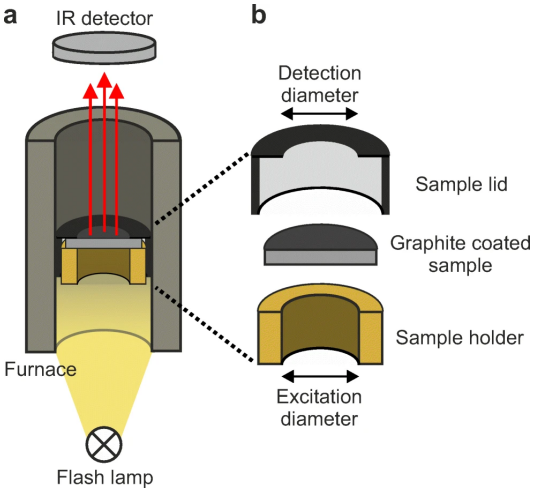

Figure 2.3: a) Simplified LFA set-up. b) Schematic illustration of the sample configuration consisting of sample holder, graphite coated sample, and sample lid.[82] Reprinted by permission from Springer Nature.

The thermal excitation in this technique is realized through optical excitation. This excitation offers the advantage of not having to contact the sample directly but requires either a highly absorbing sample or the application of an absorbing coating. Graphite is often used for this. Part or all absorbed light energy is transformed to heat through non-radiative deexcitation processes, converting the optical into a thermal excitation.[83] Following the laws of thermodynamics, the heat will spread evenly in the sample, leading to thermal equilibrium. Therefore, the backside of the sample will also rise in temperature, which is monitored using an IR detector. Depending on the sample thickness, the time evolution of the detector signal is fitted to an appropriate theoretical model to extract the thermal diffusivity.

As depicted in Figure 2.3b, the general setup measures the cross-plane properties. However, if a particular sample holder is used, the in-plane properties can be determined as well if appropriate boundary conditions are fulfilled. For cross-plane measurements, assuming an instantaneous and uniform absorption of the flash in a thin layer, and a thermally insulated solid of uniform thickness L, the temperature at the backside as a function of time t can be modeled as:[84,85]

$$T(L,t) \propto \frac{1}{L}\left[1 + 2\sum_{n=1}^{\infty}(-1)^n \exp\left(\frac{-n^2\pi^2}{L^2} D \cdot t\right)\right]. \tag{2.9}$$

The characteristic time required for the back surface to reach half of the maximum temperature rise t_c can therefore be used to determine the thermal diffusivity D via:[85]

$$D = 0.1398 \cdot \frac{L^2}{t_c}. \tag{2.10}$$

It is unnecessary to know the amount of energy absorbed in the front surface to determine the thermal diffusivity, as illustrated by the proportionality sign in equation (2.9). However, this quantity must be determined if specific heat or thermal conductivity measurements are required.[85] Another approach to determining the thermal conductivity is to measure specific heat c_p and density ρ separately.
Based on the simplest adiabatic concept shown in equations (2.9) and (2.10), further models have been developed to describe more complex experimental situations. For thermally thicker samples and the associated long measurement times (magnitude of 10^0 seconds) or high temperatures (above 1000 K), the adiabatic boundary condition can usually no longer be maintained, leading to the development of models that take thermal losses into account.[86] In contrast, for thermally thin samples and the associated short measurement times (magnitude of 10^{-3} seconds), the actual temporal shape of the excitation can no longer be neglected, as excitation (magnitude of 10^{-4} seconds) and characteristic thermal response are present in a similar magnitude of time. Suitable models have, in consequence, been developed for this purpose as well.[87] As the measurement method is particularly suitable for high-temperature measurements, where radiative transport effects often can no longer be neglected, as discussed above, models have also been developed that can also consider radiative transport.[88] The radiative transport manifests itself by an almost instantaneous (magnitude of 10^{-10} seconds) conduction through the material. Generalized models have also been developed, unifying all mechanisms.[89]

Figure 2.4 shows how the different experimental situations can affect the measurement signal. For adiabatic conditions, the signal represents the time dependency following equation (2.9), allowing the determination of the thermal diffusivity directly from the characteristic time t_c and the sample thickness. If heat losses are apparent, the situation becomes more complicated, and the signal or backside temperature, respectively, does not reach a plateau but decreases after a maximum. The signal has to be fitted to a complete model by non-linear regression. At elevated temperatures and for (semi-)transparent samples, radiation effects manifest in the measure-

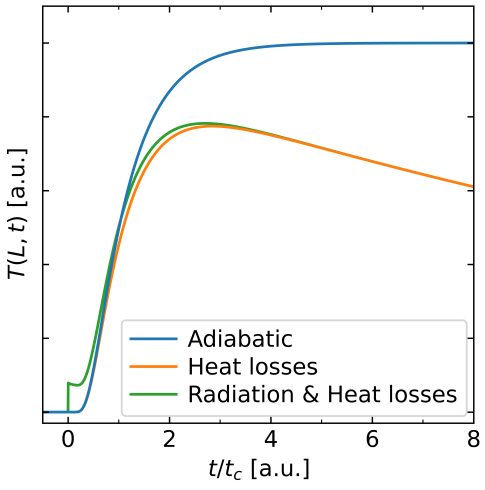

Figure 2.4: Influence of the measurement environment and the associated experimental situation on the measurement signal.

ment signal at times close to the optical excitation $t = 0$ as radiation travels through the sample almost instantaneously.
The main disadvantages of the method are that free-standing samples are required and that thermally thin samples raise problems with the detection. As the characteristic time of the samples decreases below the millisecond range, most IR detectors can no longer resolve the temporal profile.
In contrast, the light flash analysis is excellent for determining the thermal diffusivity of bulk and free-standing materials. The main advantages are a relatively simple measurement, contactless excitation, various theoretical models, and the possibility to measure at elevated temperatures.

2.3 Photoacoustic Technique

A method complementary to the LFA is the photoacoustic technique, which thermally characterizes supported thin films. Similar to LFA, the excitation is based on optical absorption and subsequent thermalization of the excited states. In contrast, the frequency domain is utilized here. The general measurement setup for the photoacoustic technique is shown in Figure 2.5.

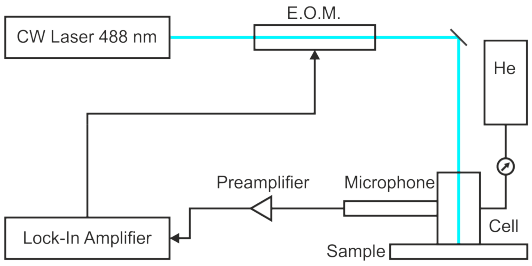

Figure 2.5: Schematic setup with a continuous wave laser being passed through an EOM to provide the modulated heat source. The photoacoustic signal is measured using a microphone in the pressurized cell.[90] Reprinted from Elsevier.

A continuous-wave laser is periodically modulated and heats the sample, and the surface temperature is related to a pressure signal in a gas-filled cell above the sample. The surface temperature can then be related to the sample thermal properties using analytical models. In fact, Bell mentioned the photoacoustic effect for the first time in 1880, who observed that disks of very many different materials emitted sounds when exposed to the action of a periodically interrupted beam of sunlight, called the photoacoustic effect.[91] For thermal characterization, Rosencwaig and Gersho proposed the basic theory of the photoacoustic effect in condensed matter in 1976.[90,92] The periodic heating of the sample enclosed beneath a gas-tight cell can have two effects, which are referred to as thermal and mechanical piston. The mechanical piston effect is dependent on the thermal expansion of the sample, which compresses the gas in the cell. In contrast, the thermal piston effect is caused by heat conduction from the sample to the gas directly above, compressing the rest of the gas due to the increased temperature and volumetric expansion. For solid samples,

where the thermal expansion coefficient is typically in the order of 10^{-5} K^{-1}, the mechanical piston can be neglected, and only the thermal piston has to be considered.[93] The surface temperature can therefore be determined from the measured pressure signal, which in turn can be fitted to an analytic model. A typical sample geometry for determining the thermal properties of a thin film is depicted in Figure 2.6. Three layers are present with a thermally thin transducer to ensure high absorption of the modulated laser, the sample with unknown thermal properties, and a thermally thick backing with sufficient thermal contrast to the sample.

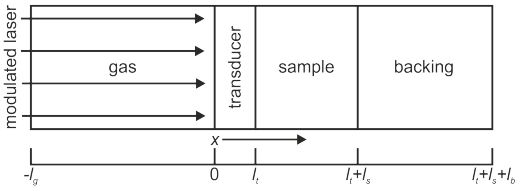

Figure 2.6: Schematic representation of the modeled sample geometry, including a transducer and a thermally thick backing.[90] Reprinted from Elsevier.

For photoacoustic measurements of this kind, it has been recognized that the one-dimensional heat transport model is adequate for describing the temperature variation under typical experimental conditions when the thermal diffusion length in gas and the target is much less than the diameter of the laser beam.[93] Therefore, based on equation (2.8), the thermal diffusion equation in layer i for a sample with N layers, in general, can then be expressed as:[93]

$$\frac{\partial^2\theta_i}{\partial x^2} = \frac{1}{D_i}\frac{\partial\theta_i}{\partial t} - \frac{\beta_i I_0}{2k_i}\exp\left(-\sum_{m=i+1}^{N} -\beta_m l_m\right) e^{\beta_i(x-l_i)}(1+e^{j\omega t}) \tag{2.11}$$

Where I_0 is the amount of incident radiation, β_i is the optical absorption coefficient of layer i, and ω is the angular frequency of the modulated excitation. The main difference to the thermal diffusion in equation (2.8) is the adapted source term which is related to the optical absorption here. The modified temperature $\theta_i = T_i - T_{\text{amb}}$ in layer i exhibits various components, which are shown exemplarily in Figure 2.7. The solution for the modified temperature θ_i of the above thermal diffusion equation consists of a transient component, a steady DC component, and a steady AC component. The transient component can be challenging to describe and is usually not of particular interest. This transient component is in the time domain exclusively before reaching a quasi steady-state, and therefore a measurement usually starts to collect data only after a certain settling time.

After reaching a quasi-steady state, only the ΔT_{AC} and ΔT_{DC} components prevail. Because lock-in detection is applied, which only picks up the AC component at the frequency of excitation, only ΔT_{AC} needs to be evaluated to solve equation (2.11). Assuming a thermally thick backing, the equation can be solved analytically, discussed in detail in Chapter 5. The equation is solved as a function of frequency and then fitted to the measurement data, similarly to Figure 2.2d.

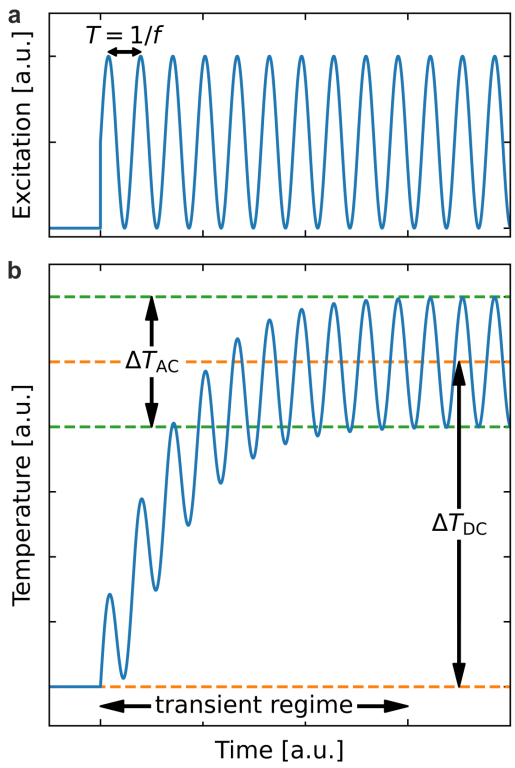

Figure 2.7: a) Periodic excitation and b) general temperature response as function of time.

To summarize, for a three-layer sample, as shown in Figure 2.6, the thin film samples need to have a thickness in a particular regime, depending on the thermal diffusivity. The backing should have a thermal effusivity in a similar order of magnitude as the sample. With known properties of backing and transducer and the sample thickness, the thermal properties of the sample thermal diffusivity D, thermal effusivity ε, and, therefore, the thermal conductivity k can be determined.

Consequently, the photoacoustic technique enables the thermal characterization of supported thin films for low diffusivity materials in a thickness range of several μm and sub-μm.[90] Main drawbacks are the necessity of the application of a transducer layer with defined thickness, as well as reliable thermal properties for substrate and transducer material. Also, the somewhat limited accessible frequency regime (magnitude of 10^1-10^4 Hz) can be considered a drawback, as thin films of materials with high thermal diffusivities or even thinner films of low diffusivity materials constitute a sensitivity problem for the technique. Still, the relatively simple measurement setup and the determination of thermal diffusivity and thermal effusivity in one measurement more than compensate for this.

2.4 Numerical Methods

Numerical methods have become all-encompassing in physical chemistry and are now indispensable. Over the last few decades, the exponential increase in computing power has opened up a wide range of possibilities that were previously impossible to implement.[94] The three most commonly used numerical methods in this work are therefore examined in a little more detail. On the one hand, this is the numerical solution of integrals based on experimental data or in analytical approximation, which can often represent measurable quantities. Likewise, the numerical solution of derivatives is of interest, as they can be used to estimate the sensitivity of a measurement to the quantity to be determined. Furthermore, this is the non-linear

fitting of a theoretical model to available measurement data in order to determine the free parameters or the material properties, respectively.

2.4.1 Numerical Integration

When functions are complicated or not analytically defined, the numerical solution of the integration provides a great approximation. To examine the basic concepts, the trapezoidal approximation for the function $f(x) = \frac{1}{4}x + \sin(x)$ is shown in Figure 2.8. The analytic function and a grid with $N = 6$ and $N = 12$ points and the resulting trapezoids are shown for this example. The trapezoids in this context are the resulting shapes when linearly connecting the function values of neighboring grid points. As the integral of every trapezoid can be determined, numerical integration can be performed for the full function as well. The area of a single trapezoid T between x_1 and x_2 is thereby determined by $T = x_2 - x_1 \frac{f(x_1)+f(x_2)}{2}$, while the total numerical integration represents the sum of all trapezoids between the lower and upper boundary.[95] Logically, the analytical function is better represented by a finer grid. A perfect match would result when taking the limit of approaching zero grid spacing. Also, errors of the approximation might cancel out, as, for $N = 6$, the function is overestimated in the range of $x = 1.5\pi$. At the same time, it is underestimated at the boundaries, which can convey a perceived sense of security. The validity of the numerical integration should therefore be verified for each case in which it is applied. The measure of how well the trapezoidal approximation represents the function is also a measure of how accurately the numerical integration value represents the analytical solution's value. The accuracy of the numerical integration as a function of grid points, or grid spacing, respectively, is shown for the example of the depicted function in Table 2.1. It is clearly evident that the integral will approach the analytic solution for a more refined grid or more integration points. However, the question of how many points are required or what upper limit can be assumed for infinite integrals should be checked on a case-by-case basis employing a convergence analysis.

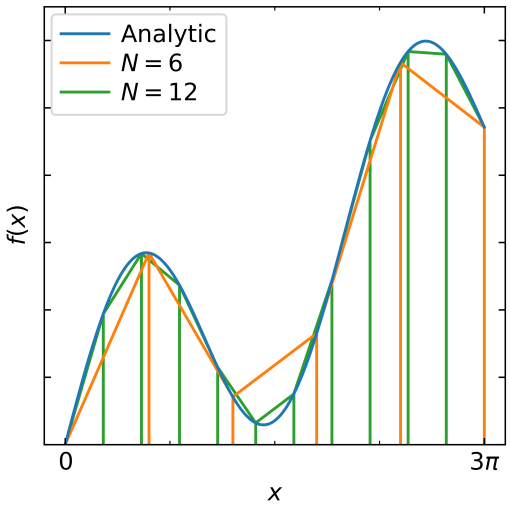

Figure 2.8: Example for numerical integration using trapezoids.

Numerical integrals are applied in this work primarily for the field of passive cooling, where the cooling power is the result of a triple integral regarding radiation in a

Table 2.1: Influence of the number of grid points N on the numerical integration for $\int_0^{3\pi} \frac{1}{4}x + \sin(x)dx$.

	Integral	Accuracy
Analytic	$2 + \frac{9\pi^2}{8} \cong 13.1033$	-
N=3	6.391	48.8%
N=6	12.473	95.2%
N=12	12.979	99.1%
N=24	13.075	99.8%
N=48	13.097	99.9%

hemisphere above the cooler. Therefore, azimuthal and polar angle integration, and energy or wavelength integration have to be performed.

2.4.2 Numerical Differentiation

Similar to numerical integration, if functions are complicated or not analytically defined, the numerical solution of the derivative can provide a great approximation. The simplest method to numerically estimate the derivative is the finite difference approximation shown in Figure 2.9.

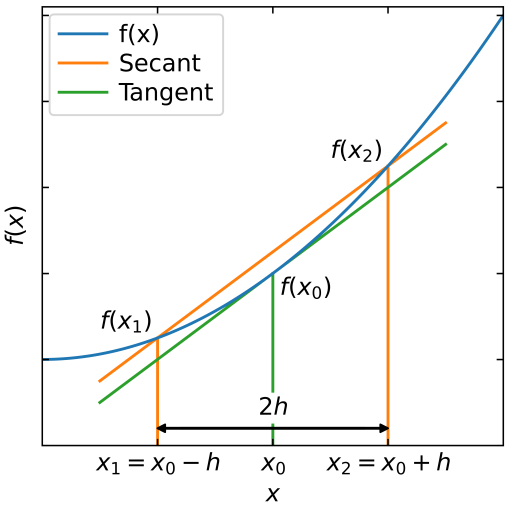

Figure 2.9: Example for numerical differentiation using the finite difference approximation.

The approach here is to approximate the analytic derivative at x_0 as the slope of a secant line through neighboring grid points. The slope of the secant $f'(x_0)_{\text{numeric}}$ can be expressed mathematically by the difference quotient as:

$$f'(x_0)_{\text{numeric}} = \frac{f(x_2) - f(x_1)}{x_2 - x_1}. \quad (2.12)$$

The secant slope is generally not equal to the tangent slope, which can be interpreted as the analytic derivative by an amount determined by the grid spacing h. With decreasing grid spacing, the secant will approach the tangent, where the analytic derivative represents the limit of h approaching zero:

$$f'(x_0)_{\text{analytic}} = \lim_{h \to 0} \frac{f(x_2) - f(x_1)}{x_2 - x_1}. \quad (2.13)$$

Again, special care must be taken when numerically approximating the function regarding the grid spacing. The subtraction can yield significant rounding errors for a very fine grid spacing due to the floating-point arithmetic with a fixed number of

digits used in computers. In fact, all the finite-difference formulae are ill-conditioned and, due to cancellation, will produce a value of zero if h is small enough.[96,97]
Numerical differentiation is mainly used for sensitivity analysis in this thesis. In sensitivity analysis, the influence of several free parameters on the measured quantity can be estimated. A high sensitivity represents a significant change in the measured quantity for a slight change in the free parameter, which can be expressed in terms of derivatives. Therefore, high sensitivity is related to a low uncertainty of the extracted values. In general, experiments should therefore be designed in such a way that a high sensitivity to the free parameters, or properties to be determined respectively, is ensured.

2.4.3 Non-Linear Regression

In general, non-linear regression is a specific regression procedure where the measured data are fitted to a model that is a non-linear function of the free parameters. In contrast to linear regression analysis, which represents one of the main principles of the classical measurement methods in physical chemistry, no analytic solution exists for this kind of regression analysis. Therefore, numerical algorithms have to be applied to find the global minimum in parameter space, representing the best fit of the measurement data based on the model used. An essential difference to linear regression resulting from this numerical approach is that initial guess values are needed for the free parameters. The choice of these initial guesses can influence the result of the numerical analysis and should therefore continually be reviewed and verified.
The main algorithm used in this work is the Levenberg-Marquardt algorithm, the procedure of which shall be briefly explained.[98,99] As computational expense does not pose restrictions for the calculations performed in this work on modern computers, the focus will be on the general principle of operation. The general approach is to minimize the squared deviations between model and measured data by adjusting the free parameters, starting from the initial guess. The solution to the problem can be expressed as follows:

$$\mathrm{argmin}_X \sum_{i=1}^{m} [y_i - f(x_i, X)]^2 \,, \tag{2.14}$$

where the difference in the sum is between measured data y_i and calculated values based on the free parameters X using model $f(x_i, X)$ at every measurement point i with a total number of m points. The minimum value that this sum can adopt is called argmin, and the solution at this point gives the best values for the free parameters X.
As mentioned above, the algorithm can converge to a local instead of the global minimum for parameter spaces with multiple minima when the initial guess is too

far from the best solution. The adjustment of the free parameters at each iteration is made either with the gradient descent or the Gauss-Newton method.[100,101] Far from their optimal value, the adjustments are made with a gradient descent method. In contrast, close to their optimal value, the Gauss-Newton method is applied, leading to faster convergence than the individual methods. An example optimization for a two-dimensional parameter space is visualized in Figure 2.10 for the well-behaved function $f(x) = x_1^2 + 3x_2^2$ which exhibits only one minimum at $X_{\text{min}} = (x_1, x_2) = (0, 0)$.

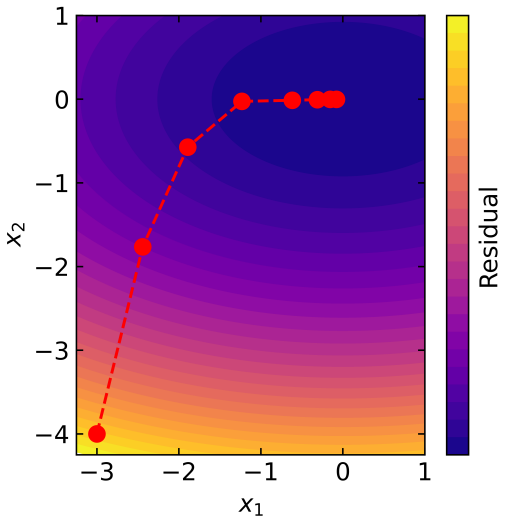

Figure 2.10: First seven iteration steps on the surface $f(x) = x_1^2 + 3x_2^2$ with an initial guess of $X_{\text{init}} = (-3, -4)$.

Starting from the initial guess $X_{\text{init}} = (-3, -4)$, the actual function is approximated to be linear around the guess values to ensure the calculability of the gradient. After calculating the gradient, the free parameters are adjusted to the opposite direction of the approximated gradient. The gradient further affects the step size. In the example, beginning from the initial guess, large steps are made for the first iteration, as the gradient is large. Approaching the minimum, steps get smaller as the gradient decreases until it formally disappears when reaching the final solution. The curved trace of the different iterations in this example is directly inferred from the function used. For a symmetric function like $f(x) = x_1^2 + x_2^2$, the various iterations would fall on a straight line between the initial guess and the final values.

The non-linear regression is applied to all thermal characterization measurements performed in this work. Those are the fitting of XFA data and PA data. These measurements are described by the thermal diffusion equation, adapted to the particular experimental situation, leading to non-linear relationships between the measured quantities and time or frequency. Non-linear regression represents the basis of all evaluations of experimental data obtained by these methods.

3 Thesis Outline

3.1 Synopsis

This thesis explores mainly two aspects of heat transport. The first part is focused on thermal conduction, which is the main transport mechanism at ambient conditions in solids. In this part, a simple and, at the same time, powerful method, the photoacoustic characterization, is discussed. This method allows for the complete thermal characterization of polymeric or other low thermal conductivity thin films. First, a methodology is developed which describes the essential measurement aspects and, based on this, optimizes the measurements for polymeric thin films. Furthermore, a rigorous error propagation based on a Monte Carlo approach is developed, which realistically reflects the measurement errors of the method. Based on this, the method is applied to regioregular poly(3-hexylthiophene-2,5-diyl) semi-crystalline thin films combined with absorption microstructural analysis to elucidate relationships between optoelectronic and thermal properties. Furthermore, the optimized measurement environment is applied to ampholytic polymers to entangle the interactions between water uptake, hydrogen bonds, and thermal conductivity in fully amorphous thin films. The transition from polymers to layered hybrid materials is made with Bragg stacks built from clay platelets and intercalated polymers. Anisotropy and differences in mechanical and thermal properties of this highly ordered material class are investigated. In contrast, the thermal conductivity of free-standing hybrid perovskite samples, another example of layered hybrid materials, is investigated using light flash analysis combined with density and specific heat measurements. The objective here is to develop a comprehensive picture of the electronic and thermal transport properties of the promising material class of 2D lead-halide hybrid perovskites.
The second part of this thesis revolves around radiative heat transport, which is present especially at high temperatures or can be utilized for special interest applications like passive cooling. Model systems in which the influence of radiative heat transport is demonstrated are hollow and solid sphere assemblies made of silica particles with diameters of several hundred nanometers up to several microns. For those thermally highly insulating and partially IR transparent materials, a continuous transition of the main thermal transport channel from conduction at ambient to radiation at around 900 °C is displayed. Therefore, the investigated material class loses part of its thermal insulation capacity with increasing temperature. Radiative heat transport is also utilized for passive cooling applications, where thermal ra-

diation is emitted through the earth's atmosphere, with outer space acting as an ultimate heat sink. Initially, the thickness dependency of passive cooling emitters is examined, revealing an optimum thickness effect for both day- and nighttime operations. Furthermore, an indoor setup is established, enabling reproducible and comparable measurements, which were unavailable in the field before.
A graphical overview of the topics covered in this thesis is shown in Figure 3.1.

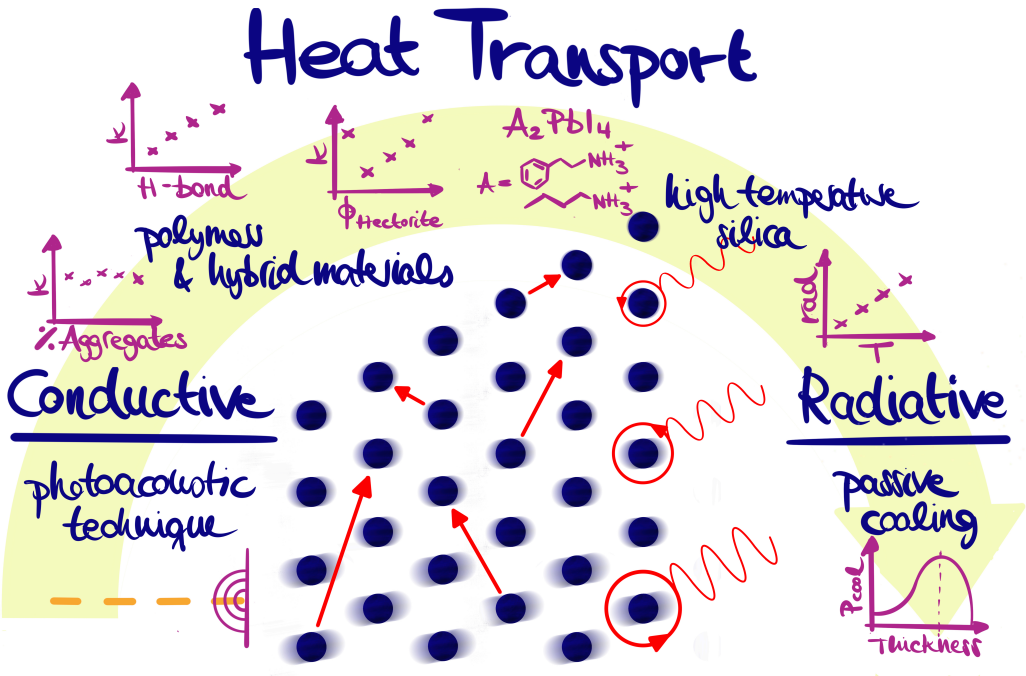

Figure 3.1: Graphical overview of the projects addressed in this thesis.

In Chapter 5, the photoacoustic technique is optimized for low thermal diffusivity thin films. Thermal characterization of thin films is an ongoing research topic since in nowadays microelectronics, coatings, or sensors, almost all materials are used as thin films.[9,90,102,103] There are several high-end thin film characterization methods, like frequency or time-domain thermoreflectance, transient thermal grating, or 3ω, which are usually accompanied by a high experimental effort.[90,104–107] In contrast to these techniques, the photoacoustic thermal characterization has been less widely used, which is even more surprising considering its suitability for low thermal diffusivity samples.[90,108]
Initially, dimensionless model analysis reveals the fundamental parameters affecting cross-plane thermal transport in the one-dimensional limit present in the applied measurement environment. A sample with unknown properties on a thermally thick backing with known properties is considered, representing a thin film measurement. As the measured pressure signal is used to infer the surface temperature, the sensitivity analysis is performed for the phase lag $\Delta\phi$ between the excitation source

and the surface temperature. Dimensionlessness is achieved by using the thermal thickness as the free variable.

The thermal thickness is the ratio of sample thickness l and thermal penetration depth $\mu = \sqrt{\pi f/D}$, depending on the frequency f and the thermal diffusivity D. The thermal penetration depth is defined as the depth in which the temperature oscillation is damped to $1/e$. The dimensionless representation is thus independent of the actual sample thickness, thermal diffusivity, and the applied frequency regime. This is shown in Figure 3.2.

Besides the dependency of the surface temperatures phase lag on the thermal thickness, a color code is used to represent the second main factor, namely the thermal reflection coefficient between the sample and backing $R_{s,b}$. The thermal reflection coefficient depends on the thermal mismatch between sample and backing, which is determined by their thermal effusivities ε via $R_{s,b} = \frac{\varepsilon_s - \varepsilon_b}{\varepsilon_s + \varepsilon_b}$. Approaching one or minus one for the thermal reflection coefficient constitutes the limit of either a orders of magnitude higher or lower thermal effusivity of the sample compared to the thermally thick backing. In contrast, a thermal reflection coefficient of zero represents the precise coincidence of the thermal effusivities of the sample and backing. There is always zero phase lag between excitation and surface temperature in this case, as the sample-backing assembly reduces to one thermally thick unit. The possibility of interpreting the surface temperature as a function of the thermal reflection coefficient, i.e., the thermal mismatch between sample and backing and subsequent superposition of incident and reflected wave, is made possible because the thermal diffusion equation is brought into a wave equation-like form by the periodic source term. Since one can find any possible measurement of a real sample in this dimensionless representation, a sensitivity analysis logically follows based on these free variables. Sensitivity analysis is performed to estimate how the measurement can be optimized for the samples of interest. The sensitivity regarding parameter i was defined as $S_i = \frac{\partial \phi}{\partial p_i} \cdot p_i$, where the derivative is normalized with the respective parameter to allow for a comparison between parameters that are different by orders of magnitude.[110] The sensitivity analysis regarding the effusivity mismatch and the thermal diffusivity, which will be the parameters to be extracted from the measurement, is shown in Figure 3.3. Since materials with low effusivities were the target of the present work,

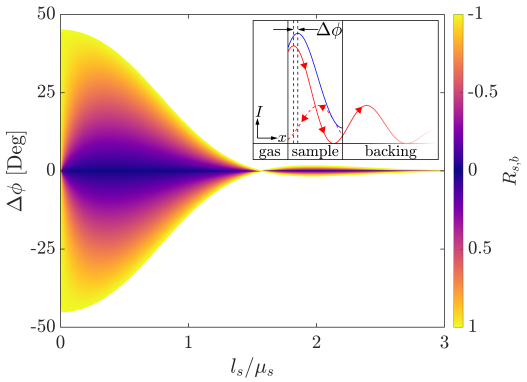

Figure 3.2: Theoretical phase shift of the surface temperature for a two-layer system with different thermal reflection coefficients $R_{s,b}$ as a function of the frequency-dependent thermal thickness l_s/μ_s.[109] The inset is intended to depict the principle of thermal wave interference.[90] Reprinted from Elsevier.

only negative reflection coefficients are shown in contrast to Figure 3.2.

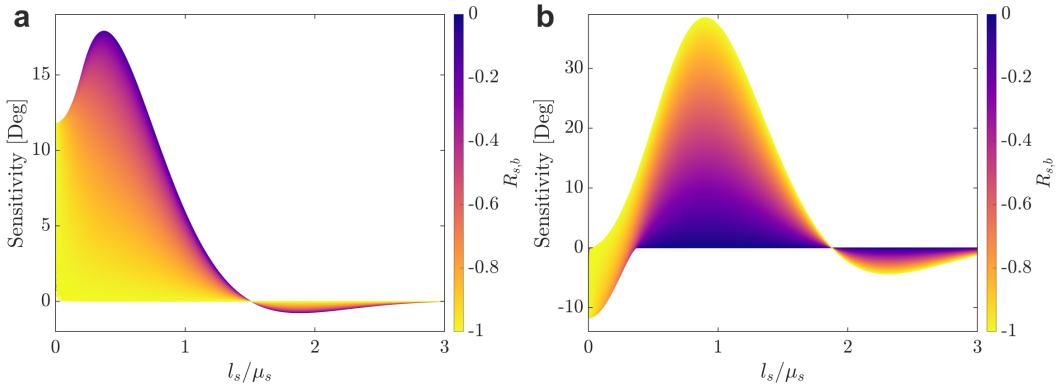

Figure 3.3: Sensitivity analysis for a polymeric sample to the fit parameters a) $\varepsilon_s/\varepsilon_b$ and b) $1/\sqrt{D_s}$ as a function of thermal thickness and thermal reflection coefficient.[90] Adapted from Elsevier.

As the maximum sensitivities are present at different thermal thicknesses, the simultaneous determination of both parameters is possible. In addition, to gain the best possible sensitivity to the free parameters, it should be the aim to cover both regimes of maximum sensitivity in a measurement. Based on this, an optimum sample thickness regime for the experimentally available frequencies could be identified, where the uncertainties of both fit parameters, namely thermal effusivity and diffusivity, are below 10%. This is the case for sample thicknesses between approximately 500 nm and 5 μm, which other measurement techniques can hardly analyze.

The outlined theoretical framework is subsequently verified experimentally. For this purpose, a thermally grown SiO_2 film on silicon with a thickness of 5 μm is characterized as a reference sample. Building upon this, the general relationships regarding thermal thickness and effusivity mismatch are clearly demonstrated using poly(methyl methacrylate) (PMMA) thin films of various thicknesses (400 nm to 3 μm) and on multiple substrates and, therefore, a varied thermal reflection coefficient (quartz, steel AISI 316 and silicon). A satisfying agreement between measured and literature values is apparent for all measurements, emphasizing the method's suitability.

In conclusion, it is pointed out how to optimize and perform the thermal characterization of low diffusivity solids in the μm and sub-μm regime with the photoacoustic technique. Moreover, our results show that the developed data evaluation allows directly extracting the thermal conductivity from a single measurement, provided that the appropriate boundary conditions are fulfilled.[90] The basic principles developed here are subsequently applied to various projects.

In Chapter 6, this optimization of the photoacoustic method is firstly applied to regioregular semi-crystalline P3HT thin films. The photoacoustic technique is ideally

suited since thin films in the sub-μm regime also enable detailed UV-Vis spectra in transmission geometry. Therefore, a quantitative analysis of absorption spectra, which provides information about the morphology, could be correlated to the thermal properties. In this way, it was possible to determine both properties on the same specimen, thus counteracting the influence of the traditionally strong sample to sample variation. Correlations between the proportion of aggregates and thermal conductivity, as well as between the exciton binding energy and thermal conductivity, are shown in Figure 3.4.

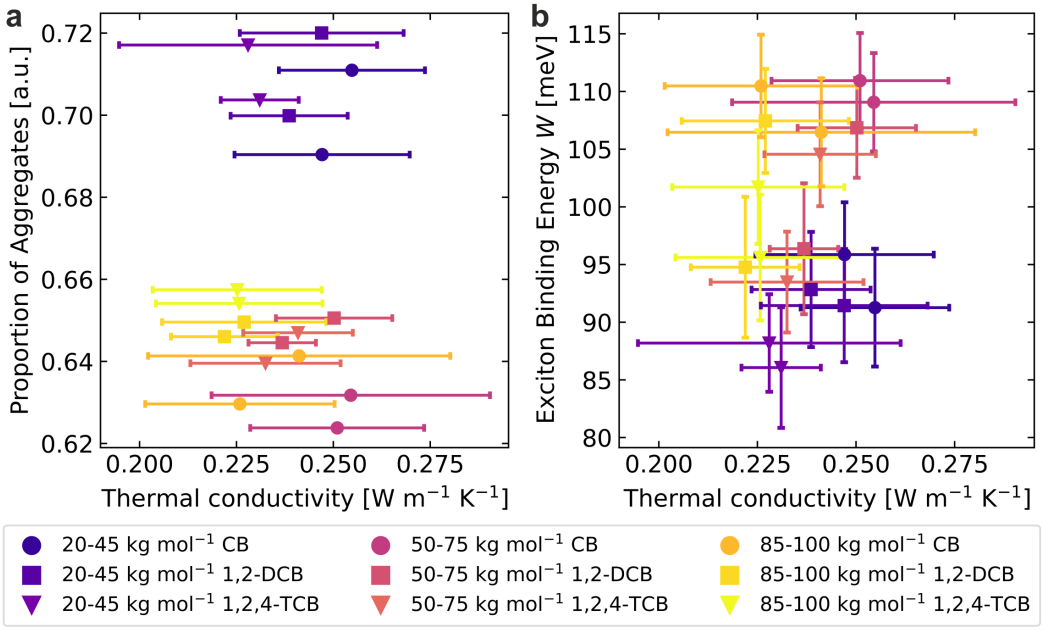

Figure 3.4: Correlations between extracted microstructural properties and thermal conductivity: a) Relation between the proportion of aggregates and the thermal conductivity. b) Relation between the exciton binding energy and the thermal conductivity.[111] Adapted from Multidisciplinary Digital Publishing Institute.

A variation of the optoelectronic properties, mainly regarding molecular weight, is apparent, while no direct influence of the solvent during preparation is discernible. In contrast, the thermal conductivities of all films examined fall within a similar range. Despite our expectations, we find no correlation between the proportion of aggregates and the thermal conductivity in the investigated range of molecular weights and generated microstructures. For the exciton binding energy, a more complex situation emerges, but considering the scatter and accuracy of our data, such potential trends need to be interpreted cautiously. Overall we have to conclude that a correlation between the structure, the optoelectronic properties, and the thermal conductivity cannot be resolved in the P3HT thin films investigated here. Therefore, the microstructural properties in the ordered regions do not significantly affect the resulting thermal properties in the sample space investigated in this work.

The main obstruction to a consistent identification of correlations between the microstructural properties and the thermal conductivity is the absence of sufficiently high contrast in the thermal conductivity. The fundamental factor underlying these results is the semi-crystalline structure of the investigated thin films. Macroscopic thermal transport in semi-crystalline polymeric thin films with molecular weights above the critical entanglement molecular weight is mainly affected by the amorphous phase. In contrast, the extracted microstructural properties are assigned to the ordered regions, as only these are included in the optoelectronic model.
This reinforces our findings that a change in the microstructural properties in the ordered regions does not affect the resulting macroscopic thermal transport properties in the examined range of molecular weights. The bottleneck for macroscopic thermal transport remains the amorphous regions, which separate the ordered parts.
In Chapter 7, the second application of the optimized measurement environment is the analysis of thermal transport in fully amorphous thin films of ampholytic polymers. This study systematically investigates the influence of hydrogen bonds (H-bonds) and water uptake on thermal conductivity. The guidelines developed above are applied for a significant thermal characterization of low thermal diffusivity thin films.
The backbone structure of the polymers is varied to exhibit different hydrogen bond donor and acceptor groups, as depicted in Figure 3.5a.

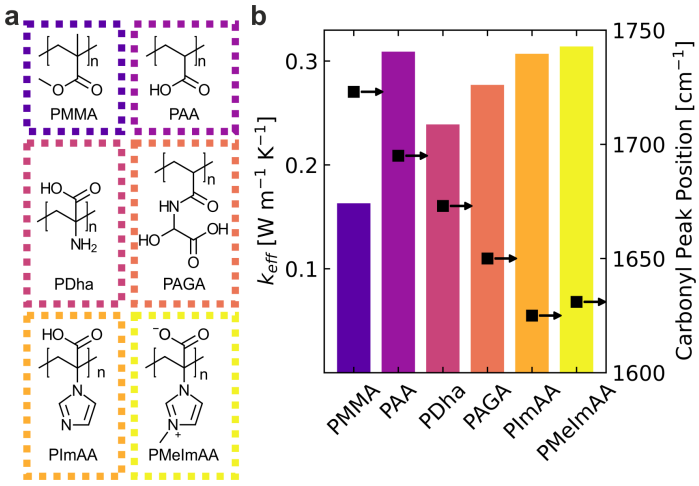

Figure 3.5: a) Structure of the ampholytic polymers and the reference polymers PAA and PMMA. The ampholytic polymers have at least two functional groups per repetition unit. b) Measured effective thermal conductivity of all samples (solid bars). The thermal conductivity correlates with the peak position (black symbols) of the carbonyl band measured by IR spectroscopy (except for PAA).[112] Adapted with permission from P. Hummel, A. M. Lechner, K. Herrmann, et al., Macromolecules, 53, 5528–5537. Copyright 2020 American Chemical Society.

The H-bond effect is investigated on Polydehydroalanine (PDha), poly(2-acrylamido glycolic acid) (PAGA), poly(2-(imidazol-1-yl)acrylic acid) (PImAA), and poly(2-

(methyl imidazolium-1-yl)acrylic acid) (PMeImAA), while poly(methyl methacrylate) (PMMA) and poly (acrylic acid) (PAA) serve as reference materials.

The H-bond strength, either intramolecular for folded chains or intermolecular between different chains, is analyzed using IR spectroscopy, as shown in Figure 3.5b. The H-bond strength is determined from the carbonyl peak position at approximately 1700 cm^{-1}. A shift of the carbonyl peak to lower wavenumbers indicates a weakening of the carbonyl bond and, consequently, a stronger H-bond. When comparing the carbonyl peak position to the measured thermal conductivity, there is an inverse dependency between thermal conductivity and carbonyl peak position for the ampholytic polymers. This inverse correlation is equivalent to a direct correlation between H-bond strength and thermal conductivity. However, although PAA is not an ampholytic polymer, it exhibits a thermal conductivity comparable to the best thermally conducting ampholytic polymer. This could indicate that additional factors have a strong influence on thermal conductivity.

Furthermore, Fourier self-deconvolution is applied to the carbonyl vibrations to gain further insights. The spectra can be deconvoluted to known interaction motifs like anhydride, free, terminal, dimer, inner, N-H, and imidazole carbonyl vibrations. This analysis is subsequently applied to samples treated at different humidities. Water is absorbed directly bound to a functional group or in a rather unbound state. When water is absorbed in unbound water clusters, the thermal conductivity can be described as composite-like behavior.

In summary, the investigation of several amorphous ampholytic polymers exhibiting H-bond donor and acceptor groups in the backbone reveals an influence of the H-bond strength on the thermal conductivity. Still, as polymeric thin films represent complex systems, complete comprehension is challenging to achieve.

The photoacoustic method is applied not only to polymeric materials but also to hybrid materials, which is discussed in Chapter 8. Anisotropic hybrid Bragg stacks, composed of highly ordered inorganic hectorite and organic polyethylene glycol (PEG) layers with periodicity in the single nanometer range, are characterized thermally and mechanically. The samples examined in this work are shown schematically in Figure 3.6a-d, where also characteristic TEM images are shown.

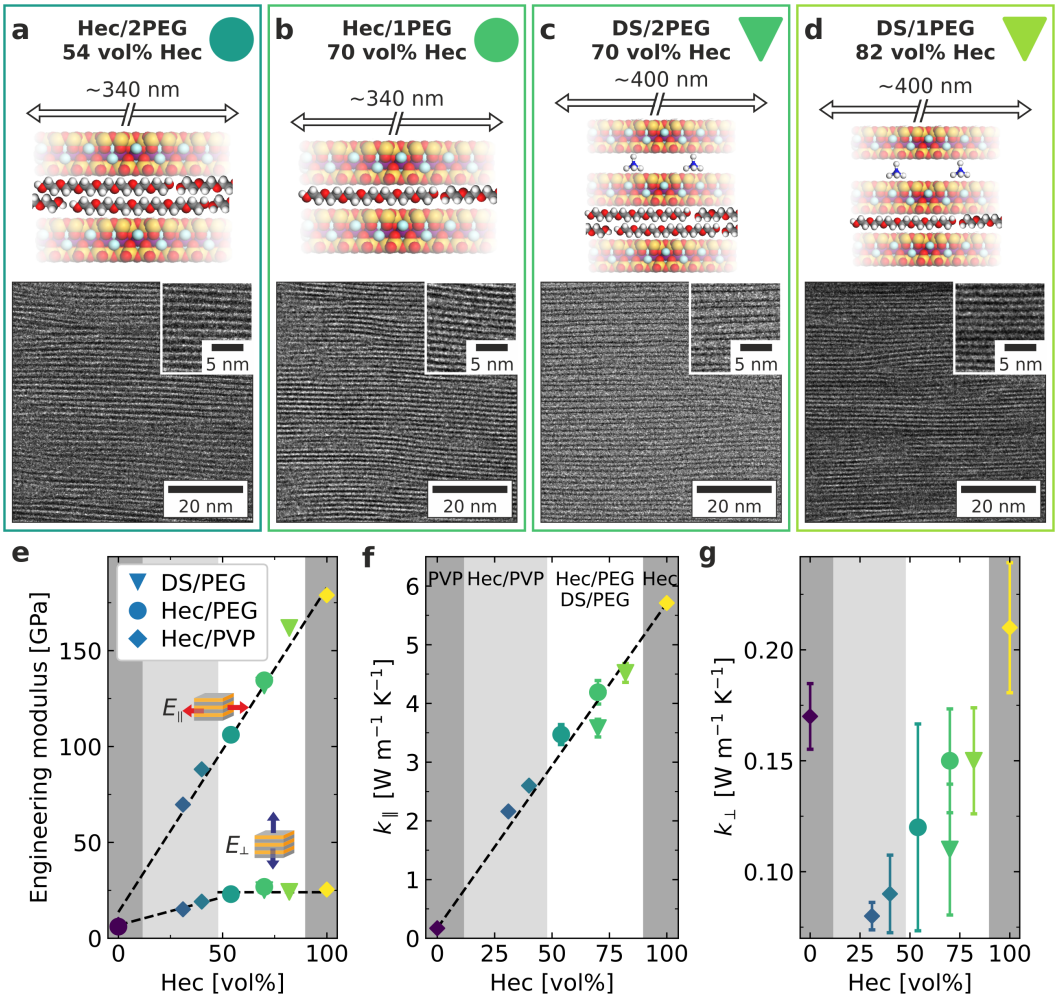

Figure 3.6: Hybrid clay nacre-mimetics with quantized composition. Increasing volume fraction of clay from left to right with a) hectorite with stacked PEG, b) hectorite with single PEG, c) double nanosheets with stacked PEG and d) double nanosheets with single PEG. Schematic structures of the hybrid Bragg stacks (top). TEM images (bottom) of Ar-milled slices confirming the superior order and long-range periodicity. The dark lines are single Hec sheets. e) Anisotropic engineering modulus as determined by Brillouin light scattering. f) In-plane and g) cross-plane thermal conductivity with comparison to Hec/PVP Bragg stacks.[60,61] Adapted from American Chemical Society.

For the first time, crystalline arrangements of clay nanosheets and polymer layers with a superior translational periodicity with 54 vol% to 82 vol% filler content are produced in discrete, material-inherent (”quantized”) compositions. The long-range order is not only confirmed by direct imaging via TEM but also verified by XRD measurements. Thereby, superior periodicity is combined with four distinct filler contents for the first time. In addition, the large-scale homogeneity and transparency allow for a unique mechanical and thermal analysis, revealing the anisotropic behavior in both property classes.

As a non-contact and non-destructive technique for measuring the elastic moduli at zero strain and submicron resolution, Brillouin light spectroscopy (BLS) is employed.

The direction-dependent inherent mechanical properties can thus be determined as a full tensor. In addition to the strong directional dependence of the mechanical properties, as shown in Figure 3.6e, an apparent discrepancy with the macroscopic stress-strain measurements also carried out can be demonstrated. This significant discrepancy is attributed to the inapplicability of the macroscopic stress-strain experiments to accessing the inherent material mechanics but instead being sensitive to macro-scaled defects.

The in-plane thermal conductivity, depicted in Figure 3.6f, is measured using lock-in thermography, supplemented by differential scanning calorimetry and helium pycnometer density measurements. The in-plane thermal conductivity follows a linear composition dependence, confirming the reported behavior for Hec/PVP Bragg stacks and the in-plane elastic moduli. Thus neither the assembly process nor the confinement of the polymer chains influences the in-plane transport. In contrast, the cross-plane thermal conductivity, determined by the photoacoustic technique, is shown in Figure 3.6g. The cross-plane thermal conductivity decreases gradually from the pure hectorite to the 54 vol% Hec/2PEG sample with decreasing filling fraction. The gradual behavior seems to be in contrast to the plateau at approximately 0.08 W m^{-1} K^{-1} for the Hec/PVP samples. Interpreted based on a serial thermal resistance network model, this suggests that unlike for the Hec/PVP system, for the Hec/PEG system, the cross-plane thermal conductivity is not dominated by the interfaces. For the Hec/PVP system, the large impact of the interface leads to a plateau, while for the Hec/PEG system, there is a gradual increase with increasing the filler volume fraction due to a reduced influence of interfaces. The different effects of the Hec/PEG and Hec/PVP interfaces could stem from the different physical states of PEG and PVP due to the vastly different glass transition temperatures (210 K vs. 445 K) and the stronger complexation between PEG and the sodium cations.[61] Both effects can influence the chain mobility within the confined space and, consequently, lead to a different interfacial adhesion between the Hec/PEG and the Hec/PVP interface, respectively.[61]

In conclusion, this work highlights the anisotropic property space of the nanoscopically well-defined periodic and layered material of hybrid Bragg stacks consisting of inorganic clay nanosheets and polymer layers. For the first time, small volume fractions of polymers (< 50 vol%) are introduced between the nanosheets to form uniform single-phase hybrid systems. The composition consisting of 82 vol% DS filler and 18 vol% single PEG shows a Young's modulus of 161.8 GPa parallel to the stacking direction, as determined by BLS, which suggests almost perfect stress transfer parallel to the clay nanosheets. Interestingly, the high modulus contrasts with macroscopic stress-strain measurements, indicating that stress-strain measurements alone are inappropriate to guide the structure-property optimization of nacre mimetics. The Young's modulus in the perpendicular direction is 6.7 times lower, indicating strong mechanical anisotropy. The anisotropy of the mechanical properties is also apparent in the thermal conductivity, wherein the cross-plane

direction reaches 4.52 W m^{-1} K^{-1} and is decreased approximately 30 times in the perpendicular direction. The results pave the way to unravel the complexity of designing hybrid stacks and may lead to combined molecular and nanostructured design approaches that allow for an independent adjustment of the mechanical and thermal properties.[61]

Additional layered hybrid materials possessing a low thermal conductivity and sheet-like structures are hybrid organic metal-halide perovskites, which are discussed in Chapter 9. Instead of supported thin films, free-standing pellets are thermally characterized by XFA. Through the collaboration of several departments, it is possible to reveal that composite metal-halide and molecular contributions govern the electronic structure and thermal transport properties of 2D lead-halide perovskites.

The influence of the organic cations on the electronic and thermal properties is investigated using first-principles calculations, ultraviolet photoelectron spectroscopy measurements, Raman measurements, molecular dynamics simulations and light flash measurements. Methylammonium lead iodide ($MAPbI_3$) is investigated as a well-studied model system, and butylammonium (BA_2PbI_4) and phenylethylammonium (PEA_2PbI_4) as large organic cations that lead to the formation of 2D structures due to their size. The ionization energies of all structures are similar, which can be assigned to lead iodide states that provide the highest energy levels for all systems. Even as the energy states originating from the organic cations lie below the valence band maximum, the distance to the valence band maximum is affected by varying the cation. Increasing the size from methylammonium to butylammonium to phenethylammonium, the states of the organic cation approach the valence band maximum. The energetic positions of the electronic states derived from the organic sublattice can be explained by the HOMO-LUMO gaps of the isolated molecular cations. Furthermore, it is shown that the differences in the energies of the molecular states arise primarily from the energetic position of the HOMO of the free-standing cations. In contrast, the LUMO shows only minor deviations between the cations. Furthermore, it is demonstrated that the distortions of the PbI_6 octahedra mainly determine the shape of the density of states near the valence band maximum. The distortions increase from methylammonium over butylammonium to phenethylammonium leading to fewer states close to the valence band maximum, which is also observed experimentally.

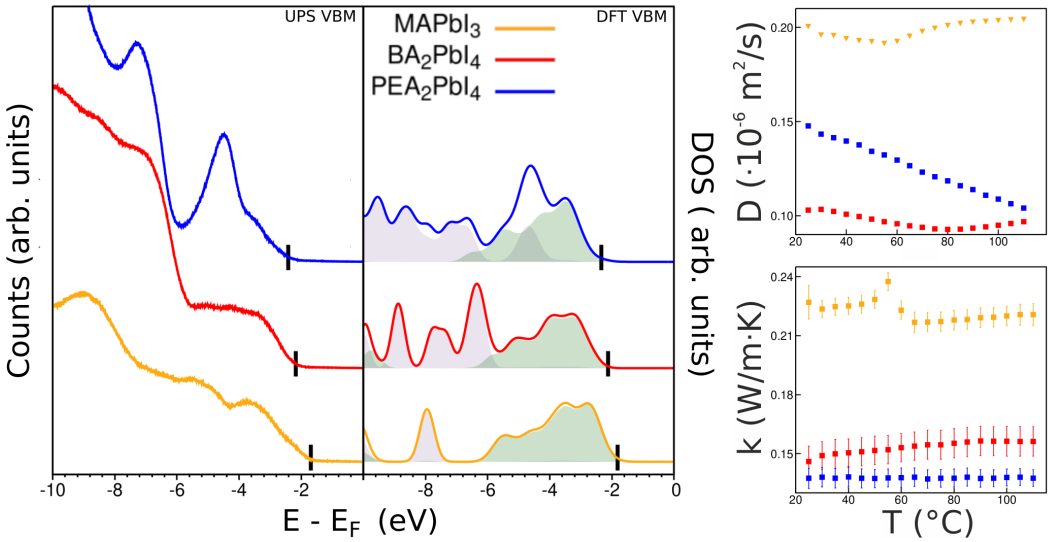

Figure 3.7: Ultraviolet photoelectron spectra (UPS) valence band maximum (VBM, left panel) regions, as well as ab-initio total DOS (middle panel) for $MAPbI_3$ (yellow), BA_2PbI_4 (red) and PEA_2PbI_4 (blue), scaled with respect to the Fermi energy level. The valence band onset is marked by a black dash line. The shaded areas in the computed DOS represent the projections onto molecular orbitals with states derived from the inorganic and organic sublattices in green and purple, respectively. Thermal diffusivity and conductivity as a function of temperature are displayed in the right panel.

The thermal conductivity displays a decrease from $MAPbI_3$ (0.22 W m^{-1} K^{-1}) over BA_2PbI_4 (0.14 W m^{-1} K^{-1}) to PEA_2PbI_4 (0.13 W m^{-1} K^{-1}). The lower thermal conductivity of BA_2PbI_4 and PEA_2PbI_4 is mainly attributed to the reduced dimensionality, which significantly impedes thermal transport perpendicular to the inorganic sublattice. Additionally, the lower thermal conductivity of PEA_2PbI_4 compared to BA_2PbI_4 is attributed to an increased organic layer thickness or an increased amount of organic constituents, respectively. Interestingly, PEA_2PbI_4 has a higher diffusivity than BA_2PbI_4, which might possibly be explained by π-stacking of the phenyl rings facilitating transport between neighboring cations, but at the same time a lower heat capacity, which leads to the lower conductivity overall.

As a result of this, an atomistic understanding of the effects of dimensional reduction on properties relevant to electronic and thermal transport was developed that pave the way for new stable hybrid materials with tailored properties.

This first part, mainly focusing on thermal conduction through solids, is now followed by the second part, where radiation effects are the objective of the investigations. The first project where substantial amounts of radiation are identified is the thermal characterization of particulate silica materials at high temperatures in Chapter 10. Several assemblies of hollow and solid silica spheres of different sizes are examined as a function of temperature, while bulk quartz glass with known thermal properties and assemblies of hollow titania spheres with complementary optical properties serve as reference material. Similar to the characterization of hybrid

organic metal-halide perovskites, free-standing samples are characterized by employing XFA. With increasing the temperature from ambient to 925 °C, the main transport channel gradually evolves from conduction at ambient to radiation at elevated temperatures. This temperature-dependent evolution is shown for the first time with a double-diffusive model, allowing for the deconvolution of the observed temperature evolution. The double-diffusive model is needed, as the established analytical models considering radiative heat transport cannot fit the measurement data.

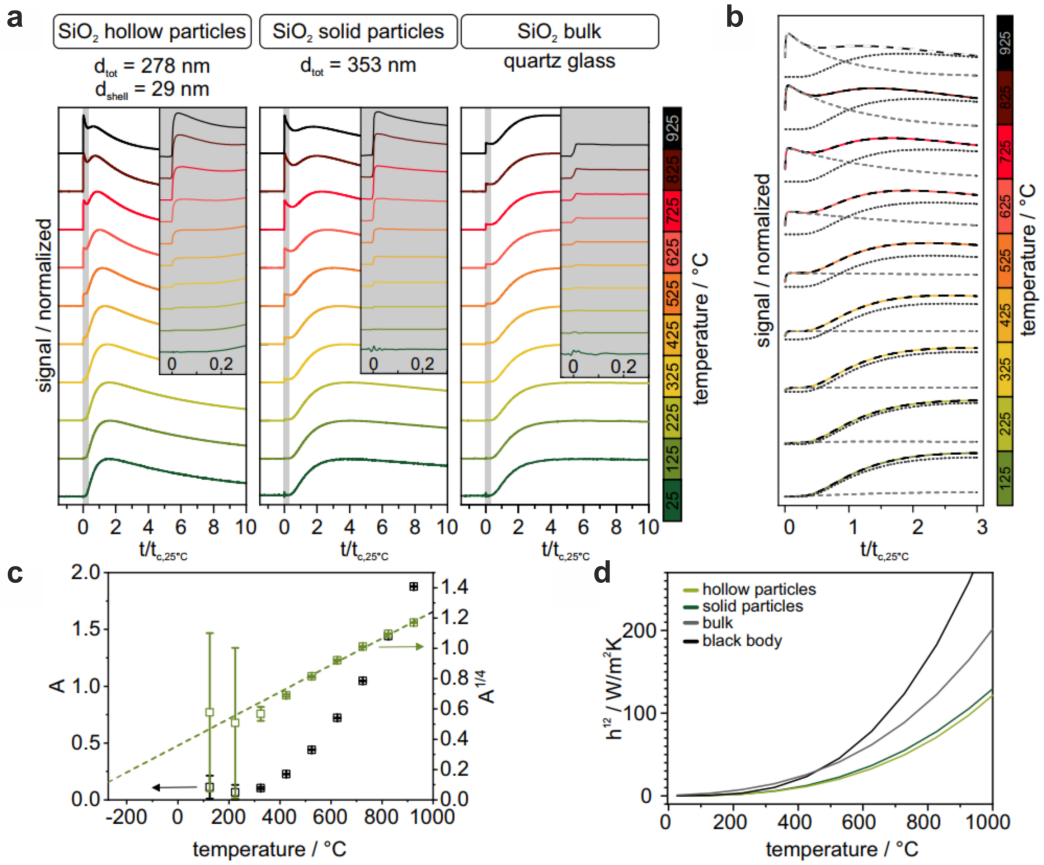

Figure 3.8: a) Temperature-dependent XFA measurements of the small silica hollow, solid particles, and bulk quartz glass. The grey insets show details of the radiative contribution. The time data are normalized by the characteristic thermal response time t_c for easier comparison. b) Double-diffusive model applied on 278 nm hollow particle measurements. c) Resulting ratio, A, of first and second diffusive process displaying T^4 dependency. d) Integrated heat transfer coefficient h_{12} for hollow and solid silica particles and bulk quartz glass, in comparison with black body radiation.[113] Adapted from John Wiley and Sons.

As shown in Figure 3.8a, a fast response of the topside surface temperature, representing the measurement signal, is apparent for hollow and solid silica particle assemblies, as well as for compact quartz glass. However, the main discovery is the comparatively slow dynamics of this process for the particulate materials. While the quartz measurements can be evaluated with existing models taking into account

radiative transport, the measurements on particulate samples cannot be reproduced with those models. The slow dynamics of this process inspired us to develop a coarse model, not taking into account coupling between the two transport processes, where the measurement signal is modeled as the superposition of two diffusive processes. This evaluation is shown in Figure 3.8b for the 278 nm hollow particles, where both processes and their superposition are depicted. Using this model, the measurement data can be reproduced well for the whole temperature regime covered in this work. As the ratio of both processes changes as a function of temperature, this ratio A is shown in Figure 3.8c, exhibiting a T^4 dependency characteristic for thermal radiation.

Quartz glass can serve as reference material for the inherent optical properties, while titania particle samples serve as reference material for the structure without optical transparency. Therefore, the measurement signal can be related to the transparency of silica in the blackbody energy regime, enabling radiative heat transport. At the same time, the particulate structure leads to the formation of the diffusive signal shape.

Simulations based on the S-matrix method using SCUFF-EM are performed to better understand the radiative transport mechanism through such bulk and particulate materials.[113] The simulations are able to show that the contribution of evanescent waves to the radiative transport decreases from bulk to solid to hollow spheres. For hollow spheres, there is no contribution of evanescent waves at all. In contrast, this loss in transmission is counteracted by a decreased optical density of the hollow spheres. Interestingly, surface waves have no significant contribution in the reststrahlen band between 8 μm and 9.3 μm. A closer examination reveals that the radiative transport between adjacent particles is determined mainly by a surface mode at $\lambda = 9.3$ μm, which is strongly attenuated when including heat transport between several successive particles.

Based on the simulations, a heat transfer coefficient is calculated as a function of temperature, describing the radiative heat flow h_{12} from the graphite bottom toward the graphite top through the sample, as shown in Figure 3.8d. The heat transfer coefficient is the largest for the bulk silica samples, where evanescent waves enhance the transmission. The particulate structures feature a similar heat transfer coefficient. This similar heat transfer coefficient is attributed to compensating for the non-existence of evanescent waves for the hollow structure by a decreased optical density.

In summary, a profound understanding of the temperature-dependent thermal transport in particular silica materials is developed. While conduction through the solid backbone dominates at ambient temperatures, radiation becomes increasingly important at elevated temperatures. This corresponds to a decrease in the insulating properties with increasing temperature. Controlling the optical properties in the mid-infrared range, either employing the composition, the structure, or adding additives, is paramount to maintaining a strong thermal insulation behavior.[113]

The last thematic unit discussed in this thesis also deals with radiation effects, focusing on passive daytime radiative cooling. For thermal radiation to have a significant effect even at ambient temperature, the earth's atmospheric transparency window can be utilized. Consequently, space at approximately 3 K acts as an ultimate heat sink. Therefore, the optical properties of the material need to be carefully adapted to the atmospheric transparency window.

The first work regarding passive daytime radiative cooling evolved around the optimum thickness of an emitter material, as shown in Chapter 11. Several parameters affecting the performance of a passive cooling device, like tailored or broadband emissivity, angle selectivity, or non-radiative heat losses, have been discussed in detail in the literature.[114] Still, the material thickness has been far less researched. Therefore a theoretical framework to calculate the thickness-dependent cooling performance of a material based on the fundamental optical constants is introduced. The theoretical framework is afterward validated through rooftop measurements, exhibiting a convincing match between theoretical expectations and practical measurement. An optimum material thickness for various polymeric materials was shown for both day- and nighttime applications. Still, the optimum thickness effect is significantly more pronounced during the daytime.

The calculations are based on the fundamental optical constants, an AM1.5 solar spectrum widely used as a reference, a simulated atmospheric transmission spectrum for the location of experiments (Bayreuth, Germany), and an average non-radiative loss coefficient taken as an average of literature values. A perfect reflector beneath the sample is assumed to enable the calculation of the material's emissivity as a function of wavelength or energy and angle. To calculate the cooling power, both wavelength and angular integrations have to be performed, which can only be achieved for the data at hand by numerical integration. Four PDMS samples of different thicknesses were prepared on silver mirrors for the rooftop measurements, and the reached equilibrium temperature below the bare reference silver mirror was determined.

The calculation in Figure 3.9a and c during day- and nighttime, respectively, suggest a strongly pronounced optimum thickness effect during daytime and a weakly pronounced optimum thickness during nighttime. The main reason for a clear optimum thickness during daytime is solar absorption. At low thicknesses, the blackbody radiation emitted by the sample increases. If the thickness gets too high, solar absorption will become apparent due to the non-zero complex refractive index of the polymer. There is no solar radiation during the nighttime, and the optimum thickness here is related to the delicate counterbalance of radiation absorbed coming from the atmosphere and radiation emitted by blackbody radiation. The cooling power tends to reach a plateau here with high thicknesses. For both day- and nighttime applications, the optimum sample thickness for PDMS is suggested to be between 10 μm and 100 μm. Experimental data determining the steady-state temperature reached below the reference silver mirror $T_{\mathrm{Ag}} - T_{\mathrm{mat}}$ are equivalent to

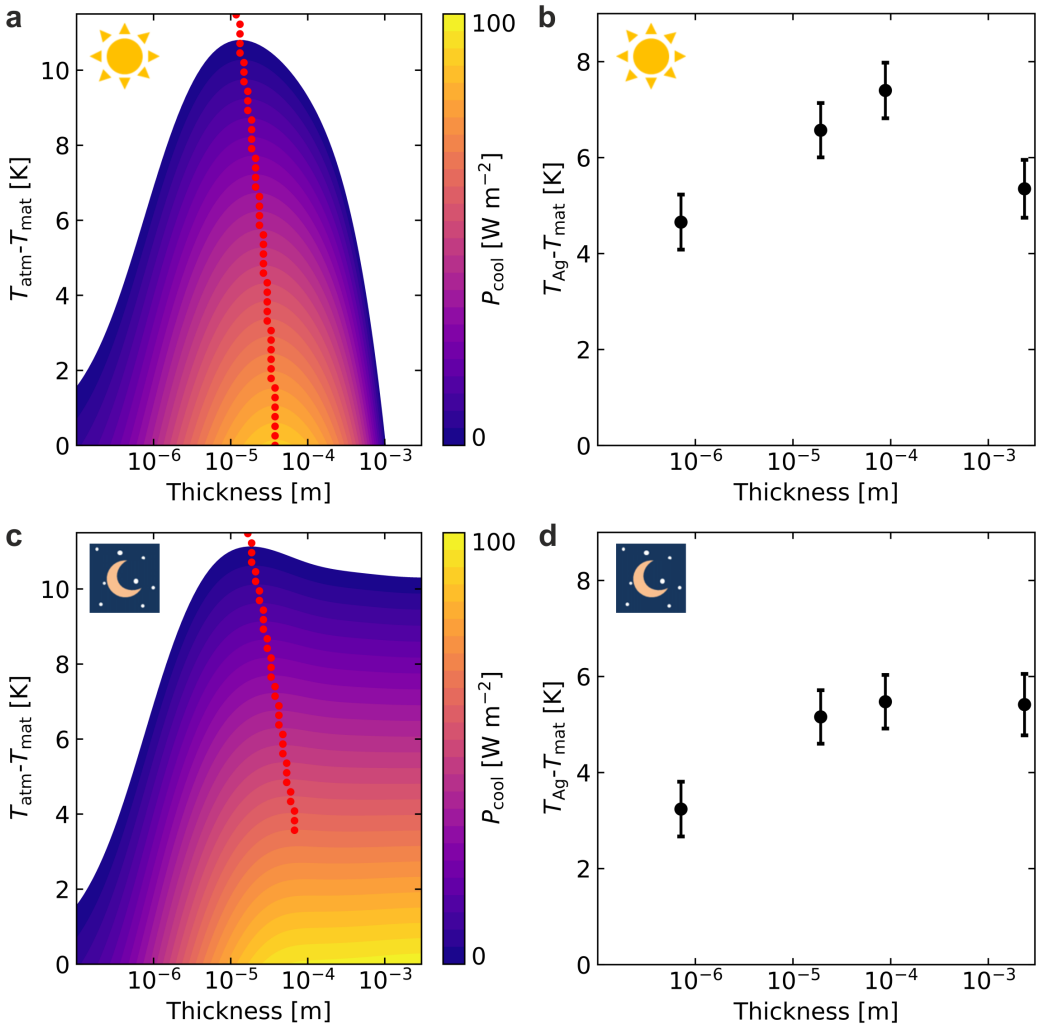

Figure 3.9: a) Calculated thickness dependent cooling power of PDMS based on the fundamental optical constants and standard conditions during daytime. b) Thickness dependent rooftop equilibrium measurement of PDMS samples during daytime. c) Calculated cooling power of PDMS during nighttime. d) Rooftop measurement during nighttime. Red dots in a) and b) indicate the sample thickness with the highest cooling power at the respective temperature.[114] Adapted from John Wiley and Sons.

the shape illustrated by the cooling power, as negative values are not shown, and the steady-state is reached at $P_{cool} = 0$. A correspondence between simulation and experiment is evident, where during daytime, an optimum thickness is apparent, while during nighttime, a plateau is reached. The main factors affecting the absolute values of ΔT and the optimum thickness in the calculations are the complex refractive index data of the material of interest and an accurate atmospheric transmission spectrum.

In summary, a theoretical approach to determining the optimum thickness of passive cooling materials in back-reflector geometry is demonstrated in this work. An optimum thickness at which the cooling power at ambient is maximized and for the lowest possible temperature to be achieved is worked out. The calculations

further confirm that those two maxima do not occur at the same material thickness or material emissivity, respectively. The effect is then validated by measuring the equilibrium temperature of samples with different thicknesses. Therefore, besides other factors like nano- or microstructure, optical properties, etc., the layer thickness is a crucial parameter that needs to be optimized for passive cooling applications. Radiative cooling is also the topic of the last work discussed here. As mentioned above, outdoor or rooftop measurements represent the standard for characterizing the cooling performance of promising materials. However, these measurements have the disadvantage that they are highly dependent on the actual weather conditions making a meaningful comparison of data from different research groups difficult or even impossible. The main factors are the altitude above sea level, humidity, and the solar radiation spectrum present. To enable this previously missing comparability in Chapter 12, a robust indoor setup is developed, which moreover offers the possibility of controlling the ambient temperature and solar power.

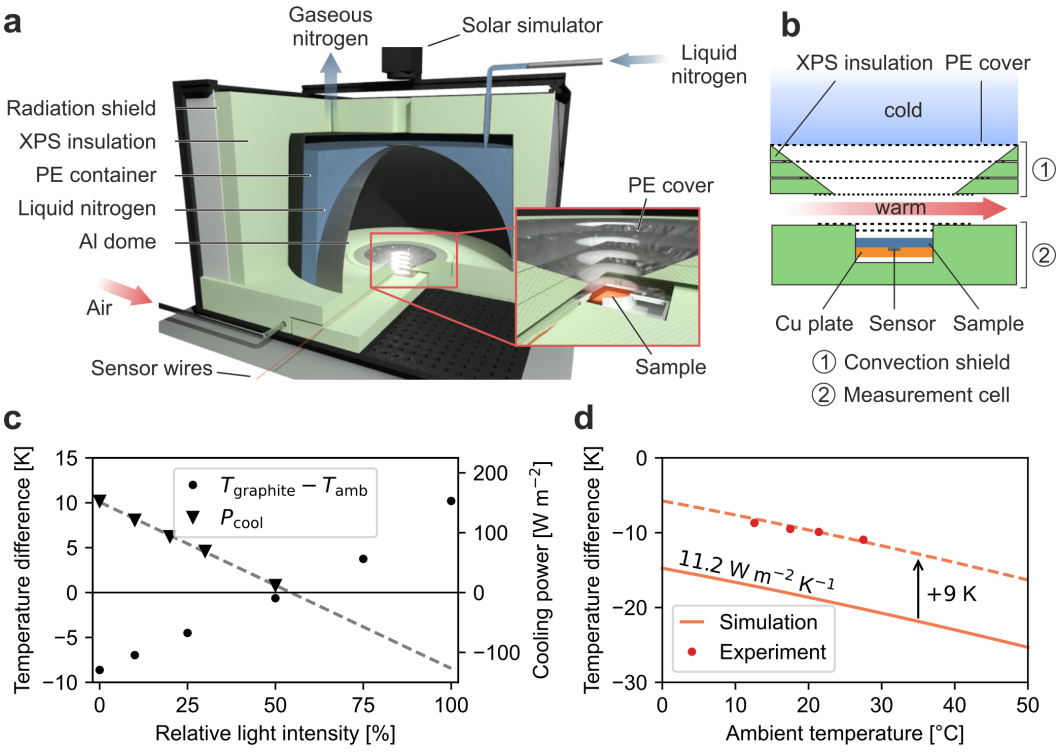

Figure 3.10: a) and b) Schematics of the indoor setup for characterizing passive daytime cooling. A liquid nitrogen-cooled aluminum dome imitates outer space, while a solar simulator illuminates the sample. A convection shield in combination with XPS minimizes non-radiative heat transfer between the dome and sample. A warm gas flow between the convection shield and the sample holder allows controlling the temperature inside of the measurement cell. c) Impact of solar intensity on the passive cooling performance of a graphite coating. d) The impact of ambient temperature (T_{amb}) on the cooling performance of a PDMS film. Both the simulation and experiment show that T_{amb} enhances the cooling performance leading to a decrease in the temperature difference.[115] Adapted from Elsevier.

The indoor setup is shown schematically in Figure 3.10a. The setup consists of a nitrogen-cooled aluminum dome covered with a graphitic layer to ensure high absorptivity in a broad wavelength range. The emittance of a blackbody at 77 K, the temperature of liquid nitrogen, is 1.99 W m^{-2}, while a blackbody at 3 K, the temperature of outer space, has an emittance of $4.56 \cdot 10^{-6}$ W m^{-2}. Still, this is a reasonable approximation, as the blackbody emittance at ambient is 375 W m^{-2}, and therefore two orders of magnitude higher. As the aluminum dome is cooled with liquid nitrogen, there is a very steep temperature gradient over a relatively short distance. A convection shield is used to suppress conductive and convective losses, as illustrated in Figure 3.10b. Several layers of PE with air constitute the thermal insulation while still being transparent to the emitted IR radiation of the sample. Afterward, the setup is validated using graphite and PDMS of different thicknesses on silver mirrors as reference samples. Reference samples are used to determine the non-radiative heat transfer coefficient of the setup.

Furthermore, solar radiation and ambient temperature can be varied as environmental parameters, which are not accessible for outdoor measurements. The solar radiation is varied for graphite, as shown in Figure 3.10c. Graphite is chosen as it exhibits the strongest interaction with light in the visible range of the samples employed in this work. At low intensities, graphite shows an excellent passive cooling performance. Still, as the intensity of the solar simulator increases, the cooling power is lost. A linear trend between light intensity and the temperature difference is found, verifying the possibility of varying the solar radiation. Furthermore, the ambient temperature's influence on the equilibrium temperature difference for PDMS is depicted in Figure 3.10d. The dependence of the emitted radiation on temperature becomes clearly evident. Lower equilibrium temperatures below ambient can be reached by increasing the ambient temperature. Also, a satisfying agreement between simulations and experimental data is demonstrated, only differing in the absolute values but showing the same temperature dependency. Since many factors influence the absolute values of the simulations, this relative agreement is more than convincing.

In summary, a versatile indoor setup to determine the passive cooling properties is demonstrated. In contrast to outdoor measurements, the setup allows the control of the measurement conditions and leads to outstanding reproducibility. Therefore, the characterization under the laboratory environment enables the comparison of the performance of passive cooling material independent of weather, time, and location. This is a first step towards standardized passive cooling measurements, enabling the development of passive cooling materials into a widespread and applied technology.

3.2 Individual Contributions to Joint Publications

The results presented in this work were prepared in cooperation with other colleagues. The individual contributions of all authors are designated below.

Chapter 5: Photoacoustic Thermal Characterization of Low Thermal Diffusivity Thin Films

Kai Herrmann, Nelson W. Pech-May, and Markus Retsch.

This work was published in *Photoacoustics*, **2021**, *22*, 100246.

I performed the simulations and outlined the underlying theoretical framework. I chose a suitable set of samples to demonstrate the basic dependencies of the measurement. I prepared the samples, performed measurements as well as established the non-linear fitting routine for data analysis. I introduced a Monte-Carlo error propagation approach for the non-linear model and wrote the manuscript. Nelson W. Pech-May gave feedback and ideas to the design of experiments and the theoretical framework while also contributing to the manuscript. Markus Retsch supervised the project and corrected the manuscript.

Chapter 6: Microstructural and Thermal Transport Properties of Regioregular Poly(3-hexylthiophene-2,5-diyl) Thin Films

Kai Herrmann, Simon Freund, Fabian Eller, Tamino Rößler, Georg Papastavrou, Eva M. Herzig, and Markus Retsch.

This work was published in *Materials*, **2022**, *15*, 7700.

I conceptualized the project, set up the appropriate methodology, and conducted preliminary testing. Simon Freund and I performed data analysis on the optical and thermal measurements. Simon Freund prepared the samples and performed the characterization measurements. Fabian Eller performed and evaluated the GIWAXS meausrements. I prepared the original draft of the manuscript and visualized the results. Tamino Rößler performed AFM measurements. Fabian Eller, Tamino Rößler, Georg Papastavrou and Eva M. Herzig contributed to the revised manuscript. Markus Retsch supervised the project and corrected the manuscript. Markus Retsch supervised the project and corrected the manuscript. I prepared the original draft of the manuscript and visualized the results. Markus Retsch supervised the project and corrected the manuscript.

Chapter 7: Thermal Transport in Ampholytic Polymers: The Role of Hydrogen Bonding and Water Uptake

Patrick Hummel, Anna M. Lechner, Kai Herrmann, Philip Biehl, Carsten Rössel, Lisa Wiedenhöft, Felix H. Schacher, and Markus Retsch.

This work was published in *Macromolecules*, **2020**, *53*, 5528-5537.

Patrick Hummel prepared the samples, performed photoacoustic measurements, density determination, IR measurements, and humidity experiments, and worked on the manuscript. Anna M. Lechner performed standard and modulated differential scanning calorimetry measurements. I optimized the photoacoustic measurement to determine the thermal conductivity of polymeric thin films. I conducted additional photoacoustic, density, and IR measurements. I performed optical microscopy measurements on the transducer-coated polymeric thin films. Philip Biehl, Carsten Rössel and Lisa Wiedenhöft synthesized and characterized the ampholytic polymers PDha, PAGA, PImAA and PMeImAA. Felix H. Schacher supervised the polymer synthesis and contributed to the manuscript. Markus Retsch supervised the project and worked on the manuscript.

Chapter 8: Nanoscale-Structured Hybrid Bragg Stacks with Orientation- and Composition-Dependent Mechanical and Thermal Transport Properties: Implications for Nacre Mimetics and Heat Management Applications

Theresa Dörres, Malgorzata Bartkiewicz, Kai Herrmann, Marius Schöttle, Daniel Wagner, Zuyuan Wang, Olli Ikkala, Markus Retsch, George Fytas, and Josef Breu.

This work was published in *ACS Applied Nano Materials*, **2022**, *5*, 4119–4129.

Theresa Dörres developed the manufacturing method and provided the hybrid Bragg stacks. Theresa Dörres performed measurements for the bulk mechanical properties and wrote the manuscript. Malgorzata Bartkiewicz performed the Brillouin light-scattering measurements for local mechanical properties and contributed to the manuscript. I performed cross-plane thermal characterization, measured density for in-plane thermal characterization, and contributed to the manuscript. Marius Schöttle performed the in-plane thermal characterization. Daniel Wagner performed TEM measurements. Zuyuan Wang and Olli Ikkala were involved in scientific discussions and contributed to the manuscript. Markus Retsch, George Fytas, and Josef Breu supervised the project and worked on the manuscript.

Chapter 9: Composite Metal-Halide and Molecular Contributions Govern the Electronic Structure and Thermal Transport Properties of 2D Lead-Halide Perovskites

Raisa-Ioana Biega, Kai Herrmann, John Mohanraj, Dominik Skrybeck, Menno Bokdam, Mukundan Thelakkat, Markus Retsch, and Linn Leppert.

Raisa-Ioana Biega performed all DFT calculations and wrote the manuscript. I performed and evaluated all thermal measurements and contributed to the manuscript. John Mohanraj and Dominik Skybrck provided the perovskite materials. John Mohanraj performed Raman and XPS measurements, as well as contributed to the manuscript. Menno Bokdam and Linn Leppert performed molecular dynamics simulations and contributed to the manuscript. Mukundan Thelakkat, Markus Retsch, and Linn Leppert supervised the project and worked on the manuscript.

Chapter 10: High-Temperature Thermal Transport in Porous Silica Materials: Direct Observation of a Switch from Conduction to Radiation

Anna M. Neuhöfer, Kai Herrmann, Flora Lebeda, Tobias Lauster, Christoph Kathmann, Svend-Age Biehs, and Markus Retsch.

This work was published in *Advanced Functional Materials*, **2021**, *32*, 2108370.

Anna M. Neuhöfer prepared the samples, performed the high-temperature laser-flash analysis experiments, UV-Vis and IR spectroscopy, scanning electron microscopy, evaluated the data, created the figures, and worked on the manuscript. I developed the double-diffusive model for the otherwise non-analyzable hollow and solid sphere measurements. I performed data analysis applying the double-diffusive model and contributed to the manuscript. Flora Lebeda performed the Comsol simulations. Tobias Lauster helped with the UV-Vis and IR measurements and performed additional measurements. Christoph Kathmann performed the SCUFF-EM calculations. Svend-Age Biehs performed the calculations of the transmission and heat transfer coefficients, was involved in the scientific discussion, and contributed to the manuscript. Markus Retsch supervised the work, was involved in the scientific discussion, and corrected the manuscript.

Chapter 11: Homogeneous Polymer Films for Passive Daytime Cooling: Optimized Thickness for Maximized Cooling Performance

Kai Herrmann, Tobias Lauster, Qimeng Song, and Markus Retsch.

This work was published in *Advanced Energy and Sustainability Research*, **2022**, *3*, 2100166.

Tobias Lauster and I identified the lack of treatment of the sample thickness for passive daytime cooling. I established a theoretical framework to depict the influence of sample thickness on cooling performance. I performed the simulations based on this theoretical framework. Tobias Lauster prepared the samples and performed the optical characterization. Tobias Lauster and I wrote the manuscript. Qimeng Song developed the outdoor setup for measuring the cooling performance, performed the cooling performance measurements, and was involved in scientific discussions. Markus Retsch supervised the project and corrected the manuscript.

Chapter 12: A Tailored Indoor Setup for Reproducible Passive Daytime Cooling Characterization

Qimeng Song, Thomas Tran, Kai Herrmann, Tobias Lauster, Maximilian Breitenbach, and Markus Retsch.

This work was published in *Cell Reports Physical Science*, **2022**, *3*, 100986.

Qimeng Song and Thomas Tran were leading the conceptualization and investigation. I contributed formal analysis and validation. Tobias Lauster contributed validation and resources. Maximilian Breitenbach was involved in the investigation. Markus Retsch led supervision, project administration, and funding acquisition. All authors contributed to the original draft writing.

References

4

[1] K. Bithas, P. Kalimeris in *Revisiting the Energy-Development Link*, Springer International Publishing, **2015**, pp. 5–10.

[2] A. Szolucha, *Energy, Resource Extraction and Society*, Routledge, **2018**.

[3] J. E. Hansen, M. Sato in *Climate Change*, Springer Vienna, **2012**, pp. 21–47.

[4] J. Yang, Y. Yu, T. Ma, C. Zhang, Q. Wang, *Chinese Journal of Population Resources and Environment* **2021**, *19*, 256–264.

[5] S. Sorrell, *Renewable and Sustainable Energy Reviews* **2015**, *47*, 74–82.

[6] C. Forman, I. K. Muritala, R. Pardemann, B. Meyer, *Renewable and Sustainable Energy Reviews* **2016**, *57*, 1568–1579.

[7] Q. Bian, *Environmental Systems Research* **2020**, *9*, 8.

[8] J. Schmidt, M. R. G. Marques, S. Botti, M. A. L. Marques, *NPJ Computational Materials* **2019**, *5*, 83.

[9] D. G. Cahill, W. K. Ford, K. E. Goodson, et al., *Journal of Applied Physics* **2003**, *93*, 793–818.

[10] X. Lan, Y. Wang, J. Peng, et al., *Materials Today Physics* **2021**, *17*, 100342.

[11] S. B. Viklund, M. T. Johansson, *Energy Conversion and Management* **2014**, *77*, 369–379.

[12] H. J. Goldsmid in *Thermoelectric Refrigeration*, Springer New York, **1964**, pp. 210–223.

[13] G. J. Snyder, E. S. Toberer, *Nature Materials* **2008**, *7*, 105–114.

[14] S. Fan, W. Li, *Nature Photonics* **2022**, *16*, 182–190.

[15] W. Thomson, *The London Edinburgh and Dublin Philosophical Magazine and Journal of Science* **1852**, *4*, 8–21.

[16] J. C. Maxwell, *Philosophical Transactions of the Royal Society of London* **1867**, *157*, 49–88.

[17] K. Carlton, *Physics Education* **2000**, *35*, 101–105.

[18] Y. Cengel, *Heat Transfer: A Practical Approach*, McGraw-Hill, **2003**.

[19] S. K. Som, *Introduction to Heat Transfer*, PHI Learning, **2008**.

[20] A. Jain, P. Kovtun, *Physical Review Letters* **2022**, *128*, 071601.

[21] C. E. Baukal Jr., *The John Zink Hamworthy Combustion Handbook*, CRC Press, **2012**.

[22] F. W. Sears, G. L. Salinger, *Thermodynamics, Kinetic Theory, and Statistical Thermodynamics*, Addison-Wesley, **1975**.

[23] P. G. Klemens, *Proceedings of the Royal Society of London. Series A. Mathematical and Physical Sciences* **1951**, *208*, 108–133.

[24] G. Chen, *Nanoscale Energy Transport and Conversion: A Parallel Treatment of Electrons, Molecules, Phonons, and Photons*, Oxford University Press, **2005**.

[25] P. M. Morse, *Physical Review* **1929**, *34*, 57–64.

[26] A. M. Stoneham, J. H. Harding, *Annual Review of Physical Chemistry* **1986**, *37*, 53–80.

[27] W. Cochran, *Reports on Progress in Physics* **1963**, *26*, 1–45.

[28] W. Lv, A. Henry, *Scientific Reports* **2016**, *6*, 37675.

[29] A. Sommerfeld, *Zeitschrift für Physik* **1928**, *47*, 1–32.

[30] E. Fermi, *Zeitschrift für Physik* **1926**, *36*, 902–912.

[31] R. Franz, G. Wiedemann, *Annalen der Physik und Chemie* **1853**, *165*, 497–531.

[32] U. Grigull, H. Sandner, *Heat Conduction*, Springer Berlin, **2012**.

[33] J. B. J. Fourier, *Théorie Analytique de la Chaleur*, Cambridge University Press, **2009**.

[34] C. Chiritescu, D. G. Cahill, N. Nguyen, et al., *Science* **2007**, *315*, 351–353.

[35] J. Feng, J. Feng, C. Zhang, *Journal of Porous Materials* **2011**, *19*, 551–556.

[36] S. Kidalov, F. Shakhov, *Materials* **2009**, *2*, 2467–2495.

[37] J. Rumble, *CRC Handbook of Chemistry and Physics*, CRC Press, **2018**.

[38] L. Peng, Z. Xu, Z. Liu, et al., *Advanced Materials* **2017**, *29*, 1700589.

[39] A. Bejan, *Convection Heat Transfer*, John Wiley & Sons, **2013**.

[40] A. K. Prasad, J. R. Koseff, *International Journal of Heat and Fluid Flow* **1996**, *17*, 460–467.

[41] U. Besson, *Science & Education* **2010**, *21*, 1085–1110.

[42] S. Basu, Z. M. Zhang, C. J. Fu, *International Journal of Energy Research* **2009**, *33*, 1203–1232.

[43] J. R. Howell, M. P. Mengüç, K. Daun, R. Siegel, *Thermal Radiation Heat Transfer*, CRC Press, **2020**.

[44] M. Planck, *The Theory of Heat Radiation*, Dover Publications, **1991**.

[45] G. Kirchhoff, *Annalen der Physik und Chemie* **1860**, *185*, 275–301.

[46] H.-S. Kim, C.-R. Lee, J.-H. Im, et al., *Scientific Reports* **2012**, *2*, 591.

[47] M. Wang, S. Lin, *Advanced Functional Materials* **2016**, *26*, 5297–5306.

[48] L. Schmidt-Mende, V. Dyakonov, S. Olthof, et al., *APL Materials* **2021**, *9*, 109202.

[49] H. S. Jung, N.-G. Park, *Small* **2014**, *11*, 10–25.

[50] P. P. Boix, S. Agarwala, T. M. Koh, N. Mathews, S. G. Mhaisalkar, *The Journal of Physical Chemistry Letters* **2015**, *6*, 898–907.

[51] C. Eames, J. M. Frost, P. R. F. Barnes, et al., *Nature Communications* **2015**, *6*, 7497.

[52] A. Pisoni, J. Jaćimović, O. S. Barišić, et al., *The Journal of Physical Chemistry Letters* **2014**, *5*, 2488–2492.

[53] R. Heiderhoff, T. Haeger, N. Pourdavoud, et al., *The Journal of Physical Chemistry C* **2017**, *121*, 28306–28311.

[54] Y. He, G. Galli, *Chemistry of Materials* **2014**, *26*, 5394–5400.

[55] T. Hata, G. Giorgi, K. Yamashita, *Nano Letters* **2016**, *16*, 2749–2753.

[56] L. N. Quan, M. Yuan, R. Comin, et al., *Journal of the American Chemical Society* **2016**, *138*, 2649–2655.

[57] I. C. Smith, E. T. Hoke, D. Solis-Ibarra, M. D. McGehee, H. I. Karunadasa, *Angewandte Chemie International Edition* **2014**, *53*, 11232–11235.

[58] N. Schuch, F. Verstraete, *Nature Physics* **2009**, *5*, 732–735.

[59] N. Lu, L. Li, N. Gao, M. Liu, *Organic Electronics* **2017**, *41*, 294–300.

[60] Z. Wang, K. Rolle, T. Schilling, et al., *Angewandte Chemie International Edition* **2019**, *59*, 1286–1294.

[61] T. Dörres, M. Bartkiewicz, K. Herrmann, et al., *ACS Applied Nano Materials* **2022**, *5*, 4119–4129.

[62] M. Stöter, D. A. Kunz, M. Schmidt, et al., *Langmuir* **2013**, *29*, 1280–1285.

[63] M. C. Wingert, J. Zheng, S. Kwon, R. Chen, *Semiconductor Science and Technology* **2016**, *31*, 113003.

[64] A. Einstein, *Annalen der Physik* **1911**, *340*, 679–694.

[65] T. Yamane, N. Nagai, S.-i. Katayama, M. Todoki, *Journal of Applied Physics* **2002**, *91*, 9772.

[66] J. L. Braun, S. W. King, E. R. Hoglund, et al., *Physical Review Materials* **2021**, *5*, 035604.

[67] A. M. Hofmeister, *Physics and Chemistry of Minerals* **2014**, *41*, 361–371.

[68] A. Henry, G. Chen, *Physical Review B* **2009**, *79*, 144305.

[69] S. Shen, A. Henry, J. Tong, R. Zheng, G. Chen, *Nature Nanotechnology* **2010**, *5*, 251–255.

[70] J. C. Duda, P. E. Hopkins, Y. Shen, M. C. Gupta, *Applied Physics Letters* **2013**, *102*, 251912.

[71] C. Huang, X. Qian, R. Yang, *Materials Science and Engineering: R: Reports* **2018**, *132*, 1–22.

[72] P. J. Flory, D. Y. Yoon, *Nature* **1978**, *272*, 226–229.

[73] R. Noriega, J. Rivnay, K. Vandewal, et al., *Nature Materials* **2013**, *12*, 1038–1044.

[74] Y. Ma, W. Hu, G. Reiter, *Macromolecules* **2006**, *39*, 5159–5164.

[75] L. H. Jimison, M. F. Toney, I. McCulloch, M. Heeney, A. Salleo, *Advanced Materials* **2009**, *21*, 1568–1572.

[76] C. G. Granqvist, A. Hjortsberg, *Journal of Applied Physics* **1981**, *52*, 4205–4220.

[77] E. Rephaeli, A. Raman, S. Fan, *Nano Letters* **2013**, *13*, 1457–1461.

[78] A. P. Raman, M. A. Anoma, L. Zhu, E. Rephaeli, S. Fan, *Nature* **2014**, *515*, 540–544.

[79] J. Mandal, Y. Fu, A. C. Overvig, et al., *Science* **2018**, *362*, 315–319.

[80] J. L. Braun, D. H. Olson, J. T. Gaskins, P. E. Hopkins, *Review of Scientific Instruments* **2019**, *90*, 024905.

[81] G. Simpson, *Practical Finite Element Modeling in Earth Science Using Matlab*, John Wiley & Sons, **2017**.

[82] A. Philipp, J. F. Eichinger, R. C. Aydin, et al., *Heat and Mass Transfer* **2019**, *56*, 811–823.

[83] H. Du, H. Hu, *IOP Conference Series: Earth and Environmental Science* **2017**, *69*, 012176.

[84] H. S. Carslaw, J. Jaeger, *Conduction of Heat in Solids*, Oxford University Press, **1959**.

[85] W. J. Parker, R. J. Jenkins, C. P. Butler, G. L. Abbott, *Journal of Applied Physics* **1961**, *32*, 1679–1684.

[86] R. D. Cowan, *Journal of Applied Physics* **1963**, *34*, 926–927.

[87] J. A. Cape, G. W. Lehman, *Journal of Applied Physics* **1963**, *34*, 1909–1913.

[88] H. Mehling, G. Hautzinger, O. Nilsson, et al., *International Journal of Thermophysics* **1998**, *19*, 941–949.

[89] A. Lunev, V. Zborovskii, T. Aliev, *International Journal of Thermal Sciences* **2021**, *160*, 106695.

[90] K. Herrmann, N. Pech-May, M. Retsch, *Photoacoustics* **2021**, *22*, 100246.

[91] A. G. Bell, *American Journal of Science* **1880**, *s3-20*, 305–324.

[92] A. Rosencwaig, A. Gersho, *Journal of Applied Physics* **1976**, *47*, 64–69.

[93] H. P. Hu, X. W. Wang, X. F. Xu, *Journal of Applied Physics* **1999**, *86*, 3953–3958.

[94] G. E. Moore, *Electronics* **1965**, *38*, 114.

[95] K. Atkinson, *An Introduction to Numerical Analysis*, John Wiley & Sons, **1988**.

[96] B. Fornberg, *ACM Transactions on Mathematical Software* **1981**, *7*, 512–526.

[97] P. Brezillon, J.-F. Staub, A.-M. Perault-Staub, G. Milhaud, *Computers & Mathematics with Applications* **1981**, *7*, 333–347.

[98] K. Levenberg, *Quarterly of Applied Mathematics* **1944**, *2*, 164–168.

[99] D. W. Marquardt, *Journal of the Society for Industrial and Applied Mathematics* **1963**, *11*, 431–441.

[100] H. B. Curry, *Quarterly of Applied Mathematics* **1944**, *2*, 258–261.

[101] R. Fletcher, *Practical Methods of Optimization*, John Wiley & Sons, **1987**.

[102] P. Peumans, A. Yakimov, S. R. Forrest, *Journal of Applied Physics* **2003**, *93*, 3693–3723.

[103] M. Dresselhaus, G. Chen, M. Tang, et al., *Advanced Materials* **2007**, *19*, 1043–1053.

[104] A. J. Schmidt, R. Cheaito, M. Chiesa, *Review of Scientific Instruments* **2009**, *80*, 094901.

[105] D. G. Cahill, *Review of Scientific Instruments* **2004**, *75*, 5119–5122.

[106] A. A. Maznev, J. A. Johnson, K. A. Nelson, *Physical Review B* **2011**, *84*, 195206.

[107] D. G. Cahill, *Review of Scientific Instruments* **1990**, *61*, 802–808.

[108] J. A. Balderas-López, A. Mandelis, *Journal of Applied Physics* **2001**, *90*, 2273–2279.

[109] C. A. Bennett, R. R. Patty, *Applied Optics* **1982**, *21*, 49.

[110] X. Wang, B. Cola, T. Bougher, et al., *Annual Review of Heat Transfer* **2013**, *16*, 135–157.

[111] K. Herrmann, S. Freund, F. Eller, et al., *Materials* **2022**, *15*, 7700.

[112] P. Hummel, A. M. Lechner, K. Herrmann, et al., *Macromolecules* **2020**, *53*, 5528–5537.

[113] A. M. Neuhöfer, K. Herrmann, F. Lebeda, et al., *Advanced Functional Materials* **2021**, *32*, 2108370.

[114] K. Herrmann, T. Lauster, Q. Song, M. Retsch, *Advanced Energy and Sustainability Research* **2021**, *3*, 2100166.

[115] Q. Song, T. Tran, K. Herrmann, et al., *Cell Reports Physical Science* **2022**, *3*, 100986.

5

Photoacoustic Thermal Characterization of Low Thermal Diffusivity Thin Films

Kai Herrmann,* Nelson W. Pech-May,§ and Markus Retsch*

* Department of Chemistry, Physical Chemistry 1, University of Bayreuth, Universitätsstraße 30, 95447 Bayreuth, Germany.

§ Bundesanstalt für Materialforschung und -prüfung (BAM), 12200 Berlin, Germany.

Published in *Photoacoustics*, **2021**, *22*, 100246.

5.1 Abstract

The photoacoustic measurement technique is a powerful yet underrepresented method to characterize the thermal transport properties of thin films. For the case of isotropic low thermal diffusivity samples, such as glasses or polymers, we demonstrate a general approach to extract the thermal conductivity with a high degree of significance. We discuss in particular the influence of thermal effusivity, thermal diffusivity, and sample layer thickness on the significance and accuracy of this measurement technique. These fundamental thermal properties guide sample and substrate selection to allow for a feasible thermal transport characterization. Furthermore, our data evaluation allows us to directly extract the thermal conductivity from this transient technique, without separate determination of the volumetric heat capacity, when appropriate boundary conditions are fulfilled. Using silica, poly(methyl methacrylate) (PMMA) thin films, and various substrates (quartz, steel, and silicon), we verify the quantitative correctness of our analytical approach.

5.2 Introduction

Rosencwaig and Gersho proposed the basic theory of the photoacoustic effect in condensed matter in 1976.[1] A periodically modulated laser beam is guided onto the material. Part or all absorbed light energy is transformed to heat through non-radiative deexcitation processes.[2] Therefore, a periodic heat source is realized. If a solid sample is enclosed in a gas-tight cell, an alternating expansion and contraction of the gas layer adjacent to the solid surface is induced due to the modulated surface temperature.[3] This generates the photoacoustic pressure signal, depending on the properties of the sample.[1,4] The proposed one-layer model by Rosencwaig and Gersho has been continuously extended to a two- and N-layer model to access more complex sample structures.[4–6]

Thermal characterization of thin films is an ongoing research topic since it is highly relevant because in nowadays microelectronics, coatings, or sensors, almost all materials are used as thin films.[7–9] The main goals are either dissipating the heat away as efficiently as possible, as with computer processors and solar cells, or maintaining a temperature gradient as in thermal barriers or thermoelectrics. There are several high-end thin film characterization methods, like frequency or time-domain thermoreflectance, transient thermal grating, or 3ω, which are usually accompanied by a high experimental effort and or revolve around thermally highly conductive materials where the heat carrier mean free path is in the order of the film thickness.[10–13] Furthermore, specific requirements for the sample geometry and layout cannot always be met by the mentioned techniques. Typical issues are surface roughness, optical transparency, or electrical isolation, respectively. Compared to these techniques,

the photoacoustic thermal characterization has been less widely used, which is even more surprising considering its suitability for low thermal diffusivity samples that we want to highlight in this contribution.[14]

The photoacoustic thermal characterization technique is comparatively simple and affordable. It can be applied to a wide range of materials with little restriction on the surface roughness, optical properties, or electrical insulation. Based on the existing framework, we develop this technique further to show its feasibility for many low diffusivity materials and the high degree of significance of the data evaluation. The performed analysis is based on the assumption of one-dimensional heat conduction in a multilayer system, in the absence of thermal contact resistances, stating continuity of temperature and heat flux at the interfaces. For ensuring a high signal-to-noise ratio, a closed-cell approach is utilized, where helium can be employed as the gas medium. Furthermore, we focus on the thermal piston effect since the mechanical piston effect can be estimated to contribute less than 1% to the measurement signal.[4]

At first, a rigorous sensitivity analysis is performed to outline general dependencies and relationships. Thereby, the influences of thermal effusivity and diffusivity can be understood rather descriptively in the framework of the one-dimensional thermal diffusion equation. Building upon this, uncertainty analysis for the concrete case of a low thermal diffusivity material is performed. In doing so, the limits of the significance of the measurement technique are theoretically covered for such samples. Experimental data subsequently verify the outlined theoretical framework. Thermally grown SiO_2 films of 5 μm thickness on silicon are characterized as reference samples. Furthermore, general relationships regarding thermal thickness and effusivity mismatch have been addressed using poly(methyl methacrylate) (PMMA) thin films. For both, a satisfying agreement between measured and literature values is found.

In conclusion, we point out how to optimize and perform the thermal characterization of low diffusivity solids in the μm and sub-μm regime with the in comparison relatively simple experimental setup of the photoacoustic measurement.

5.3 Theory

Thermal Wave Interferometry

Thermal wave interference is implicitly contained in the Rosencwaig-Gersho theory. Still, it is worth pointing out the role of interference by using an approach incorporating thermal wave reflection and transmission coefficients.[15]

Due to the periodic nature of the thermal excitation and therefore a harmonic heat flow, highly damped so-called thermal waves are generated. For thermally thick

materials, which are considered semi-infinite, such thermal waves propagate freely into the bulk and exhibit a constant phase shift of the surface temperature relative to the modulated heat source of $\frac{\pi}{2}$.[16] The surface temperature can hereby directly be related to the photoacoustic signal, as explained in detail in Appendix 5.7.
Introducing a finite layer on top of a semi-infinite one leads to the presence of an interface. This interface prevents the free propagation of thermal waves and results in an altered phase shift $\Delta\phi$ relative to the semi-infinite bulk material.

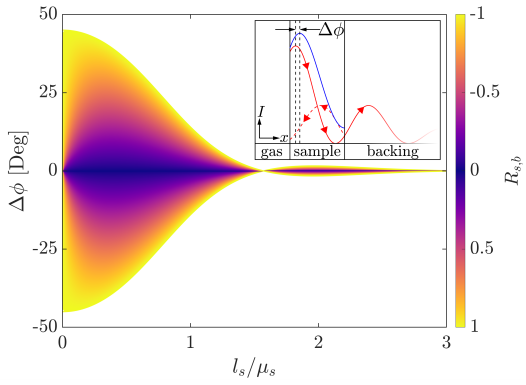

Figure 5.1: Theoretical phase shift of the surface temperature for a two-layer system with different thermal reflection coefficients $R_{s,b}$ as a function of the frequency-dependent thermal thickness l_s/μ_s.[15] The inset is intended to depict the principle of thermal wave interference.

The general concept of thermal wave interference can be explained rather simply for a two-layer system with the help of a gedankenexperiment. The second layer is considered semi-infinite in this case. A diagram of the gedankenexperiment is depicted in the inset of Figure 5.1, where x denotes the one-dimensional space coordinate, while I represents the wave intensity. Here a damped heat wave, comprising diffusive phonon transport, propagates freely in a medium in the positive x-direction (solid red line). If wave-like properties were assigned, the introduction of an interface would lead to reflection in the negative x-direction (dashed red line), and a superposition within the sample (solid blue line) would be the consequence. This superposition manifests in a phase shift and an altered amplitude, which can be detected by measuring the surface temperature. For illustration purposes, we assumed total reflection at the sample backing interface in Figure 5.1. The amount of reflection as well as the thickness, and thus damping, therefore directly influence $\Delta\phi$, which will be further elucidated in the performed sensitivity analysis.
Although the heat transport is diffusive, and, as Salazar pointed out, the thermal waves do not transport energy, wave-like properties such as reflection and interference are still instructive to understand the influence of thermal effusivity mismatch and thermal diffusivity on $\Delta\phi$.[17,18] When a thermal wave strikes the interface between the sample and backing with thermal effusivities ε_s and ε_b the thermal reflection coefficient $R_{s,b}$ for normal incidence and in the absence of contact resistances reduces to:[18]

$$R_{s,b} = \frac{1 - \varepsilon_b/\varepsilon_s}{1 + \varepsilon_b/\varepsilon_s} = \frac{\varepsilon_s - \varepsilon_b}{\varepsilon_s + \varepsilon_b}. \tag{5.1}$$

Therefore, the magnitude of $R_{s,b}$ is determined by the ratio of thermal effusivities, which may be regarded as a measure of the thermal mismatch between the two media.[19] The presence of contact resistances would lead to discontinuities in tem-

perature and heat flux at the interface and are not considered in this work. For samples between the thermally thin and thermally thick limiting cases, thermal wave interference effects are observable and can be utilized for thermal characterization. In addition to the thermal wave interferometry explanation, fundamental parameters affecting the phase shift on the sample's surface can be identified from the one-dimensional heat diffusion model in a multi-layered system in Appendix 5.7. The phase shift is based primarily on the thermal effusivity ratios $\varepsilon_{i+1}/\varepsilon_i$ and the dimensionless thermal thickness l_i/μ_i (see equations (5.9b) and (5.9c)), and therefore the sample thickness and diffusivity, as well as the modulation frequency of the heat source.

The phase shift can be calculated for different values of $R_{s,b}$ between the sample and the thermally thick backing. By introducing the dimensionless thermal thickness l_s/μ_s, a representation is obtained, which is independent of the actual values of D_s, l_s, and the frequency regime is shown in Figure 5.1.

For $R_{s,b} \neq 0$, a maximum ($R_{s,b} < 0$, $\varepsilon_s < \varepsilon_b$) or minimum ($R_{s,b} > 0$, $\varepsilon_s > \varepsilon_b$) in phase shift is present. Moreover, the effusivity ratio between sample and backing affects the extremums resulting shape and position. Increasing the absolute value of $R_{s,b}$ thereby shifts the extremum to lower thermal thicknesses (l_s/μ_s) while the resulting change in phase shift ($\Delta\phi$) also increases in absolute value. For a fixed thermal diffusivity and measurement frequency regime, the sample thickness shifts the extremum's position. Increasing the sample thickness shifts the maximum to lower frequencies, while decreasing it causes a shift to higher frequencies. Considering $R_{s,b} < 0$, which is a substrate with higher thermal effusivity than the sample, the thermal wave is phase-shifted upon reflection, similar to the behavior of electromagnetic waves. This leads to the symmetric split of the phase shift depending on the sign of $R_{s,b}$.

An interesting point is the zero-crossing at $l_s/\mu_s = \pi/2$, regardless of the thermal reflection coefficient. At this point, the sample thickness is equal to a quarter of the thermal wave with $\lambda = 2\pi\mu_s$ leading to a zero-crossing. Zero-crossings are theoretical also present for $l_s/\mu_s = n \cdot \pi/2$ with $n \in \mathbb{N}$, but not recognizable due to the heavily damped nature of the thermal wave.

Summing up, thermal effusivity affects the amount of heat being reflected at the sample backing interface, while thermal diffusivity affects the damping of the thermal wave. In the one-dimensional limit of the heat diffusion equation with a periodic heat flow, general correlations between the effusivity ratios $\varepsilon_{i+1}/\varepsilon_i$ and thermal thickness l_i/μ_i, which affect the surface temperature, can now be identified. The question of how these parameters affect the measurement is addressed with the help of sensitivity analysis in Section 5.3.1.

Model

The samples investigated in this work follow a geometry, as shown in Figure 5.2. A transducer layer with a high absorption coefficient at the excitation wavelength is used to ensure a sufficiently high photoacoustic signal. Therefore, the sample is exposed to a modulated heat flux instead of heat being generated in the sample itself. This, furthermore, enables the measurement of transparent solids. Additionally, the optical properties of the sample are not relevant for the measurement and data evaluation.

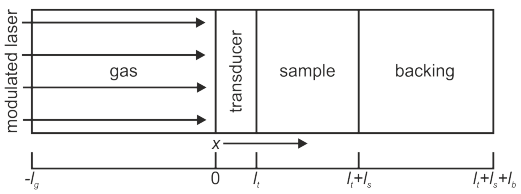

Figure 5.2: Schematic representation of the modeled sample geometry, including a transducer and a thermally thick backing.

In the following, the subscripts b, s, t, and g will represent the backing, sample, transducer, and gas, respectively. For studying thermal transport across an N-layered film, Xu *et. al* proposed a matrix-based solution for the one-dimensional heat diffusion equation.[4] We consider the solution corresponding to three layers (transducer, sample, and backing) in this work. Additionally, heat conduction to the gas is also considered. The mathematical development and physical boundary conditions applied to the one-dimensional heat diffusion equation are given in detail in Appendix 5.7 and agree with previous reports.[1,4]

In equations (5.9) the main factors affecting the thermal model can be identified. Explicitly those are the effusivity ratios between gas and transducer, transducer and sample, and sample and backing in equations (5.9b) and (5.9c). Furthermore, here, the thermal thicknesses of transducer and sample enter in the exponential terms, while gas and backing are assumed to be thermally thick. Heat generation is taken into account in equations (5.9d) and (5.9e). As the model has low sensitivity to the effusivity ratio between transducer and sample $\varepsilon_t/\varepsilon_s$ in the studied regime, this ratio is expressed in terms of the effusivity ratio between the sample and backing $x = \varepsilon_s/\varepsilon_b$ by $\varepsilon_t/x \cdot \varepsilon_b$. Due to the high absorption coefficient of the transducer at the wavelength of excitation ($1.1 \cdot 10^6$ cm^{-1}), the intensity of the pump is decreased by a factor of $1 \cdot 10^{-5}$ for a 100 nm transducer layer.[20] The model, therefore, gets insensitive to the optical properties of the layers below.

We determine the sample's thermal transport properties via the thermal effusivity ratio between the sample and backing $\varepsilon_s/\varepsilon_b$ and the sample's thermal diffusivity D_s, not the thermal conductivity directly. Therefore, specific heat and density, or volumetric heat capacity, are not required as known parameters. Only knowledge about the sample thickness is crucial. In an optimized measurement system, thermal

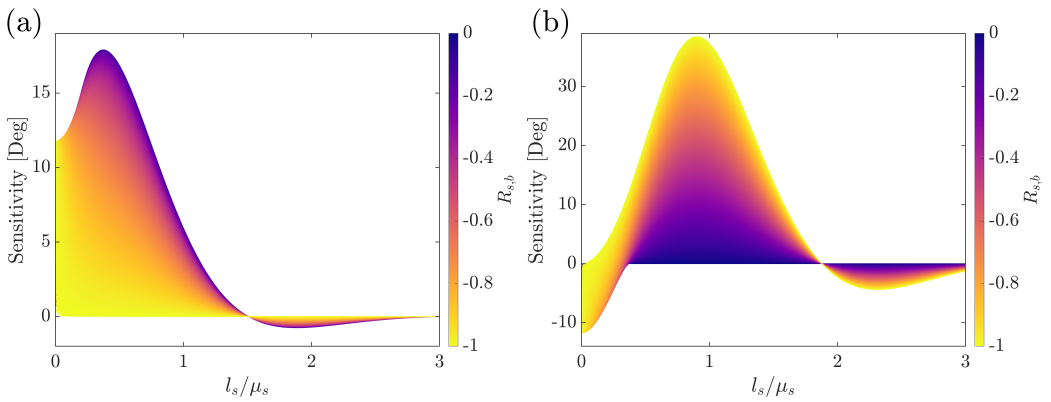

Figure 5.3: Sensitivity analysis for a polymeric sample to the fit parameters $\varepsilon_s/\varepsilon_b$ (a) and $1/\sqrt{D_s}$ (b) as a function of thermal thickness and thermal reflection coefficient.

diffusivity and effusivity can both be determined. Hence, sensitivity to both variables is essential to derive the thermal conductivity correctly by:[19,21]

$$k = \varepsilon\sqrt{D}. \tag{5.2}$$

5.3.1 Sensitivity Analysis

A sensitivity analysis was performed to estimate the influence of the sample's thermal properties on the measured phase shift. For this purpose, a local method was applied where the sensitivity to the parameter i is defined as:[22]

$$S_i = \frac{\partial\phi}{\partial p_i} \cdot p_i. \tag{5.3}$$

With p_i being the value of parameter i and ϕ being the phase. The partial derivative is calculated numerically by perturbing the value p_i by 1% and determining the resulting change in phase. Normalizing by multiplying with the parameter value p_i is performed to compare the sensitivity to properties that are different by orders of magnitude.[23]

Only negative reflection coefficients are considered since almost every solid substrate material exhibits a higher thermal effusivity than the polymeric samples investigated in this work. For the sensitivity analysis, the parameters in Table 5.1 were used. For a polymeric sample with $D_s = 0.12 \cdot 10^{-6}$ $\mathrm{m^2 s^{-1}}$, $\varepsilon_s = 520$ $\mathrm{Ws^{0.5} m^{-2} K^{-1}}$, a transducer layer of 100 nm nickel and for thermal reflection coefficients $-1 \leq R_{\mathrm{s,b}} \leq 0$, which represents a variation of the substrate material, the sensitivity analysis is shown in Figure 5.3.

An interesting point is the inversed dependency of the two fit parameters on the thermal reflection coefficient $R_{s,b}$. While the sensitivity to the effusivity ratio $\varepsilon_s/\varepsilon_b$ is maximized for a thermal reflection coefficient of zero (see Figure 5.3a), meaning the

sample and the substrate exhibit the same thermal effusivity, the sensitivity to the thermal thickness is non-existing in this case (see Figure 5.3b). With increasing the thermal mismatch, and therefore $R_{s,b}$ approaching -1, the sensitivity to the effusivity ratio decreases. On the other hand, the sensitivity to the thermal diffusivity increases with an increased thermal mismatch.
Briefly, for estimating both thermal effusivity and diffusivity, the thermal reflection coefficient $R_{s,b}$ is supposed to be in an intermediate range, which means sample and substrate have thermal effusivities in the same order of magnitude, while a thermal thickness regime between approximately 0.1 to 1 thermal thicknesses l_s/μ_s should be covered.

5.3.2 Uncertainty Analysis

To determine in which thickness regime samples can be measured significantly, besides the general dependencies covered in the sensitivity analysis, an uncertainty analysis was carried out. Yang *et al.* developed a procedure to take into account uncertainties in so-called controlled parameters.[24] The general idea is to treat all errors as Gaussian distributed and to approximate the non-linear model in close proximity to the determined fit parameters as a first-order Taylor expansion. This approach was furthermore validated using Monte Carlo simulations.[24] The procedure to calculate the uncertainties is shown in Appendix 5.7. A fixed frequency regime between 310 Hz and 10 kHz is used to relate this uncertainty analysis to the measurement.

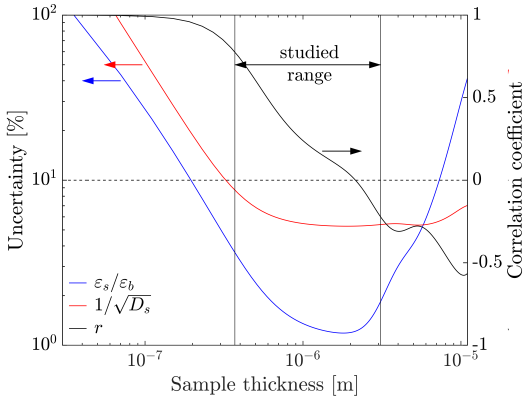

Figure 5.4: Calculated uncertainties and correlation coefficient r of the fit parameters for a polymeric thin film on quartz, plotted as a function of sample thickness. The dotted line is a guide to the eye for 10% uncertainty and no correlation, while the range of sample thicknesses studied in this work is highlighted.

The uncertainties in the controlled parameters transducer and sample thickness are estimated to be 5%, and the uncertainty of the measured phase values are taken to be 0.5 deg. All other parameters are the same as in the sensitivity analysis except for a fixed thermal reflection coefficient of -0.48, which is approximated for a polymeric sample on quartz and supposed to offer sensitivity to thermal effusivity and diffusivity, based on the sensitivity analysis in Figure 5.3. The uncertainty of the thermal properties is taken as the $\pm 1/e$ confidence interval in this paper. The calculated uncertainties and the correlation coefficient r, a measure of the strength and direction of the relationship between two variables, for the two fit parameters

are shown in Figure 5.4.
In general, for thinner and thicker samples than studied in this work, an approximately exponential increase in uncertainty is observable. The uncertainty for the thermal effusivity is lower than the uncertainty for the thermal diffusivity for sample thicknesses below and vice versa above 6 μm. This is due to the different positions of maximum sensitivity in thermal thickness, where the maximum sensitivity for thermal effusivity is present at lower thermal thicknesses than the maximum sensitivity for thermal diffusivity. Furthermore, for low sample thicknesses, the parameters get highly correlated with r approaching unity. This renders a simultaneous determination impossible due to the existence of multiple solutions. An optimum sample thickness regime for a polymeric sample can be identified, where both estimated uncertainties are below 10%. This is the case for sample thicknesses between approximately 500 nm and 5 μm, which can hardly be analyzed by other measurement techniques.
Therefore, the photoacoustic measurement is inherently well suited for thermally characterizing low thermal diffusivity thin films with a high degree of significance. To confirm these numerical calculations, various thin films were examined to estimate how they could be translated into actual measurements.

5.4 Experiment

5.4.1 Samples

Silicon wafers (n-type) with a 5 μm thermally grown SiO_2 layer were purchased from MicroChemicals. Polymeric samples were prepared using the spin-coating technique. Quartz substrates were bought from Präzisions Glas und Optik GmbH, steel AISI 316 substrates were bought from Goodfellow GmbH, while undoped silicon (111) substrates were purchased from MicroChemicals GmbH. Prior to spin-coating, the substrates were cleaned using ultrasonication in a detergent solution (2 V% Hellmanex III in Milli-Q water) twice and in ethanol p.a. once.
For spin-coating various concentrations of poly(methyl methacrylate) (PMMA) 7N, purchased from Evonik Industries, in chlorobenzene were prepared.
All samples and a thermally thick reference material (quartz) to determine the setup's transfer function were coated with a 100 nm nickel layer by thermal evaporation.[16] The layer thickness was monitored using a quartz crystal microbalance and verified with AFM measurements.
The thicknesses of the polymeric films were determined using an Olympus OLS5000 laser confocal microscope.

5.4.2 Photoacoustic Measurement

Photoacoustic measurements were performed with a continuous wave Coherent Genesis MX488-1000 laser. The laser is modulated using a ConOptics 350-160 electro-optic modulator driven by a ConOptics M25A amplifier and a sine signal of a Zurich Instruments lock-in amplifier HF2LI. The generated acoustic signal was detected using a Bruel & Kjaer 4398-A-011 microphone. The signal was then amplified with a Bruel & Kjaer 2690-0S1 preamplifier by 1 V/Pa. The settling time after changing a sweep parameter, as well as the averaging time, was set to 30 s. The laser power was measured to be 35 mW at the sample position using a Coherent FieldMaxII. The $1/e$ diameter of the spot was determined to be 2.19 mm using a DataRay Beam'R2 XY Scanning Slit Beam Profiler. The pressure in the photoacoustic cell was set to 1.379 bar of helium, which corresponds to 20 psi. Helium was used as the cell gas for this work because of its high thermal conductivity, leading to a high signal to noise ratio. The experimental setup is shown schematically in Figure 5.5.

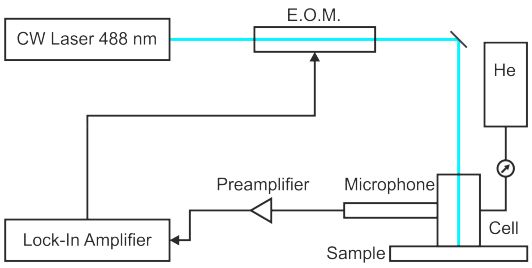

Figure 5.5: Schematic setup with a continuous wave laser being passed through an EOM to provide the modulated heat source. The photoacoustic signal is measured using a microphone in the pressurized cell.

The cell itself is made of MACOR® to prevent cell fracture and consists of a cell volume of 4 mm in diameter, which corresponds to the measured sample area, and 8.4 mm height. The microphone is connected via a side bore of 2.2 mm in diameter, and the helium connection via a side bore of 1.6 mm in diameter.[22,25] Sealing of the samples at the backside of the cell is realized using a ring seal. The front side of the cell is sealed with a sapphire window using epoxy resin.

The true phase shift of the sample, without the setup's transfer function, is calculated as $\Delta\phi = \phi_{\text{sample}} - \phi_{\text{reference}}$, where ϕ_{sample} is the measured phase shift for the respective sample and $\phi_{\text{reference}}$ is the measured phase shift of a thermally thick quartz sample.[22]

5.4.3 Data Analysis

Appendix 5.7 describes the model being used to perform data analysis. A least-squares fitting method employing the Levenberg-Marquardt algorithm is performed to determine the parameters $\varepsilon_s/\varepsilon_b$ and $1/\sqrt{D_s}$. The approach for error estimation is described in Appendix 5.7. In doing so, three independent measurements are analyzed using a Monte Carlo approach for the controlled parameters. Simultaneously, the uncertainty of every fit procedure is taken into account by the respective covariance

Table 5.1: Literature values used for sensitivity and data analysis.[a]

Material	Diffusivity $\left[\frac{m^2}{s}\right]$	Effusivity $\left[\frac{W \cdot s^{0.5}}{m^2 \cdot K}\right]$
Helium	not needed	17.4 [b]
Nickel	$22.95 \cdot 10^{-6}$	18932
Quartz	not needed	1503
Steel AISI 316	not needed	7188
Silicon	not needed	15669

[a] Values are taken from Ref. [18] if not stated explicitly.

[b] Value is taken from Ref. [26].

matrix.

The literature values used for the data analysis are shown in Table 5.1.

5.5 Results and Discussion

In contrast to previous works, we consider the need and influence of an optimized measurement for performing data analysis with a high degree of significance. In doing so, we verify our theoretical findings from Section 5.3 on a silicon dioxide sample reference with known properties. Subsequently, the proposed approach is applied to polymeric thin films to extract their thermal effusivity and diffusivity simultaneously.

As with any measurement technique, testing a sample with known properties is crucial to ensure the accuracy and reproducibility of the performed measurements. Silicon with a thermally grown silicon dioxide layer is one of the most commonly used calibration samples for the photoacoustic technique to validate the present setup before moving on to self-produced polymeric thin films.[23] A 525 μm thick silicon wafer with a 5 μm thick silicon dioxide layer is appropriate for this purpose since it is on the lower boundary of the significantly analyzable sample thickness compared to its inherent thermal diffusivity. This is an improvement over previous work, as they use reference samples with insufficient layer thickness, hence suboptimal sensitivity. The phase shift data of this silicon dioxide on silicon sample with an exemplary performed fit is depicted in Figure 5.6.

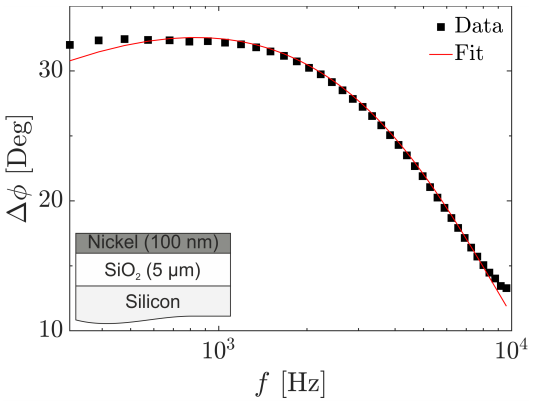

Figure 5.6: Phase shift data of a 5 μm thermally grown SiO_2 on a Si substrate with an exemplary performed fit.

Table 5.2: Extracted thermophysical properties in comparison to literature values. Thermal conductivity is calculated based on thermal diffusivity and effusivity.

Material	Substrate	Thermal diffusivity D $\left[\cdot 10^{-6}\ \frac{\mathrm{m}^2}{\mathrm{s}}\right]$	Thermal effusivity ε $\left[\frac{\mathrm{W}\cdot\mathrm{s}^{0.5}}{\mathrm{m}^2\cdot\mathrm{K}}\right]$	Thermal conductivity k $\left[\frac{\mathrm{W}}{\mathrm{m}\cdot\mathrm{K}}\right]$
Silicon dioxide				
Literature values [a]		0.87	1503	1.4
$l = 5\ \mu$m	Silicon	0.809 ± 0.013	1560 ± 49	1.40 ± 0.05
PMMA				
Literature values		0.12 [b]	522 [c]	0.18
$l = 370 \pm 19$ nm	Quartz	0.146 ± 0.024	490 ± 26	0.188 ± 0.019
$l = 1095 \pm 55$ nm	Quartz	0.119 ± 0.013	507 ± 8	0.175 ± 0.010
$l = 3096 \pm 155$ nm	Quartz	0.112 ± 0.012	540 ± 10	0.181 ± 0.010
$l = 1120 \pm 56$ nm	Steel	0.117 ± 0.012	552 ± 11	0.189 ± 0.011
$l = 1075 \pm 54$ nm	Silicon	0.111 ± 0.012	509 ± 26	0.169 ± 0.013

[a] Values are taken from Ref. [18].

[b] Value is taken from Ref. [27].

[c] Value is taken from Ref. [28].

The extracted thermophysical properties, as well as literature values, are listed in Table 5.2. A good agreement between the literature and determined thermal properties is evident, verifying this technique's use.

To demonstrate the crucial influence of the thermal reflection coefficient and the thermal thickness of the samples to be measured, a series of Poly(methyl methacrylate) thin films is investigated where the thickness and substrate material, and therefore effusivity mismatch, are varied. Poly(methyl methacrylate) was chosen as a well-characterized, basic polymeric material to verify general dependencies. As substrates materials, silicon, steel AISI 316, and quartz were used to cover a wide range of thermal effusivities.

The influence of the thermal thickness is investigated on PMMA thin films with thicknesses of 370 ± 19 nm, 1095 ± 55 nm, and 3096 ± 155 nm, respectively, on quartz substrates. The measured phase shift and exemplary performed fits are shown in Figure 5.7.

The thickness dependency could be presented convincingly, and quantitative data analysis with a high degree of significance is possible. It is clearly recognizable that the maximum in phase is shifted to lower frequencies with increasing sample thickness. The slight increase of the maximums absolute value in phase shift $\Delta\phi$ with increasing layer thickness can, furthermore, be attributed to the presence of a transducer layer. For opaque samples without a transducer layer, the maximums absolute value would be thickness-independent.

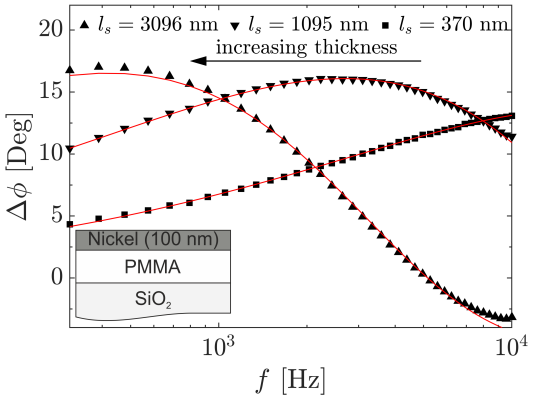

Figure 5.7: Phase shift data of PMMA thin films on quartz substrates. Exemplary performed fits are depicted by red lines in each case.

Substantial deviations from the sample thicknesses shown here (< 500 nm or > 3 μm) lead to a shift of the maximum outside of the detectable frequency regime. Hence, only a monotonous increase or decrease in phase shift is detected, making a significant data analysis very difficult.

Compared to literature values, the determined thermal properties in Table 5.2 based on the input parameters in Table 5.1 are reasonable. For the thinnest film, deviations start to become apparent due to the increasing uncertainty, as well as the increasing correlation of the parameters to be determined.

The influence of thermal effusivity mismatch between sample and substrate is investigated on three different substrate materials. PMMA thin films with thicknesses of 1095 ± 55 nm on quartz, 1120 ± 56 nm on steel AISI 316, and 1075 ± 54 nm on silicon are studied for this purpose. The measured phase shift and exemplary performed fits are shown in Figure 5.8.

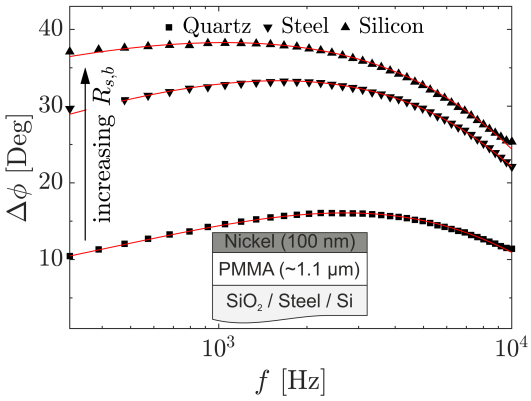

Figure 5.8: Phase shift data of approximately 1.1 μm PMMA thin films on various substrates, for precise thickness see Table 5.2. Exemplary performed fits are depicted by red lines in each case.

The influence of effusivity mismatch could likewise be clearly confirmed. Additionally, the determined thermal properties show an evident consistency with the literature values. While a high sensitivity to thermal diffusivity was expected due to the sample thickness for all substrates, the thermal effusivity could still be determined quite accurately for all substrates. Still, the uncertainty is increased on the silicon substrate representing the decreasing sensitivity at a high effusivity mismatch.
These experiments confirm that the photoacoustic measurement technique enables the full thermal characterization of low thermal diffusivity materials in the micron and submicron regime. General dependencies affecting the measurement and how to efficiently design the sample environment have been pointed out. These are crucial to enable highly sensitive measurements of both thermal diffusivity and effusivity.
Furthermore, the employed analytical approach can be applied to other samples and other measurement techniques working with the one-dimensional approximation of the heat diffusion equation.

5.6 Conclusion

In this work, we introduced a reliable approach to extract the thermal conductivity of low thermal diffusivity thin films using the photoacoustic technique. In particular, thermal conductivity uncertainties of around 6% to 10% were obtained for PMMA thin films with thicknesses on the order of microns and a few hundreds of nanometers, respectively. Furthermore, we discussed the influence of parameters such as thermal effusivity, thermal diffusivity, and sample layer thickness on the significance and accuracy of this measurement technique. This was performed within the framework of a one-dimensional heat conduction model in a three-layer system. From this analysis, we deduced guidelines for the selection of sample and substrate configuration allowing for a feasible thermal transport characterization of any low thermal diffusivity thin film. Possible applications are, therefore, the accurate thermal characterization of polymeric thin films or emerging hybrid thermoelectric materials. Moreover, our results show that the developed data evaluation allows to directly extract the thermal conductivity from a single measurement, provided that the appropriate boundary conditions are fulfilled.

Acknowledgments

This work was funded by the German Research Foundation (DFG, SFB 840, project B7). The authors thank Tobias Lauster and Paul Markus for performing AFM measurements, and Baratunde A. Cola, Thomas L. Bougher, and the Heat Lab at the Georgia Institute of Technology for introducing us to the photoacoustic measurement technique. Furthermore, Patrick Hummel is gratefully acknowledged for knowledge transfer and the initial setup of the measurement technique in our group.
N.W. Pech-May acknowledges an Adolf Martens fellowship at BAM, Berlin.
We thank A. Christmann (University of Bayreuth) for fruitful discussion and feedback.

5.7 Appendix

Multilayer Model

The model from Hu *et al.* can be adapted for the $N = 2$ layer system depicted in Figure 5.2 with a highly absorbing transducer layer.[4] The backing layer is thereby represented as $i = 0$, the sample as $i = 1$, the transducer as $i = 2$, and the gas as $i = 3$. Neither the gas nor the backing is assumed to absorb any of the incident radiation and are considered to be thermally thick. Furthermore, multiple reflections between interfaces and convective heat transfer in the gas are neglected. Thermal contact resistances are not taken into account in this work, and one-dimensional heat diffusion is assumed. For easy comparison with the Rosencwaig-Gersho model, the same notation is adopted. Therefore f or $\omega = 2\pi f$ is the modulation frequency, β_i the optical absorption coefficient, k_i the thermal conductivity of material i, ε_i the thermal effusivity of material i, D_i the thermal diffusivity of material i, $a_i = \sqrt{\pi f / D_i}$ the thermal diffusion coefficient of material i, $\sigma_i = (1 + j)a_i$ the complex-valued thermal diffusion coefficient of material i and $\theta_i = T_i - T_{\mathrm{amb}}$ represents the temperature rise of material i with respect to the ambient temperature.
In general, at low frequencies ($2\pi f\tau << 1$), where τ is the thermal relaxation time, both parabolic and hyperbolic solutions coincide, which is expected to be the case in the frequency regime below 20 kHz.
It has been recognized that the one-dimensional heat transfer model is adequate for describing the temperature variation under typical experimental conditions when the thermal diffusion length in gas and the target is much less than the diameter of

the laser beam.[29] Therefore, the thermal diffusion equation in layer i can then be expressed as:[16]

$$\frac{\partial\theta_i}{\partial x^2} = \frac{1}{D_i}\frac{\partial\theta_i}{\partial t} - \frac{\beta_i I_0}{2k_i}\exp(-\sum_{m=i+1}^{N} -\beta_m l_m)e^{\beta_i(x-l_i)}(1+e^{j\omega t}) \tag{5.4}$$

Here $\theta_i = T_i - T_{\text{amb}}$ is the modified temperature in layer i. The solution θ_i in general consists of three parts: a transient component, a steady direct component, and a steady alternating component. Since the experiment uses lock-in detection, only the steady alternating component $\tilde{\theta}_i$ is measured, only this component needs to be evaluated.[16] It results from the periodic source term in eq. (5.4) and has a particular solution in the form of $-E_i e^{\beta_i(x-l_i)}e^{j\omega t}$, where $E_i = G_i/(\beta_i^2 - \sigma_i^2)$ with $G_i = (\beta_i I_0)/(2k_i)\exp(-\sum_{m=i+1}^{N}\beta_m l_m)$ for $i < N$, $G_N = \beta_N I_0/2k_N$, and $G_{N+1} = 0$.[16] The general solution can be expressed in the form of:

$$\tilde{\theta}_i = [A_i e^{\sigma_i(x-h_i)} + B_i e^{-\sigma_i(x-h_i)} - E_i e^{x-h_i}]e^{j\omega t}. \tag{5.5}$$

A_i and B_i are coefficients to be determined, while h_i is calculated as $h_i = l_i$ for $i < N$ and $h_{N+1} = 0$. To solve this, the gas and backing layer are assumed to be thermally thick, meaning $|\sigma_0 l_0| >> 1$ and $|\sigma_g l_g| >> 1$. Based on this assumption, the coefficients A_{N+1} and B_0 can be taken as zero. Using interfacial conditions, stating that the heat flux is continuous between layers,

$$k_i\frac{\partial\tilde{\theta}_i(l_i)}{\partial x} - k_{i+1}\frac{\partial\tilde{\theta}_{i+1}(l_i)}{\partial x} = 0. \tag{5.6}$$

Similarly, continuity of the temperature at the interfaces is assumed,

$$\tilde{\theta}_i(l_i) - \tilde{\theta}_{i+1}(l_i) = 0, \tag{5.7}$$

the recurrence formula of the coefficients A_i and B_i is obtained in matrix form:

$$\begin{bmatrix} A_i \\ B_i \end{bmatrix} = U_i \begin{bmatrix} A_{i+1} \\ B_{i+1} \end{bmatrix} + V_i \begin{bmatrix} E_i \\ E_{i+1} \end{bmatrix}, \tag{5.8}$$

where

$$U_i = \tfrac{1}{2}\begin{bmatrix} u_{11,i} & u_{12,i} \\ u_{21,i} & u_{22,i} \end{bmatrix}; \quad V_i = \tfrac{1}{2}\begin{bmatrix} v_{11,i} & v_{12,i} \\ v_{21,i} & v_{22,i} \end{bmatrix}, \tag{5.9a}$$

$$u_{1n,i} = \left(1 \pm \tfrac{\varepsilon_{i+1}}{\varepsilon_i}\right)\cdot\exp\left(\mp(1+j)\tfrac{l_{i+1}\cdot\sqrt{\pi f}}{\sqrt{D_{i+1}}}\right), \tag{5.9b}$$

$$u_{2n,i} = \left(1 \mp \tfrac{\varepsilon_{i+1}}{\varepsilon_i}\right)\cdot\exp\left(\mp(1+j)\tfrac{l_{i+1}\cdot\sqrt{\pi f}}{\sqrt{D_{i+1}}}\right), \tag{5.9c}$$

$$v_{n1,i} = 1 \pm \tfrac{\beta_i}{\sigma_i}, \tag{5.9d}$$

$$v_{n2,i} = \left(-1 \mp \tfrac{k_{i+1}\beta_{i+1}}{\varepsilon_i(1+j)\sqrt{\pi f}}\right)\cdot\exp(-\beta_{i+1}l_{i+1}). \tag{5.9e}$$

The coefficients A_i and B_i are obtained as:

$$B_{N+1} = -\frac{\begin{bmatrix} 0 & 1 \end{bmatrix} \sum_{m=0}^{N} \left(\prod_{i=0}^{m-1} U_i \right) V_m \begin{bmatrix} E_m \\ E_{m+1} \end{bmatrix}}{\begin{bmatrix} 0 & 1 \end{bmatrix} \left(\prod_{i=0}^{N} U_i \right) \begin{bmatrix} 0 \\ 1 \end{bmatrix}} \tag{5.10}$$

$$\begin{bmatrix} A_i \\ B_i \end{bmatrix} = \left(\prod_{m=i}^{N} U_m \right) \begin{bmatrix} 0 \\ B_{N+1} \end{bmatrix} + \sum_{m=i}^{N} \left(\prod_{k=i}^{m-1} U_k \right) V_m \begin{bmatrix} E_m \\ E_{m+1} \end{bmatrix}. \tag{5.11}$$

Where $\prod_{k=i}^{i-1} U_k$ is taken as $\left[\begin{smallmatrix} 1 & 0 \\ 0 & 1 \end{smallmatrix}\right]$. In particular, the complex time-dependent temperature distribution in the gas can be found as:[16]

$$\theta_{N+1} = B_{N+1} \cdot \exp\left(-\sigma_{N+1} x\right) \exp\left(j\omega t\right). \tag{5.12}$$

Photoacoustic Signal Generation

The measured photoacoustic pressure signal is due to the acoustic wave in the gas cell induced by the incident light on the sample.[4] To draw conclusions about the temperature oscillations at the sample surface by evaluating the generated acoustic signal, surface temperature and pressure have to be set into a relation. According to the basic principle of thermodynamics, there are relations among intensive thermodynamic properties, namely the equations of state.[4] For the gas in the photoacoustic cell, the pressure can, therefore, be expressed by temperature and volume. Assuming an ideal gas behavior yields the shown simplification.

$$dp = \left(\frac{\partial p}{\partial T} \right)_V dT + \left(\frac{\partial p}{\partial V} \right)_T dV = \frac{p}{T} dT - \frac{p}{V} dV \tag{5.13}$$

As the dimension of the cell l_g is required to be less than half of the minimum wavelength of the sound wave in the gas cell during the measurement, the pressure can be assumed uniform.[4] As there is a temperature distribution due to the incident radiation, the differential temperature dT in equation (5.13) can be replaced by a volume-averaged temperature variation $\langle dT \rangle$ yielding

$$dp = \frac{p}{T} \langle dT \rangle - \frac{p}{V} dV \tag{5.14}$$

The differential pressure dp generates the photoacoustic signal. As shown by Hu *et al.*, this can be interpreted as a composite piston model with the differential temperature being related to a thermal piston, while the differential volume is related to a mechanical piston.[4] We focus on the thermal piston effect since the mechanical piston effect can be estimated to contribute less than 1% to the measurement signal. As the volume average of the temperature $\langle dT \rangle$ in equation (5.14) is equivalent to

the modified temperature in the gas due to periodic heating of the sample $\langle\theta_{N+1}\rangle$ as derived in equation (5.12), the measured photoacoustic signal phase can be reduced to the surface temperature phase $\mathrm{Arg}(B_{N+1}) - \frac{\pi}{4}$.[4]

This relationship is used to determine the unknown parameters in B_{N+1} by fitting the theoretical model to the experimentally measured phase-shift data. If sample thickness and transducer and backing properties are known, the sample's thermal properties can be extracted.

The difference between the piston models developed by Hu *et al.* compared to the ones developed by Rosencwaig and Gersho lies in the ratio of specific heats $\gamma = c_p/c_v$, which is apparent in the RG theory.[1,4] In the model by Rosencwaig and Gersho, both the thermal and mechanical compressing processes in the gas cell are assumed to be adiabatic. However, the process is isochoric for the thermal piston and polytropic for the mechanical piston as shown by Hu *et al.*[4]

Uncertainty Analysis

Uncertainty analysis was carried out according to Yang *et al.*[24] Thereby, the measurement uncertainties of the phase signal and uncertainties in the controlled parameter are taken into account. The controlled parameters contributing the largest uncertainties in this measurement are the transducer and sample thickness. Thermal properties of backing, transducer, and gas materials are taken as absolute values. Jacobian matrices for the unknown and controlled parameters were calculated numerically by a local approach of perturbing the parameter of interest and evaluating the resulting change in phase. By assuming that the controlled parameters, as well as the experimental noise, are Gaussian distributed around their mean values and that both are independent variables, the variance-covariance matrix of the unknown parameters is given by:[24]

$$\begin{aligned}\mathrm{Var}\left[\hat{X}_U\right] =& (J_U^{\star\prime} J_U^{\star})^{-1} J_U^{\star\prime}(\mathrm{Var}[\Phi] + \\ & J_C^{\star}\mathrm{Var}\left[X_C\right] J_C^{\star\prime}) J_U^{\star}\left(J_U^{\star\prime} J_U^{\star}\right)^{-1}\end{aligned} \tag{5.15}$$

with the Jacobians for unknown ($J_U^{\star}$) and controlled parameters ($J_C^{\star}$)

$$J_U^{\star} = \begin{pmatrix} \frac{\partial\phi(f_1,X_U,X_C)}{\partial x_1}\,|_{X_U^{\star},X_C^{\star}} & \frac{\partial\phi(f_1,X_U,X_C)}{\partial x_2}\,|_{X_U^{\star},X_C^{\star}} \\ \vdots & \vdots \\ \frac{\partial\phi(f_M,X_U,X_C)}{\partial x_1}\,|_{X_U^{\star},X_C^{\star}} & \frac{\partial\phi(f_M,X_U,X_C)}{\partial x_2}\,|_{X_U^{\star},X_C^{\star}} \end{pmatrix} \tag{5.16a}$$

$$J_C^{\star} = \begin{pmatrix} \frac{\partial\phi(f_1,X_U,X_C)}{\partial x_3}\,|_{X_U^{\star},X_C^{\star}} & \frac{\partial\phi(f_1,X_U,X_C)}{\partial x_4}\,|_{X_U^{\star},X_C^{\star}} \\ \vdots & \vdots \\ \frac{\partial\phi(f_M,X_U,X_C)}{\partial x_3}\,|_{X_U^{\star},X_C^{\star}} & \frac{\partial\phi(f_M,X_U,X_C)}{\partial x_4}\,|_{X_U^{\star},X_C^{\star}} \end{pmatrix} \tag{5.16b}$$

where $X_U^\star$ is a column vector with the least-square estimates of the unknown parameters, $X_C^\star$ is a column vector with the determined controlled parameters, M is the number of measurement points, x_1 and x_2 are the unknown fit parameters $\varepsilon_s/\varepsilon_b$ and $1/\sqrt{D_s}$, x_3, and x_4 the controlled parameters l_t and l_s, respectively. Furthermore, $J_U^{\star\prime}$ represents the transponse of $J_U^\star$. The variance-covariance matrix of the measured phase and the controlled parameters can be written as

$$\mathrm{Var}\left[\Phi\right] = \begin{pmatrix} \sigma_{\phi_1}^2 & 0 & \cdots & 0 \\ 0 & \sigma_{\phi_2}^2 & \cdots & 0 \\ \vdots & \vdots & \ddots & 0 \\ 0 & 0 & 0 & \sigma_{\phi_M}^2 \end{pmatrix} \tag{5.17a}$$

$$\mathrm{Var}\left[X_C\right] = \begin{pmatrix} \sigma_{l_t}^2 & 0 \\ 0 & \sigma_{l_s}^2 \end{pmatrix} \tag{5.17b}$$

where $\sigma_{\phi_i}^2$ is the variance of the measured phase data point at the modulation frequency f_i and $\sigma_{l_t}^2$ and $\sigma_{l_s}^2$ are the variances of the controlled parameters.
The variances of the unknown parameters can then be retrieved from the diagonal elements of equation (5.15) using the experimentally determined variances in the phase data and the variances in the controlled parameters.

$$\mathrm{Var}\left[\hat{X}_U\right] = \begin{pmatrix} \sigma_{x_1}^2 & \mathrm{cov}\left[x_1, x_2\right] \\ \mathrm{cov}\left[x_1, x_2\right] & \sigma_{x_2}^2 \end{pmatrix} \tag{5.18}$$

Therefore, the standard deviation of the determined parameters is given by the square root of the diagonal elements, while the off-diagonal elements represent the covariance between the two parameters. The correlation coefficient is determined as $r = \frac{\mathrm{cov}[x_1,x_2]}{\sigma_{x_1} \cdot \sigma_{x_2}}$.

Error Estimation

Error estimation on the determined thermophysical properties was done by joining Monte Carlo error estimations with Jacobian based confidence intervals. As in the uncertainty analysis, the controlled parameters for the Monte Carlo error estimation are transducer and sample thickness. Based on the assumption of Gaussian distributed errors in the controlled parameters, the Monte Carlo error estimation was carried out. Therefore, 1000 iterations with randomly selected controlled parameters on three data sets, measured on the same sample but at different positions, were performed using the *nlinfit* algorithm in Matlab. For every iteration, the confidence intervals, based on the Jacobian and the mean square error resulting from the non-linear regression algorithm of the fit parameters were collected using *nlparci* in Matlab. Afterward, the errors due to uncertainty in the controlled

parameters and the errors due to fitting, resulting from the Jacobian matrices and the mean square error, were added following $\frac{\Delta x}{x} = \sqrt{(\frac{\Delta x}{x})^2_{\mathrm{MonteCarlo}} + (\frac{\Delta x}{x})^2_{\mathrm{Fit}}}$. Still, all errors were assumed to be Gaussian distributed, and the $\pm 1/e$ confidence intervals are used as error bars.
The resulting error in thermal conductivity was then calculated using:[30]

$$\sigma_k^2 = \left(\frac{\partial k}{\partial \varepsilon}\right)^2 \sigma_\varepsilon^2 + \left(\frac{\partial k}{\partial D}\right)^2 \sigma_D^2 + 2\frac{\partial k}{\partial \varepsilon}\frac{\partial k}{\partial D}\mathrm{cov}\left[\varepsilon, D\right]. \tag{5.19}$$

Substituting eq. (5.2) into eq. (5.19) yields

$$\sigma_k^2 = D\sigma_\varepsilon^2 + \frac{\varepsilon^2}{4D}\sigma_D^2 + \varepsilon \cdot \mathrm{cov}\left[\varepsilon, D\right] \tag{5.20}$$

where the average covariance regarding the performed Monte Carlo iterations and different measurements was used.

5.8 References

[1] A. Rosencwaig, A. Gersho, *Journal of Applied Physics* **1976**, *47*, 64–69.

[2] H. Du, H. Hu, *IOP Conference Series: Earth and Environmental Science* **2017**, *69*, 012176.

[3] A. C. Tam, *Reviews of Modern Physics* **1986**, *58*, 381–431.

[4] H. P. Hu, X. W. Wang, X. F. Xu, *Journal of Applied Physics* **1999**, *86*, 3953–3958.

[5] N. C. Fernelius, *Journal of Applied Physics* **1980**, *51*, 650–654.

[6] M. Morita, *Japanese Journal of Applied Physics* **1981**, *20*, 835–842.

[7] D. G. Cahill, W. K. Ford, K. E. Goodson, et al., *Journal of Applied Physics* **2003**, *93*, 793–818.

[8] P. Peumans, A. Yakimov, S. R. Forrest, *Journal of Applied Physics* **2003**, *93*, 3693–3723.

[9] M. Dresselhaus, G. Chen, M. Tang, et al., *Advanced Materials* **2007**, *19*, 1043–1053.

[10] A. J. Schmidt, R. Cheaito, M. Chiesa, *Review of Scientific Instruments* **2009**, *80*, 094901.

[11] D. G. Cahill, *Review of Scientific Instruments* **2004**, *75*, 5119–5122.

[12] A. A. Maznev, J. A. Johnson, K. A. Nelson, *Physical Review B* **2011**, *84*, 195206.

[13] D. G. Cahill, *Review of Scientific Instruments* **1990**, *61*, 802–808.

[14] J. A. Balderas-López, A. Mandelis, *Journal of Applied Physics* **2001**, *90*, 2273–2279.

[15] C. A. Bennett, R. R. Patty, *Applied Optics* **1982**, *21*, 49.

[16] X. Wang, H. Hu, X. Xu, *Journal of Heat Transfer* **2001**, *123*, 138–144.

[17] A. Salazar, *European Journal of Physics* **2006**, *27*, 1349–1355.

[18] D. P. Almond and P. M. Patel, *Photothermal Science and Techniques*, Chapman & Hall, **1996**.

[19] A. Salazar, *European Journal of Physics* **2003**, *24*, 351–358.

[20] W. S. M. Werner, K. Glantschnig, C. Ambrosch-Draxl, *Journal of Physical and Chemical Reference Data* **2009**, *38*, 1013–1092.

[21] N. W. Pech-May, Á. Cifuentes, A. Mendioroz, A. Oleaga, A. Salazar, *Measurement Science and Technology* **2015**, *26*, 085017.

[22] B. A. Cola, J. Xu, C. Cheng, et al., *Journal of Applied Physics* **2007**, *101*, 054313.

[23] X. Wang, B. Cola, T. Bougher, et al., *Annual Review of Heat Transfer* **2013**, *16*, 135–157.

[24] J. Yang, E. Ziade, A. J. Schmidt, *Review of Scientific Instruments* **2016**, *87*, 014901.

[25] V. Singh, T. L. Bougher, A. Weathers, et al., *Nature Nanotechnology* **2014**, *9*, 384–390.

[26] H. Petersen, *Technical Report: Danish Atomic Energy Commission Risoe. Research Establishment* **1970**.

[27] A. Philipp, N. W. Pech-May, B. A. F. Kopera, et al., *Analytical Chemistry* **2019**, *91*, 8476–8483.

[28] G. M. Lima, S. M. M. d. Lima e Silva, *Journal of the Brazilian Society of Mechanical Sciences and Engineering* **2011**, *33*, 393–399.

[29] R. S. Quimby, W. M. Yen, *Journal of Applied Physics* **1980**, *51*, 1252–1253.

[30] J. Taylor, *Introduction To Error Analysis: The Study of Uncertainties in Physical Measurements*, University Science Books, **1997**.

6

Microstructural and Thermal Transport Properties of Regioregular Poly(3-hexylthiophene-2,5-diyl) Thin Films

Kai Herrmann,[*] Simon Freund,[*] Fabian Eller,[§] Tamino Rößler,[†] Georg Papastavrou,[†,‡] Eva M. Herzig,[§] and Markus Retsch[*,‡]

[*] Department of Chemistry, Physical Chemistry 1, University of Bayreuth, Universitätsstraße 30, 95447 Bayreuth, Germany.

[§] Department of Physics, Dynamik und Strukturbildung - Herzig Group, University of Bayreuth, Universitätsstraße 30, 95447 Bayreuth, Germany.

[†] Department of Chemistry, Physical Chemistry 2, University of Bayreuth, Universitätsstraße 30, 95447 Bayreuth, Germany.

[‡] Bavarian Polymer Institute, Bayreuth Center for Colloids and Interfaces and Bavarian Center for Battery Technology (BayBatt), University of Bayreuth, Universitätsstraße 30, 95447 Bayreuth, Germany.

Published in *Materials*, **2022**, *15*, 7700.

6.1 Abstract

Polymeric thin films offer a wide range of exciting properties and applications, with several advantages compared to inorganic counterparts. The thermal conductivity of such thin films ranges typically between $0.1 - 1$ W m^{-1} K^{-1}. This low thermal conductivity can cause problems with heat dissipation in various applications. Detailed knowledge about thermal transport in polymeric thin films is desired to overcome these shortcomings, especially in light of the multitude of possible microstructures for semi-crystalline thin films. Therefore, poly(3-hexylthiophene-2,5-diyl) (P3HT) is chosen as a model system to analyze the microstructure and optoelectronic properties using x-ray scattering and absorption spectra along with the thermal transport properties using the photoacoustic technique. This combination of analysis methods allows for determining the optoelectronic and thermal transport properties on the same specimen, supplemented by structural information. The effect of different molecular weights and solvents during film preparation is systematically examined. A variation of the optoelectronic properties, mainly regarding molecular weight, is apparent, while no direct influence of the solvent during preparation is discernible. In contrast, the thermal conductivities of all films examined fall within a similar range. Therefore, the microstructural properties in the ordered regions do not significantly affect the resulting thermal properties in the sample space investigated in this work. We conclude that mainly the amorphous regions determine the thermal transport properties, as these represent a bottleneck for thermal transport.

6.2 Introduction

Polymeric thin films have become increasingly important in recent decades and are now used in various applications. Their usage includes separation membranes for fuel cells, electrodes in batteries, or active layers in organic photovoltaics.[1–3] Low cost, mechanical flexibility, solvent processability, and tailor-made functionalities make polymeric thin films attractive alternatives compared to their inorganic counterparts. Conjugated polymers are particularly interesting as they exhibit a backbone chain of alternating single- and double bonds, leading to the formation of a delocalized π-electron system when adequately doped.[4,5] Delocalized π-electron systems often result in interesting optical and electronic properties.[6] A well-established class of conjugated polymers are polythiophenes. In polythiophenes, charge conduction occurs via intrachain and interchain charge transport in the crystalline regions, while the amorphous part conducts via hopping or tunneling.[7–9] Within the material class of polythiophenes, the most studied system is poly(3-hexylthiophene-2,5-diyl) (P3HT) due to its electrical and optical properties.[7,10,11]

To extract information about the aggregation behavior of P3HT in thin films through

a relatively simple measurement, Spano developed a model to describe the absorption from H-aggregates comprising parallelly aligned, cofacially packed conjugated chains in the case of weak excitonic coupling.[12,13] Using this model, the UV-vis absorption A as a function of the photon energy E results via:[14]

$$A(E) \propto \sum_{m=0} \left(\frac{S^m}{m!}\right) \left(1 - \frac{We^{-S}}{2E_p} \sum_{n \neq m} \frac{S^n}{n!\, n-m}\right)^2 \cdot \exp\left(-\frac{(E - E_{0-0} - mE_p - 0.5WS^m e^{-S})^2}{2\sigma^2}\right) \tag{6.1}$$

through transitions between the vibrational levels m and n. Herein S is the Huang-Rhys factor, E_p the intermolecular vibrational energy, E_{0-0} the 0-0 transition energy, W the exciton bandwidth, and σ the Gaussian linewidth.[15]

A characteristic feature of both bulk polymers and polymeric thin films is their low thermal conductivity, mainly in the order of $0.1 - 1$ W m^{-1} K^{-1}.[16] Depending on the application, this low thermal conductivity can be disadvantageous if generated heat is not supposed to accumulate. It can also be advantageous if heat losses need to be prevented or a thermal gradient should be maintained. For P3HT, several investigations examined the influence of film thickness, blending, or preparation parameters on their thermal transport properties.[17–20] As pointed out by many studies, a holistic understanding of thermal transport in polymer thin films is still missing. Up to now, most investigations have focused on the influence of structural properties such as the degree of crystallinity or the thin film thickness. Particularly in the case of semiconducting polymers, the interplay between the optoelectronic and thermal transport properties has not been investigated. Nevertheless, it is difficult to establish a consistent understanding since many parameters simultaneously influence the thermal properties of polymeric thin films. Our approach, consequently, is to relate the thermal properties to the structural properties.

This work, therefore, explores possible structure-property relationships between the thermal conductivity and nanostructure as well as morphology-related properties of P3HT thin films. We systematically investigate the optoelectronic and structural properties of three regioregular P3HT polymers with distinct molecular weights and solvent processing conditions. After providing details on the employed materials and methods, the extracted morphologic information based on the absorption spectra and scattering analysis are presented. The set of samples analyzed using UV-vis absorption spectra is subsequently thermally analyzed using the photoacoustic technique, resulting in the direct determination of the thin film cross-plane thermal conductivity without requiring further measurements. We finally correlate our structural analysis to the thermal transport properties. Potential correlations are discussed, focusing on the fraction of aggregates and the exciton binding energy.

6.3 Materials and Methods

Regioregular P3HT with different molecular weights was purchased from Sigma-Aldrich (average M_w $20-45$ kg mol^{-1}, $50-75$ kg mol^{-1} and $85-100$ kg mol^{-1} with regioregularity $\geq$90%) and used as received. Chlorobenzene, CB (anhydrous $\geq$99.8%), 1,2-dichlorobenzene, 1,2-DCB (anhydrous 99%) and 1,2,4-trichlorobenzene, 1,2,4-TCB (anhydrous $\geq$99%) were also purchased from Sigma-Aldrich and used as received.

Thin films were prepared by dissolving the respective polymer in the respective solvent at 100 °C for 20 min and spin-coating the solutions on Quartz substrates (Präzisions Glas und Optik GmbH). The spin-coating parameters are given in Table 6.1. The films were annealed for about 16 hrs at 40 °C in a vacuum oven.

Table 6.1: Utilized spin-coating parameters (concentration c and rotation speed ω) for all combinations of molecular weights and solvents.

Solvent	$\overline{M}_w$=32.5 $\frac{\text{kg}}{\text{mol}}$	$\overline{M}_w$=62.5 $\frac{\text{kg}}{\text{mol}}$	$\overline{M}_w$=92.5 $\frac{\text{kg}}{\text{mol}}$
Chlorobenzene	$c = 50$ mg mL^{-1}	$c = 50$ mg mL^{-1}	$c = 30$ mg mL^{-1}
	$\omega = 750$ rpm	$\omega = 750$ rpm	$\omega = 500$ rpm
1,2-Dichlorobenzene	$c = 55$ mg mL^{-1}	$c = 55$ mg mL^{-1}	$c = 55$ mg mL^{-1}
	$\omega = 500$ rpm	$\omega = 500$ rpm	$\omega = 1000$ rpm
1,2,4-Trichlorobenzene	$c = 70$ mg mL^{-1}	$c = 70$ mg mL^{-1}	$c = 70$ mg mL^{-1}
	$\omega = 500$ rpm	$\omega = 500$ rpm	$\omega = 1000$ rpm

UV–vis absorption was measured with a UV–vis spectrometer (Cary 5000, Agilent Technologies) between 350 nm and 750 nm, corresponding to 1.65 eV to 3.54 eV, with an integration time of 0.1 ms in transmission geometry. To ensure a good resolution also at high absorption for thicker samples ($A_{\text{max}} \geq 3$), the reference beam was attenuated using an attenuation grid and the integration time increased to 0.5 ms.

The data analysis on the absorption spectra was performed according to Ref. [14]. For the fit to equation (6.1), a lower boundary of 1.95 eV and an upper boundary of 2.35 eV were applied using the Matlab function *nlinfit* employing the Levenberg–Marquardt algorithm.[15] The 95% confidence intervals are calculated using the Matlab function *nlparci* based on the residuals for the fitted model and the estimated variance-covariance matrix for the fitted coefficients.

Grazing incidence wide-angle x-ray scattering (GIWAXS) was performed on a laboratory system at the University of Bayreuth (Xeuss 3.0, Xenocs SAS, Grenoble, France) with a Cu Kα source ($\lambda = 1.54$ Å), a Dectris EIGER 2R 1M detector, and a sample-to-detector distance of 72 mm. Scattering experiments were carried out at room temperature under vacuum on samples on Quartz substrates with a length

of 4 mm. The incident angle was set to 0.20° well above the critical angle of 0.16°, which probes the full depth of the films. The presented q-profiles are cake cuts covering an azimuthal angle of $70 - 110°$ for the cuts in the vertical direction and $0 - 20°$ as well as $160 - 180°$ for the cuts in the horizontal direction.
The data analysis is based on fitting the horizontal and vertical cuts. All performed fits are Pseudo-Voigt fits, described by the following expression for a single peak:

$$f(q) = A \cdot [\eta \cdot L(q) + (1 - \eta) \cdot G(q)], \quad \text{with } 0 < \eta < 1 \tag{6.2}$$

$$G(q) = \exp\left[-\ln(2) \cdot \left(\frac{q-c}{b}\right)^2\right], \quad L(q) = \frac{1}{1 + \left(\frac{q-c}{b}\right)^2} \tag{6.3}$$

Where A is the peak amplitude, c is the peak position, $2b$ is the full width at half maximum of the Pseudo-Voigt peak, and η the Pseudo-Voigt mixing parameter. To fit the superposition of various peaks, we fitted the sum of five Pseudo-Voigt peaks for both directions. Moreover, background scattering was fitted with the functional form of $d_h \cdot q^{-4} + e_h$ in the horizontal and of $d_v \cdot q^{-5} + f \cdot q^{-2} + e_v$ in the vertical direction, where d_h, e_h, d_v, e_v and f are constants. For the fitting, we used *lmfit* in Python. Normalization of the peak amplitude is based on the absorption spectra of the respective samples. The areas of the aggregate and amorphous fit are added, while the aggregate area is divided by 1.39 due to its higher molar extinction coefficient.[21]
The samples for thermal transport characterization and a thermally thick reference material (quartz) were coated with a 100 nm gold layer by thermal evaporation to ensure high and near-surface absorption for the photoacoustic characterization. The layer thickness was monitored using a quartz crystal microbalance. Photoacoustic measurements were performed with a continuous wave Coherent Genesis MX488-1000 laser. The laser was modulated with a ConOptics 350-160 electro-optic modulator, operated by a sinusoidal signal of a Zurich Instruments lock-in amplifier HF2LI. The acoustic signal was measured using a Bruel & Kjaer 4398-A-011 microphone, which is subsequently demodulated in the lock-in amplifier.
The pressure in the photoacoustic cell was set to 1.379 bar of helium, corresponding to 20 psi. A comprehensive explanation of the experimental setup is given in Ref. [22] for more practical information.
The data analysis on the photoacoustic measurements is performed according to Ref. [22]. To determine the sample's thermal properties using the multilayer model from Hu et al., the thermal properties of the substrate (quartz) and transducer (gold) are required.[23] Therefore the thermal effusivity and diffusivity of gold are taken as $\varepsilon_{\mathrm{Au}} = 22271$ W s$^{1/2}$ m^{-2} K^{-1} and $D_{\mathrm{Au}} = 8.06 \cdot 10^{-5}$ m^2 s^{-1}.[24] The thermal effusivity and diffusivity of quartz are taken as $\varepsilon_{\mathrm{Quartz}} = 1499.8$ W s$^{1/2}$ m^{-2} K^{-1} and $D_{\mathrm{Quartz}} = 8.47 \cdot 10^{-7}$ m^2 s^{-1}.[24] Again, the least-squares fitting function *nlinfit* is used to determine the sample's thermal effusivity and diffusivity. The thermal

conductivity is subsequently calculated from these parameters. The approach for error estimation is described in Ref. [22]. In doing so, two independent measurements are analyzed using a Monte Carlo approach for the controlled parameters sample and transducer thickness. Therefore, 1000 iterations with randomly selected controlled parameters on two data sets, measured on the same sample but at different positions, were performed. Simultaneously, the uncertainty of every fit procedure is taken into account by the respective residuals and the estimated variance-covariance matrix.
The thicknesses of the polymeric films were determined using an Olympus OLS5000 laser confocal microscope and a 50X microscope objective. The error is calculated by measuring five areas of 260x260 μm at the top, left, center, right, and bottom of the circular area with a radius of 2 mm probed by the photoacoustic measurement and assuming a Gaussian distribution.

6.4 Results

To enable both the optical and the photoacoustic characterization, specific requirements for the sample thickness have to be met. For optical characterization, the samples should not be excessively thick to ensure a detectable transmission. In contrast, due to the limited frequency regime of the photoacoustic technique, the samples should have a certain thickness to allow the significant determination of the thermal conductivity.[22] Therefore, the film thickness should be about 500 nm to allow quantitative measurements of both optoelectronic and thermal properties. This is also an adequate thickness for GIWAXS characterization[25,26]. Quartz substrates are well suited for all these measurements because they exhibit high optical transparency in the wavelength regime of interest and thermal effusivity in a similar order of magnitude as polymers.
First, the parameters displayed in Table 6.1 were determined to produce films in the desired thickness range from the different solvents chlorobenzene, 1,2-dichlorobenzene, and 1,2,4-trichlorobenzene to achieve a variation in the microstructure.[21,27] An exemplary resulting film for the molecular weight of 32.5 kg mol^{-1} spin-coated from chlorobenzene is shown in Figure 6.1a. The polymeric films are partially removed from the substrate by scraping off with a glass pipette to produce a sharp edge. The color code here contains information about the z-axis, where the height of the substrate is normalized to zero. Based on this, the film thickness can be determined as shown with a cumulative frequency distribution in Figure 6.1b. In addition to the average film thickness, the surface roughness can also be determined from the

respective measurements as a further quality characteristic. For this, we use the root mean square roughness S_q as one of the most widely used defined by

$$S_q = \sqrt{\frac{1}{A}\iint_A Z^2(x,y)\partial x \partial y}, \tag{6.4}$$

where A represents the evaluated area and Z the respective height.[28] The parameter S_q, therefore, corresponds to the standard deviation of the height distribution. For all samples examined, S_q is in the range of 10 nm to 40 nm, allowing a proper data analysis. This surface roughness is corroborated by atomic force microscopy measurements on P3HT samples spin cast from chlorobenzene solutions. The height images reveal a granular surface topology with undulations of a few 10 nm (Figure 6.6). Neither in the height nor the phase image were we able to resolve microcrystalline regions regardless of the molecular weight.

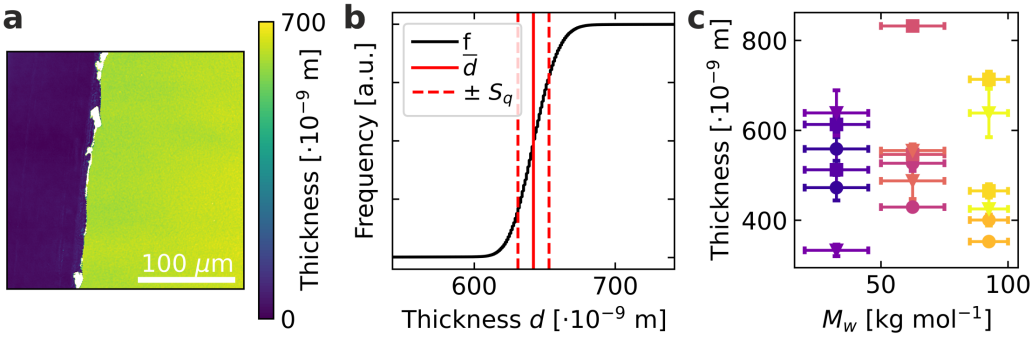

Figure 6.1: **a** Exemplary confocal microscopy image of $\overline{M}_w$=32.5 kg mol^{-1} spin-coated from chlorobenzene. The height is color-coded, which visualizes the quartz substrate as blue and the thin film as green. **b** Exemplary cumulative frequency distribution f as a function of thickness, as well as the average thickness $\overline{d}$ and the surface roughness S_q calculated from subfigure **a**. **c** Resulting film thicknesses, errors are derived from the inhomogeneities at different measurement points. Circular symbols represent films spin-coated from chlorobenzene, squares films from 1,2-dichlorobenzene, and triangles films from 1,2,4-trichlorobenzene.

For the cross-plane thermal conductivity determination, however, not only the local surface roughness is of interest, but especially inhomogeneities and fluctuations of the film thickness in the investigated measuring area, which corresponds to approximately 12.6 mm^2.[22] To represent these inhomogeneities realistically, the film thickness was determined at five locations in the area of the thermal measurement, and the mean value and standard deviation were determined under the assumption of a Gaussian distribution. The film thickness results obtained from this procedure are shown in Figure 6.1c. To map a sample to sample variation, two separate films were examined for every combination of molecular weight and solvent. All produced films are in the required range between 330 nm to 830 nm, ensuring a significant

analysis of optoelectronic and thermal properties.

Having verified the fundamental requirements for the thin films, we can now turn to optoelectronic characterization. The acquired absorption spectra are evaluated according to Equation (6.1), which is demonstrated for the example of a molecular weight of 32.5 kg mol^{-1} spin-coated from chlorobenzene in Figure 6.1a. For the data analysis, W, E_{0-0}, σ, and a global proportionality factor were varied as free parameters, while S was taken as 1.0 and E_p was taken as 0.179 eV, as reported in the literature.[21,29,30] Certain deviations between the model and measured values can be seen but are taken into account by the uncertainty estimation discussed in Section 6.3. The most common deviations are based on the model's assumptions, simplifying the actual situation. It, therefore, would be expected that the amorphous residual is unstructured. However, it can be seen that the amorphous contribution resulting from the analysis exhibits structuring.[15] This structuring above approximately 2.5 eV is most likely an artifact due to electronic transitions at higher energies.[12,14,15] Furthermore, slightly structured residuals in the energy range below 2.5 eV are recognizable, suggesting that the Gaussian disorder is too simple to describe the thin films' absorption spectrum fully.[14,15] Despite these deviations, the model used is nevertheless a practical possibility to estimate certain microstructural properties of the thin films.

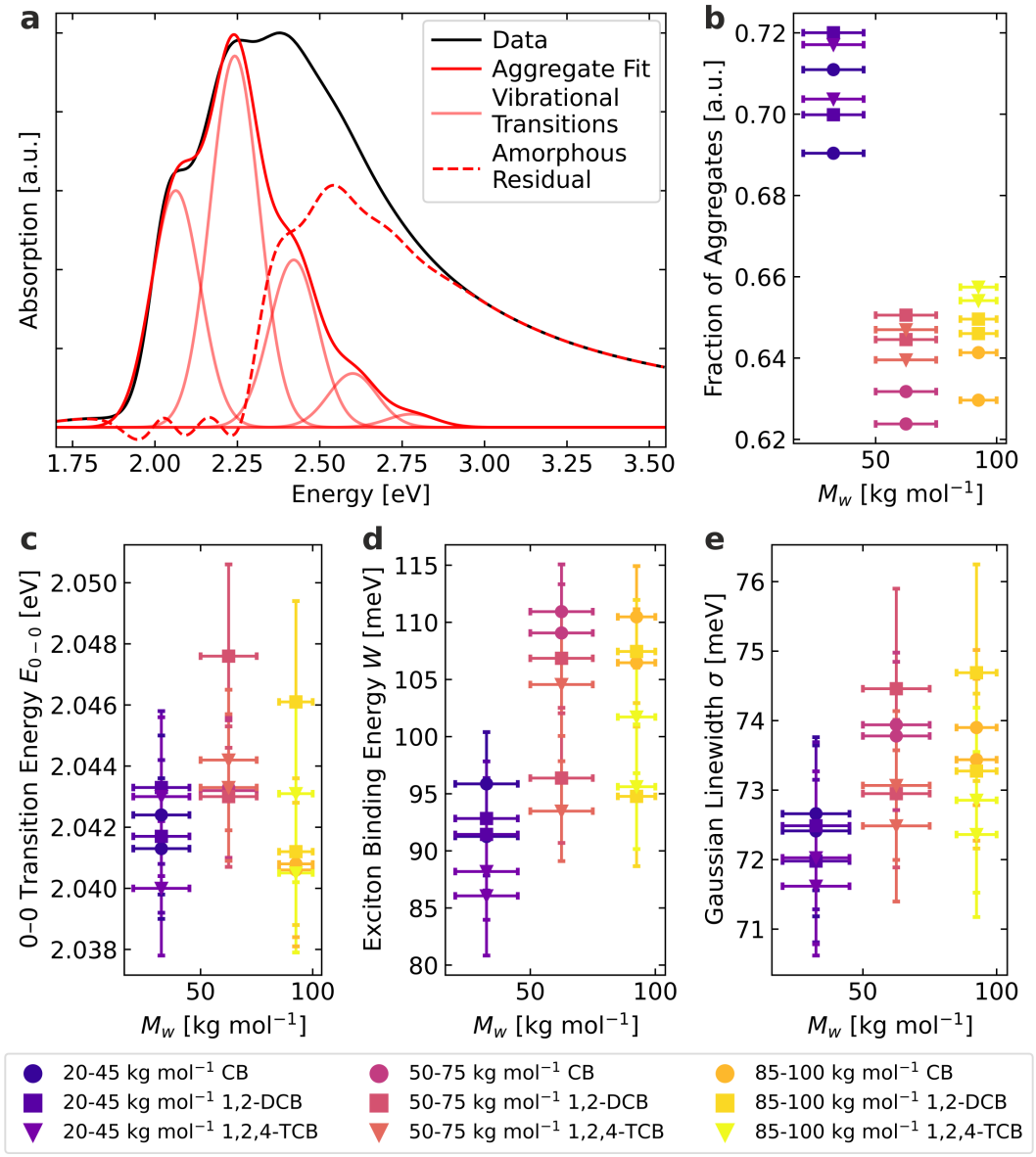

Figure 6.2: Performed UV-Vis absorption spectra data analysis: **a** Exemplary fit on the absorption spectrum of $\overline{M}_w$=32.5 kg mol^{-1} spin-coated from chlorobenzene. The individual vibrational transitions sum up to the aggregate fit. **b-e** Extracted proportion of aggregates, 0-0 transition energy, exciton binding energy and Gaussian linewidth.

The fraction of aggregates extracted from the absorption spectra is displayed in Figure 6.2b and calculated from the numerically integrated absorptions of the aggregate fit and the amorphous residual. Normalizing the aggregate integral with the factor of 1.39 is based on the different extinction coefficients of aggregated and non-aggregated P3HT.[31,32] The low molecular weight ($\overline{M}_w$=32.5 kg mol^{-1}) exhibits the highest fraction of aggregates, with the two higher molecular weights ($\overline{M}_w$=62.5 kg mol^{-1} and $\overline{M}_w$=92.5 kg mol^{-1}) being at a lower and similar level. Furthermore, it can be seen that the different films of the same molecular weight polymer display slightly different microstructures. However, we could not establish

a direct and unambiguous correlation between the solvent used for spin-coating and the fraction of aggregates.

There is an inverted dependency for the extracted fit parameters in Figure 6.2c-e. Generally, the low molecular weight exhibits the lowest 0-0 transition energy, exciton binding energy, and Gaussian linewidth, while the two higher molecular weights are at a higher and similar level. Again, no direct influence of the solvent is discernible. The 0-0 transition energy is related to the peak position of the first vibrational transition in Figure 6.2a. The similar transition energies for the two higher molecular weights suggest that the local electronic properties of the chains in the ordered domains are only weakly affected by the molecular weight in this range.[14] The lower 0-0 transition energy is possibly due to fewer local torsions of the conjugated backbones within the aggregates for the low molecular weight.[14] Still, the relative differences appear to be minor. The exciton binding energy is related to the relative intensities of the vibrational transitions. It can be interpreted as a measure of the average conjugation length of planarized chain segments in the ordered domains.[33] A lower exciton binding energy is related to a higher conjugation length above a certain minimum length, which is the case for all films examined here.[33] Therefore, the fraction of aggregates is higher for the low molecular weight, and the conjugation length inside the aggregate domains is increased. The Gaussian linewidth is a measure of the energetic disorder inside the ordered domains and is related to the width of the vibrational transitions in Figure 6.2a. Again, the energetic disorder is the lowest for the lower molecular weight, while for the two higher molecular weights, it is higher and on a similar level.

In summary, the lower molecular weight exhibits the highest fraction of aggregates, the highest average conjugation length, and the lowest energetic disorder. The two higher molecular weights are more disordered in all respects, with both being at a similar level. The apparent cause is probably the increased entanglements in the forming film and the number of refolded or bridging polymer chains between the aggregates.[14,34,35] In any case, the used spin-coating solvent plays a minor role in influencing the optoelectronic properties compared to the molecular weight for our preparation parameters.

While the UV-vis absorption measurements examine the electronic interaction of neighboring polymer chains, we can characterize the stacking of polymer chains using x-ray diffraction. To examine the influence of molecular weight and processing solvent on the nanostructure beyond individual chains we carry out GIWAXS measurements.

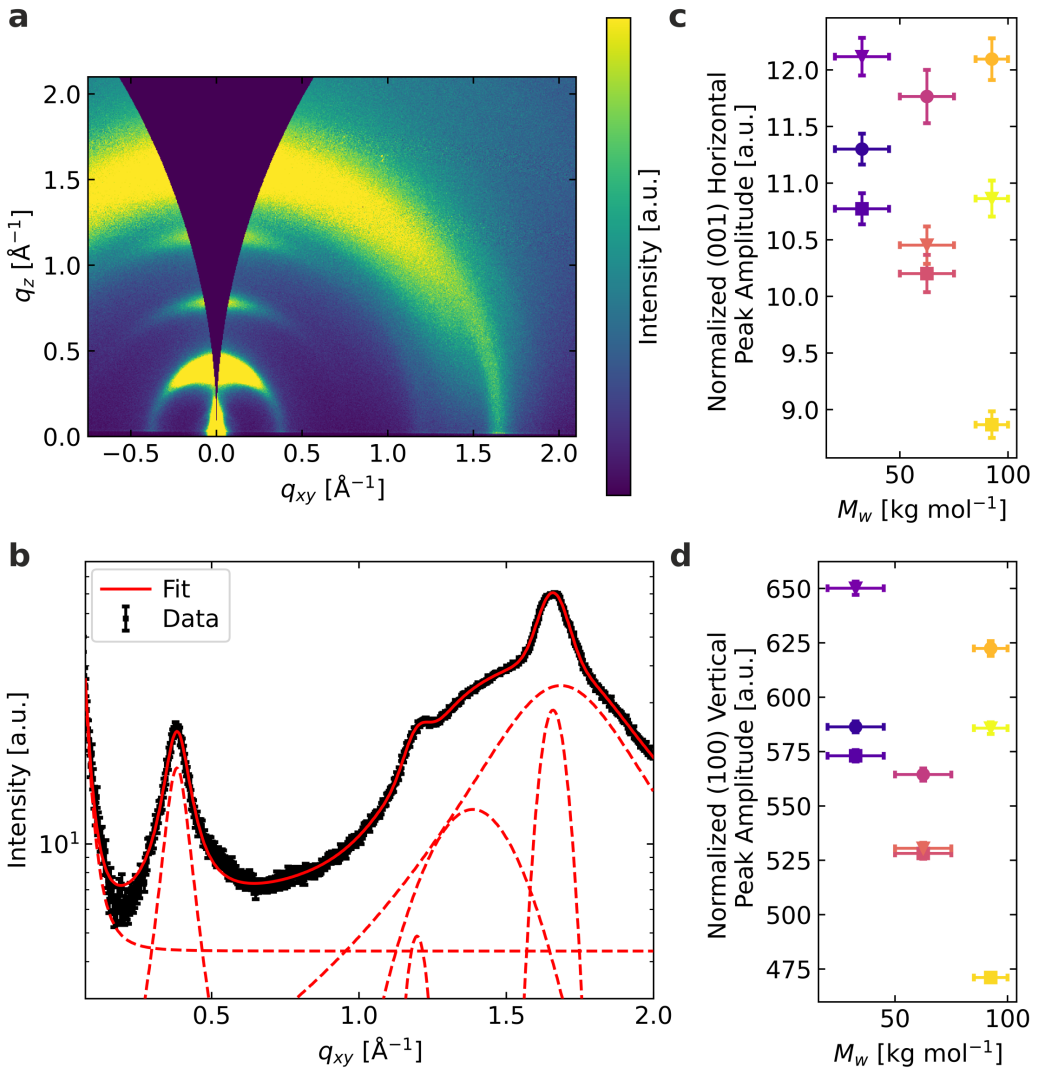

Figure 6.3: Performed GIWAXS analysis: **a** 2D GIWAXS data of $\overline{M}_w$=92.5 kg mol^{-1} spin-coated from 1,2,4-trichlorobenzene. **b** Horizontal cut of the 2D data showing the individual fitting contributions. **c** Normalized peak amplitude of the horizontal π-π stacking signal (001). **d** Normalized peak amplitude of the vertical lamellar stacking signal (100). The shown data sets are carried out on samples with a comparable thickness. The obtained peak amplitudes are normalized with the amount of examined material from individual absorption measurements.

In Figure 6.3a, example 2D GIWAXS data are displayed. P3HT is known to stack in two directions within a single crystallite, i.e., along the side chains (lamellar stacking) and by stacking the backbones via π-π stacking. As the short intermolecular distance of the π-π stacking enables electronic coupling, it more strongly regulates the optoelectronic and thermal properties than the lamellar stacking with its larger intermolecular distance across the non-conductive hexyl sidechains. Therefore, the lamellar stacking serves as an indicator for the aggregate quantity and quality, but the π-π stacking is expected to relate to transport properties.
We examine both stacking directions using GIWAXS. The spin coating procedure

yielded P3HT films with a variation in layer thicknesses as outlined in Figure 6.1c. Therefore, we used the weighted combination of amorphous (weight=1.39) and aggregated (weight=1.0) material obtained from the individual absorption spectra of each film as a measure for the amount of scattering polymer in the X-ray beam to normalize the peak amplitudes. We are then able to use the normalized peak amplitudes for a quantitative comparison of stacking features between different molecular weight samples. For all samples, in the vertical direction at about $q = 0.39$ Å^{-1} ((100) peak, $d = 16$ Å), 0.78 Å^{-1} ((200) peak) and 1.16 Å^{-1} ((300) peak) the first three orders of the lamellar stacking scattering are clearly visible. In the horizontal direction, only the (100) lamellar peak stands out significantly from the background. Moreover, at about $q = 1.66$ Å^{-1} ($d = 3.79$ Å) in the horizontal direction the well-defined π-π peak can be observed. This is a typical signature of edge-on-oriented P3HT. Between about 1.2 Å^{-1} and 1.7 Å^{-1} scattering of disordered P3HT can be seen but also scattering of the Quartz substrate (reference measurement see Figure 6.9) is contributing to the same q-range, especially in the vertical direction. To extract information on the lamellar and π-π stacking, we include the broad peaks of the disordered P3HT and Quartz underneath the π-π stacking peak into our fitting routine. The fit of the horizontal cut of the example data from Figure 6.3a in the horizontal direction is displayed in Figure 6.3b.

In Figure 6.3c and Figure 6.3d, the normalized peak amplitudes of the (001) peak in the horizontal direction (π-π stacking) and the (100) peak in the vertical direction (dominant lamellar peak) are shown. The normalized peak amplitudes resemble the amount of material involved in π-π stacking and lamellar stacking, respectively. In all samples, we observed material containing polymer π-π stacking and lamellar stacking. However, we could not determine a systematic trend concerning the relative amounts among the different samples. Neither the different molecular weights nor the various spin-coating solvents resulted in a systematic trend favoring one or the other stacking type quantitatively. The variability of the normalized peak amplitudes is highest for samples with the highest molecular weight, indicating that this polymer seems the most challenging to reproduce the nanostructures in a controllable way.

In contrast to the optical analysis presented in Figure 6.2, the GIWAXS data do not confirm a higher degree of order, in particular in the case of the low molecular weight species. This does not contradict the optoelectronic properties but is based on the differences in length scales probed. In Figure 6.10a and Figure 6.10b, the peak widths of the same peaks are displayed. For the π-π stacking as well as the lamellar stacking, the differences between the values for the various solvents and molecular weights are rather small, and no systematic behavior is observable. The peak width is a measure for the range of ordering, where a smaller peak width signals a longer-range order. Neither for the lamellar nor the π-π stacking, the peak width indicates the highest order for the low molecular weight as observed in the optoelectronic characterization, where shorter length scales are probed. Therefore, we

conclude that despite systematic differences in the backbone ordering and energetic disorder, this does not translate to a systematic impact on the longer range π-π and lamellar stacking, as measured by GIWAXS.

Having dealt with the microstructural properties, we now turn to the thermal properties. An exemplary measurement of the photoacoustic phase shift $\Delta\phi$ as a function of frequency, and the performed multilayer fit, are shown for the molecular weight of 32.5 kg mol^{-1} spin-coated from chlorobenzene in Figure 6.4a. The frequency position in combination with the sample thickness determines mainly the thermal diffusivity, while the phase shift values determine mainly the thermal effusivity in the one-dimensional limit of the thermal diffusion equation, which can be applied here.[22,36] The combination of both parameters then provides the thermal conductivity. The thermal conductivity for all samples investigated in this work is reported in Figure 6.4b.

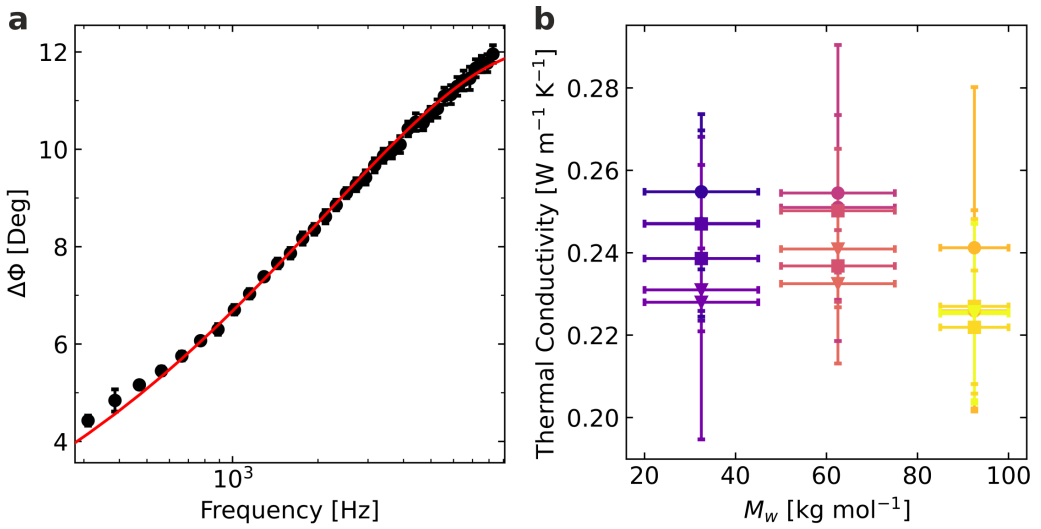

Figure 6.4: Performed photoacoustic data analysis: **a** Exemplary fit on the measured phase shift of $\overline{M}_w$=32.5 kg mol^{-1} spin-coated from chlorobenzene. **b** Extracted thermal conductivities for the different molecular weights and solvents. Circular symbols represent films spin-coated from chlorobenzene, squares films from 1,2-dichlorobenzene, and triangles films from 1,2,4-trichlorobenzene.

The primary sources of errors are the inhomogeneities and fluctuations in the film thickness. Since layer thickness is one of the most critical parameters of the multilayer model, these uncertainties directly affect the resulting thermal conductivity. The thermal conductivity for all samples is between 0.22 W m^{-1} K^{-1} and 0.26 W m^{-1} K^{-1} which are generally in line with or slightly above literature values.[18,20] Furthermore, no thickness dependence effects are apparent for the investigated thickness regime, as shown in the Supporting Information (Figure 6.7). No direct influence of the solvent on the resulting properties is discernible for the thermal properties, similar to the microstructural properties. However, the impact of the molecular weight

seems to be different here. The two lower molecular weights appear to be on a similar level at approximately 0.24 W m^{-1} K^{-1} on average, while the high molecular weight exhibits an average thermal conductivity of roughly 0.23 W m^{-1} K^{-1}. This molecular weight dependency contrasts the microstructure parameters, where the two higher molecular weights are at a similar level while the lowest molecular weight deviates from them. Nevertheless, the relative deviations in thermal conductivity between the different molecular weights are comparatively small.
Since all structural, optoelectronic, and thermal transport properties have been determined on the same specimen, we can now correlate these properties to identify possible relationships.

6.5 Discussion

Correlations between the microstructural properties, determined by absorption spectra analysis, and thermal properties determined on the same samples are investigated below. The microstructural properties are plotted against the thermal conductivity to identify possible correlations or independencies. Figure 6.5 shows this for the fraction of aggregates and the exciton binding energy.

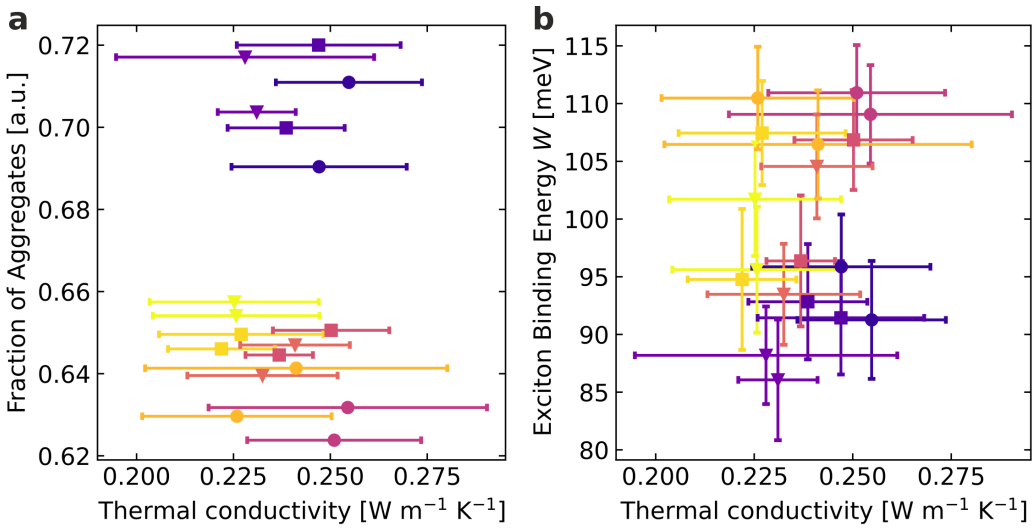

Figure 6.5: Correlations between extracted microstructural properties and thermal conductivity: **a** Relation between the proportion of aggregates and the thermal conductivity. **b** Relation between the exciton binding energy and the thermal conductivity.

Within the accuracy of the measurement, we do not find a correlation between the fraction of aggregates and the thermal conductivity in the investigated range of molecular weights and generated microstructures. Although a significant variation in the fraction of aggregates can be seen depending on the molecular weight, it does not

affect the thermal conductivity. The thermal conductivity proves robust concerning the present fraction of aggregates and is, therefore, not affected in the evaluated domain. This is supported by the structural investigations on the longer length scales obtained from the GIWAXS measurements. While the fraction of aggregates obtained from spectroscopy correlates with the trend of peak amplitudes with molecular weight and solvent, the peak widths of the scattering data, which correlate with the length scale of ordered domains, do not show any systematic changes. For the exciton binding energy, a more complex situation emerges. For the high molecular weight, a similar situation as for the fraction of aggregates is present, where similar thermal conductivities for different exciton binding energies can be identified. In contrast, for the low and especially medium molecular weight, one could infer a connection between the exciton binding energy and the thermal conductivity. Slightly higher thermal conductivities accompany higher exciton binding energies. Considering the scatter and accuracy of our data, such a potential trend needs to be interpreted cautiously. Taking into account the 0-0 transition energy and the Gaussian linewidth, this trend is not confirmed (Supporting Information, Figure 6.8). Overall we have to conclude that a correlation between the structure, the optoelectronic properties, and the thermal conductivity cannot be resolved in the P3HT thin films investigated here.

We interpret the main obstruction to a consistent identification of correlations between the microstructural properties and the thermal conductivity by the lack of sufficiently high difference in the thermal conductivity of the crystalline and amorphous regions, respectively. The fundamental factor underlying these results is the semi-crystalline structure of the investigated thin films. The amorphous regions mainly affect macroscopic thermal transport in semi-crystalline polymeric thin films with molecular weights above the critical entanglement molecular weight.[37–39] The critical entanglement molecular weight for P3HT is assumed to be approximately 35 kg mol^{-1}.[37,40,41] Especially for the high concentrations used in this work during spin-coating to enable a sufficient film thickness for the thermal characterization, chain entanglements are likely to have a very significant influence. The molecular weights used in this work are either on the order or above the critical entanglement molecular weight, which presumably leads to the amorphous domains forming the bottleneck for macroscopic thermal transport. Even though preferential chain orientation can significantly enhance the thermal conductivity of the amorphous phase, mostly through increased short-range ordering while long-range order remains absent, this is only achieved with special preparation procedures.[42] The amorphous phase for the relatively high film thickness and preparation by spin coating examined in this work is, therefore, not considered to be oriented.

In contrast, the extracted microstructural properties are assigned to the ordered regions, as only these are included in the optoelectronic model and detectable in x-ray diffraction.[12] This reinforces our findings that a change in the microstructural properties in the ordered regions does not affect the resulting macroscopic thermal

transport properties in the examined range of molecular weights. The bottleneck for macroscopic thermal transport remains the amorphous regions, which separate the ordered parts.

6.6 Conclusions

This work investigated possible relationships between nanostructure, optoelectronic, and thermal transport properties for regioregular P3HT thin films. Three different molecular weights ($\overline{M}_w$=32.5 kg mol^{-1}, 62.5 kg mol^{-1} and 92.5 kg mol^{-1}) and three different solvents (chlorobenzene, 1,2-dichlorobenzene and 1,2,4-tricholorobenzene) were chosen for this purpose. Absorption spectra were analyzed using the model from Spano, which showed that the two higher molecular weights exhibit similar optoelectronic properties.[12] In contrast, the lower molecular weight shows slight differences with a higher fraction of aggregates and a lower 0-0 transition energy, a lower exciton binding energy, and a lower Gaussian linewidth, corresponding to the highest degree of order in the crystalline domains. The spin-coating solvent used played a minor role in influencing the optoelectronic properties compared to the molecular weight of the P3HT. GIWAXS measurements also support this behavior. The spatial extension of the ordered domains shows no systematic changes with molecular weight or processing solvent. The thermal conductivity was determined on the same set of samples, revealing very similar values in the range of 0.22 – 0.26 W m^{-1} K^{-1}. The fraction of aggregates proved to be unrelated to the thermal conductivity in the investigated sample space. In general, we find the microstructural properties not to be related to the thermal conductivity. This can be explained by the fact that non-oriented amorphous regions separate the ordered regions. These apparently dictate the macroscopic heat transport. The optoelectronic properties, however, are mainly governed by the ordered parts. Consequently, we cannot resolve an unambiguous relation between the optoelectronic and the thermal transport properties. Therefore, we would like to further encourage the field to explore possible relationships between microstructure and thermal properties, at best with a stronger focus on the amorphous region. This will be of immediate relevance for a range of polymer-based materials, where the thermal performance strongly depends on the structural arrangement across several length scales. Important related materials are polymer-based photovoltaics, organic light-emitting diodes, hybrid thermoelectric systems, or thermal interface materials. Similar to the structure of P3HT investigated in this study, these materials comprise ordered and disordered regions with significant contributions of the involved interfaces. Efficient heat transfer between the various compartments of these materials will only be possible with stringent control of the polymer morphology in each of these nanostructured spaces and requires a better fundamental understanding of this intricate interplay.

Acknowledgments

The authors thank Tobias B. Lauster for assistance and advice on the UV-vis measurements. F.E. and E.M.H. thank for funding from SolarEraNet (No. NFA4R2ROPV) and the DFG (INST 91/443-1). F.E. thanks the Elite Study Program Macromolecular Science within the Elite Network of Bavaria (ENB) for support.

6.7 Supporting Information

6.7.1 Height and Phase Atomic Force Microscopy Images

Height and phase images of spin cast P3HT films from chlorobenzene are shown in Figure 6.6. The granular surface exhibits height undulations of a few 10 nm. P3HT lamellar stacks could not be resolved.

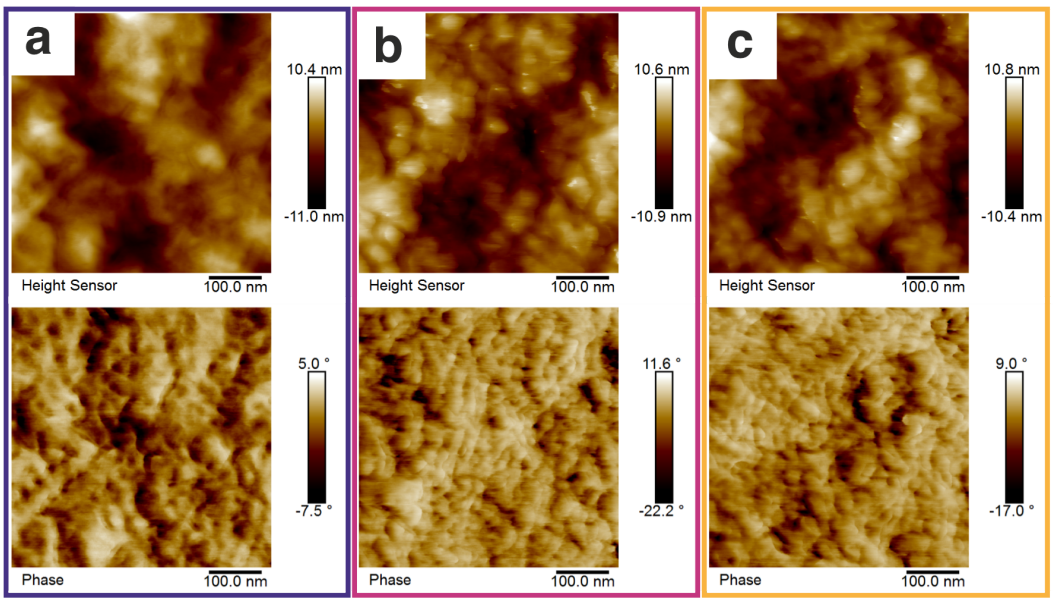

Figure 6.6: AFM measurement of the surface topography of spin cast films. **a** $\overline{M}_w$ = 32.5 kg mol^{-1}, **b** $\overline{M}_w$ = 62.5 kg mol^{-1}, **c** $\overline{M}_w$ = 92.5 kg mol^{-1}. All AFM images were acquired at a Bruker Dimension Icon equipped with a Nanoscope V Controller. Tapping mode was applied under ambient conditions (f_{nom} = 300 kHz, k_{nom} = 26 N m^{-1}). Topography and phase data is depicted.

6.7.2 Thickness Dependence of Thermal Conductivity

The thickness dependence of the thermal conductivity for all samples examined in this work is shown in Figure 6.7. No influence of the film thickness can be seen here, which verifies that the thermal conductivity in the investigated thickness range is independent of the film thickness. Typically, the influence of the film thickness on the thermal conductivity of polymers is only present below 100 nm.

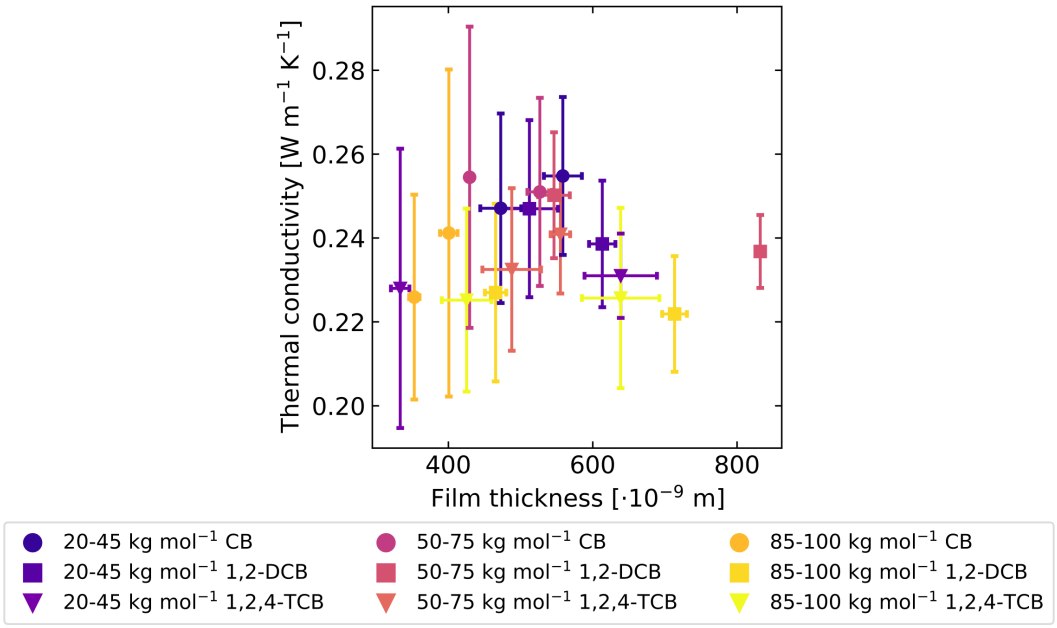

Figure 6.7: Thermal conductivity as a function of film thickness for all samples examined in this work.

6.7.3 Additional Correlations of Microstructure and Thermal Conductivity

Further correlations between microstructure parameters and thermal conductivity not shown in the main manuscript are shown in Figure 6.8. In this respect, there do not appear to be any direct correlations between the 0-0 transition energy or the Gaussian linewidth and the thermal conductivity in the range of measurement inaccuracies.

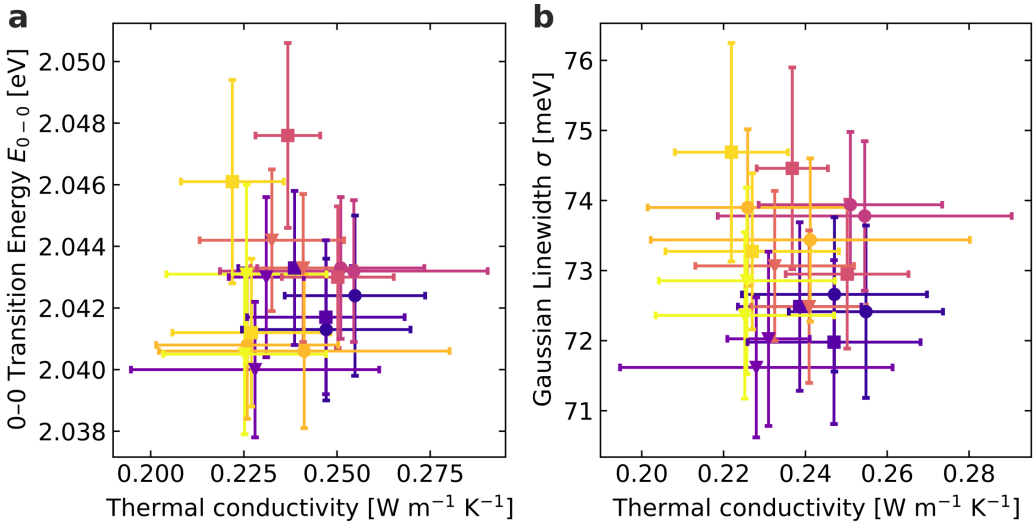

Figure 6.8: Correlations between extracted microstructural properties and thermal conductivity: **a** Relation between the 0-0 transition energy and the thermal conductivity. **b** Relation between the Gaussian linewidth and the thermal conductivity.

6.7.4 GIWAXS of Quartz Reference

The background scattering of the GIWAXS measurements originating from substrate scattering is a broad feature as shown in the GIWAXS measurement of a Quartz substrate in Figure 6.9. This feature is found underneath the π-π stacking signal.

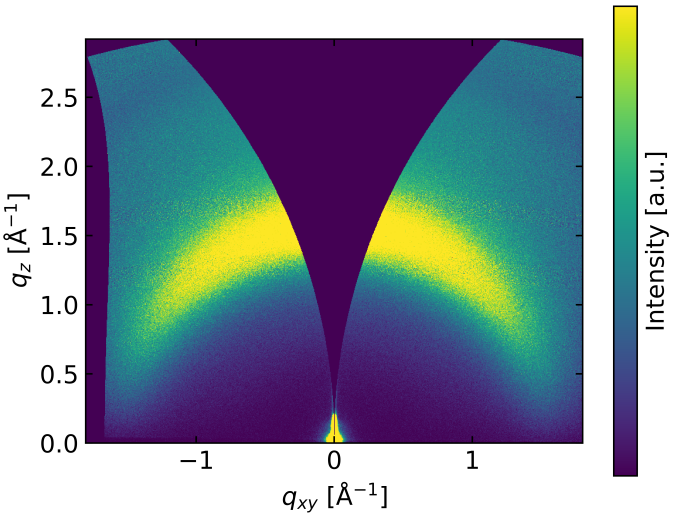

Figure 6.9: 2D GIWAXS data of the Quartz substrate.

6.7.5 Additional Extracted GIWAXS Parameters

Figure 6.10 shows the peak widths of the π-π and the dominant lamellar peak from the GIWAXS measurements, two further fit parameters of the data presented in the main manuscript. The color code is analogous to that of the main manuscript.

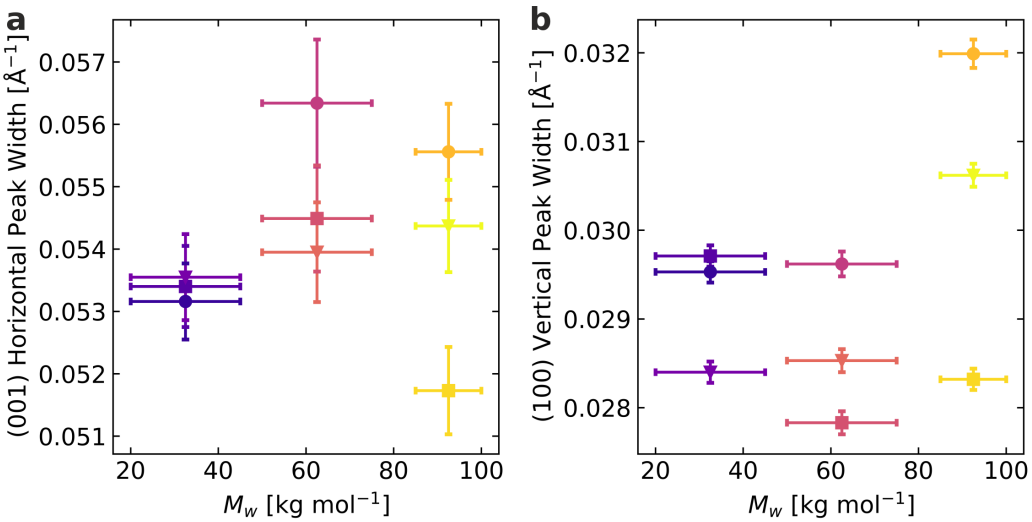

Figure 6.10: Fit parameters from GIWAXS data: **a** Peak width of the horizontal π-π stacking signal (001). **b** Peak width of the vertical lamellar stacking signal (100).

6.8 References

[1] H. Zhang, P. K. Shen, *Chemical Reviews* **2012**, *112*, 2780–2832.

[2] W. Du, X. Du, M. Ma, et al., *Advanced Functional Materials* **2022**, 2110871.

[3] G. Li, R. Zhu, Y. Yang, *Nature Photonics* **2012**, *6*, 153–161.

[4] T. L. Stott, M. O. Wolf, *Coordination Chemistry Reviews* **2003**, *246*, 89–101.

[5] D. Derewjanko, D. Scheunemann, E. Järsvall, et al., *Advanced Functional Materials* **2022**, 2112262.

[6] X. Guo, C. Cui, M. Zhang, et al., *Energy & Environmental Science* **2012**, *5*, 7943.

[7] S. Agbolaghi, S. Zenoozi, *Organic Electronics* **2017**, *51*, 362–403.

[8] M. Brinkmann, *Journal of Polymer Science Part B: Polymer Physics* **2011**, *49*, 1218–1233.

[9] A. Salleo, *Materials Today* **2007**, *10*, 38–45.

[10] S. Joshi, S. Grigorian, U. Pietsch, et al., *Macromolecules* **2008**, *41*, 6800–6808.

[11] Z. Wu, A. Petzold, T. Henze, et al., *Macromolecules* **2010**, *43*, 4646–4653.

[12] F. C. Spano, *The Journal of Chemical Physics* **2005**, *122*, 234701.

[13] F. C. Spano, *Chemical Physics* **2006**, *325*, 22–35.

[14] P. Pingel, A. Zen, R. D. Abellón, et al., *Advanced Functional Materials* **2010**, *20*, 2286–2295.

[15] S. T. Turner, P. Pingel, R. Steyrleuthner, et al., *Advanced Functional Materials* **2011**, *21*, 4640–4652.

[16] A. Henry, *Annual Review of Heat Transfer* **2014**, *17*, 485–520.

[17] S. Rausch, D. Rauh, C. Deibel, S. Vidi, H. P. Ebert, *International Journal of Thermophysics* **2012**, *34*, 820–830.

[18] J. C. Duda, P. E. Hopkins, Y. Shen, M. C. Gupta, *Applied Physics Letters* **2013**, *102*, 251912.

[19] M. K. Smith, V. Singh, K. Kalaitzidou, B. A. Cola, *ACS Nano* **2015**, *9*, 1080–1088.

[20] Y. Xu, X. Wang, J. Zhou, et al., *Science Advances* **2018**, *4*, eaar3031.

[21] J. Clark, J.-F. Chang, F. C. Spano, R. H. Friend, C. Silva, *Applied Physics Letters* **2009**, *94*, 163306.

[22] K. Herrmann, N. Pech-May, M. Retsch, *Photoacoustics* **2021**, *22*, 100246.

[23] H. P. Hu, X. W. Wang, X. F. Xu, *Journal of Applied Physics* **1999**, *86*, 3953–3958.

[24] J. Yang, E. Ziade, A. J. Schmidt, *Review of Scientific Instruments* **2016**, *87*, 014901.

[25] Y. Zhong, D. Seeberger, E. M. Herzig, et al., *ACS Appl. Mater. Interfaces* **2021**, *13*, 45365–45374.

[26] K. Yamamoto in *X-ray Scattering*, InTech Open, **2017**, pp. 45365–45374.

[27] F. Niefind, S. Karande, F. Frost, B. Abel, A. Kahnt, *Nanoscale Advances* **2019**, *1*, 3883–3886.

[28] E. DeGarmo, *Materials and Processes in Manufacturing*, John Wiley & Sons, **2003**.

[29] J.-F. Chang, J. Clark, N. Zhao, et al., *Physical Review B* **2006**, *74*, 115318.

[30] J. Clark, C. Silva, R. H. Friend, F. C. Spano, *Physical Review Letters* **2007**, *98*, 206406.

[31] C. Scharsich, R. H. Lohwasser, M. Sommer, et al., *Journal of Polymer Science Part B: Polymer Physics* **2011**, *50*, 442–453.

[32] D. Kajiya, S. Ozawa, T. Koganezawa, K.-I. Saitow, *The Journal of Physical Chemistry C* **2015**, *119*, 7987–7995.

[33] J. Gierschner, Y.-S. Huang, B. V. Averbeke, et al., *The Journal of Chemical Physics* **2009**, *130*, 044105.

[34] A. Zen, M. Saphiannikova, D. Neher, et al., *Macromolecules* **2006**, *39*, 2162–2171.

[35] M. Brinkmann, P. Rannou, *Macromolecules* **2009**, *42*, 1125–1130.

[36] H. Du, H. Hu, *IOP Conference Series: Earth and Environmental Science* **2017**, *69*, 012176.

[37] F. P. V. Koch, J. Rivnay, S. Foster, et al., *Progress in Polymer Science* **2013**, *38*, 1978–1989.

[38] S. Lu, Q. Zhou, Y. Ouyang, et al., *Nature Communications* **2018**, *9*, 1–8.

[39] E. Selezneva, R. D. Pietro, X. Jiao, C. R. McNeill, H. Sirringhaus, *APL Materials* **2019**, *7*, 081118.

[40] H. Hu, K. Zhao, N. Fernandes, et al., *Journal of Materials Chemistry C* **2015**, *3*, 7394–7404.

[41] N. R. Tummala, C. Risko, C. Bruner, R. H. Dauskardt, J.-L. Brédas, *Journal of Polymer Science Part B: Polymer Physics* **2015**, *53*, 934–942.

[42] V. Singh, T. L. Bougher, A. Weathers, et al., *Nature Nanotechnology* **2014**, *9*, 384–390.

7

Thermal Transport in Ampholytic Polymers: The Role of Hydrogen Bonding and Water Uptake

Patrick Hummel,* Anna M. Lechner,* Kai Herrmann,* Philip Biehl,§ Carsten Rössel,§ Lisa Wiedenhöft,§ Felix H. Schacher,§ and Markus Retsch*

* Department of Chemistry, Physical Chemistry 1 and Bavarian Polymer Institute, Universitätsstraße 30, 95447 Bayreuth, Germany.

§ Institute of Organic Chemistry and Macromolecular Chemistry and Jena Center for Soft Matter (JCSM), Friedrich Schiller University Jena, 07743 Jena, Germany.

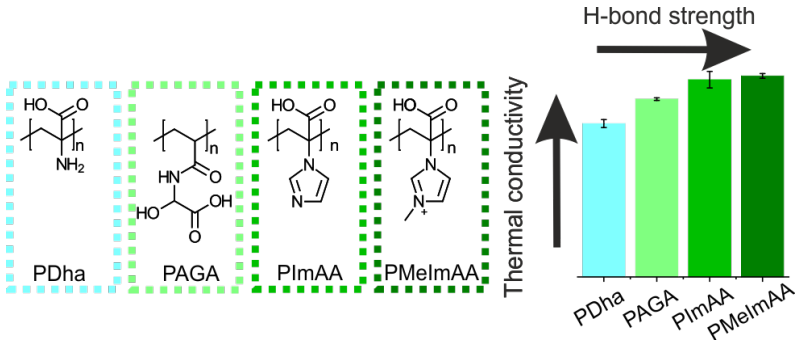

Published in *Macromolecules*, **2020**, *53*, 5528.

7.1 Abstract

The low thermal conductivity of amorphous polymers typically prevents their usage in thermal management applications. Therefore, increasing their intrinsic thermal conductivity poses an exciting scientific challenge. One approach is to promote attractive interchain interactions. Here, we investigate the thermal conductivity of several ampholytic polymers. This unique class of polymers offers H bond donor and acceptor groups in each repeat unit and constitutes a one-component system. We use IR spectroscopy to characterize the bonding strength and motifs based on the carbonyl peak. For the dry ampholytic polymers, we find a correlation between H bond strength and thermal conductivity. We also characterized the influence of hydration under various relative humidity conditions, which mostly led to an increase in thermal conductivity. This increase can be rationalized by the formation of a water-polymer nanocomposite material and can be described by volume-weighted mixing models.

7.2 Introduction

Easy processability, lightweight, low cost, and electrical insulation make polymers promising candidates for various applications in electronic devices. The continuously increasing energy density in such electronic devices demands a wholistic concept for thermal management at the same time.[1] The usually low thermal conductivity of polymers represents a significant obstacle in this context.

For that reason, the ambitious goal of polymer chemists is to create thermally highly conducting polymers. Similar to the discovery of (semi)conducting polymers, this would open up an entirely new space for the application of amorphous polymers. Two general strategies have been pursued to reach this goal: the creation of polymer (nano)composites and polymer processing. In the case of processing, a variety of methods such as mechanical stretching,[2,3] electrospinning,[4] and nanotemplating[5] have been investigated. In these cases, an increase in thermal conductivity is mostly attributed to a high chain orientation.[6,7] The polymer chain orientation is often accompanied by some degree of crystallization. The chain alignment can be further enhanced by the proper design of the polymer backbone to promote stiffer polymer chains.[8] Consequently, impressively high thermal conductivities, of around 20 W m^{-1} K^{-1}, were measured along the axis of crystalline polymer fibers with a high modulus.[2] However, the radial thermal conductivity stays low.[9] Even a commercial product is already available, making use of stretched polymers with a high degree of crystallinity. The organic heat spreader Temprion OHS (DuPont) with a crystallinity of 99.9% demonstrates a remarkable in-plane thermal conductivity of 45 W m^{-1} K^{-1} and a typical polymer-like cross-plane thermal conductivity of

0.2 W m^{-1} K^{-1}. Amorphous polymers, in general, have a lower thermal conductivity than crystalline ones. However, their heat-spreading capabilities would be less affected by the orientation in space owing to the random polymer coiling. Furthermore, the processing of amorphous polymers is less sophisticated because of the lack of a nucleation and growth phase compared to (semi)crystalline samples. Ways to beat the intrinsically low thermal conductivity of amorphous polymers are mixing with highly conducting components or the introduction of functional groups.

In that regard, the field of (nano)composite materials has been actively investigated over the past years. The effective material properties strongly depend on a multitude of parameters such as the filler shape and composition, the interfacial interaction between the filler and matrix, and the filler concentration.[10,11] Depending on the filler shape, anisotropic thermal transport properties may evolve at the same time.[12,13]

The introduction of functional groups to the polymer backbone or its side groups is an alternative approach to increase the thermal conductivity. The main driving force for an increased thermal conductivity is stretching of the polymer to a more elongated conformation and an improved interchain transfer of heat. Amorphous polymers with hydrogen bond-forming functional groups are consequently well-suited to realize improved thermal conductivities.[14] The strong hydrogen bonding between adjacent polymer chains could improve the transfer of thermal energy. In addition to this, the thermal conductivity can be further increased by the use of polyelectrolytes.[14,15] Polyelectrolytes react sensitively to external stimuli such as ionic strength or pH, which influence the polymer conformation and polymer packing.

The engineering of these interchain interactions can lead to high thermal conductivities of up to 1.5 W m^{-1} K^{-1}, as shown in amorphous polymer blends.[16] However, demixing is a significant issue in polymer blends, and controversial findings on the role of H bonds were published.[14] Miscibility is always an enormous challenge in polymer blends, and the resulting microstructure can be hard to characterize.

In this work, we present a new approach to prevent the issue of miscibility. Ampholytic polymers exhibit donor and acceptor groups for the formation of H bonds covalently attached to one polymer chain, which inevitably prevents demixing. We present four different ampholytic polymers (Figure 7.1) with a detailed characterization of their microstructure (measured by IR spectroscopy) and their thermal transport properties (measured by the photoacoustic method).

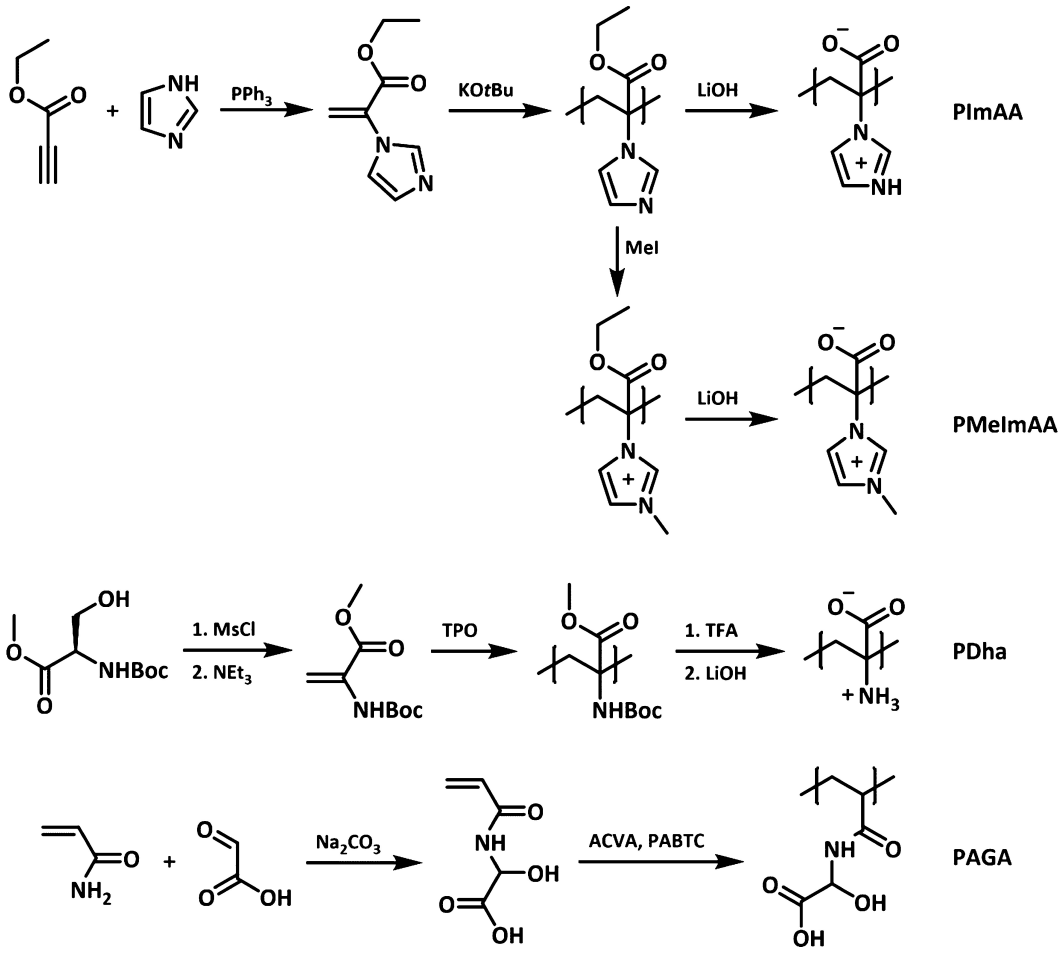

Figure 7.1: Synthesis of PImAA, PMeImAA, PDha, and PAGA.

7.3 Materials and Methods

7.3.1 Polymer Synthesis

Synthesis of poly(2-(imidazole-1-yl)acrylic acid) (PImAA), (Figure 7.1): The synthesis of ethyl 2-(imidazole-1-yl)acrylate (EImA) and anionic polymerization in tetrahydrofuran (THF) with potassium tert-butoxide (KOtBu) as an initiator, as well as the polymer modifications, were performed as described in the literature.[17] The polymers were characterized by proton nuclear magnetic resonance (1H NMR) (300 MHz, D2O) and size exclusion chromatography (SEC, 0.1 M NaCl/0.3% TFA in water, P2VP calibration).

Synthesis of polydehydroalanine (PDha), (Figure 7.1): PDha was synthesized as reported by Günther et al. or von der Lühe et al.[18,19] Briefly, a solution of 2.9 mg (0.0084 mmol) of Lucirin TPO in 300 μL of 1,4-dioxane was added to 300 mg (1.49 mmol) of tert-butoxycarbonylaminomethyl acrylate (tBAMA; M/I = 200:1). The mixture was placed in an ultraviolet (UV) cube (100 W) for 5 min. Afterward, the polymer was precipitated in 4 mL of n-hexane and subsequently deprotected. Therefore, 500 mg of the obtained PtBAMA was dissolved in 7.5 mL of trifluoric acetic acid and stirred at 50 °C for 1 h. The mixture was precipitated in methanol. The so-obtained PAMA was dissolved in 10 mL of 1,4-dioxane, and a saturated solution of LiOH (10 mL) was added. The mixture was stirred at 100 °C for 3 h and neutralized with diluted HCl aq. During neutralization, PDha precipitated. PDha was characterized by 1H NMR (300 MHz, D2O/NaOD, pH 8).

Synthesis of poly(2-acrylamido glycolic acid) (PAGA), (Figure 7.1): 2-acryloylamido glycolic acid was synthesized as described in the literature. Reversible addition–fragmentation chain transfer (RAFT) polymerization was performed according to a previously published protocol[20] with [M]/[CTA]/[I] = 145:1:0.3. PAGA was characterized by 1H NMR (D2O, 300 MHz) and SEC (0.1 M NaNO3/0.05% NaN3, PEO calibration).

Synthesis of poly(methyl methacrylate) (PMMA): The RAFT synthesis of PMMA was adapted from Mayadunne et al.[21] Therefore, 38.25 g (0.382 mol) of MMA, 750.6 mg (2.17 mmol) of 2-cyano-2-propyl dodecyl trithiocarbonate (CPDTTC), 3.7 mg (0.0225 mmol) of azobisisobutyronitrile (AIBN), and 11.9 g (0.129 mol) of toluene were placed in a flask. The mixture was heated to 80 °C for 33.5 h. The polymer was precipitated in methanol.

Poly(acrylic acid) (PAA) was purchased from Sigma-Aldrich as a sodium salt solution. The pH of the solution was adjusted to 1. The sodium ions were removed by dialysis of the solution against Milli-Q water until pH was constant.

7.4 Sample Preparation

7.4.1 Spin-Coating

The polymers were dissolved in the respective solvent to achieve concentrations between 15 and 25 wt%. PMMA was dissolved in toluene and PDha was dissolved in DMSO, while all other polymers were processed from water. The solutions were then spin-casted on glass substrates with dimensions of 25x25 mm at 3000 rpm for 150 s. These samples were used for thermal conductivity measurements and IR investigations. The dry samples were kept in a vacuum oven at 100 °C for 24 h.

7.4.2 Humidity Annealing

Saturated salt solutions in a desiccator achieved different relative humidities. We used $MgCl_2$, NaCl, and K_2SO_4 for relative humidities of 45, 77, and 92%, respectively.[22] The spin-cast samples were equilibrated in a humid atmosphere for 24 h before further investigations. The transducer layer surface is shown in Figure 7.16 and demonstrates holes or cracks. Therefore, equilibration with the environment is not prevented by the evaporated transducer layer on top of the polymer. Photoacoustic (PA), atomic force microscopy (AFM), and IR measurements were conducted immediately after receiving the samples from the humidity-adjusted desiccator.

7.4.3 Thermal Conductivity Measurements

The PA method was used to determine the thermal conductivity of the spin-coated polymer films.[23,24] A gold transducer layer was applied to the top of the sample before the measurement. The sample is fixed to the measurement cell. The cell is gas-tight and filled with 20 psi helium. A modulated laser heats the transducer layer periodically. The induced temperature change on the surface of the sample leads to an acoustic wave propagating into the gas. The acoustic signal is detected using a microphone and coupled to a lock-in amplifier. The frequency-dependent phase shift between the modulated laser beam and the acoustic wave is measured. The experimental data are fitted using a multilayer model, describing the temperature distribution in the sample. The primary fitting result is the total layer resistance. Dividing the total layer resistance by the film thickness, the effective thermal conductivity is obtained. Each sample was measured three times. The mean values of these measurements are presented with the standard deviations as error bars. The humidity-dependent data were measured without additional external control of the surrounding humidity. We did not observe a drift in the photoacoustic signal

during the measurement time and conclude that the humidity water uptake remains constant for this duration (Figure 7.7c). More details can be found in the Supporting Information Section 7.7.

7.4.4 Fourier Transform Infrared Spectroscopy

The Fourier transform infrared (FTIR) measurements were conducted on a Bruker (Billerica, MA, USA) VERTEX 70 IR spectrometer with an attenuated total reflection (ATR) measurement unit. The measurements were performed from 380 to 4000 cm^{-1} with a resolution of 4 cm^{-1} and 128 scans. The samples were taken from the desiccators or vacuum oven, respectively, and directly measured under ambient conditions. Normalized spectra were used to calculate the difference spectra relative to the dry polymer samples.[25] Therefore, the normalized spectrum of the dry sample was subtracted from the spectra at the different relative humidities. The CH_2 deformation vibration at 1450 cm^{-1} was used as a reference peak for normalization, which is unaffected by water adsorption.

7.4.5 Fourier Self-Deconvolution

Fourier self-deconvolution (FSD) is a mathematical method to increase spectral resolution. By this, it is possible to separate overlapping absorption bands in an IR spectrum.[26] We applied the FSD according to Hu et al.[27] The software OPUS 7.5 (Bruker, Billerica, MA, USA) was used for all steps. First, the carbonyl region (between 1800 and 1540 cm^{-1}) was cut-off. A baseline correction with one iteration was performed, and the spectrum was smoothed by 5–9 points. In the next step, the FSD was performed with a Lorentzian shape with a half-bandwidth of 25 and a noise reduction of 0.30. Another baseline correction was conducted before the peaks were selected according to the minima of the second derivative of the initial spectrum. Finally, the peaks were fitted with a Gaussian profile with the Levenberg–Marquardt method.

7.4.6 Differential Scanning Calorimetry

Differential scanning calorimetry (DSC) measurements were performed on a TA instruments Discovery DSC 2500. Two heating cycles were conducted; only the second cycle was used for evaluation. The temperature profile ranged from −40 to 140 °C using a heating rate of 10 K min^{-1} with a nitrogen flow of 50 mL min^{-1}. The measurements are shown in Figure 7.14. Modulated DSC (MDSC) measurements were performed to determine the c_p of the samples. The optimum MDSC parameters have been calculated and evaluated following the instructions described in the

Table 7.1: Summary of the Measured Polymer Properties.[a]

Name	M_n [g mol^{-1}]	PDI	Density [g cm^{-3}]	c_p [J g^{-1} K^{-1}]
PImAA	5500 [b]	1.31 [b]	1.48	1.045
PMeImAA	3300 [b]	1.45 [b]	1.37	0.896
PDha	13,000 [c]	2.5 [c]	1.24	1.009
PAGA	28,500 [d]	1.32 [d]	1.22	1.245
PAA	15,000		1.26	1.202
PMMA	17,400 [e]	1.15	1.15	1.217

[a] The density and c_p values were used for the determination of thermal conductivity.

[b] Determined by SEC using aqueous 0.3% TFA/0.1 M NaCl as an eluent and calibrated against P2VP standards.

[c] Determined for the protected precursor of PDha by SEC using 0.1% LiCl in DMAc as an eluent and calibrated against PMMA standards.

[d] Determined by SEC using 0.1 M NaNO3/0.05% NaN_3 as an eluent and calibrated against PEO standards.

[e] Determined by SEC using THF as an eluent and calibrated against PMMA standards.

literature. The modulations in the transition range and the modulation period were controlled and adjusted to a heating rate of 2 K min^{-1}, a period of 80 s, and an amplitude of 1.6 K. The final samples were measured in hermetic pans to avoid loss of water during the measurement. The experiments were performed in a temperature range from 5 to 60 °C. c_p at 25 °C of each polymer is given in Table 7.1.

7.4.7 Helium Pycnometer

An Ultrapyc 1200e (Quantachrome Instruments, Boynton Beach, FL, USA) was used for the determination of the density of the dry samples. Before each run, the volume of the measurement cell was calibrated. Subsequently, a defined mass of the polymer was put into the cell. The volume of the polymer was determined by 100 runs. The division of mass and volume calculated the density. The obtained values are summarized in Table 7.1.

7.5 Results and Discussion

We investigate the effective thermal conductivity of four different ampholytic polymers, PDha, PAGA, PImAA, and its methylated derivative poly(2-(3-methylimidazolium-1-yl)acrylic acid) (PMeImAA, Figure 7.2a). All polymers have at least two different functional groups per repetition unit. We also analyzed PAA with only one functional group, which was reported to play a crucial role in the formation of a highly conducting pathway.[16] PMMA is not able to form hydrogen bonds and was also measured as a reference system.

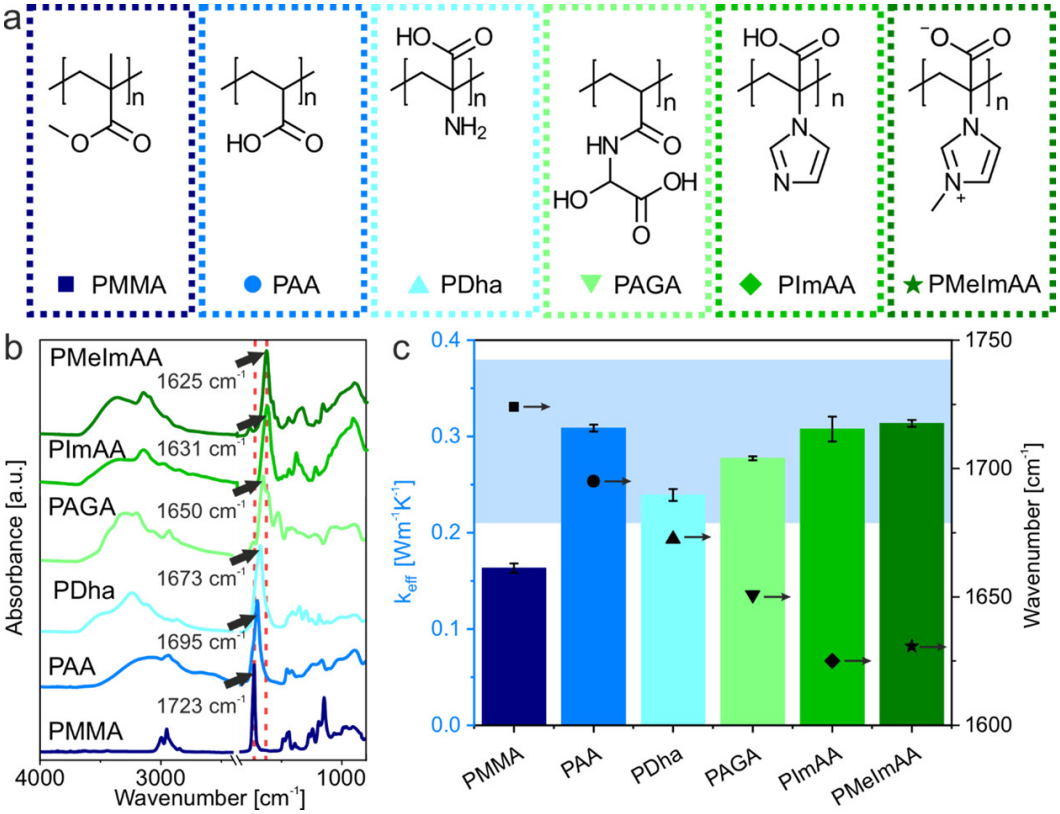

Figure 7.2: (a) Structure of the ampholytic polymers and the reference polymers PAA and PMMA. The ampholytic polymers have at least two functional groups per repetition unit. (b) IR spectra of all investigated polymer samples in the dry state. The red dashed lines present the carbonyl peak position of PMMA and PMeImAA, respectively. (c) Measured effective thermal conductivity of all samples (solid bars). The thermal conductivity correlates with the peak position (black symbols) of the carbonyl band measured by IR spectroscopy (except for PAA). The light blue area indicates the range of literature values for amorphous, water-soluble polymers.[14]

We start our analysis by the polymer characterization under dry conditions, that is, after storing the samples in a vacuum oven. In the IR spectra shown in Figure 7.2b, it can be seen that, except PMMA, all polymers form intra- and intermolecular hydrogen bond interactions as indicated by the broad bands between 2500 and 3600 cm^{-1}. These bands originate from the O–H and N–H stretching vibrations. OH-wagging at 900 cm^{-1} is another indicator for the presence of COOH under these vacuum-dried conditions. This band is broad due to various spatial orientations of the H bond-forming functional groups. Because of this variety of possible bonds, the underlying C–H stretching vibrations, and several overtones, this region of an IR spectrum is challenging to evaluate.

We, consequently, focus our analysis on another strong peak connected to hydrogen bonds: the carbonyl stretching vibration around 1700 cm^{-1}. This peak is very strong, possesses a small full width at half-maximum, and is sensitive to the local environment.[27–29] Therefore, it provides a suitable target for further investigations of H bonds. Furthermore, it was shown that the absorption coefficient of the carbonyl

stretching vibration, in comparison with the O–H and N–H stretching, does not depend significantly on the strength of the H bonds.[30,31] One disadvantage is that H bonds between functional groups without a carbonyl group contribution cannot be resolved. A first indication of the strength of a hydrogen bond is the position of the carbonyl peak, whereby lower frequencies indicate an increasing strength of the H bond.[32] We see a systematic shift of the carbonyl peak from PAA to PMeImAA, indicating an overall increase in strength of the carboxylic H bonds.

The effective thermal conductivities (Figure 7.2c) show typical values for water-soluble amorphous polymers compared to values reported in the literature (shaded area).[14]

Comparing our values for PMMA (0.16 W m^{-1} K^{-1}) and PAA (0.31 W m^{-1} K^{-1}) with the literature (0.20 W m^{-1} K^{-1}[14] and 0.34 W m^{-1} K^{-1}[15]/0.37 W m^{-1} K^{-1}[14]), we find slightly lower values. The lower values are reasonable because the PA method determines the total layer resistance of the sample. The effective thermal conductivity is calculated based on the polymer film thickness. Also, it takes the thermal resistances between the polymer layer and the support structure and transducer layer, respectively, into account. We attribute the relatively large standard deviation of the PImAA sample to the lowest layer thickness (<1 μm) of the PImAA sample, which reduces the fitting accuracy.

Considering the systematic increase in H bond strength derived from the carbonyl peak position, we find the expected increase in thermal conductivity for the ampholytic samples under investigation. Rather unexpected from this point of view is the exceptionally high thermal conductivity of PAA.

For further insight into the strength of the H bonds, we provide a detailed analysis of the IR spectra. We base our analysis on FSD of the carbonyl resonance between 1600 and 1750 cm^{-1}, according to Hu et al.[27] The fitted spectra are shown in Figure 7.3. The peaks are assigned to different configurations of the carbonyl group. Dark yellow is anhydrides (1805–1760 cm^{-1}), green is free carbonyl groups (1740–1730 cm^{-1}), cyan is the terminal oligomeric form of carboxylic acid (1716–1680 cm^{-1}), blue is the cyclic dimer (1700–1665 cm^{-1}), and gray-blue is the inner oligomeric form (1675–1650 cm^{-1}). These peaks can be found in all samples containing a carboxylic acid group. The assignment is based on Dong et al.,[28] who investigated different H bond motifs in PAA samples. The introduction of amino groups in our ampholytic polymers introduces additional peaks marked in purple, ascribed to H bonds with primary or secondary amino groups (PDha and PAGA). A final category of H bonds is assigned to the interaction of the carbonyl group with the imidazole ring in PImAA and PMeImAA depicted in dark blue. Further contributions arising from vibrations other than the carbonyl stretching, such as NH bending vibration/Amide II and vibrations of the aromatic ring, are summarized in orange. As a consequence, the orange bands were excluded for the evaluation of the carbonyl ratio.

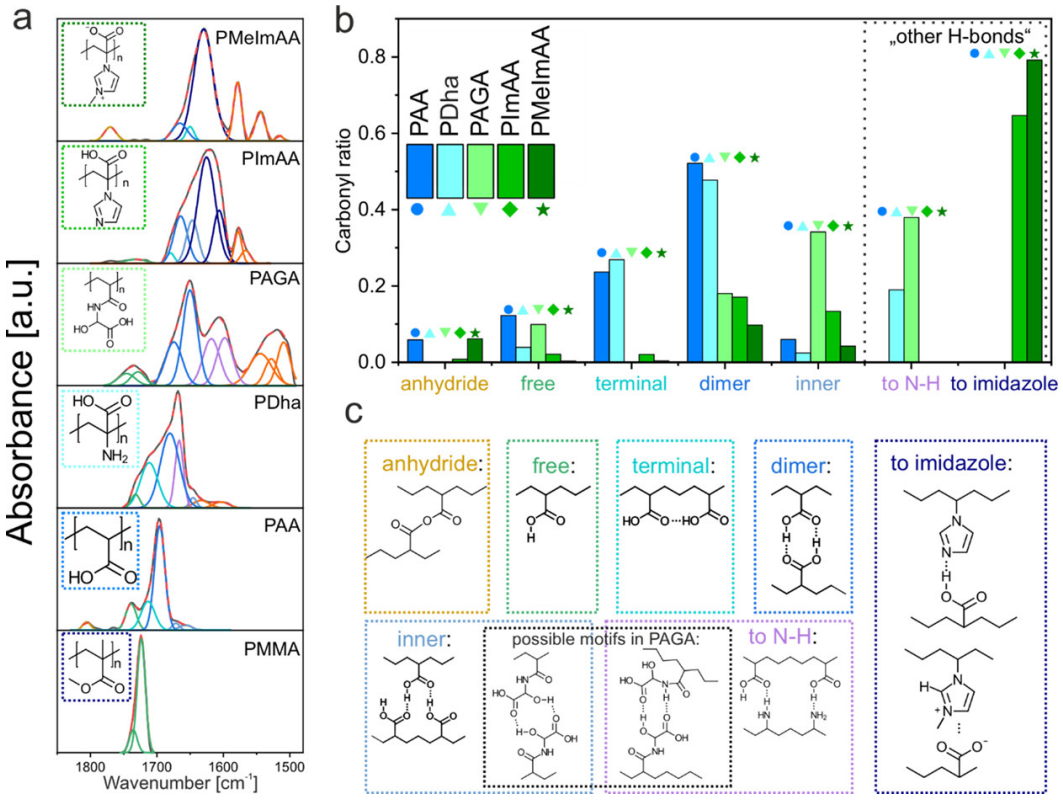

Figure 7.3: (a) Deconvoluted IR spectra of all investigated samples. The films were dried before the measurements. (b) Relative ratio of different motifs of the carbonyl bond. (c) Schematic illustration of different H bond motifs.

The relative contribution of all these different classes of hydrogen bonds is summarized in Figure 7.3b. Most notably, PAA comprises a range of strongly coordinated H bonds (dimer, inner, terminal) and even covalently condensed moieties (anhydride). The interplay of these structural motifs facilitates thermal transport between the polymer chains. Please note that the strength of the H bond is the lowest in the case of PAA compared to all other ampholytic polymers (Figure 7.2b, 1723 cm–1 peak position of the carbonyl band). Thus, the bonding scheme in PAA may additionally facilitate an elongated conformation, which also improves thermal transport. As soon as an additional functional group is introduced (NH2 in the case of PDha), the thermal conductivity drops considerably. However, the nature of the H bond environment is still comparable to PAA. Merely, the anhydride and free-carboxyl bonds are replaced by O–H–N moieties ("other bonds" in Figure 7.3b). The overall stiffer carbonyl peak (1695 cm^{-1}) should even favor a higher thermal conductivity. Thus, it is difficult to unambiguously relate the thermal conductivity reduction to subtle differences in the way hydrogen bonds are formed in the respective polymers. Additional contributions, such as the side chain structure[33] or the influence of the side groups on the polymer morphology,[8] are important at the same time. Thus, the alleged beneficial influence of additional hydrogen bonds to the primary amino group is counteracted by conformational changes that cannot be resolved by IR characterization. The transition from PDha to PAGA, PImAA, and PMeImAA demonstrates a monotonic increase in the class of other hydrogen bonds. Along this direction, the strength of the carbonyl bond also increases. The combination of both effects translates into the general trend of increasing thermal conductivity.

PAA and all herein used ampholytic polymers are strongly sensitive to humidity. We, consequently, determined its influence on the effective thermal conductivity. We gravimetrically measured the moisture content after prolonged exposure to specific humidities (Figure 7.4a). PMMA, as a control, demonstrates no sensitivity to increasing humidity. PAA exhibits a considerable absorption of water on the order of 40%, whereas in the case of the herein used, ampholytic polymer values from 35 to 60% are found. The quaternized PMeImAA exhibits the most significant water uptake and doubles its weight. These mass changes are comparable to literature data on PAA[34] and other polyelectrolytes,[35] respectively. The uptake of water influences not only the H bonding within the polymers but also the specific heat capacity and density. Both quantities are highly relevant when determining the thermal conductivity under these conditions. The measurement of the effective polymer density under various humidity conditions is not possible in a direct manner. We, therefore, used the measured moisture content to calculate the humidity-dependent density. The specific heat capacity was determined experimentally by MDSC measurements, using hermetic pans (Figure 7.4b). The shaded areas indicate the expected c_p based on a mass-weighted mixing model considering the measured moisture contents. Although the overall trend of an increasing c_p is well-captured in all cases, some degree of variability in a range of ≈20% is seen. This variation

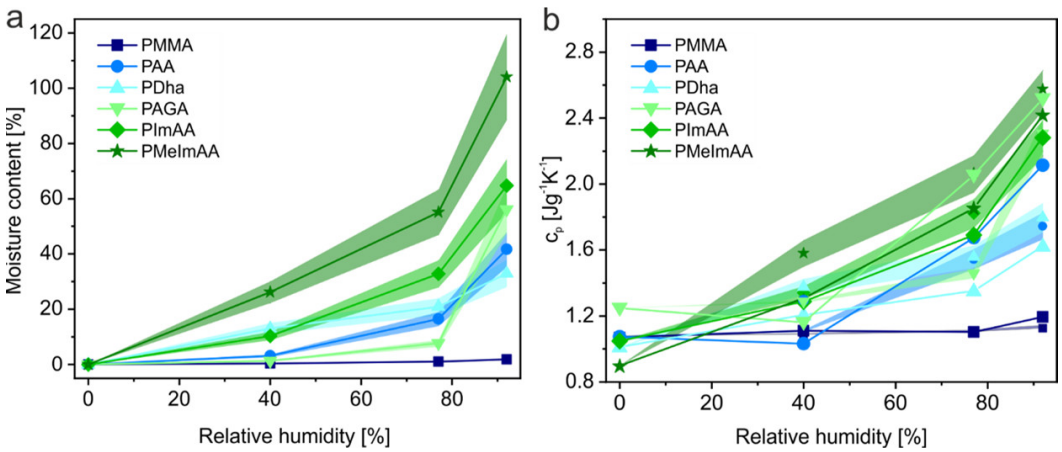

Figure 7.4: Humidity dependence of the samples. (a) Moisture content increases with humidity for all polymers with functional groups. Shaded areas mark the variability. (b) c_p, measured by MDSC, increases with humidity (solid lines and symbols). Shaded areas rationalize the expected trend of the c_p based on the water uptake in (a) calculated using a mass-weighted mixing model.

can be explained by the difficulty of accurately retaining the moisture uptake and polymer conformation during the measurement itself.

The uptake of water also affects the polymer microstructure and H bond environment. Consistently, with our previous analysis, we used FSD of the carbonyl peak of our FTIR spectra. Figure 7.5 summarizes three distinct cases: PAA, PImAA, and PMeImAA. The spectra show a distinctly different way of water uptake in the case of PAA compared to PImAA and PMeImAA. In the literature, there is a differentiation between unbound and bound water.[34,36] We define bound water as directly coordinated to the polymer, while unbound water interacts with other water molecules and forms clusters.

Our results of the absorbed amount of water in PAA (moisture content of 0.42 g/g polymer) are in good agreement with the literature value (0.47 g/g polymer).[34] Also, the FTIR difference spectrum is in good agreement with the findings of Daniliuc et al.[34] They reported a negative contribution in the difference spectra for free C=O (around 1735 cm^{-1}) and dimer (around 1700 cm^{-1}) and a positive peak between 1672 and 1634 cm^{-1}. The negative contributions are attributed to disconnected polymer–polymer interactions, while the positive contributions are newly formed polymer–water interactions.[34] They interpreted the spectra such that only bound water exists in their PAA sample.

Despite a higher moisture content, the difference spectra of PImAA and PMeImAA show overall fewer variations. Although the negative contributions between 1675 and 1600 cm^{-1} represent disconnected polymer–polymer interactions, the overall lack of significant positive contributions indicates that the water is adsorbed in a less bound state in the case of PImAA and PMeImAA. The variation between these two polymers is smaller because polymers with similar functional groups show similar peaks in IR spectroscopy when adsorbing/absorbing water.[37] The same data

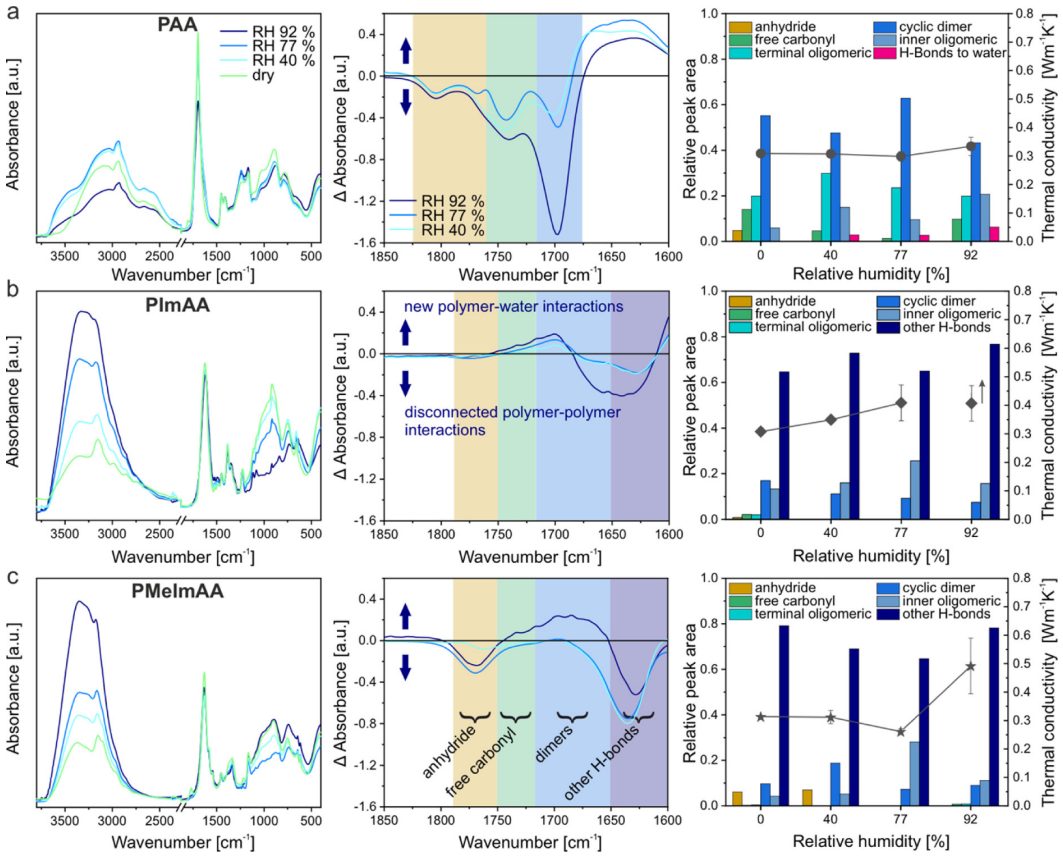

Figure 7.5: From left to right: IR spectra of samples stored at different relative humidities. Difference spectra in the region of the carbonyl stretching vibration. The relative peak area of different H bond structures dependent on the relative humidity. (a) PAA, (b) PImAA, and (c) PMeImAA.

evaluation and representation for PDha and PAGA are summarized in Figure 7.14. When considering the deconvoluted peaks (right panels of Figure 7.5), one has to be cautious while interpreting the respective contributions. The major difficulty is that the thermal conductivity is governed by various parameters, which were already pointed out in the discussion of the dry samples. We can, however, extract reasonable trends. PAA shows that the adsorption of bound water hardly influences the thermal conductivity. Consequently, bound water intercalates tightly between the PAA chains without affecting its conformation nor impeding interchain thermal transport. The IR spectra of PImAA do not show significant changes in the carbonyl peak region. Consequently, the uptake of bound and unbound water itself seems to be the driving force for the monotonic increase in thermal conductivity. PMeImAA hints toward the fact that the creation of inner oligomeric groups on the expense of anhydride, cyclic dimer, and charged heterocycle interactions impedes thermal transport up to the humidity of RH ≈77%. Finally, considering reports in the literature, the uptake of water was also reported to increase the effective thermal conductivity strongly. Mehra et al.[38] worked with polyvinylalcohol and ascribed the thermal conductivity increase to the formation of thermal bridges by bound water molecules. All these examples demonstrate that the influence of humidity on the thermal transport in hydrophilic polymers is hard to predict and certainly depends on the specific polymer–water combination.

Although the previous discussion focused on a microscopic interpretation of inter- and intramolecular interaction between the constituting polymers, we also want to draw the attention to an alternative consideration comprising a much more coarse-grained point of view. The uptake of unbound water can be understood as a way to generate a two-phase material, where water clusters are formed.[36] This heterogeneous material can then be analyzed in a similar way to other nanocomposite materials using effective medium models as described by Carson.[39] For this, we use the vacuum (dry) polymer thermal conductivity as the pure phase of one component and literature data of the thermal conductivity of water as the second component. In combination with our data of the moisture uptake (Figure 7.4a) and two volume-weighted mixing models (parallel mixing model and effective medium model)[39], the humidity-dependent thermal conductivity is calculated (Figure 7.6). For PDha, PAGA, and PImAA, both mixing models describe the experimental data adequately well, particularly when considering the accuracy of the mixing models themselves and the thermal conductivity determination. For the case of PAA, where a high amount of bound water can be expected, both mixing models systematically overestimate the effective thermal conductivity.

The parallel mixing model is based on the presence of extended percolation paths through the entire polymer structure. In contrast, if the water uptake happened in a random and dispersed fashion within the polymer, it should be better represented by the EMT mixing model (also compared to the schematic depiction in the inset of Figure 7.6a).[39] The small difference between the pure polymer and the pure water

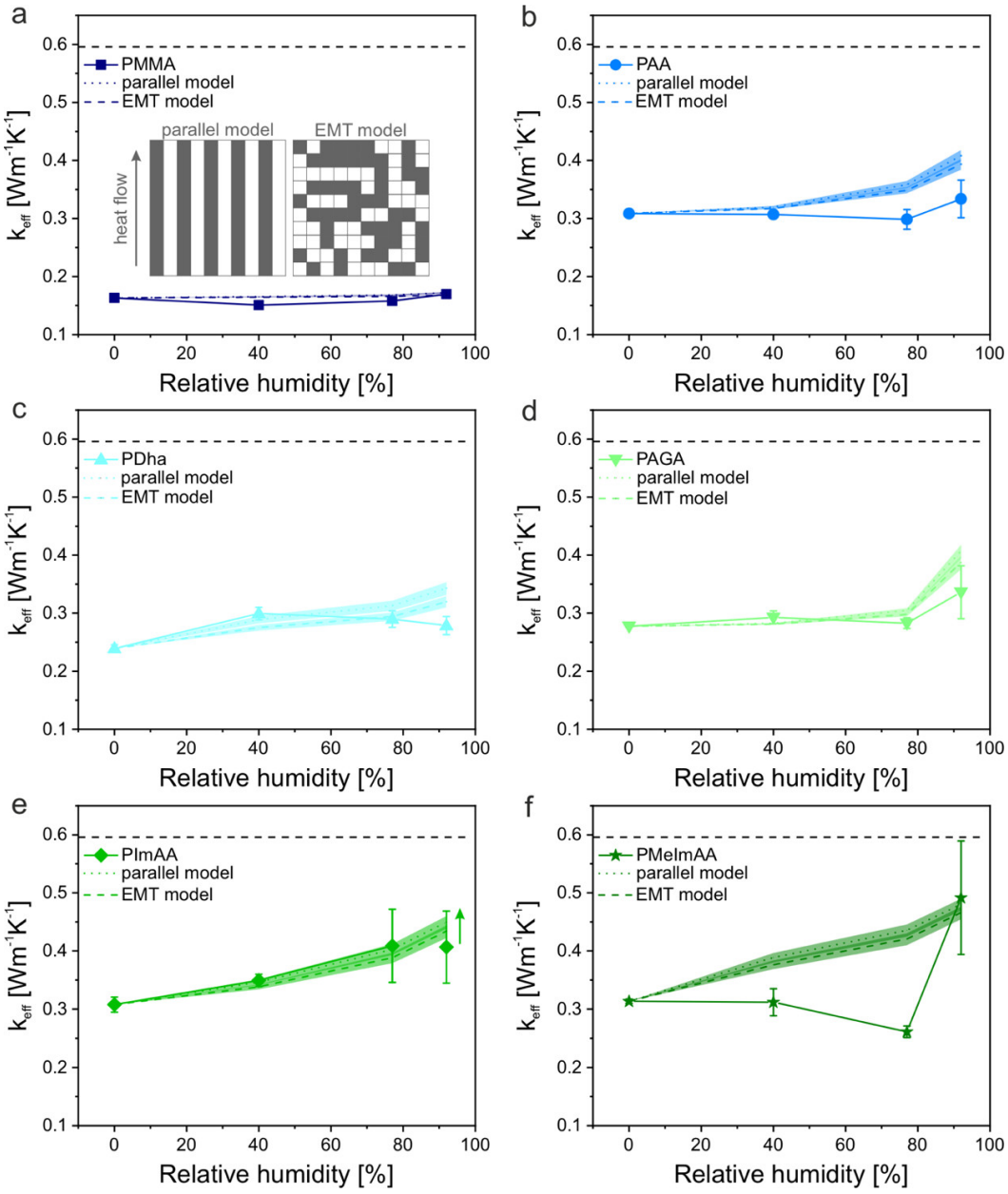

Figure 7.6: Effective thermal conductivity vs relative humidity for all investigated polymer samples. From (a–f) PMMA, PAA, PDha, PAGA, PImAA, and PMeImAA. The solid symbols depict the experimental data, while the dashed and dotted lines are calculated values using the parallel and the EMT mixing model, respectively. A schematic illustration of these models is shown as an inset in (a). The shaded areas consider the variability because of the deviation of the moisture content determination. The dashed black line represents the thermal conductivity of water.

thermal conductivity prevents an unambiguous judgment on the presence of dispersed or percolated water inside the polymer. Both mixing models, however, support the straight-forward interpretation in the sense of a water–polymer nanocomposite material. Only the ionic PMeImAA sample deviates strongly from the mixing models, which could be understood in a way that the uptake of water first disrupts thermal transport pathways. Once water condensation sets in at very high humidity (RH ≈92%), the thermal conductivity is again dominated by the water phase.

7.6 Conclusions

We employed a set of polyampholytes featuring a high density of functional groups to investigate how thermal transport can be controlled by hydrogen bonding in amorphous polymers. We, therefore, compared four types of ampholytic polymers to PAA and PMMA as reference materials. The investigation of ampholytic polymers is particularly interesting because this opens an elegant pathway to study the influence of H-donor and H-acceptor groups in a one-phase system. We employed a detailed IR spectroscopy investigation for a holistic understanding of the involved H bond motifs.

In summary, we can deduce three major trends. First, PAA is an exceptionally well-conducting hydrophilic polymer, which we attribute to a stretched polymer conformation. Second, for all ampholytic polymers, we find an overall trend of increasing thermal conductivity along with an increase in the H bond strength under dry conditions. This can be deduced from a systematic red shift of the carbonyl peak. Third, the presence of humidity leads to a polymer-specific uptake of water and, consequently, to a variety of changes to the H bond motifs. However, the thermal transport in ampholytic polymers can be well-described using mixing models, where the uptake of water is considered as the formation of a nanocomposite material. Deviations from this straight-forward description are PAA, where a high amount of strongly bound water is observed, and PMeImAA, where ionic interactions are dominant. The deconvolution of the carbonyl resonance peak demonstrates a range of binding motifs between the respective polymers. However, an unambiguous assignment of a particular H bond moiety to an increased or decreased thermal transport behavior is not possible. Additional factors such as scattering effects along the polymer backbone or on polymer side groups have to be taken into account, as well as subtle changes to the polymer conformation. Overall, our contribution adds to a better understanding of the role of H bonds for thermal transport in polymer materials.

Most importantly, not only the specific design of H bond motifs determines the capability to conduct thermal energy. Even in the case of one-phase systems, the various influences of polymer conformation, side groups, and interaction have to

be balanced. We are still far away from a predictive model to molecularly design amorphous polymers to a specific high or low thermal conductivity. This is an ongoing challenge to be addressed by polymer chemists and engineers over the next years.

Acknowledgments

This project was funded through a Lichtenberg professorship by the Volkswagen Foundation and by the German Research Foundation by the SFB 840 (project B7). Additional support was provided by ERC StG VISIRday #714968, DFG RE3550/2-1, SCHA1640/12-1, and the collaborative research center SFB 1278 "PolyTarget" (project number 316213987, project C03). P.B. (Landesgraduiertenstipendium) and L. W. (CarlZeiss-Foundation) are grateful for Ph.D. fellowships.

7.7 Supporting Information

7.7.1 Thermal Conductivity Measurements

The thermal conductivity was determined by the photoacoustic method. For photoacoustic characterization, the samples were spin-coated on glass substrates. The layout of the measurement set-up is described in the literature.[13]
The frequency-dependent phase-shift is plotted in Figure 7.7 - two measurements and the respective fits are shown in Figures 7.7a and b. They correspond to the dry and the RH 77% PImAA sample, respectively. The phase shift data are fitted by a multilayer model developed by Hu et al.[23] The fit was performed according to Singh et al.[5], which yields the total layer resistance. Figure 7.7c shows three consecutive measurements. The change of the phase shift is minimal. Therefore, we conclude that the moisture content keeps constant over the course of at least three measurements, which corresponds to about 30 min.
For the fit, the sample thickness, the specific heat capacity, and the density are necessary. The thickness was obtained by AFM measurements (Table 7.2). For each humidity condition, a separate and individual sample was prepared using the same stock solution and spin coating parameters. Overall the layer thicknesses show a good consistency from sample to sample. The applied humidity conditions do not lead to an excessive degree of swelling. Only for PImAA, the layer thickness at RH 92% could not be quantified by AFM directly. The low molecular weight of PImAA (5500 g/mol) - in comparison to the other polymer samples (13000 – 28000 g/mol) - led to a viscous polymer film that prevented the evaluation of the step height at a scratch in the sample. Consequently, we provide for this single case a lower estimate

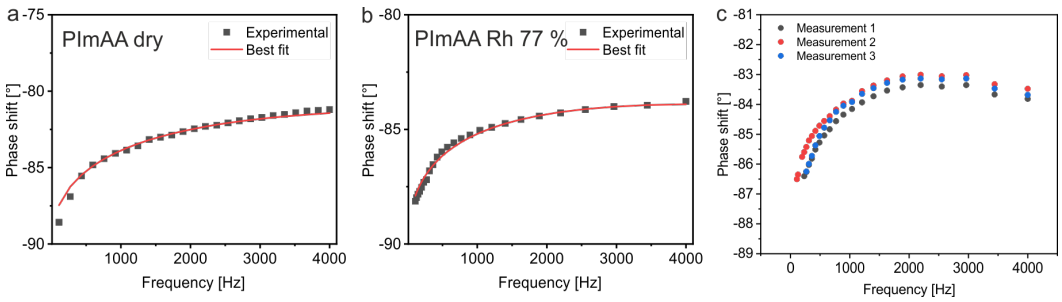

Figure 7.7: The frequency-dependent phase shift of (a) the dry PImAA sample and (b) the PImAA sample at 77% humidity. The red lines present the best fit. (c) Three consecutive measurements of PAA at 77% humidity. The data shows only slight deviations between the measurements. Therefore, we conclude that the moisture content of the sample is stable over the time of the measurements.

of the thermal conductivity based on the dry polymer layer thickness of ≈900 nm.The humidity dependent specific heat capacity was determined by MDSC measurements. The density of the dry samples was measured with a helium pycnometer. The density of the samples with absorbed water was calculated from the moisture content, and the bulk densities of water and the polymers. Dividing the total layer resistance by the sample thickness leads to the effective thermal conductivity. All relevant data are shown in Table 7.2.

Table 7.2: Summary of the data used for the determination of the effective thermal conductivity.

Sample	Relative Humidity [%]	Total layer resistance [mm^2 K W^{-1}]	SD	Thickness [μm]	SD	Effective thermal conductivity [W m^{-1} K^{-1}]	SD
PMMA	0	9.44	0.28	1.540	0.071	0.163	0.005
PMMA	45	10.41	0.11	1.569	0.011	0.151	0.002
PMMA	77	9.94	0.17	1.569	0.024	0.158	0.003
PMMA	92	9.26	0.25	1.570	0.016	0.170	0.004
PAA	0	3.74	0.18	1.182	0.010	0.309	0.004
PAA	45	4.10	0.06	1.258	0.052	0.307	0.005
PAA	77	4.26	0.25	1.270	0.005	0.299	0.017
PAA	92	4.56	0.42	1.511	0.197	0.334	0.032
PDha	0	7.10	0.19	1.697	0.017	0.239	0.006
PDha	45	6.28	0.20	1.680	0.022	0.299	0.011
PDha	77	5.96	0.29	1.724	0.025	0.290	0.014
PDha	92	6.20	0.33	1.723	0.020	0.279	0.016
PAGA	0	5.70	0.04	1.580	0.194	0.277	0.002
PAGA	45	5.77	0.22	1.688	0.108	0.293	0.011
PAGA	77	6.50	0.21	1.838	0.143	0.283	0.009
PAGA	92	3.31	0.42	1.100	0.016	0.336	0.046
PImAA	0	2.87	0.12	0.881	0.035	0.307	0.013
PImAA	45	2.57	0.08	0.891	0.024	0.349	0.011
PImAA	77	2.45	0.35	0.983	0.071	0.409	0.062
PImAA	92	2.25	0.33	>0.900	-	0.407	0.061
PMeImAA	0	3.54	0.04	1.110	0.048	0.314	0.004
PMeImAA	45	3.64	0.28	1.132	0.170	0.312	0.023
PMeImAA	77	4.08	0.16	1.064	0.071	0.261	0.010
PMeImAA	92	2.47	0.35	1.200	0.096	0.492	0.098

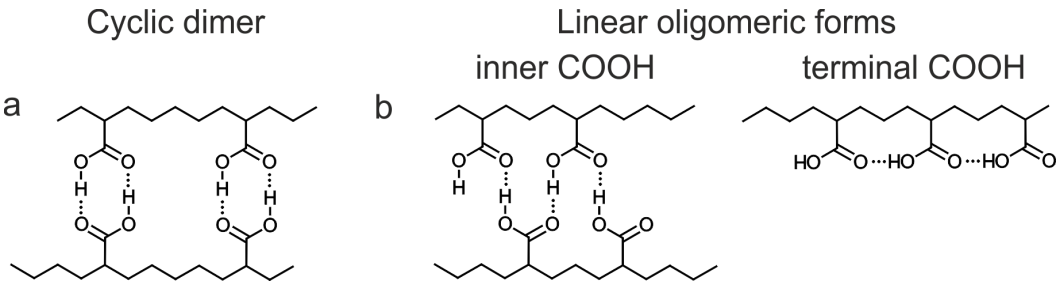

Figure 7.9: Forms of hydrogen bonding in PAA.[28].

7.7.2 IR Spectroscopy of Dry Samples

PAA

In Figure 7.8 the IR spectrum of a dry PAA film in the region of the C=O stretching vibration is shown. We attributed the different peaks in the deconvoluted spectrum to specific configurations of the C=O bond, according to Dong et al.[28]. Therefore, we could distinguish between the free, the dimeric, and two oligomeric forms of the C=O bond. The peak with the highest wavenumber of 1735 cm^{-1} is attributed to the free monomer of the COOH group, whereas the peak at around 1700 cm^{-1} represents the cyclic dimer. The linear oligomeric forms of the terminal COOH groups lie in between, at 1716 cm^{-1}, while the inner COOH appears at two peaks with the lowest wavenumbers around 1674 cm^{-1}. The H-bond conformations are illustrated in Figure 7.9. At least some anhydride groups have formed due to the drying process, as indicated by the bands at 1806 cm^{-1} and 1765 cm^{-1}. Extending the assignment from Dong et al., we attributed different forms of H-bonds in the other investigated polymers.

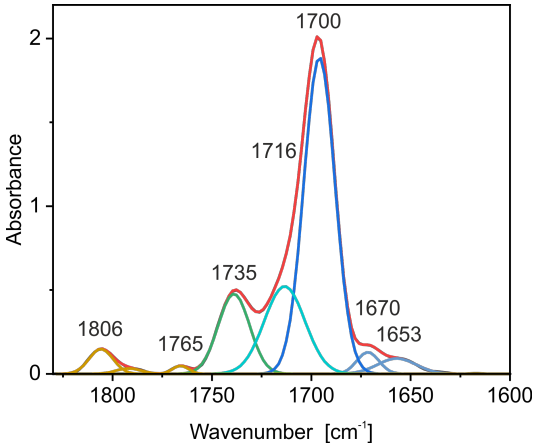

Figure 7.8: IR spectrum of PAA in the region of the C=O band. The spectrum was deconvoluted for better interpretation. The bands were attributed to distinct configurations of the C=O bond, according to Ref. [28].

PDha

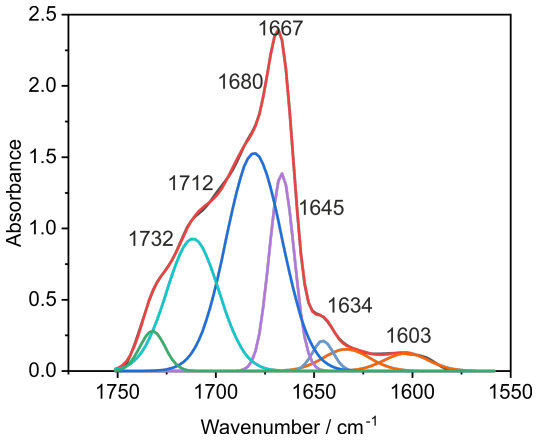

Figure 7.10: Deconvoluted IR spectrum of the dry PDha sample in the region of the C=O stretching vibration.

Compared to PAA, an amino group is added to the repetition unit of PDha. Therefore, more motifs to form H-bonds are available. Similar peaks for the PAA sample could be detected (Figure 7.10). However, we found a slight shift to lower frequencies of all peaks. While the shift is only a few wavenumbers for the free C=O stretching and the terminal H-bonds, the shift is 20 cm^{-1} and 50 cm^{-1} for the cyclic dimers and the inner H-bonds. The shift is an incidence of the increased strength of the H-bonds. Furthermore, new peaks arose at 1667 cm^{-1}, 1634 cm^{-1}, and 1603 cm^{-1}. The peak at 1667 cm^{-1} is ascribed to the H-bonds formed between the carbonyl and the amino group. The peaks at 1634 cm^{-1} and 1603 cm^{-1} belong to the NH2 deformation vibration and are, therefore, excluded from the evaluation of the C=O stretching vibration. We want to note that it is also possible that H-bonds between two amino groups are formed. The analysis of these H-bonds is not approachable by the investigation of the carbonyl stretching vibration.

PAGA

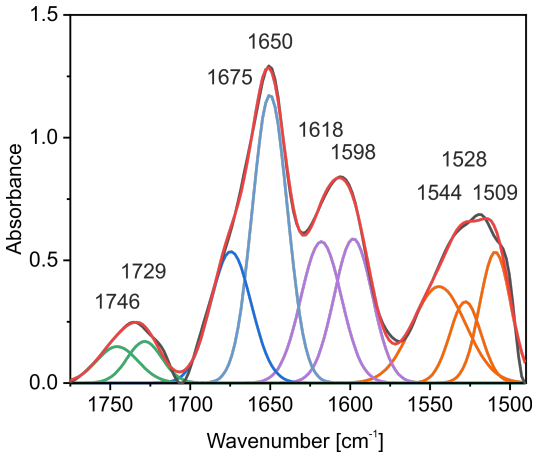

Figure 7.11: Deconvoluted IR spectrum of the dry PAGA sample in the region of the C=O stretching vibration.

Due to the presence of two different carbonyl groups, the spectrum of PAGA exhibits many peaks in the region between 1500 cm^{-1} and 1800 cm^{-1}. Besides the carboxylic acid group, also another carbonyl group is located in the amide bond. As a consequence, we detect amide I and amide II vibrations. While the amide I band derives from the C=O stretching of the amide carbonyl group, the amide II band consists of N-H bending and C-N stretching. Therefore, the amide II band is not relevant for the H-bond analysis, which is focused on the carbonyl bands. Stretching vibrations of free carbonyl groups from the carboxylic acid appear at 1735 cm^{-1}. The peak at 1675 cm^{-1} is attributed to the carboxylic acid dimer, as this is a wavenumber comparable to

the other samples. The band at 1650 cm^{-1} is ascribed to the inner H-bonds of the COOH group. Additional H-bonds to the single OH group could be a reason for the exceptional strength of this band. The two bands at 1618 cm^{-1} and 1598 cm^{-1} belong to different conformations of H-bonds but are not easily distinguishable.

PImAA

In the literature, it has been described that mixing PAA with poly(vinyl imidazole) (PVI) leads to a decrease of the carbonyl band of the PAA at 1716 cm^{-1} and to a new peak at 1547 cm^{-1}. The new peak is explained by the exchange of the proton from the carboxylic acid group to the imidazole group. Hence, the new peak is ascribed to the asymmetric stretching vibration of COO-.[40] In comparison, the PImAA film shows a strong carbonyl stretching peak at 1625 cm^{-1}. The peak 1578 cm^{-1} is ascribed to the C=C and C=N stretching in the aromatic ring. We do not attribute any of those peaks to the asymmetric stretching vibration of COO-, because of the high wavenumber of the first and the missing of the symmetric stretching vibration around 1330 cm^{-1}. Nevertheless, the low frequency of the C=O peak is an incident for a strong interaction between the carboxylic acid and the imidazole groups. This band, in turn, is relatively broad, which indicates a variety of interactions with different coordinations and bond strengths. The two peaks with the highest wavenumbers at 1770 cm^{-1} and 1732 cm^{-1} are ascribed to anhydride bonds and free carbonyl groups, respectively. Both show a very weak intensity and are almost overlooked. Accordingly, most of the carbonyl groups participate in H-bond interactions. We distinguish the H-bonds in two categories: H-bonds between acid groups like in PAA (1680 cm^{-1}, 1664 cm^{-1}, and 1647 cm^{-1}) and H-bonds between the carboxylic acid and an imidazole group ("other H-bonds", 1625 cm^{-1} and 1606 cm^{-1}).

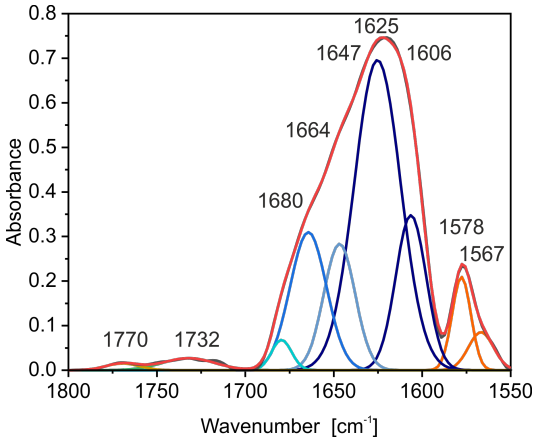

Figure 7.12: Deconvoluted IR spectrum of the dry PImAA sample in the region of the C=O stretching vibration.

PMeImAA

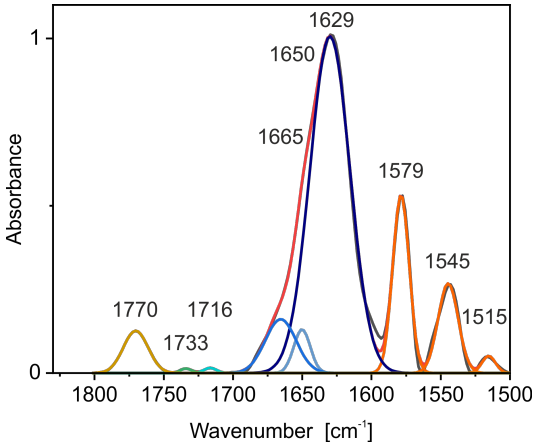

Figure 7.13: Deconvoluted IR spectrum of the dry PMeImAA sample in the region of the C=O stretching vibration.

In comparison to PImAA, PMeImAA has a methyl group attached to the imidazole ring, leading to a positive charge. Consequently, there is no free electron pair available at the nitrogen. The C=O band is again composed of different parts. At 1770 cm^{-1} a relatively strong anhydride band is detected, whereas the vibration of free carbonyl at 1733 cm^{-1} is only marginal. Also, the H-bonds between the carboxylic acid groups decreased in intensity. The very narrow peak at 1629 cm^{-1} is ascribed to the interactions between carbonyl and imidazole ring. The narrow width of the peak indicates a relative uniform strength and conformation of the interactions. The bands at 1579 cm^{-1} and 1515 cm^{-1} are ascribed to the C=C and C=N stretching in the aromatic ring.

7.7.3 Humidity Dependent IR Spectra

Figure S8 shows the humidity dependent IR analysis for PDha and PAGA analogous to the presentation in Figure 4 in the main manuscript.

PDha shows a comparable behavior to PAA. The difference IR spectra show negative and positive contributions in the same wavenumber regions. However, the effects are less pronounced. This indicates a similar mechanism of water absorption in PAA and PDha.

PAGA shows moderate water uptake for RH 40% and RH 77%. At RH 92%, the moisture content strongly increases. This behavior is also observed in the IR spectrum, with a drastic increase of the OH stretching vibration at 3500 cm^{-1}. The difference spectra in the carbonyl region show small deviations. The spectra for RH 40% and RH 77% show a slight decrease in H-bonds, whereas a small positive contribution is observed for the RH 92% sample. The newly formed interactions probably also lead to a slight increase in thermal conductivity at RH 92%.

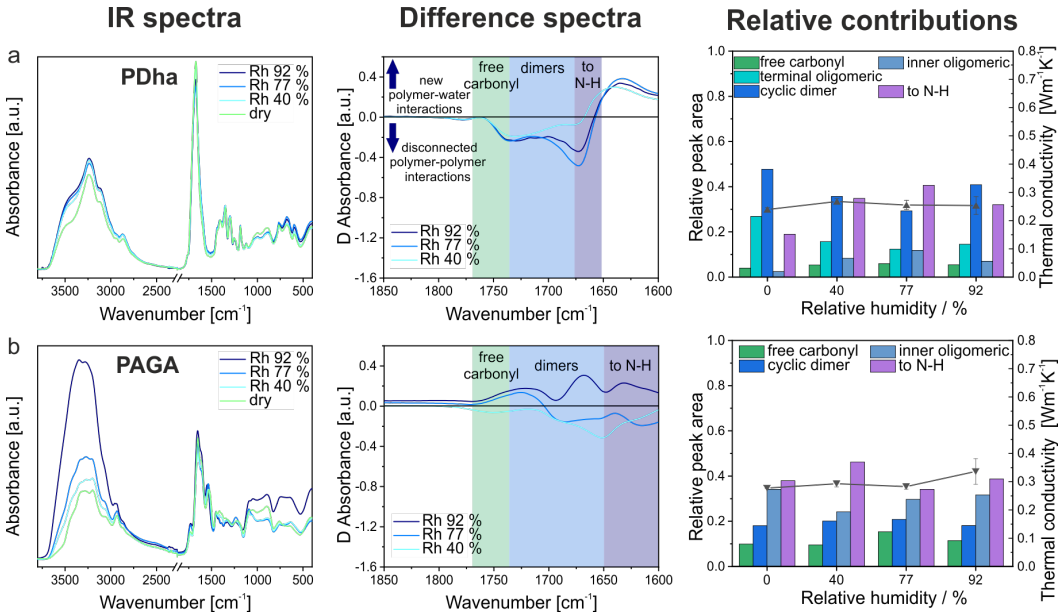

Figure 7.14: (a) PDha, and (b) PAGA. From left to right: IR-spectra of samples with various humidity exposure. Difference spectra in the region of the carbonyl stretching vibration. The relative peak area of different H-bond structures dependent on the relative humidity.

7.7.4 Polymer/Water Effective Medium Model (EMT)

The following equations were used to calculate the values for the parallel mixing model and the effective medium model, according to Carson et al.[39]
Parellel mixing model:

$$k_{\text{parallel}} = (1 - x_2)k_1 + x_2 k_2 \tag{7.1}$$

Effective medium model:

$$k_{\text{EMT}} = \frac{1}{4}(3x_2 - 1)k_2 + [3(1 - x_2) - 1]k_1 + \sqrt{[(3x_2 - 1)k_2 + (3(1 - x_2) - 1)k_1]^2 + 8k_1k_2} \tag{7.2}$$

With $x_{1,2}$ and $k_{1,2}$ the volume ratio and the thermal conductivity of components 1 and 2, respectively.

7.7.5 DSC Measurements

Besides the MDSC measurements, to determine the c_p of all samples, we performed DSC measurements of the dry samples in the range between −40 °C and 140 °C. Figure 7.15 shows direct DSC measurements with a heat rate of 10 K min^{-1}.

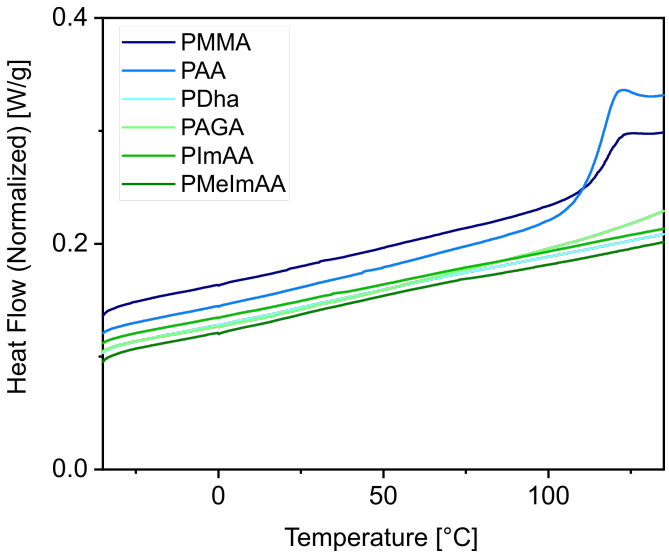

Figure 7.15: DSC measurements of dry polymer samples. The experiments were performed in the range from −40 °C to 140 °C with a heating rate of 10 K/min under nitrogen atmosphere.

7.7.6 Transducer Layer

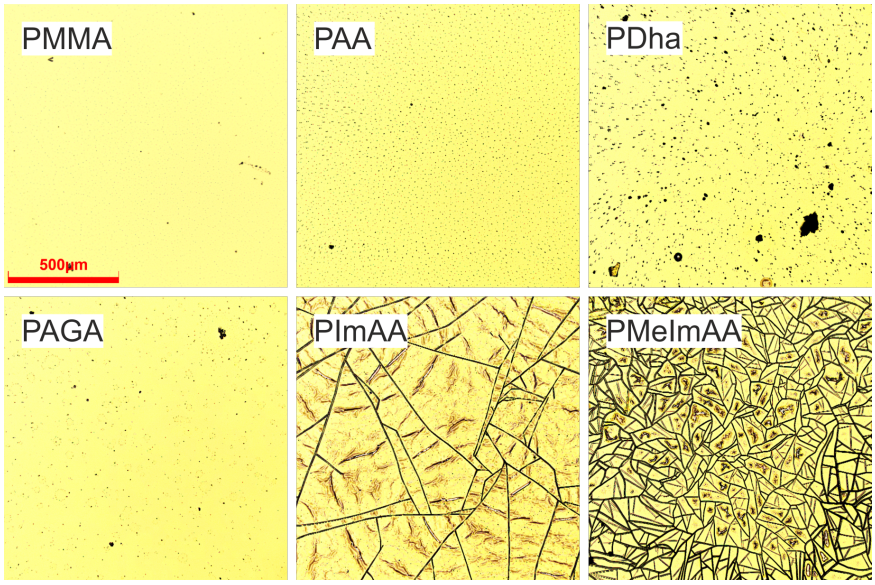

Figure 7.16: Optical microscopy of the surface of the Au transducer layer after measuring at humid conditions. Dark speckles and cracks indicate imperfections in the Au transducer layer, which facilitates equilibration to environmental conditions.

7.8 References

[1] A. L. Moore, L. Shi, *Materials Today* **2014**, *17*, 163–174.

[2] X. Wang, V. Ho, R. A. Segalman, D. G. Cahill, *Macromolecules* **2013**, *46*, 4937–4943.

[3] S. Shen, A. Henry, J. Tong, R. Zheng, G. Chen, *Nature Nanotechnology* **2010**, *5*, 251–255.

[4] Z. Zhong, M. C. Wingert, J. Strzalka, et al., *Nanoscale* **2014**, *6*, 8283–8291.

[5] V. Singh, T. L. Bougher, A. Weathers, et al., *Nature Nanotechnology* **2014**, *9*, 384–390.

[6] A. Henry, G. Chen, *Physical Review Letters* **2008**, *101*, 235502.

[7] J. Liu, R. Yang, *Physical Review B* **2012**, *86*, 104307.

[8] T. Zhang, T. Luo, *The Journal of Physical Chemistry B* **2016**, *120*, 803–812.

[9] Y. Lu, J. Liu, X. Xie, D. G. Cahill, *ACS Macro Letters* **2016**, *5*, 646–650.

[10] C. Huang, X. Qian, R. Yang, *Materials Science and Engineering: R: Reports* **2018**, *132*, 1–22.

[11] H. S. Kim, J.-U. Jang, H. Lee, et al., *Advanced Engineering Materials* **2018**, *20*, 1800204.

[12] N. Song, D. Jiao, S. Cui, et al., *ACS Applied Materials & Interfaces* **2017**, *9*, 2924–2932.

[13] Z. Wang, K. Rolle, T. Schilling, et al., *Angewandte Chemie International Edition* **2019**, *59*, 1286–1294.

[14] X. Xie, D. Li, T.-H. Tsai, et al., *Macromolecules* **2016**, *49*, 972–978.

[15] A. Shanker, C. Li, G.-H. Kim, et al., *Science Advances* **2017**, *3*, e1700342.

[16] G.-H. Kim, D. Lee, A. Shanker, et al., *Nature Materials* **2014**, *14*, 295–300.

[17] C. Rössel, M. Billing, H. Görls, et al., *Polymer* **2017**, *127*, 182–191.

[18] U. Günther, L. V. Sigolaeva, D. V. Pergushov, F. H. Schacher, *Macromolecular Chemistry and Physics* **2013**, *214*, 2202–2212.

[19] M. von der Lühe, A. Weidner, S. Dutz, F. H. Schacher, *ACS Applied Nano Materials* **2017**, *1*, 232–244.

[20] L. Volkmann, M. Köhler, F. H. Sobotta, et al., *Macromolecules* **2018**, *51*, 7284–7294.

[21] R. T. A. Mayadunne, E. Rizzardo, J. Chiefari, et al., *Macromolecules* **2000**, *33*, 243–245.

[22] P. W. Winston, D. H. Bates, *Ecology* **1960**, *41*, 232–237.

[23] H. P. Hu, X. W. Wang, X. F. Xu, *Journal of Applied Physics* **1999**, *86*, 3953–3958.

[24] X. Wang, H. Hu, X. Xu, *Journal of Heat Transfer* **2001**, *123*, 138–144.

[25] Y. Park, S. Lee, S. S. Ha, et al., *Polymers* **2019**, *11*, 858.

[26] J. K. Kauppinen, D. J. Moffatt, H. H. Mantsch, D. G. Cameron, *Applied Spectroscopy* **1981**, *35*, 271–276.

[27] X. Hu, D. Kaplan, P. Cebe, *Macromolecules* **2006**, *39*, 6161–6170.

[28] J. Dong, Y. Ozaki, K. Nakashima, *Macromolecules* **1997**, *30*, 1111–1117.

[29] M. M. Coleman, M. Sobkowiak, G. J. Pehlert, P. C. Painter, T. Iqbal, *Macromolecular Chemistry and Physics* **1997**, *198*, 117–136.

[30] D. J. Skrovanek, S. E. Howe, P. C. Painter, M. M. Coleman, *Macromolecules* **1985**, *18*, 1676–1683.

[31] D. J. Skrovanek, P. C. Painter, M. M. Coleman, *Macromolecules* **1986**, *19*, 699–705.

[32] Z. Shen, F. Luo, H. Bai, et al., *RSC Advances* **2016**, *6*, 17510–17518.

[33] X. Xie, K. Yang, D. Li, et al., *Physical Review B* **2017**, *95*, 035406.

[34] L. Daniliuc, C. David, *Polymer* **1996**, *37*, 5219–5227.

[35] M. Wieland, C. Dingler, R. Merkle, J. Maier, S. Ludwigs, *ACS Applied Materials & Interfaces* **2020**, *12*, 6742–6751.

[36] S. Popineau, C. Rondeau-Mouro, C. Sulpice-Gaillet, M. E. Shanahan, *Polymer* **2005**, *46*, 10733–10740.

[37] K. Ichikawa, T. Mori, H. Kitano, et al., *Journal of Polymer Science Part B: Polymer Physics* **2001**, *39*, 2175–2182.

[38] N. Mehra, L. Mu, T. Ji, Y. Li, J. Zhu, *Composites Science and Technology* **2017**, *151*, 115–123.

[39] J. K. Carson, S. J. Lovatt, D. J. Tanner, A. C. Cleland, *International Journal of Heat and Mass Transfer* **2005**, *48*, 2150–2158.

[40] A. Arslan, S. Kıralp, L. Toppare, A. Bozkurt, *Langmuir* **2006**, *22*, 2912–2915.

8

Nanoscale-Structured Hybrid Bragg Stacks with Orientation- and Composition-Dependent Mechanical and Thermal Transport Properties: Implications for Nacre Mimetics and Heat Management Applications

Theresa Dörres,* Malgorzata Bartkiewicz,§ Kai Herrmann,* Marius Schöttle,* Daniel Wagner,* Zuyuan Wang,† Olli Ikkala,‡ Markus Retsch,* George Fytas,§ and Josef Breu*

* Bavarian Polymer Institute and Department of Chemistry, University of Bayreuth, Universitätsstraße 30, 95447 Bayreuth, Germany.

§ Max Planck Institute for Polymer Research, Ackermannweg 10, 55128 Mainz, Germany.

† School of Mechanical and Electrical Engineering, University of Electronic Science and Technology of China, Chengdu, Sichuan 611731, China.

‡ Department of Applied Physics, Aalto University, Finland.

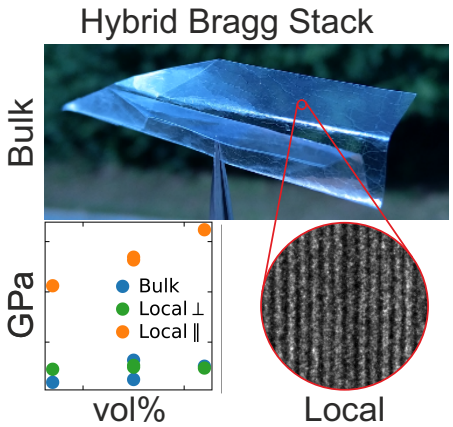

Published in *ACS Applied Nano Materials*, **2022**, *5*, 4119–4129.

8.1 Abstract

Layered nanomaterials fascinate researchers for their mechanical, barrier, optical, and transport properties. Nacre is a biological example thereof, combining excellent mechanical properties by aligned submicron inorganic platelets and nanoscale proteinic interlayers. Mimicking nacre with advanced nanosheets requires ultra-confined organic layers when aiming at nacre-like high reinforcement fractions. We describe inorganic/polymer hybrid Bragg stacks with one or two fluorohectorite clay layers alternating with one or two poly(ethylene glycol) layers. As indicated by XRD, perfect 1D-crystallinity allows for homogeneous single-phase materials with up to 84% clay volume fraction. Brillouin light spectroscopy allows to explore the ultimate mechanical moduli without disturbance by flaws, suggesting an unprecedentedly high Young's modulus of 162 GPa along the aligned clays, indicating almost ideal reinforcement under these conditions. Importantly, low heat conductivity is observed across films $\kappa_\perp = 0.11 - 0.15$ W m^{-1} K^{-1} with a high anisotropy of $\kappa_\parallel/\kappa_\perp = 28 - 33$. The macroscopic mechanical properties show ductile-to-brittle change upon increasing the clay volume fraction from 54% to 70%. Conceptually, this work reveals the ultimate elastic and thermal properties of aligned layered clay nanocomposites in flaw-tolerant conditions.

8.2 Introduction

Biological composites attract growing interest as they are concomitantly strong, tough, and have a low density.[1–3] While strong materials resist plastic deformations, tough materials are resistant to catastrophic fracture. A classic strong and tough biological composite is pearl of nacre, which consists of a high volume fraction (95 vol%) of aligned reinforcing inorganic aragonite platelets (Young's modulus $E = 70$ GPa, thickness $200 - 900$ nm, and lateral sizes $5 - 8$ μm) and a soft biopolymer layer (thickness $10 - 50$ nm), which are hierarchically arranged in a so-called "brick-and-mortar" structure.[2,4,5] In spite of extensive research, the reasons for the extraordinary mechanical properties are not fully understood due to the complex combination of several mechanisms, hampering rational designs of advanced bioinspired materials. Grossly oversimplified, it has been postulated that the ceramic component provides reinforcement, whereas the biopolymer enables distribution of localized stresses and provides fracture energy dissipation. But the actual behaviour is much more complex also involving mineral bridges between the reinforcements.[5] What is significant in nacre is the considerable thickness of *ca.* $10 - 50$ nm of the macromolecular layers, which in turn requires a large thickness of the reinforcing platelets, while assuring the high volume fraction of the reinforcements. It has been conceived that, in this way, the dynamic polymer chains can promote the fracture

energy dissipative transformations. Two opposite approaches can be considered for nacre-mimetic designs: 1) If thick submicron inorganic layers are really needed to concomitantly allow for high filler content while keeping the thick polymer layers, they have to be biomineralised in-situ, otherwise excessive packing defects remain. A high volume fraction cannot be achieved using prefabricated, thick, solid, inorganic sheets. 2) By contrast, if nanometric sheets which are strong in tension but flexible in bending are used, their packing defects can be largely relieved but high reinforcement volume fraction cannot be easily achieved unless the polymer layers are ultrathin. Both approaches have been adopted towards nacre-inspired materials, ranging from in-situ mineralization to use of various nanosheets.[6–20] The latter approach has been widely exploited as they may allow stronger reinforcements than using the relatively brittle ceramics. Nanosheets can also serve other functions, such as improving gas barrier properties[21–24] or incorporating electrical conductivity by using, for example, mXene.[25]

Although approaches have been provided to allow high ultimate strength in nacre-mimetic materials[20] and some approaches have shown even nacre-like toughness in notched fracture mechanical studies,[18,26,27] the composite elastic moduli have typically remained much smaller than expected from the constituents. For example, the nacre-mimetic materials based on clay typically show E modulus values of some tens of GPa, while pure clay nanosheets show E values of $146 - 171$ GPa.[28,29] Even complex combinations of graphene modifications, clay, and carbon nanotubes show only a modest E modulus value of 130 GPa,[20] signifying a fundamental problem of transferring the reinforcement elastic properties to the composite system. There remains a question as to whether the low modulus value is due to insufficient stress transfer across the interfaces or due to defects. A second question relates to using nanometric 2D nanosheets, of which several types have been used, such as clays, graphene and its modifications, mXenes, and titanates: Could a high volume fraction of the reinforcements still be achieved in cases that use an organic "matrix"? And what are the mechanical properties, in particular the elastic moduli, of the composite systems, considering the ultra-confinement of the polymer layers? Thirdly, if such properties are achieved, does the presence of elastic anisotropy indicate the presence of thermal anisotropy? Finally, how much does a defect tolerance affect the macroscopic mechanical properties?

Herein we address these questions by constructing one-dimensional (1D) crystalline arrangements ("hybrid Bragg stacks") of nanosheets and polymer layers with a superior translational periodicity. We use synthetic sodium fluorohectorite ($[Na_{0.5}]^{inter}$ $[Mg_{2.5}Li_{0.5}]^{oct}$ $[Si_4]^{tet}$ $O_{10}F_2$), which delaminates based on the rare phenomenon of repulsive osmotic swelling, yielding an unprecedented thickness homogeneity and complete separation.[30,31] This contrasts the standard liquid phase exfoliation of classically used natural clays, such as montmorillonite, which only provides a broad distribution of thicknesses and poorly defined materials. Importantly, the osmotic swelling produces a nematic liquid crystalline phase that can be

homogenously mixed with a polymer.

Regarding the selection of the polymer, so far only two polymers, polyvinylpyrrolidone (PVP)[21,32,33] and poly(ethylene glycol) (PEG),[34–36] have been discovered to allow for the formation of single-phase hybrid Bragg stacks with a discrete composition. This is contrasted by polyvinyl alcohol,[16,18,22] ethoxylated polyethyleneimine/poly(acrylic acid),[23] or sodium carboxymethyl cellulose,[37] which undergo (partial) phase separation due to insufficient interaction of the polymer with the clay surface or the interlayer cation.

The osmotic swelling of fluorohectorite leads to single (Hec) or double nanosheets (DS), allowing for controlled fabrication of nanosheets that are either 1 or 2 nm thick.[38] Dispersions with appropriately adjusted volume fractions of fluorohectorite and PEG can be spray-coated to generate hybrid Bragg stacks. Thereby, PEG can be intercalated as single or stacked macromolecule between these two filler morphologies, resulting in four types of 1D crystalline, transparent hybrid Bragg stack monodomain films (i.e., Hec/2PEG, Hec/1PEG, DS/2PEG, DS/1PEG) with the filler content spanning from 54 vol% to 82 vol% in discrete, material-inherent ("quantized") compositions. This allows for the first time to combine a superior periodicity with four distinct filler contents. In combination with its large-scale homogeneity and transparency it allows for an unprecedented mechanical and thermal analysis. As a non-contact and non-destructive technique for measuring the elastic moduli at zero strain and a submicron resolution, Brillouin light spectroscopy (BLS) provides a unique access to the full elastic tensor of anisotropic materials.[32,39] The present single phase, transparent, and to some degree tunable periodic structures enable rich information to be extracted from the BLS spectra. These requirements, however, are not satisfied by the classic montmorillonite-filled clay-based nacre-mimetics. Insights from BLS can be complemented by thermal transport properties that in view of the nanometer spacing correlate with the speed of sound from the BLS experiments and also probe the fundamental properties and anisotropy of the hybrid Bragg stacks.

8.3 Results

8.3.1 Fabrication of 1D Crystalline, Quantized Hybrid Bragg Stacks

Among the 2D materials, only a handful compounds are known to show repulsive osmotic swelling[40] to allow for a gentle delamination into nanosheets of uniform thickness while preserving the equivalent diameter of the pristine crystals. Synthetic sodium fluorohectorite ($[Na_{0.5}]^{inter}$ $[Mg_{2.5}Li_{0.5}]^{oct}$ $[Si_4]^{tet}$ $O_{10}F_2$), obtained by melt synthesis,[41] followed by long-term annealing,[38] shows such a rare phenomenon. Additionally, it possesses phase purity, homogeneous charge density, and thus uni-

form intracrystalline reactivity. Due to its exceptional charge homogeneity, the as-synthesized fluorohectorite can be transformed into an ordered interstratification by partial ion exchange with NH_4^+. Na^+ and NH_4^+ ions segregate to different interlayers, and the two types of inter¬layers strictly alternate in this ordered heterostructure that represents a thermodynamically stable state. Due to the lower hydration enthalpy of NH_4^+, hydration in this interlayer type is completely blocked. When the pristine fluorohectorite is immersed into deionized water, individual 1-nm thick nanosheets are obtained.[38] This suspension is not isotropic but represents a nematic phase, where the nanosheets are held in a cofacial arrangement due to their electrostatic repulsion. When the heterostructure (selective Na^+ exchange to NH_4^+ in every other interlayer) is immersed into water, every other interlayer type is blocked from osmotic swelling and it, consequently, spontaneously delaminates into 2-nm-thick nanosheets (DS),[29] where two hectorite layers are connected via a non-swelling interlayer of NH_4^+ ions. To obtain the most frequently used montmorillonite platelet diameter (typically less than 300 nm), ultra-sonication is applied to reduce the equivalent diameter of Hec and DS to 340 nm and 406 nm, respectively (Figure 8.6, Supporting Information). In nacre, the macromolecules in the organic layers are particularly soft;5 therefore PEG with a low glass transition temperature ($T_g = -20$ °C) was selected. Being water-soluble and non-ionic, it does not interfere with the electrostatic stabilization of the nematic suspensions. Moreover, PEG is known to form complexes with Na^+[42] and, consequently, intercalated phases with two different PEG volumes may be obtained,[36] since phase separation is counterpoised by the interaction with the interlayer cation.

Independent of the nanosheet lateral sizes and thickness, dilute (< 1 vol%) suspensions represent nematic phases in water with nanosheets being separated by large distances (> 50 nm).[31] Therefore, solution compounding could be achieved simply by mixing the nematic suspensions with different amounts of an aqueous PEG solution, which preserves the nematic character of the suspension, as evidenced by small angle X-ray scattering (SAXS) (Figure 8.7, Supporting Information). Spray coating onto polyethylene terephthalate foils followed by gentle drying produced transparent hybrid films (Figure 8.1). The nanosheets align parallel to the substrate due to their large aspect ratio and form a monocrystalline film with the stacking direction oriented perpendicular to the foil. Transmission electron microscopy (TEM) images corroborate the nice periodic homogeneity of the sample films. Such films are self-supporting and can be easily peeled off from the substrate. A comparison of the characteristic length scale to illustrate the difference between the hybrid Bragg stacks produced here and typical nacre is shown in Figure 8.1b and c.

Previous studies have reported intercalated phases of layered silicates with PEG volume contents of 46 vol%[34–36,44,45] and 30 vol%[36] corresponding to periodicities of 1.8 nm and 1.4 nm, respectively. The present observed periodicities (1.77 nm and 1.38 nm for Hec/2PEG and Hec/1PEG, respectively, Figure 8.2 bottom) agree well with the published values. The PEG volume contents were iteratively optimized to

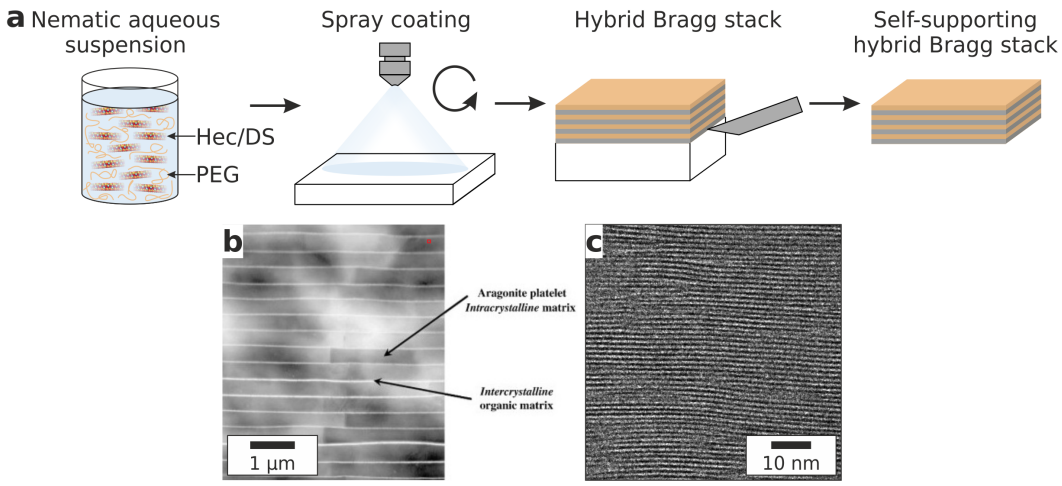

Figure 8.1: (a) Preparation of the self-supporting hybrid Bragg stacks. Nematic aqueous suspensions are repeatedly spray-coated and can be peeled off for achieving self-supporting films. (b) Typical TEM view of the microarchitecture of sheet nacre.[43] The red square corresponds to the dimension of Subfigure (c). (c) Comparison to the TEM view of an exemplary hybrid Bragg stack highlighting the vastly different length scales. Subfigure (b) Reprinted from Materials Science and Engineering C, Volume 30 Issue 5, Stempflé, P.; Pantalé, O.; Rousseau, M.; Lopez, E.; Bourrat, X., 'Mechanical properties of the elemental nanocomponents of nacre structure', Page 715, Copyright (2010), with permission from Elsevier.

yield these superior periodicities. According to Meuring's rule,[46] the quality of the 1D crystallinity is exhibited by a small FWHM. Our samples with optimized PEG contents feature intense basal reflections of a rational 00l series up to the 5th and 4th order and a very low coefficient of variation (CV) of the 00l series (0.3 to 0.6% for Hec/2PEG and Hec/1PEG, respectively) (Figure 8.2 bottom, Table Figure 8.3, Supporting Information). As expected, the FWHM minima (Figure 8.8, Supporting Information) at 54 vol% (Hec/2PEG) and 70 vol% (Hec/1PEG) of Hec coincide with the coefficient of variation (CV) minima (Figure 8.8, Supporting Information). Such low CVs imply extraordinarily uniform interlayer heights, which usually require ionic or molecular interlayer cations of the same type and well-defined size and shape. Observing such a low CV for a hybrid Bragg stack with intercalated macromolecules is quite surprising, because even low-molecular-weight polymers are intrinsically polydisperse and thus are expected to adopt different conformations.

Similar to the Hec-based films, the periodicity and filler content of the films could be varied systematically at discrete steps by applying the DS filler without compromising the homogeneity or quality of the 1D crystallinity. As described for Hec/2PEG and Hec/1PEG, the PEG content was carefully optimized, and the optimum 1D crystallinity was observed for 70 vol% and 82 vol% of DS fillers with CV values of 1.6 and 1.0 for DS/2PEG and DS/1PEG, respectively (Figure 8.2, bottom). The DS/1PEG hybrid exhibits a record filler content of 82 vol%. As expected, the *d*-spacings increase by 1 nm when going from Hec to DS for DS/2PEG and DS/1PEG (2.79 and 2.38 nm, respectively), corresponding to the thickness

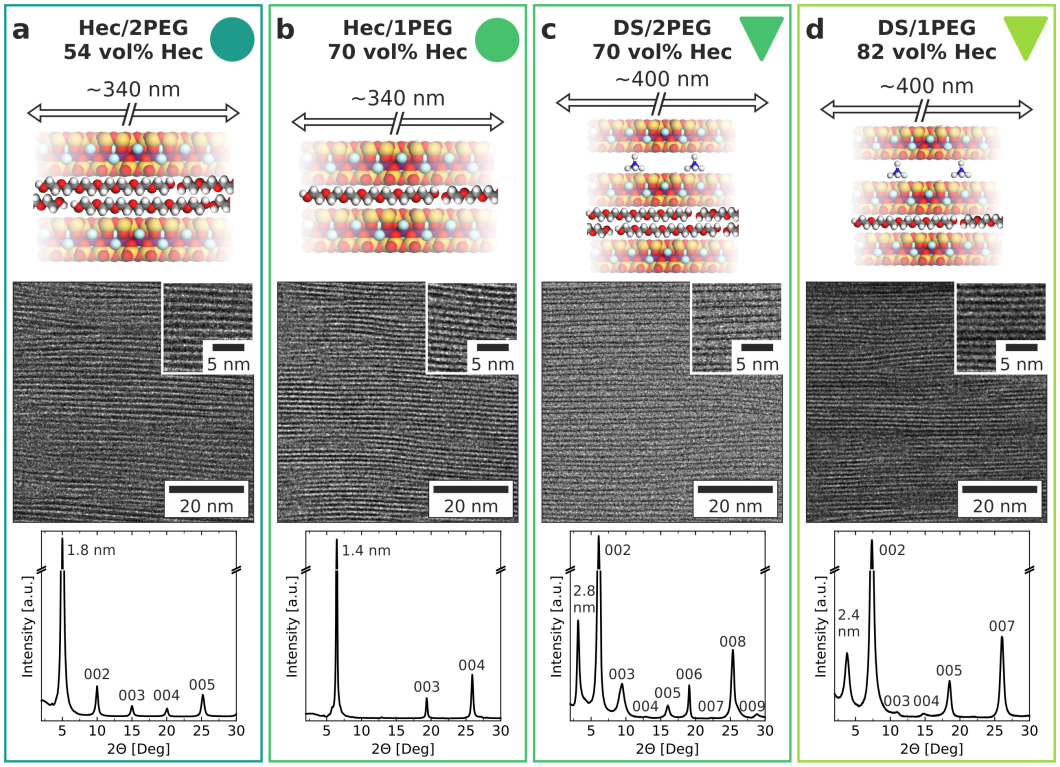

Figure 8.2: Hybrid clay nacre-mimetics with quantized composition. Schematic structures of the hybrid Bragg stacks (top). TEM images (middle) of Ar-milled slices confirming the superior order and long-range periodicity. The dark lines are single Hec sheets. The XRD patterns confirm the nearly perfect 1D crystallinity, as indicated by the intense basal reflections, rational 00l-series, and long-range periodicity. Increasing volume fraction of clay from left to right with (a) hectorite with stacked PEG, (b) hectorite with single PEG, (c) double nanosheets with stacked PEG, and (d) double nanosheets with single PEG.

of a hectorite nanosheet as NH_4^+ fits into the surface corrugations and does not require additional space. The quality of the 1D crystallinity of the DS Bragg stacks is comparable to the Hec Bragg stacks as indicated by the intense reflections, and a rational 00l-series visible up to the 9th and 7th order for DS/2PEG and DS/1PEG, respectively (Figure 8.2, bottom). Moreover, the TEM images of both DS hybrids also showed an exceptional long-range order (Figure 8.2, middle). The compositions of Hec/1PEG and DS/2PEG differ only by the additional NH_4^+-interlayer in the latter which shows up by slight variations in the wt% content (Figure 8.9, Supporting Information) while the volume content is the same within experimental errors (Table 8.3, Supporting Information). As shown by the XRD patterns and TEM images, the periodicity of DS/2PEG is doubled, and thus the interface density between PEG and the clay is halved. We use these four distinct, transparent samples with an ultimate structural control, maximum filler content, and polymer confinement to test the intrinsic, direction-dependent thermal and mechanical properties. We include in our analysis an alternative polymer, PVP, which is also capable of forming distinct, crystalline hybrid Bragg stacks with 31 vol% and 40 vol% of Hec, respectively.[32]

8.3.2 Anisotropic Elastic Moduli

BLS has important advantages compared to macroscopic mechanical experiments; (i) the measurement of the elastic moduli under zero-strain, utilizing the thermal phonons in the materials, (ii) the determination of the elastic tensor components, probing direction-dependent phonon propagation in anisotropic materials, and (iii) the insensitivity to material defects due to the submicron resolution of the BLS technique ensures the determination of the ultimate material elasticity, which should be the ultimate goal of defect engineering. BLS results from the inelastic scattering of light by the longitudinal and transverse phonons propagating in the medium with a wave vector q. The magnitude, q, depends on the incident laser wavelength, $\lambda = 532$ nm, the scattering angle, θ, and the material refractive index n (Section 3, Supporting Information). Hence, the probed phonon wavelength varies in the range of about $200 - 2000$ nm.

For elastically isotropic media, the BLS spectrum is Doppler shifted at $f = \pm cq/2\pi$ around the central Rayleigh line with c being the longitudinal (c_{L}) or transverse (c_{T}) sound velocity that determine the corresponding longitudinal, $M = \rho c_{\mathrm{L}}^2$, shear, $G = \rho c_{\mathrm{T}}^2$, and Young's, $E = 2G(1 + v)$ moduli, with ρ being the density and $v = (c_{\mathrm{L}}^2/c_{\mathrm{T}}^2 - 2)/(2c_{\mathrm{L}}^2/c_{\mathrm{T}}^2 - 2)$ the Poisson's ratio. Due to the high frequencies of the probed phonons, for all materials at temperatures in the range of $T_{\mathrm{g}} < T < T_{\mathrm{g}}+100$, where T_{g} is the glass transition temperature, the moduli are truly elastic (i.e., frequency independent).[47]

For elastically anisotropic materials like the hybrid Bragg stacks in this work, the determination of the stiffness constants of the elastic tensor requires access to the direction-dependent polarized and depolarized BLS spectra. The methodology has recently been reported for several hard and soft materials (Section 4, Supporting Information).[47–49] However, for an unambiguous determination of the elastic constants, the full utilization of the BLS geometries and polarizations is needed. We performed measurements at three different scattering geometries - transmission, reflection, and backscattering - to probe phonon propagation along directions parallel, normal, and oblique to the present Hec/PEG films, respectively (Insets to Figure 8.8a-c, Section 3, Supporting Information). The polarization of the incident and scattered light was selected to be either vertical (V) or horizontal (H). Different polarization configurations (e.g., VV, VH) allow for selective examination of the existing modes (Section 4, Supporting Information).

Figure 8.3a shows exemplary VV and VH (left inset) BLS spectra recorded in the transmission geometry (right inset) at different laser incident angles, β. In the case of the VV and VH transmission geometry, the spectra should respectively display the in-plane $L_{\parallel}$ and $T_{\parallel}$ modes. However, we also observe additional modes (i.e., quasi-longitudinal Q-L and quasi-transverse Q-T) from back scattering contributions due to the internal reflection of the laser beam on the sample's backside (right inset

to Figure 8.8a).[32,50,51] Figure 8.8b displays VV and VH (left inset) BLS spectra recorded at the reflection geometry (right inset) at different β angles. There is only a single out-of-plane longitudinal mode ($L_\perp$) and a single out-of-plane transverse mode ($T_\perp$) present in the VV and VH spectra, respectively. Note that the latter VH spectrum is much weaker than the corresponding in-plane mode (inset to Figure 8.3a). Figure 8.3c presents typical VV and HV (left inset) BLS spectra obtained at the backscattering geometry (right inset) at different β angles. The two peaks in VV spectrum are assigned to Q-T and Q-L modes, whereas the HV spectrum displays an anticipated P-T mode. The second Q-L is due to the polarization scrambling (VV). Figure 8.3a-c refers to the Hec/1PEG sample, while the spectra for the other samples are shown in Figure 8.10, Supporting Information. It is noteworthy that the three different scattering geometries and different polarization configurations allow for the complete characterization of the transversely anisotropic material.

After representation of the spectral peaks by Lorentzian lines (solid lines in Figure 8.3a-c) to yield the frequencies of the observed modes, we computed the direction-dependent sound velocities, $c = 2\pi f/q$ (Section 3, Supporting Information). We started from the transmission geometry, for which the magnitude of $q_\parallel$ is independent of the refractive index n. The dispersion relation $f(q_\parallel)$ for both $L_\parallel$ and $T_\parallel$ is linear (Figure 8.11, Supporting Information) and hence, $c(\alpha = 90°)$ for both phonons is q-independent (Section 3, Supporting Information, for details). To determine $q_\perp$ at the reflection geometry and qbs at the backscattering geometry, the refractive index of the sample has to be known. We have thus recorded the dispersion $f(q_\perp)$, which was forced to be linear through the origin (Figure 8.11, Supporting Information), to determine the value of n. In this way, we obtained the sound velocities $c(\alpha = 0°)$ for both out-of-plane modes ($L_\perp$ and $T_\perp$). For the oblique q directions in the backscattering measurements (Figure 8.3c) of a transversely isotropic material, we took into account only those q vectors that lie in one plane containing the axis of symmetry. The direction is then defined by the angle α between q and the normal to the sample film, in the range of $0° - 90°$; this angle, inside the film (Inset to Figure 8.3a), cannot exceed beyond 50° (Figure 8.3d) due to the material refractive index (Snell' law).

For a transversely isotropic material, the elastic stiffness tensor contains 5 independent elastic constants, which we determined through ξ^2 fitting (Section 4, Supporting Information). Due to the relationship between the elasticity tensor components and the sound velocities (Equations 1-8, Supporting Information), a theoretical framework of the direction-dependent sound velocities was obtained. The sound velocities of the Q-L, Q-T, and P-T modes are shown in Figure 8.3d as a function of the angle α in the case of the Hec/1PEG sample along with their theoretical representations (solid lines). Similar results were obtained for the other samples, as shown in Figure 8.12, Supporting Information. The reflection and transmission measurements yield $c(Q-L)$ and $c(Q-T)$ at $\alpha = 0°$, and $c(Q-L)$ and $c(P-T)$ at $\alpha = 90°$, respectively. Note that the backscattering measurements address all

three modes (Q-L, Q-T, and P-T) at intermediate α angles, which are limited below about 50° by the sample's refractive index.

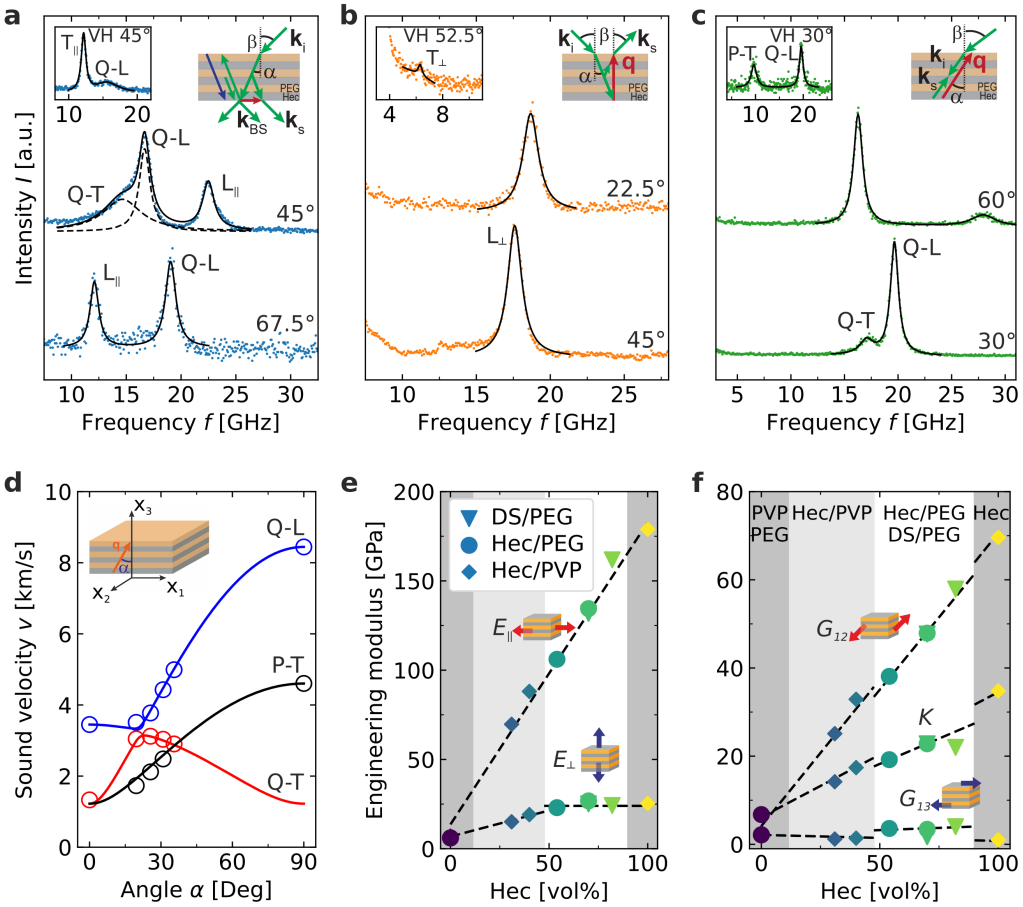

Figure 8.3: Orientation dependent elasticity. BLS spectra of the Hec/1PEG sample (with the Lorentzian fits as black lines) recorded at (a) transmission, (b) reflection, and (c) backscattering geometries in polarized (main panels) and depolarized (left insets) configurations. The solid lines denote the sum of the individual Lorentzians (dotted lines). The right insets in (a) (b) and (c) show schematics of the transmission, reflection, and backscattering geometries, respectively, where β denotes the incident angle of the laser beam, α is the directional angle between q, labeled by red arrows, and the normal to the sample film. k_i, k_s and k_{BS} are the wave vectors of the incident, scattered, and backscattered light inside the sample, respectively. The blue arrow in the right inset to (a) indicates the wave vector in the artificial backscattering geometry. The assignment of the peaks in the spectra is explained in the text. (d) Direction-dependent sound velocities of the observed acoustic phonons in the BLS spectra (circles) and from theoretical representation (solid lines) of Hec/1PEG. (e), (f) Composition dependence of the engineering moduli of the hybrid samples (Hec/PEG - circles, DS/PEG - triangles) and the pure PEG sample (circles at 0% of Hec content). (e) and (f) also contain the results for the Hec/PVP system (diamonds).[32] The included data for this system correspond to PVP (0%), double layer of PVP (31 vol% Hec), single layer of PVP (40 vol% Hec), and pure Hec (100%). The schematics in (e) and (f) visualize the physical meanings of the corresponding moduli.

Table 8.1: Engineering mechanical moduli of the hybrid Bragg stack films based on BLS analysis: $E_{\parallel}$: in-plane Young's modulus; $E_{\perp}$: cross-plane Young's modulus; G_{13}, G_{23}: sliding shear moduli; G_{12}: torsional shear modulus; v_{31}, v_{32}, v_{12}: Poisson's ratios (v_{ij} represents the strain response in the j-direction due to a strain in the i-direction); K: bulk (compression) modulus.

Sample	Hec (vol%)	$E_{\parallel}$ (GPa)	$E_{\perp}$ (GPa)	$E_{\parallel}/E_{\perp}$	G_{13} (GPa)	G_{12} (GPa)	v_{31}	v_{12}	K (GPa)
Hec/2PEG	54	106.1 ±2.7	23.0 ±0.5	4.6 ±0.3	3.6 ±0.5	38.1 ±1.5	0.02 ±0.01	0.39 ±0.03	19.2 ±0.7
Hec/1PEG	70	134.5 ±2.3	26.8 ±0.5	5.0 ±0.2	3.4 ±0.1	47.9 ±1.2	0.01 ±0.01	0.40 ±0.02	22.6 ±0.8
DS/2PEG	70	132.0 ±3.0	25.2 ±0.5	5.2 ±0.2	1.6 ±0.6	47.7 ±1.6	0.03 ±0.01	0.38 ±0.02	22.7 ±0.7
DS/1PEG	82	161.8 ±3.3	24.2 ±0.6	6.7 ±0.6	4.0 ±0.2	57.9 ±1.8	0.02 ±0.01	0.40 ±0.02	22.0 ±0.8

The theoretical representation of the sound velocities also allowed for the designation of the engineering moduli (Figure 8.3e,f). These are the in-plane Young's modulus ($E_{\parallel}$), cross-plane Young's modulus ($E_{\perp}$), sliding shear modulus (G_{13}), torsional shear modulus (G_{12}), bulk modulus (K), and two characteristic Poisson's ratios (v_{31} and v_{12}, not shown in Figure 8.3).[52] For simplicity, we denote the in-plane Young's modulus as $E_{\parallel}$ (and not as E_{11} or E_{22}), and the out-of-plane Young's modulus as $E_{\perp}$ (and not E_{33}). The exact values of elastic stiffness constants and engineering moduli are summarized in Table 8.5), Supporting Information and Table 8.1 below, respectively. The results are based on fitting with two free parameters. The uncertainties are computed according to the principles of uncertainty propagation. Depending on the direction, a systematic variation of the elastic moduli with composition is displayed in Figure 8.3e and Figure 8.2f. We can use this composition variation for a better understanding of the actual contribution of the hybrid structure to the mechanical properties. For the 1D hybrid lattice, different composition dependencies were proposed for the in-plane and cross-plane effective moduli.[53] For the in-plane moduli, it is a linear interpolation of the volume-weighted elastic properties of the individual layers, as also implied by the experimental $E_{\parallel}$ in Figure 8.3e. $E_{\parallel}(\phi\ \text{Hec})$ is well represented by a linear regression using $E_{\parallel,\text{Hec}} = 179$ GPa and $E_{\text{PEG}} = 6.1$ GPa, suggesting a weak impact of the predominantly parallel Hec/PEG interfaces; $E_{\text{PEG}} = 6.1$ GPa is a meaningful value for glassy or crystalline polymers in a stretched conformation. The large elasticity mismatch between the Hec and soft polymer layers obscures any conclusion on the polymer specificity (PVP vs. PEG) on $E_{\parallel}$. Furthermore, the conformity of $E_{\parallel}$ to the predictive mixing rule suggests that $E_{\parallel}$ is an inherent material property which should monotonically depend on the filling ratio.

Along the 1D periodicity direction, the phonon dispersion relation at long wavelength predicts the Wood's law for the composition dependence of the cross-plane modulus $E_{\perp}$.[53,54] However, as previously reported for Hec/PVP Bragg stacks,[32] Figure 8.3e

implies failure of this law for $E\perp$, as the predicted dependence is of a concave form (Figure 8.13, Supporting Information) in contrast to the experimental convex form. For the high filling fractions ($> 50\%$), we find a plateau region with $E_\perp$ comparable to that at 100% Hec. The very high filler contents applied here cause a severe confinement of the thin polymer layers. As a consequence, the polymer interlayers fail to efficiently decouple adjacent nanosheets in the stack, which would be required for energy dissipation.

Down to a content of approximately 50 vol% Hec, $E_\perp$ is unaffected by the presence of confined polymer, whereas at < 50 vol% Hec, the increasing volume fraction of PVP does lead to a decreasing $E_\perp$ but stronger than the Wood's law prediction (Figure 8.13, Supporting Information). The clearly different composition dependence of $E_\perp$ and $E_\parallel$ emphasizes the role of the interface density solely for the cross-plane elasticity (above approximately 50 vol% Hec). Due to this difference, the elasticity anisotropy, $E_\parallel/E\perp$, increases with the Hec content from 4.6 at 54 vol% Hec to 6.7 at 82 vol% Hec (Table 8.1. This extraordinary anisotropy is induced by the structure and depends on the large elastic mismatch of the components. Moreover, it is rather polymer unspecific, as becomes obvious when comparing PVP and PEG samples.

Analogous to $E_\parallel$, the in-plane torsional shear modulus, G_{12}, lies between the values of the two bulk components and displays an effective medium behavior (Figure 8.3e,f). Consistently, the in-plane moduli show no difference for DS and Hec samples. Both moduli (i.e., $E_\parallel$ and G_{12}) increase by about 50%, as the Hec content increases from 54 vol% to 82 vol%. The bulk modulus K increases only by about 15% and is comparable to $E_\perp$ with a similar saturation above approximately 60 vol% Hec, as both are primarily controlled by the elastic constant C_{33}. Consistently, the cross-plane moduli, $E_\perp$ and G_{13}, are hardly influenced by the composition (Figure 8.3e,f). The sliding shear modulus, G_{13}, remains low but is higher (by almost two times) for Hec/PEG than Hec/PVP hybrid Bragg stacks. This is the only indication of a polymer specificity that we see in the two investigated systems. We attribute this to the more compact PEG intercalation between the Hec sheets with less free volume. The Poisson's ratio (Table 1) v_{12} represents how the sample shrinks in the "2" direction due to an applied stretching strain in the "1" direction. Note that the "1-2" plane means the sample plane, and hence the high v_{12} value is polymer-like. The second Poisson's ratio v_{31} expresses how the sample expands in the "1" direction due to an applied compressing strain in the "3" direction. Hence, the almost zero value of v_{31} implies negligible deformation of the PEG layer along the "1" direction; we note that wine corks have a Poisson's ratio of nearly zero. Among the different elasticity parameters, G_{13} and v_{12} reflect the properties of the confined polymer.

8.3.3 In-Plane and Cross-Plane Thermal Conductivities

Another approach to characterize the anisotropy of the hybrid Bragg stacks is to measure their thermal transport properties. Therefore, we characterized the in-plane and cross-plane thermal conductivities using lock-in thermography and photoacoustic measurements, respectively.[55–57] Analogous to the BLS characterization, we include the previously reported Hec/PVP system with one (40 vol% Hec) and two (31 vol%) layers of PVP, respectively. The in-plane thermal conductivity $\kappa_{\parallel}$ follows a linear composition dependency. According to the parallel thermal resistance network model, $\kappa_{\parallel} = \kappa_{\mathrm{PEG}} + (\kappa_{\mathrm{Hec(DS)}}) - \kappa_{\mathrm{PEG}})\phi_{\mathrm{Hec(DS)}}$ with $\kappa_{\mathrm{Hec(DS)}}$ and κ_{PEG} being the thermal conductivities of Hec (or DS) and PEG, respectively, and $\phi_{\mathrm{Hec(DS)}}$ the Hec volume fraction (dashed line in Figure 8.4a). This behavior confirms the reported behavior of Hec/PVP hybrid Bragg stacks[32] and the in-plane elastic moduli (Figure 8.3e,f). Apparently, neither the delamination and re-assembly process of Hec/DS, nor the extreme polymer confinement influences the in-plane transport of the two components.

Owing to the large thermal conductivity contrast between the polymers and Hec/DS, we do not see a polymer-specific behavior. The cross-plane thermal conductivity $\kappa_{\perp}$ however, decreases gradually from 0.21 to 0.08 W m^{-1} K^{-1}, as the Hec composition decreases from 100 vol% to 31 vol% (Figure 8.4b), which contrasts with the plateau of $\kappa_{\perp}$ (approximately 0.08 W m^{-1} K^{-1}) in the Hec/PVP system.[32] According to the serial thermal resistance network model, $1/\kappa_{\perp} = (-1/\kappa_{\mathrm{PEG}} + 1/\kappa_{\mathrm{Hec}} + 2R_{\mathrm{Hec/PEG}}/d_{\mathrm{Hec},\perp})\phi_{\mathrm{Hec}} + (1/\kappa_{\mathrm{PEG}})$, with $R_{\mathrm{Hec/PEG}}$ and $d_{\mathrm{Hec},\perp}$ being the thermal resistance per unit area of a Hec/PEG interface and the thickness of one Hec layer, respectively. The increasing $\kappa_{\perp}$ with ϕ_{Hec} then suggests that $(-1/\kappa_{\mathrm{PEG}} + 1/\kappa_{\mathrm{Hec}} + 2R_{\mathrm{Hec/PEG}}/d_{\mathrm{Hec},\perp}) < 0$. Therefore, the cross-plane thermal resistances of the Hec/PEG samples are not dominated by the Hec/PEG interfaces, unlike the situation of the Hec/PVP samples, where the stronger influence of the interfaces leads to a plateau of $\kappa_{\perp}$ in the considered Hec vol% range. The different effects of the Hec/PEG and Hec/PVP interfaces could stem from the different physical states of PEG and PVP, due to the vastly different glass transition temperatures (210 K vs. 445 K) and the stronger complexation between PEG and Na^{+}.[42] Both effects can influence the chain mobility within the confined space and, consequently, lead to a different interfacial adhesion between the Hec/PEG and the Hec/PVP interface, respectively. In the case of PEG, the decrease can be also driven by the introduction of different types of interfaces in the hybrid material. While the samples with 1PEG involves only polymer-hectorite interfaces, for 2PEG an additional polymer-polymer interface is introduced (if a stretched PEG conformation is assumed). One should further note that $\kappa_{\perp}$ is more strongly reduced for DS than for Hec nanosheets. We attribute this to an additional type of interface characteristic for the DS filler, namely, the NH_4^{+} cation interlayer "gluing" two Hec sheets to form a DS.

Table 8.2: Thermal measurement results of the hybrid Bragg stack films.

Sample	Hec (vol%)	ρ ($\frac{g}{cm^3}$)	c_p ($\frac{J}{g \cdot K}$)	$\alpha_\parallel$ ($\frac{mm^2}{s}$)	$\kappa_\parallel$ ($\frac{W}{m \cdot K}$)	$\kappa_\perp$ ($\frac{W}{m \cdot K}$)	$\kappa_\parallel/\kappa_\perp$
Hec/2PEG	54	2.01 ±0.03	1.27 ±0.06	1.358 ±0.021	3.47 ±0.17	0.12 ±0.05	29
Hec/1PEG	70	2.29 ±0.03	1.12 ±0.05	1.636 ±0.031	4.19 ±0.20	0.15 ±0.03	28
DS/2PEG	70	2.01 ±0.06	1.08 ±0.03	1.645 ±0.020	3.58 ±0.15	0.11 ±0.03	33
DS/1PEG	82	2.35 ±0.05	1.04 ±0.03	1.854 ±0.019	4.52 ±0.16	0.15 ±0.03	30

In Figure 8.4c and d we provide correlation plots between the thermal transport and mechanical properties. We should note, however, that thermal conductivity and elastic moduli are not generally directly correlated for all materials, because of their different influencing factors, but many materials of a high thermal conductivity are also accompanied with high elastic moduli. Therefore, it is worth studying the correlation between the thermal conductivity and elastic moduli of the Hec/PEG Bragg stacks. For the in-plane direction we find a direct correlation between $\kappa_\parallel$, $E_\parallel$, and G_{12}, which is emphasized by the black dashed line (Figure 8.4c). We used the thermal conductivity and mechanical moduli of PVP as a reference for the correlation plots of both systems. This is justified since the bulk PVP microstructure is amorphous and, therefore, more similar to the confined case as we would expect for the semicrystalline bulk PEG. This direct correlation demonstrates that the in-plane mechanical moduli and in-plane thermal transport are interrelated with each other.

Even more intriguing is the comparison of the composition sensitivity between the mechanical and thermal properties in the cross-plane direction. Whereas $E_\perp$ remains almost constant for the highly filled Hec/PEG and DS/PEG samples (> 50 vol%), a monotonic decrease with decreasing filler content can be observed in the case of $\kappa_\perp$. This decrease is even more dramatic considering that the $\kappa_\perp$ of the hybrid films is consistently lower than those of the pure components. We can, therefore, conclude that the interface chemistry has a significant contribution to the cross-plane heat transport. As outlined above, the cross-plane thermal transport continuously decreases with the introduction of additional types of interfaces (Hec-PEG, PEG-PEG, Hec-Hec). The cross-plane mechanical moduli ($E_\perp$, G_{13}) are not influenced by these different types of interfaces. This becomes also apparent in the correlation plots (Figure 8.4d), where $E_\perp$ vs. $\kappa_\perp$ exhibits a flat line (black dashed line) for filler contents > 50 vol%. This difference in sensitivity to the presence of the nanostructure and interfaces is further translated into a four- to five-fold increased anisotropy compared to the mechanical anisotropy. The similar composition dependencies of

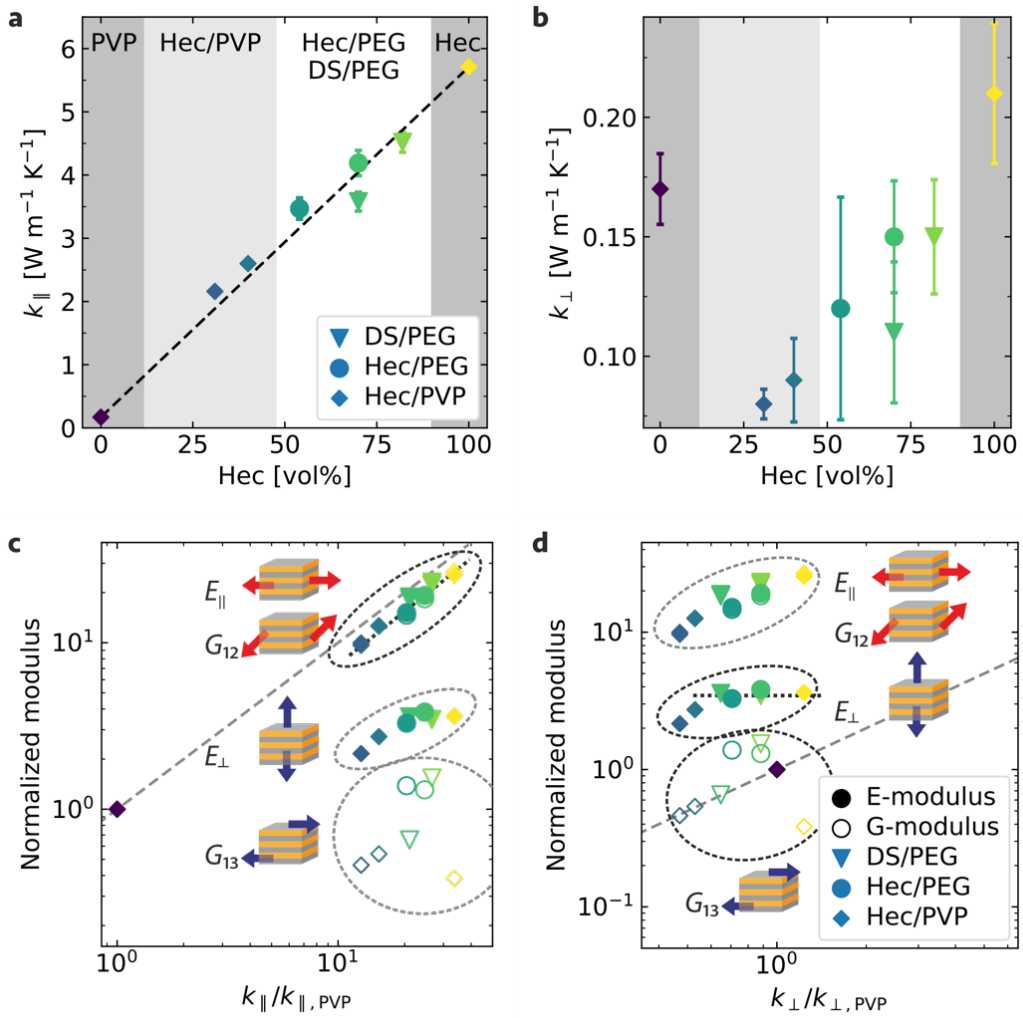

Figure 8.4: Anisotropic thermal transport and correlation to elasticity. Thermal conductivity of crystalline hybrid Bragg stacks in (a) in-plane and (b) cross-plane directions. Analogous Hec/PVP samples are shown as diamonds. Samples consisting of Hec/PEG and DS/PEG are represented by circles and triangles, respectively. Correlation between the relative changes in the mechanical moduli and the corresponding relative changes in the (c) in-plane and (d) cross-plane thermal conductivity. All data are normalized by the respective value of the pure PVP polymer. The symbol colors indicate the volume fraction of Hec.

$\kappa_\perp$ and $\kappa_\parallel$ result in a roughly constant anisotropy ratio ($\kappa_\parallel/\kappa_\perp = 28-33$, Table 8.2) of the hybrid Bragg stack films.

8.3.4 Mechanical Testing

The macroscopic mechanical properties are obtained from the stress-strain curves of the hybrid Bragg stack films measured at 53% relative humidity (RH), as shown in Figure 8.5a. First, Young's modulus E ($10-30$ GPa in Figure 8.5b) and strength σ ($40-200$ MPa in Figure 8.5a and Table 8.4, Supporting Information) are interestingly high, as comparable values in nanocomposites are only achieved with high T_g polymers[16,58] in combination with cross-linking[10,59] or by combining low T_g polymers with hydrogen bonding networks.[24,60] Second, the correlation between E and ε (%) at different Hec or DS contents is not straightforward. In contrast to the other Hec/PEG hybrid materials, Hec/2PEG displays a plastic deformation at $\sigma = 48$ MPa and breaks at a high elongation of 8.4% (inset of Figure 8.5a). This transparent nacre-mimetic Hec/2PEG can be folded like a paper without breaking. Hec/2PEG features the smallest E value, but is still comparable to the Hec/1PEG system that has the smallest elongation at break ($\varepsilon = 0.4\%$). Hec/2PEG, consequently, represents a unique and singular property, which is elusive to a predictive material engineering based on effective material properties. This finding suggests that macroscopic stress-strain measurements alone are inappropriate to guide the structure property optimization of nacre mimetics. Third, E does not follow the expected increasing trend with the filler content. While DS hybrids are indeed stronger than the corresponding single Hec counterparts, DS/1PEG with 82 vol% Hec is weaker than DS/2PEG (70 vol% Hec) (Table 8.4, Supporting Information). The missing correlation of E with the filler content suggests that even in the linear-elastic region at very low strain, non-local contributions, for instance by defects, are significant.

Such defects do not play a role in BLS measurements, unless they feature a length scale of a few 100 nm, which we can rule out based on the structural integrity of our hybrid materials. It is still surprising that the in-plane Young's modulus, $E_\parallel$, from BLS (Figure 8.3e) is about an order of magnitude higher than the value obtained from the tensile test experiment (Figure 8.5b). Both techniques should, in principle, yield the same $E_\parallel$ for glassy, frequency-independent systems. The observed large disparity demonstrates the inapplicability of the stress-strain experiments to accessing the inherent "true" material mechanics. In addition, the weak composition dependence and the large increase of E for the samples with DS fillers in Figure 8.5b corroborate the notion that the macroscopic E cannot be determined from the $E_\parallel$ from the microscopic BLS probe. Albeit E is obtained from unidirectional stretching, it is remarkable that its value is of the same order of magnitude with the cross-plane $E_\perp$ from the BLS experiment and that both also exhibit a similar weak

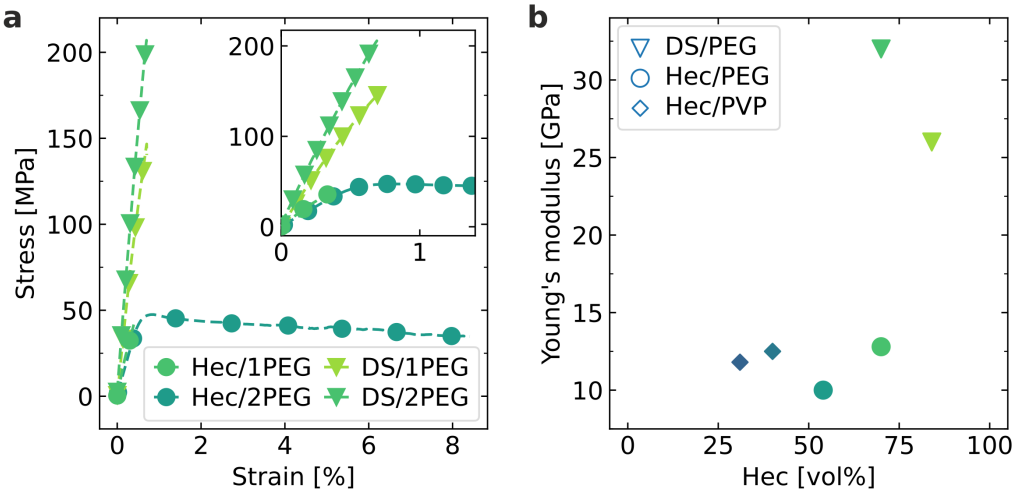

Figure 8.5: Bulk mechanical properties by tensile testing. (a) Stress-strain curves of the hybrid Bragg stack Hec/PEG films indicated in the plot. Influence of the thickness of the filler (Hec vs. DS) and of the polymer layer (1PEG vs. 2PEG). Inset: Zoom-in of the data in the main plot in the low strain range. (b) Young's modulus as a function of the Hec filler content for PEG and PVP hybrids.

composition dependence (Figure 8.5b and Figure 8.3e). In the case of BLS, we do find – depending on the direction – a systematic variation of the elastic moduli. The macroscopic mechanical properties based on stress-strain measurements show considerably lower values, thus emphasizing the role of flaw intolerance. Still, the results indicate a high sensitivity to the exact nanoscale structure; when keeping 2 PEG layers in the interlayer spaces, a brittle to ductile change is observed by replacing DS fillers with Hec fillers. These results demonstrate that the complexity hampers a rational design of the multidimensional property space of hybrid Bragg stacks. Further research is needed to bridge the gap between the inherent "true" hybrid properties on the sub-micrometer scale and those in the macroscopic world.

8.4 Conclusion

This work highlights the rich material parameters and anisotropy property space of seemingly simple 1D hybrid materials consisting of alternating inorganic clay nanosheets and polymer layers. We construct nanoscopically well-defined periodic and anisotropic layered materials and use advanced characterization techniques to assess the ultimate properties of the stacks. We use fluorohectorite clay that uniquely allows osmotic swelling, which is central to well-defined structures allowing discrete "quantized" compositions of one or two clay layers to be combined with one or two layers of PEG polymer. This clay allows for the first time comparatively small volume fractions of polymers within the nanosheets to form uniform single-phase 1D

hybrid Bragg stacks. The anisotropic elastic moduli are characterized using Brillouin light spectroscopy. Notably, the composition consisting of 82 vol% DS fillers and 18 vol% single PEG layers shows a Young's modulus of 161.8 GPa, which suggests almost ideal stress transfer parallel to the clay nanosheets. The corresponding elastic moduli in the transverse direction is 6.7 times smaller, indicating strong mechanical anisotropy. The anisotropy is also manifested in the thermal conductivity, where it is 4.52 W m^{-1} K^{-1} in the direction of the platelets and 30 times less in the transverse direction. The macroscopic mechanical properties based on stress-strain measurements do not reach such high Young's modulus values, possibly due to the presence of defects. High sensitivity to the exact nanoscale structure is also emphasized by comparing the two samples with 2 PEG layers in the interlayer spaces, where a brittle to ductile change is observed by replacing the double layer clays with single layer clays.

The results pave the way to unravel the complexity of designing hybrid stacks. Maximizing the filler content and the interaction of the polymer chains with the ceramic surface tends to result in brittle materials with little flaw tolerance. The challenge to translate the superior nanoscale mechanical properties to the macroscopic behavior seems to be a hierarchical integration of such Bragg stack into optimized matrices with tailored gradient-type interfaces between them. This may eventually lead to combined molecular and nanostructured design approaches that allow for an independent adjustment of the mechanical and thermal properties, and may be even expanded to realize additional functionalities, such as magnetism, molecular, or electric transport.

8.5 Experimental Section/Methods

Materials: The synthetic clay sodium fluorohectorite $[Na_{0.5}]^{inter}$ $[Mg_{2.5}Li_{0.5}]^{oct}$ $[Si_4]^{tet}$ $O_{10}F_2$ was obtained via melt synthesis followed by long-term annealing, according to an established procedure.[38,41] The synthesis of ordered heterostructures (interstratifications), consisting of strictly alternating sodium and ammonium interlayers was performed according to an already published procedure.[29] PEG ($M_w = 1500$ g mol^{-1}) was provided by Sigma Aldrich.

Film preparation and characterization: The as-synthesized fluorohectorites and heterostructures were delaminated by immersing them into Millipore water (0.4 vol%) producing nematic liquid crystalline suspensions of Hec (1 nm) and DS (2 nm), respectively. For the reduction of the original diameter of Hec and DS, the suspensions were sonicated with an ultrasonic horn. PEG was dissolved in Millipore water (0.8 vol%) and added in the desired weight ratio. The suspension was mixed for at least one day in an overhead shaker. The quality of the suspension, in terms of homogeneity, was crosschecked by small angle X-ray scattering (SAXS).

Self-supporting films were prepared by employing a fully automatic spray coating system. Every spraying cycle was followed by a drying cycle of 90 s at a temperature of 40 °C. The films were characterized by X-ray diffraction (XRD), transmission electron microscopy (TEM), and thermogravimetric analysis (TGA). The mechanical characteristics were determined by tensile testing with a ZwickRoell testing machine equipped with a 20 N load cell. Contrary to the pure components PEG and Hec, nanocomposite with such high filler contents have been shown to be hardly sensitive to ambient relative humidities.[21] Consequently, we conducted all our experiments at ambient humidity conditions, without further environmental control. Additional information about the sample preparation and characterization methods can be found in Supporting Information Sections 1 and 2.

Brillouin light spectroscopy (BLS): BLS records the phonon dispersion, $\omega(q)$, by detecting the Doppler frequency shift, ω, of the inelastically scattered light by sound waves ("phonons") with a wave vector, q. We recorded BLS spectra utilizing three scattering geometries (transmission, reflection, and backscattering) and two polarization configurations of the incident ($\lambda = 532$ nm) and scattered light (polarized VV, depolarized VH), which allowed us to establish the nature of the observed phonons. We varied the incidence angle to obtain the direction-dependent sound velocities necessary for the determination of the anisotropic elasticity. The elastic stiffness tensor was obtained from the representation of the direction-dependent sound velocities by the Christoffel equation assuming transverse isotropy. The characteristic Young's moduli, shear moduli, and Poisson's ratios of the Bragg stacks were subsequently calculated. More details can be found in Supporting Information Sections 3 and 4.

In-plane thermal conductivity measurements: Lock-in thermography measures the temperature spreading across the free-standing samples upon thermal excitation by a line-laser beam with a modulated intensity. To prevent convective heat losses, the experiments were conducted in a vacuum chamber. The amplitude and phase data were extracted from the temperature distribution perpendicular to the laser-line. The thermal diffusivity was then fitted by the slope method for thermally thin films.[56] With the density, determined by helium pycnometry, and the specific heat, determined by differential scanning calorimetry (DSC), the thermal conductivity was calculated. More details are provided in Supporting Information Section 5.

Cross-plane thermal conductivity measurements: The photoacoustic method uses a modulated laser beam to heat the sample periodically. The surface temperature is converted into an acoustic wave propagating into a gas-tight cell above the sample, filled with helium at 20 psi. A sensitive microphone detected the phase shift between the acoustic signal and the modulated heat source by a lock-in amplifier. The frequency-dependent phase shift was then compared to a multilayer model (Au transducer, sample, Quartz substrate), assuming 1D heat transfer. With the film thickness determined by laser scanning microscopy, the thermal conductivity

was obtained, neglecting thermal contact resistances. More details are provided in Supporting Information Section 5.

8.6 Supporting Information

8.6.1 Sample Preparation

Materials:
The synthetic clay sodium fluorohectorite ($[Na_{0.5}]^{inter}$ $[Mg_{2.5}Li_{0.5}]^{oct}$ $[Si_4]^{tet}$ $O_{10}F_2$, Hec) was synthesized by melt synthesis followed by long-term annealing, according to an already published procedure.[38,41] The material featured a cation exchange capacity of 1.18 mmol g^{-1}.[38,41] Upon immersion in deionized water, the pristine material swells osmotically producing a nematic suspension with nanoplatelets of mean diameters of approximately 18 μm being separated by $>$ 100 nm at 0.4 vol%.[31] The synthesis of double stacks (DS), consisting of strictly alternating sodium and ammonium interlayers was performed according to an already published procedure.[29] To reduce the original diameter into the range of natural montmorillonites, a 0.4 vol% suspension of delaminated Hec or DS was sonicated for 15 minutes in an ice bath applying a UIP 1000hd (Hielscher Ultrasonic GmbH, Germany) equipped with a ultrasonic horn BS2d22 and a booster B2-1.2, at 20 kHz with a maximal output power of 1000 W.
The sonicated suspensions were diluted (0.0004 vol%), drop casted on a plasma-treated silicon wafer and sputtered with 10 nm carbon for scanning electron microscopy (SEM) applying a Zeiss Ultra plus (Carl Zeiss AG, Germany) at an operating voltage of 3 kV. ImageJ was used to evaluate the average diameter of 150 nanoplatelets. (Figure 8.6). The average diameters of Hec and DS are 340 and 406 nm, respectively.

Film preparation:
An aqueous Polyethylene glycol (PEG-1500, $M_w = 1500$ g mol^{-1}, Sigma Aldrich) solution (0.8 vol%) was added in appropriate amounts to obtain the desired volume ratio of Hec or DS to PEG. To assure homogenization, the suspension was mixed for 1 day in the overhead shaker. The self-supporting films were prepared by spray coating. The fully automatic spray coating system was equipped with a SATA 4000 LAB HVLP 1.0 mm spray gun (SATA GmbH & Co. KG, Germany). Suspensions were sprayed on a corona-treated polyethylene terephthalate (PET) foil (Optimont 501, Bleher Folientechnik, Germany). The spraying and nozzle pressures were set at 2 and 4 bar, respectively. The round per flat fan control was set to 6 with a flow speed of 3 mL s^{-1}. The distance between the spraying gun and the substrate was 17 cm. The thickness of the suspension layer applied in one spraying step is

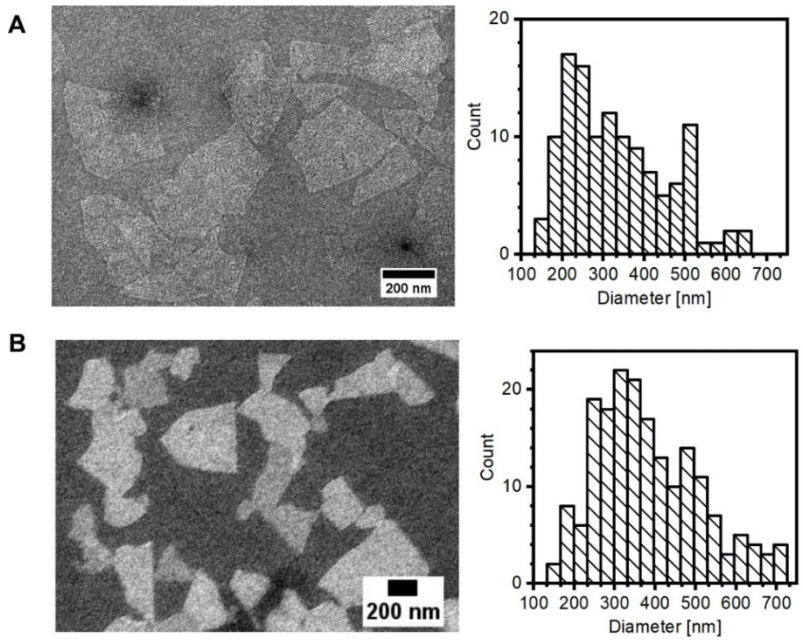

Figure 8.6: Typical SEM images and histograms of the platelet diameter distribution of sonicated (a) Hec and (b) DS as evaluated by *ImageJ*.

about 2 μm which corresponds to about 20 nm dry film thickness. For drying the suspension layer, the sample was stopped under infrared lamps until evaporation of the solvent was complete. After every spraying cycle, a drying cycle of 90 s with a temperature of 40 °C took place. The spraying/drying cycle was repeated until the desired barrier film thickness of 30 μm was obtained. Afterward, the film was dried at 60 °C for 7 days, and peeled off from the PET foil for achieving self-supporting films. For characterization by photoacoustic analysis, thinner films on the order of a few μm were spray coated onto clean 1 mm thick quartz slides.
In total, we prepared four different samples: Hec/2PEG, Hec/1PEG, DS/2PEG, DS/1PEG. The nomenclature is based on the two different volume contents of PEG. A detailed explanation is given in Table 8.3.

8.6.2 Characterization of the Suspensions and Films

Small Angle X-Ray Scattering (SAXS):
SAXS data were measured using the small-angle X-ray system "Double Ganesha AIR" (SAXSLAB, Denmark). The X-ray source of this laboratory-based system is a rotating anode (copper, MicroMax 007HF, Rigaku Corporation, Japan), providing a micro-focused beam. The data were recorded by a position-sensitive detector (PILATUS 300 K, Dectris). To cover the range of scattering vectors different detector positions were used. The measurements of the suspensions were done in 1 mm glass capillaries (Hilgenberg, code 4007610, Germany) at room temperature. To improve the detection limit of the in-house machine, the suspensions were first concentrated

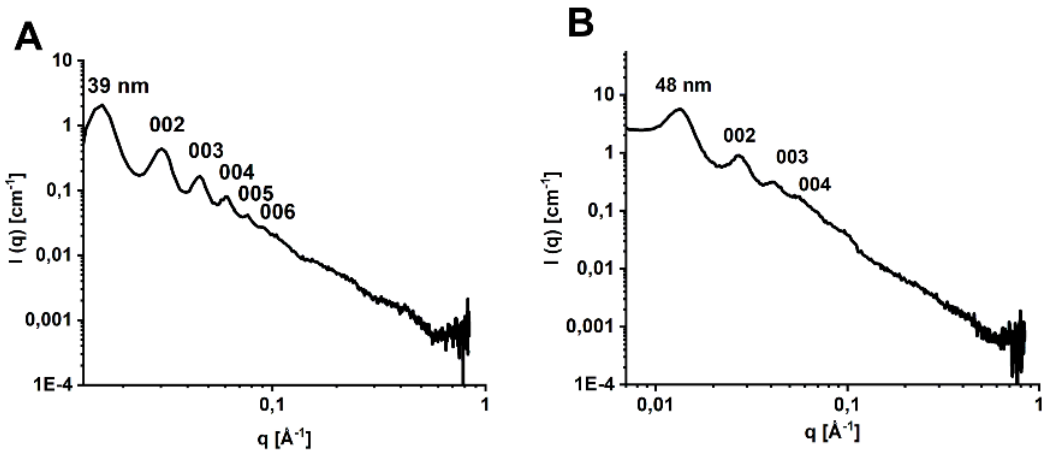

Figure 8.7: One-dimensional SAXS pattern of the concentrated gel samples (a) Hec/2PEG, (b) DS/2PEG. The varying layer separations observed are related to the clay content of the suspensions rather than the Hec/PEG ratio.

Table 8.3: Overview of the structural and chemical characterization.

Sample	nominal Hec:PEG ratio (wt%)	nominal Hec:PEG ratio (vol%)	PEG content (wt%)*	PEG content (vol%)**	Nominal *d*-spacing (nm)	Observed *d*-spacing (nm)
Hec/2PEG	73:27	54:46	27	46	1.77	1.77
Hec/1PEG	84:16	70:30	16	30	1.38	1.38
DS/2PEG	84:16	70:30	16	30	2.77	2.79
DS/1PEG	91:9	82:18	9	18	2.38	2.39

* determined by TGA (Figure 8.9).

** recalculated from vol% PEG assuming bulk density.

by centrifugation at 10000 rpm for 1 hour. The data were radially averaged and background corrected. As background, a water-filled capillary was used.

X-Ray diffraction (XRD) analysis:

XRD patterns for the films were recorded in Bragg-Brentano-geometry on an Empyrean diffractometer (PANalytical B.V.; the Netherlands) using Cu Kα radiation ($\lambda = 1.54187\mathring{A}$). The self-supporting films were placed on glass slides (Menzel-Gläser; Thermo Scientific). Before the measurements, samples were dried at 100 °C for one week in a vacuum chamber.

As a measure of the quality of the one-dimensional crystallinity of the films, the coefficient of variation (CV) and the full width at half maximum (FWHM) were determined (Table 8.3). Large CV-values ($> 3\%$)[29] and large FWHM indicate non-rationality of the diffraction pattern as caused by a random interstratification of different interlayer heights, which represent defects in the periodicity.

The FWHM and CV criteria were applied to examine the stoichiometry of the hybrid films. Even slight deviations from the ideal compositions can lead to significant increase in both CV and FWHM of the 001 reflection (Figure 8.8).

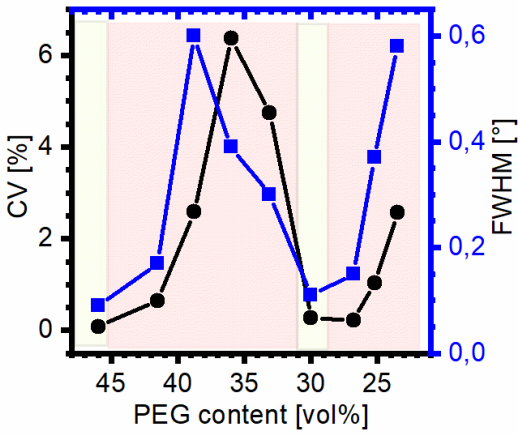

Figure 8.8: Optimization of the PEG content of Hec/2PEG and Hec/1PEG to improve the 1D crystallinity of hybrid Bragg stacks. Best 1D crystallinity corresponds to minima in CV and FWHM, which are observed at 46 and 30 vol% for Hec/2PEG and Hec/1PEG, respectively.

Thermogravimetric analysis (TGA):
The Hec to PEG ratios were cross-checked (Table 8.3) for the dried films by thermogravimetric analysis (TGA), using a Mettler Toledo SDTA851 equipped with the gas control unit TS0800GC1 (Mettler Toledo, USA). Changes in mass observed upon heating in synthetic air up to 900 °C were attributed to the combustion of PEG (Figure 8.9).

Transmission electron microscopy (TEM):
TEM images of the self-supporting films were taken on a JEOL JEM-2200FS (JEOL GmbH, Germany) at an acceleration voltage of 200 kV. Cross-section pictures of the self-supporting films were prepared with a Cryo Ion Slicer IB-09060CIS (JEOL, Germany).

Tensile testing:
The stress-strain curves were recorded with a ZwickRoell material testing machine of the type BT1-FR0.5TN.D14 (ZwickRoell, Ulm, Germany) equipped with a 20 N load cell (Xforce HP, ZwickRoell, Ulm, Germany). The test strips had a dimension of 20 mm x 2 mm x 30 μm. The test speed was set to 0.5 mm min^{-1}. Before testing, the test strips were conditioned in a desiccator with a relative humidity of 53% RH for 7 days. A minimum of 7 test strips was measured for every sample.

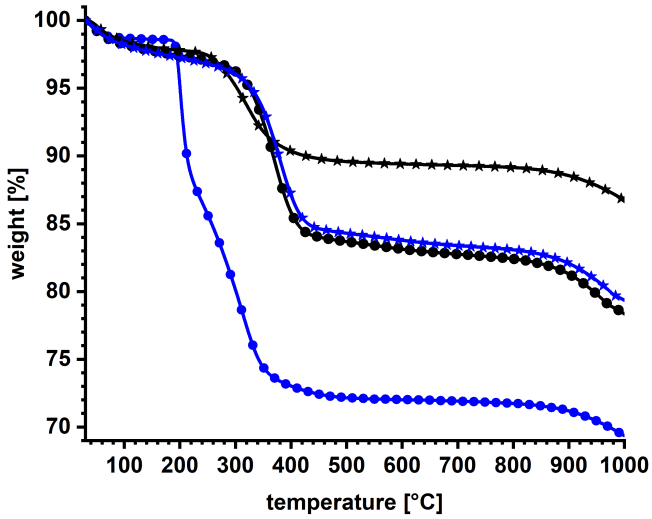

Figure 8.9: TGA curves of Hec/2PEG (blue curve, circle), Hec/1PEG (blue curve, asterisk), DS/2PEG (black curve, circle) and DS/1PEG (black curve, asterisk). The weight loss below 150 °C corresponds to adsorbed water.

Table 8.4: Bulk mechanical properties obtained by tensile testing at 53% RH. The mean and standard deviation values are calculated based on seven individual measurements.

Sample	Hec:PEG ratio (vol%)	Young's modulus (GPa)	Maximum tensile strength (MPa)	Elongation at break (%)	Work of fracture (MJ/m^3)
Hec/2PEG	54:46	10 ± 1	48 ± 5	8.4 ± 2.0	3.4 ± 0.9
Hec/1PEG	70:30	13 ± 1	42 ± 8	0.4 ± 0.1	0.1 ± 0.0
DS/2PEG	70:30	32 ± 3	202 ± 16	0.7 ± 0.1	0.8 ± 0.1
DS/1PEG	82:18	26 ± 3	149 ± 19	0.7 ± 0.1	0.6 ± 0.1

8.6.3 Brillouin Light Scattering (BLS)

BLS is an optical, nondestructive, and noninvasive technique which measures the inelastic scattered light caused by thermally excited hypersonic (GHz) phonons. The scattering wave vector q is defined as $q = k_s - k_i$, where k_i and k_s are the wave vectors of the incident and scattered light, respectively. The polarization of the incident and scattered light was selected to be either vertical (V) or horizontal (H) to the scattering plane defined by k_i and k_s. To take full advantage of the vector nature of the phonon wave vector we used three scattering geometries, transmission, reflection, and backscattering. They allowed us to probe phonon propagation in directions parallel, normal, and oblique to the sample film, respectively. For the transmission and reflection geometries the laser source was mounted on a goniometer and rotated around the sample. In the transmission geometry, q lies in the plane of the sample film with a magnitude, $q_{\parallel} = \frac{4\pi}{\lambda} \sin\beta$, where β is the incident angle and λ (= 532 nm) the wavelength of the laser beam in vacuum. In the reflection geometry, q is directed normal to the sample film with a magnitude, $q_{\perp} = \frac{4\pi}{\lambda}\sqrt{n^2 - \sin^2\beta}$ where n is the samples refractive index. In the backscattering geometry, the incident and scattered light follow the same path, and $q_{bs} = \frac{4\pi}{\lambda} n$. The BLS spectra (Figure 8.10) were recorded by a six-pass tandem Fabry-Perot interferometer and the frequency shift (f) of the phonons at the three different geometries was obtained from the Lorentzian representation of the BLS data. The longitudinal c_L (transverse c_T) phonon sound velocity is computed from the dispersion $f(q)$ (Figure 8.11) relation obtained from the VV (VH) BLS spectra. For linear acoustic dispersion (in the absence of relaxation phenomena), $c = \frac{2\pi f}{q}$, and moreover for an elastically isotropic sample, the longitudinal (transverse) sound velocity c_L (c_T) is independent of the propagation direction. In this case, the in-plane (transmission geometry) and out-of-plane (reflection geometry) $f(q)$ coincide, leading to the determination of the refractive index, n. In the case of linear acoustic dispersion but elastically anisotropic samples, both sound velocities are direction-dependent.

8.6.4 Transversely Isotropic Elasticity Model

It is well known that the elastic tensor for an anisotropic material contains 21 independent components. We assume transversely anisotropic films with the axis of symmetry normal to the film which reduces the number of independent tensor components to 5 (e.g., C_{11}, C_{13}, C_{33}, C_{44}, C_{66}). The elastic stiffness tensor has the

following form in the Voigt notation.[52]

$$C = \begin{pmatrix} C_{11} & C_{12} & C_{13} & 0 & 0 & 0 \\ C_{12} & C_{22} & C_{13} & 0 & 0 & 0 \\ C_{13} & C_{13} & C_{33} & 0 & 0 & 0 \\ 0 & 0 & 0 & C_{44} & 0 & 0 \\ 0 & 0 & 0 & 0 & C_{44} & 0 \\ 0 & 0 & 0 & 0 & 0 & C_{66} \end{pmatrix} \tag{8.1}$$

where $C_{66} = (C_{11} - C_{12})/2$.

Considering the symmetry, we take into account only q vectors in one plane containing the axis of symmetry, which allows us to define the direction as $0° \leq \alpha \leq 90°$ - the angle between q and the normal to the sample film. For a particular direction, there exist one quasi-longitudinal (Q-L) mode, one quasi-transverse (Q-T) mode measured in the VV polarization configuration, and one pure-transverse (P-T) mode measured in the VH polarization configuration. The following three scattering geometries, reflection, backscattering and transmission correspond to $\alpha = 0°$, $0° \leq \alpha \leq 90°$, and $\alpha = 90°$, respectively. The components of the stiffness elastic tensor are determined by representing the sound velocities (Figure 8.12) by the Christoffel's equation:

$$c_{\mathrm{Q-L}}(\alpha) = \sqrt{\frac{-A_1 + \sqrt{A_1^2 - 4A_2}}{2\rho}} \tag{8.2}$$

$$c_{\mathrm{Q-T}}(\alpha) = \sqrt{\frac{-A_1 - \sqrt{A_1^2 - 4A_2}}{2\rho}} \tag{8.3}$$

$$c_{\mathrm{P-T}}(\alpha) = \sqrt{\frac{A_3}{\rho}} \tag{8.4}$$

where

$$A_1 = -\left(C_{11}\sin^2\alpha + C_{33}\cos^2\alpha + C_{44}\right) \tag{8.5}$$

$$A_2 = C_{11}C_{44}\sin^4\alpha + \sin^2\alpha\cos^2\alpha\left(C_{11}C_{33} - C_{13}^2 - 2C_{13}C_{44}\right) + C_{33}C_{44}\cos^4\alpha \tag{8.6}$$

$$A_3 = C_{66}\sin^2\alpha + C_{44}\cos^2\alpha \tag{8.7}$$

and ρ being the mass density.

Based on the BLS-measured, direction-dependent sound velocities, nonlinear χ^2 fitting was conducted to obtain the elastic stiffness constants. The χ^2 is defined as:

$$\chi^2 = \sum_i \frac{\left[c_{i,fit}(C_{11}, C_{13}, C_{33}, C_{44}, C_{66}, \alpha) - c_{i,exp}(\alpha)\right]^2}{(\Delta c_{i,exp})} \tag{8.8}$$

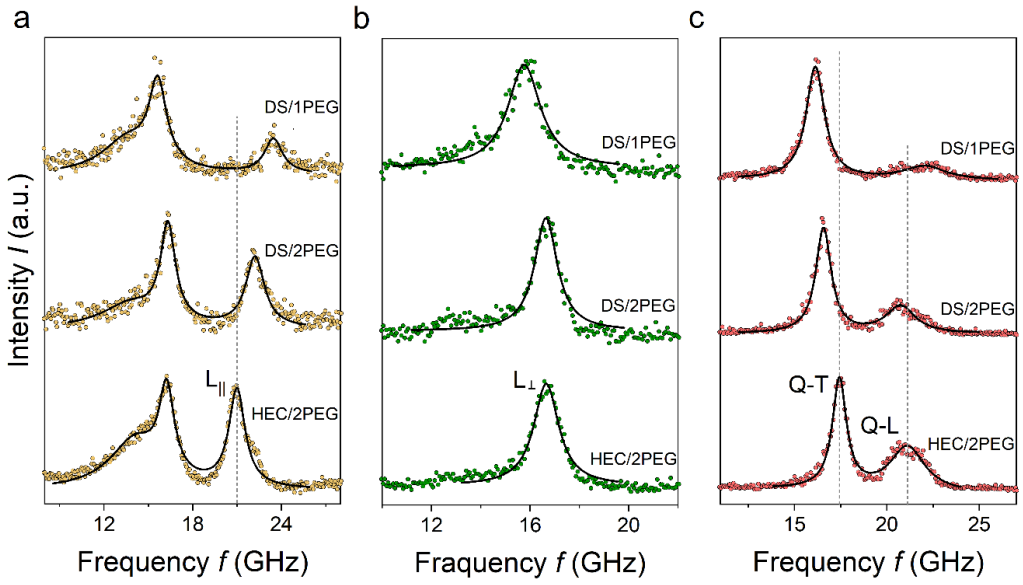

Figure 8.10: Experimental VV BLS spectra recorded in (a) transmission, (b) reflection, and (c) backscattering geometries at an incident angle $\beta = 45°$. The top spectra are for DS/1PEG with 82 vol% Hec content. The middle spectra are for DS/2PEG with 70 vol% Hec content. The bottom spectra are for Hec/2PEG with 54 vol% Hec content.

where $c_{i,fit}$ and $c_{i,exp}$ are the fitted and experimental sound velocities, respectively, $\Delta c_{i,exp}$ is the uncertainty of the measured sound velocity,[61] and the summation is over all experimental sound velocities.

The use of the independent constants of the elastic tensor is not limited to the theoretical representation of the sound velocities $c_{\mathrm{Q-L}}$, $c_{\mathrm{Q-T}}$ and $c_{\mathrm{P-T}}$. They were used to calculate the engineering mechanical properties,[52] including the in-plane and cross-plane Young's moduli ($E_{\parallel}$, $E_{\perp}$), shear moduli (G_{12}, G_{13}), and Poisson's ratios (v_{31}, v_{12}).

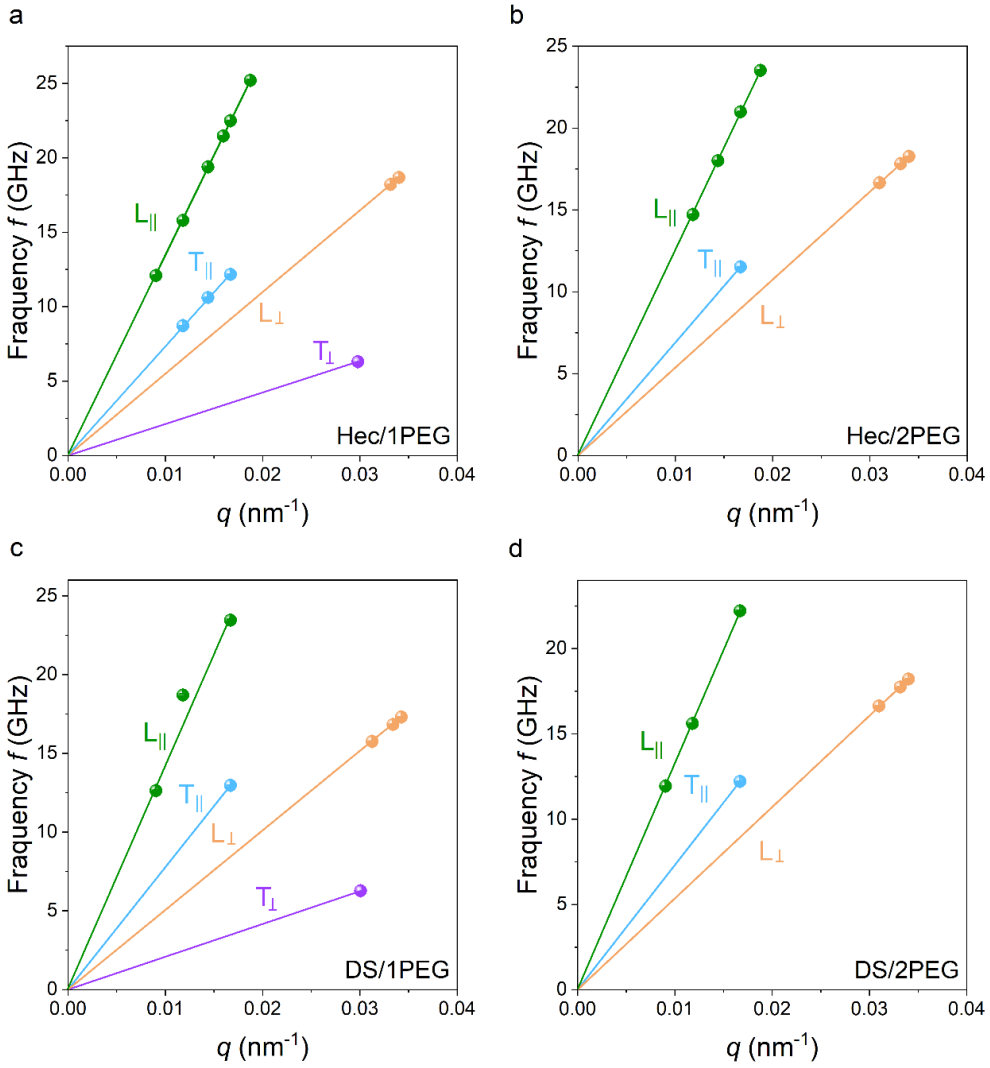

Figure 8.11: Dispersion relation $f(q)$ for acoustic modes of (a) Hec/1PEG, (b) Hec/2PEG, (c) DS/1PEG, and (d) DS/2PEG recorded at the transmission geometry in VV ($L_{\parallel}$) and VH ($T_{\parallel}$) polarization configurations and at the reflection geometry in VV ($L_{\perp}$) and VH ($T_{\perp}$) polarization configurations. For the representation of the data in the reflection geometry for Hec/2PEG, $n = 1.50$ was used. For the other samples, $n = 1.49$ was used. Because of the very weak VH signal in the reflection geometry, we were unable to measure in this configuration for the Hec/2PEG and DS/2PEG samples.

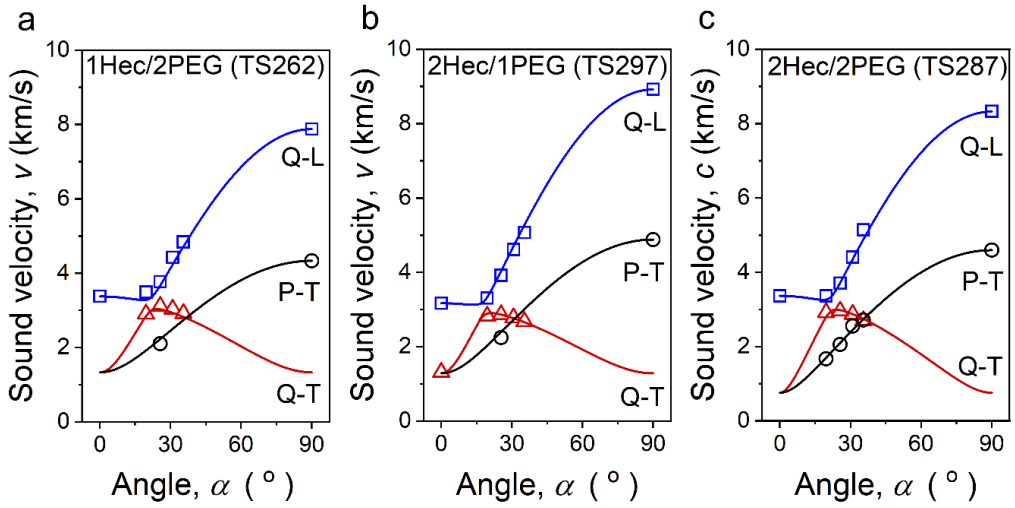

Figure 8.12: Experimental direction-dependent sound velocities (symbols) with theoretical representations (lines) for (a) Hec/2PEG, (b) DS/1PEG, and (c) DS/2PEG.

Table 8.5: Summary of elastic stiffness constants. Composition (Hec vol%, Hec wt%), density (ρ), refractive index (n), and elastic stiffness constants (C_{11}, C_{12}, C_{13}, C_{33}, C_{44}, and C_{66}) of the Hec/PEG hybrid Bragg stack films. The results are based on fitting with two free parameters. The uncertainties are computed by assuming that the sound velocities have a relative uncertainty of 2%.

Sample	Hec vol%	Hec wt%	ρ (g/cm^3)	n	C_{11}	C_{12}	C_{13}	C_{33}	C_{44}	C_{66}
Hec/2PEG	54	73	2.03	1.49	125.9	49.7	3.0	23.1	3.6	38.1
					±3.0	±4.2	±1.7	±0.5	±0.5	±1.5
Hec/1PEG	70	84	2.26	1.49	161.1	65.3	2.9	26.9	3.4	47.9
					±3.2	±4.0	±2.2	±0.5	±0.1	±1.2
DS/2PEG	70	84	2.26	1.49	156.6	61.2	6.7	25.6	1.6	47.7
					±3.6	±4.8	±1.8	±0.5	±0.6	±1.6
DS/1PEG	82	91	2.43	1.50	193.3	77.5	5.5	24.4	4.0	57.9
					±4.1	±5.5	±2.5	±0.6	±0.2	±1.8

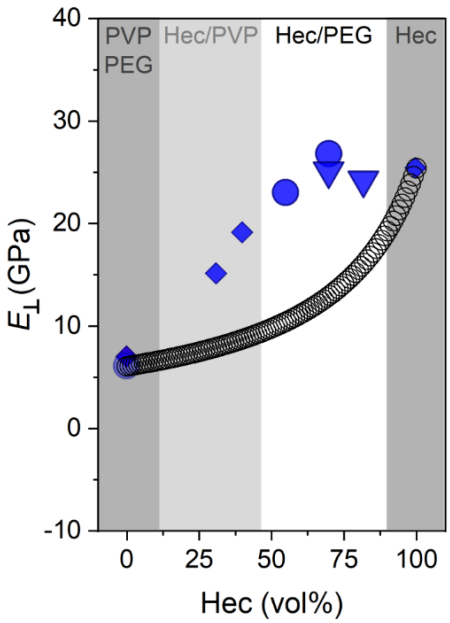

Figure 8.13: Composition dependence of The experimental cross-plane Young's modulus ($E_\perp$, blue symbols) plotted vs. the Hec vol%. The open symbols denote the computed Young's modulus predicted from the Wood's law.

8.6.5 Thermal Measurements

The in-plane thermal diffusivity was determined by lock-in thermography, and the cross-plane thermal conductivity by the photoacoustic method. For the determination of the in-plane thermal conductivity, the density and the specific heat are needed. Therefore, Helium pycnometry and differential scanning calorimetry (DSC) were used.

Helium pycnometry:
The density of the samples was measured by helium pycnometry. Therefore, an Ultrapyc 1200e (Quantachrome Instruments) was used. Prior to each measurement the volume of the empty measurement cell was measured. Afterwards, small pieces of the free-standing films were weighed into the sample cell with a nominal volume of 1.8 cm^3. One hundred runs were performed to determine the volume of the films at room temperature. By knowing the mass (measured on a fine balance) and the volume, the density of the samples was calculated.

Differential scanning calorimetry:
The specific heat capacity was determined by DSC measurements according to the ASTM E1269 standard. The samples were freeze ground for better processability and contact to the DSC pans. The measurements were performed on a TA instruments

Discovery DSC 2500. The temperature profile ranged from −40 to 200 °C using a heating rate of 20 K min^{-1} with a nitrogen flow of 50 mL min^{-1}. For all calculations the specific heat capacity at 250 °C was used.

Lock-in Infrared Thermography:
Thermal diffusivity measurements are conducted using Lock-in Infrared Thermography (LIT, Figure 8.14). Samples are coated with 20 nm of carbon on either side and mounted on a sample holder. The holder is set in a vacuum chamber with an optically transparent window behind and an IR-transparent sapphire window in front of the sample. This allows measurements at approximately 0.01 mbar and minimizes heat losses to the environment, which would cause an overestimation of the thermal diffusivity. An intensity modulated line laser (Schäfter+Kirchhoff, $\lambda = 520$ nm, $P_0 = 55$ mW) is focused on the back side of the sample. This causes temperature modulations inside the free-standing sample that are monitored with an Infratec ImageIR 9430 research IR-camera (spectral window: $2.0 - 5.5$ μm) mounted with an M=1.0x microscopy objective. Measurements are conducted at an excitation frequency of 2.0 Hz, a duty cycle of 50%, camera frame rate of 20 Hz and over the course of 200 periods. Online lock-in evaluation using the IRBIS active online software directly provides phase and amplitude images (Figure 8.15). Linearization of both signals and fitting perpendicular to the laser line allows calculation of the thermal diffusivity by means of the slope method for thermally thin films.
From the linearized data the slope (m) of both amplitude (T) and phase data (ϕ) are obtained. The in-plane thermal diffusivity ($\alpha_{\parallel}$) can then be calculated according to:

$$m_{\phi} \cdot m_{\ln(T)} = \frac{\pi f_{\text{lock-in}}}{\alpha_{\parallel}} \tag{8.9}$$

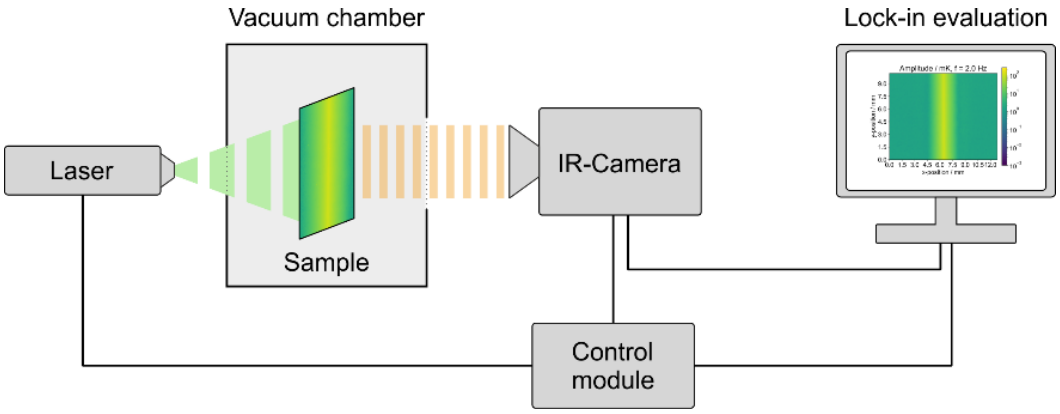

Figure 8.14: Schematic of the Lock-in Infrared Thermography measurement setup and online data evaluation.

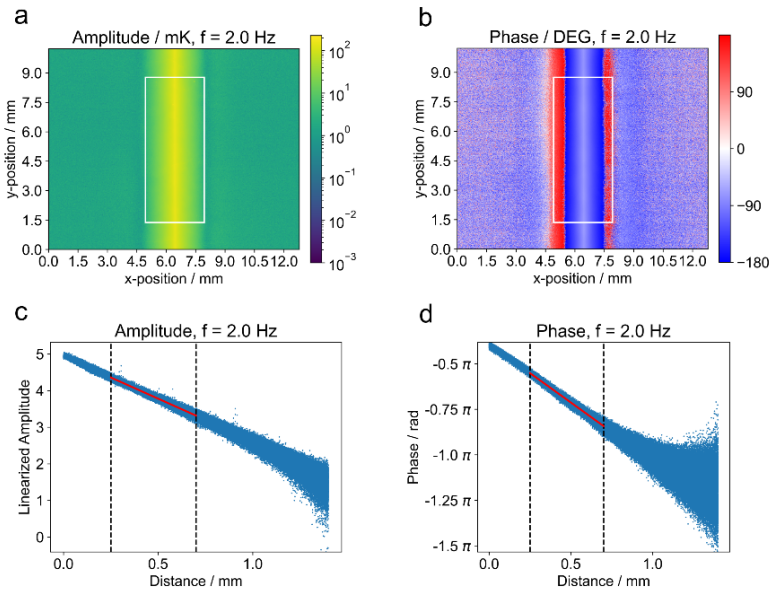

Figure 8.15: Typical analysis procedure of LIT. The raw Amplitude (a) and Phase data (b) are evaluated perpendicular to the laser-line inside the area shown by the white box. The respective 2D plots with linear regression are shown in (c) and (d).

Together with the density (ρ), determined via helium pycnometry, and the specific heat capacity (c_p), determined via DSC, the in-plane thermal conductivity can be calculated as:

$$\kappa_\parallel = \alpha_\parallel \cdot c_\mathrm{p} \cdot \rho \tag{8.10}$$

Two films are measured for each composition.

Photoacoustic method:

The cross-plane thermal conductivity was determined by the photoacoustic method. The thermal properties are determined by relating a measured pressure signal to the sample surface temperature and fitting the phase shift to a multilayer model. Therefore, a modulated laser beam (λ = 488 nm) periodically heats the sample. For good absorption of the laser energy, a thin Au transducer layer (approximately 100 nm) was coated on the sample surface. For photoacoustic characterization, the samples were spray-coated on a glass substrate. The layout of the measurement cell above the sample is shown in Figure 8.16. The gas tight cell is filled with a helium pressure of 20 psi. The microphone (Bruel&Kjaer, 4398-A-011) connected to the cell measures the pressure signal, which is induced by the periodic heat conduction from the sample surface to the gas phase. As shown in Figure 8.16, the microphone is linked to a lock-in amplifier with integrated signal generator (Zurich instruments, HF2LI). The signal generator feeds the electro-optic modulator (EOM, Conoptics, M25A) with a sinusoidal signal, and therefore the frequency of the modulated laser beam can be swept.

The phase shift is detected as a function of the frequency in a range from 310 to

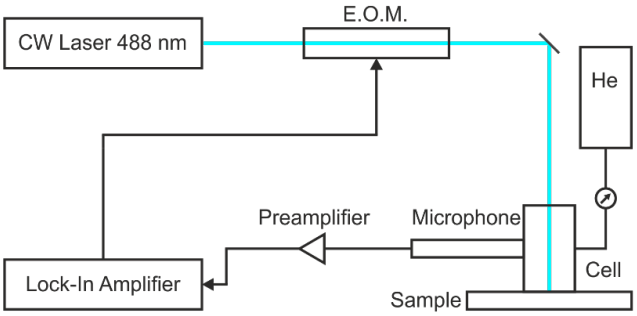

Figure 8.16: Schematic setup with a continuous wave laser being passed through an EOM to provide the modulated heat source. The photoacoustic signal is measured using a microphone in the pressurized cell.[62]

9210 Hz. The signal is normalized with the phase shift signal of a thermally thick glass sample (1 mm) with known thermal properties, to determine the setups transfer function. Fitting was done according to the generalized multilayer model of Hu et al.[63] assuming one-dimensional heat transfer. Contact resistances are not taken into account. The thickness of the samples was determined by confocal microscopy. Input parameters are the thermal properties of the quartz substrate and the Au transducer layer. While the transducer layer thickness is needed, the substrate is assumed to be thermally thick. Uncertainties in sample and transducer thickness are taken into account by using a Monte-Carlo approach. In doing so, three independent measurements are analyzed using 1000 iterations with randomly selected sample and transducer thickness based on their Gaussian distribution. Afterwards, the errors due to uncertainty in thickness and the errors due to fitting, based on the Jacobian matrices and the mean square error, were added.[62] Still, all errors were assumed to be Gaussian distributed, and the $\pm 1/e$ confidence intervals are used as error bars. For every composition three samples were measured and averaged.

8.7 References

[1] R. O. Ritchie, *Nature Materials* **2011**, *10*, 817–822.

[2] U. G. K. Wegst, H. Bai, E. Saiz, A. P. Tomsia, R. O. Ritchie, *Nature Materials* **2014**, *14*, 23–36.

[3] J. W. Dunlop, P. Fratzl, *Annual Review of Materials Research* **2010**, *40*, 1–24.

[4] Z.-H. Xu, Y. Yang, Z. Huang, X. Li, *Materials Science and Engineering: C* **2011**, *31*, 1852–1856.

[5] M. A. Meyers, P.-Y. Chen, A. Y.-M. Lin, Y. Seki, *Progress in Materials Science* **2008**, *53*, 1–206.

[6] Z. Tang, N. A. Kotov, S. Magonov, B. Ozturk, *Nature Materials* **2003**, *2*, 413–418.

[7] P. Podsiadlo, A. K. Kaushik, E. M. Arruda, et al., *Science* **2007**, *318*, 80–83.

[8] D. A. Dikin, S. Stankovich, E. J. Zimney, et al., *Nature* **2007**, *448*, 457–460.

[9] E. Munch, M. E. Launey, D. H. Alsem, et al., *Science* **2008**, *322*, 1516–1520.

[10] A. Walther, I. Bjurhager, J.-M. Malho, et al., *Nano Letters* **2010**, *10*, 2742–2748.

[11] K. W. Putz, O. C. Compton, M. J. Palmeri, S. T. Nguyen, L. C. Brinson, *Advanced Functional Materials* **2010**, *20*, 3322–3329.

[12] R. M. Erb, R. Libanori, N. Rothfuchs, A. R. Studart, *Science* **2012**, *335*, 199–204.

[13] M. Zhang, L. Huang, J. Chen, C. Li, G. Shi, *Advanced Materials* **2014**, *26*, 7588–7592.

[14] J. J. Richardson, M. Björnmalm, F. Caruso, *Science* **2015**, *348*, 6233.

[15] L.-B. Mao, H.-L. Gao, H.-B. Yao, et al., *Science* **2016**, *354*, 107–110.

[16] P. Das, J.-M. Malho, K. Rahimi, et al., *Nature Communications* **2015**, *6*, 5967.

[17] M. Liu, Y. Ishida, Y. Ebina, et al., *Nature* **2014**, *517*, 68–72.

[18] M. Morits, T. Verho, J. Sorvari, et al., *Advanced Functional Materials* **2017**, *27*, 1605378.

[19] T. Verho, P. Karppinen, A. H. Gröschel, O. Ikkala, *Advanced Science* **2017**, *5*, 1700635.

[20] X. G. Zhao, G. M. Dalpian, Z. Wang, A. Zunger, *Physical Review B* **2020**, *101*, 1–19.

[21] T. Schilling, C. Habel, S. Rosenfeldt, M. Röhrl, J. Breu, *ACS Applied Polymer Materials* **2020**, *2*, 3010–3015.

[22] E. S. Tsurko, P. Feicht, C. Habel, et al., *Journal of Membrane Science* **2017**, *540*, 212–218.

[23] E. S. Tsurko, P. Feicht, F. Nehm, et al., *Macromolecules* **2017**, *50*, 4344–4350.

[24] A. Eckert, T. Rudolph, J. Guo, T. Mang, A. Walther, *Advanced Materials* **2018**, *30*, 1802477.

[25] Z. Ling, C. E. Ren, M.-Q. Zhao, et al., *Proceedings of the National Academy of Sciences* **2014**, *111*, 16676–16681.

[26] S. Deville, E. Saiz, R. K. Nalla, A. P. Tomsia, *Science* **2006**, *311*, 515–518.

[27] F. Bouville, E. Maire, S. Meille, et al., *Nature Materials* **2014**, *13*, 508–514.

[28] D. A. Kunz, J. Erath, D. Kluge, et al., *ACS Applied Materials & Interfaces* **2013**, *5*, 5851–5855.

[29] M. Stöter, S. Gödrich, P. Feicht, et al., *Angewandte Chemie International Edition* **2016**, *55*, 7398–7402.

[30] M. Stöter, S. Rosenfeldt, J. Breu, *Annual Review of Materials Research* **2015**, *45*, 129–151.

[31] S. Rosenfeldt, M. Stöter, M. Schlenk, et al., *Langmuir* **2016**, *32*, 10582–10588.

[32] Z. Wang, K. Rolle, T. Schilling, et al., *Angewandte Chemie International Edition* **2019**, *59*, 1286–1294.

[33] K. Rolle, T. Schilling, F. Westermeier, et al., *Macromolecules* **2021**, *54*, 2551–2560.

[34] C. Habel, J. Maiz, J. L. Olmedo-Martinez, et al., *Polymer* **2020**, *202*, 122734.

[35] A. Eckert, M. Abbasi, T. Mang, K. Saalwächter, A. Walther, *Macromolecules* **2020**, *53*, 1716–1725.

[36] J. Wu, M. M. Lerner, *Chemistry of Materials* **1993**, *5*, 835–838.

[37] P. Das, S. Schipmann, J.-M. Malho, et al., *ACS Applied Materials & Interfaces* **2013**, *5*, 3738–3747.

[38] M. Stöter, D. A. Kunz, M. Schmidt, et al., *Langmuir* **2013**, *29*, 1280–1285.

[39] N. G. Bowery, *Encyclopedia of Polymer Science and Technology*, John Wiley & Sons, **2014**.

[40] A. Lerf, *Dalton Transactions* **2014**, *43*, 10276–10291.

[41] J. Breu, W. Seidl, A. J. Stoll, K. G. Lange, T. U. Probst, *Chemistry of Materials* **2001**, *13*, 4213–4220.

[42] G. Arkhipovich, S. Dubrovskii, K. Kazanskii, A. Shupik, *Polymer Science U.S.S.R.* **1981**, *23*, 1827–1841.

[43] P. Stempfle, O. Pantale, M. Rousseau, E. Lopez, X. Bourrat, *Materials Science and Engineering: C* **2010**, *30*, 715–721.

[44] P. Aranda, E. Ruiz-Hitzky, *Chemistry of Materials* **1992**, *4*, 1395–1403.

[45] K. E. Strawhecker, E. Manias, *Chemistry of Materials* **2003**, *15*, 844–849.

[46] D. Moore, *X-ray Diffraction and the Identification and Analysis of Clay Minerals*, Oxford University Press, **1997**.

[47] P. Voudouris, N. Gomopoulos, A. L. Grand, et al., *The Journal of Chemical Physics* **2010**, *132*, 074906.

[48] Y. Cang, Z. Wang, C. Bishop, et al., *Advanced Functional Materials* **2020**, *30*, 2001481.

[49] M. Ryu, Y. Cang, Z. Wang, G. Fytas, J. Morikawa, *The Journal of Physical Chemistry C* **2019**, *123*, 17148–17154.

[50] Z. Wang, Y. Cang, F. Kremer, E. L. Thomas, G. Fytas, *Biomacromolecules* **2020**, *21*, 1179–1185.

[51] J. K. Krueger, H. Bastian, G. I. Asbach, M. Pietralla, *Polymer Bulletin* **1980**, *3*, 633–640.

[52] S. Cusack, A. Miller, *Journal of Molecular Biology* **1979**, *135*, 39–51.

[53] D. Schneider, F. Liaqat, E. H. E. Boudouti, et al., *Nano Letters* **2012**, *12*, 3101–3108.

[54] B. Liu, C. Pavlou, Z. Wang, et al., *2D Materials* **2021**, *8*, 035040.

[55] V. Singh, T. L. Bougher, A. Weathers, et al., *Nature Nanotechnology* **2014**, *9*, 384–390.

[56] A. Mendioroz, R. Fuente-Dacal, E. Apinaniz, A. Salazar, *Review of Scientific Instruments* **2009**, *80*, 074904.

[57] A. Philipp, J. F. Eichinger, R. C. Aydin, et al., *Heat and Mass Transfer* **2019**, *56*, 811–823.

[58] E. Alonso-Redondo, L. Belliard, K. Rolle, et al., *Scientific Reports* **2018**, *8*, 16986.

[59] A. Walther, I. Bjurhager, J.-M. Malho, et al., *Angewandte Chemie International Edition* **2010**, *49*, 6448–6453.

[60] B. Zhu, N. Jasinski, A. Benitez, et al., *Angewandte Chemie International Edition* **2015**, *54*, 8653–8657.

[61] M. Zgonik, P. Bernasconi, M. Duelli, et al., *Physical Review B* **1994**, *50*, 5941–5949.

[62] K. Herrmann, N. Pech-May, M. Retsch, *Photoacoustics* **2021**, *22*, 100246.

[63] H. P. Hu, X. W. Wang, X. F. Xu, *Journal of Applied Physics* **1999**, *86*, 3953–3958.

9

Composite Metal-Halide and Molecular Contributions Govern the Electronic Structure and Thermal Transport Properties of 2D Lead-Halide Perovskites

Raisa-Ioana Biega,[*] Kai Herrmann,[§] John Mohanraj,[†] Dominik Skrybeck,[†] Menno Bokdam,[‡] Mukundan Thelakkat,[†,¶] Markus Retsch,[§,¶] and Linn Leppert[*,‡]

[*] Institute of Physics, University of Bayreuth, Bayreuth 95440, Germany.

[§] Department of Chemistry, University of Bayreuth, 95440 Bayreuth, Germany.

[†] Applied Functional Polymers, University of Bayreuth, 95440 Bayreuth, Germany.

[‡] MESA+ Institute for Nanotechnology, University of Twente, 7500 AE Enschede, The Netherlands.

[¶] Bavarian Polymer Institute, University of Bayreuth, 95440 Bayreuth, Germany.

9.1 Abstract

Halide perovskite with Ruddlesden-Popper structure are quasi-2D materials with alternating organic and inorganic sublattices and extraordinary optical properties that are governed by dielectric and quantum confinement. Due to their robust moisture stability, they have been used as active materials in LEDs, lasers, and solar cells. Despite these successful applications, the fundamental electronic and thermal properties of these materials are little explored. Here we systematically study the effects of dimensionality and the choice of the organic sublattice in a combined experimental and computational study of the $n = 1$ Ruddlesden-Popper perovskites A_2PbI_4 (A=butylammonium, phenylethylammonium) and the quintessential 3D perovskite $CH_3NH_3PbI_3$. We show that the electronic and thermal properties of these materials can be understood as arising from composite contributions of the inorganic and organic sublattices. Interactions between the sublattices are responsible for subtle changes in the electronic and vibrational density of states. However, these effects are small as compared to contributions of the individual sublattices. Our results provide an atomistic understanding of the effects of dimensional reduction on properties relevant for electronic and thermal transport and pave the way for the design of new stable hybrid materials with tailored properties.

9.2 Introduction

Hybrid organic-inorganic halide perovskites are intensely studied due to their suitability for a wide range of optoelectronic applications, from solar cells with power conversion efficiencies exceeding 25%[1], to LEDs[2–4] and radiation detectors.[5,6] Reducing the dimensionality of the inorganic sublattice by incorporation of large organic molecules such as butylammonium (BA) or phenylethylammonium (PEA) affords bulk materials that combine many of the outstanding optoelectronic properties of the 3D parent materials while exhibiting features of quantum and dielectric confinement and improved moisture stability.[7,8] Much of the focus has been on the quasi-2D Ruddlesden-Popper (RP) perovskites $A_{n-1}A_2'B_nX_{3n+1}$,[7,9–13] because of their good performance as active materials in LEDs, lasers and solar cell devices.[14] In hybrid organic-inorganic RP perovskites, A is an aliphatic or aromatic alkylammonium cation separating the n-layer perovskite framework, which consists of a 2D network of corner-sharing BX_6 (B=Pb^{+2}, X=I^-, Br^-) octahedra with small cations A' (A'=$CH_3NH_3^+$, Cs^+) providing charge balance.

The optical properties of RP perovskites are governed by dielectric and quantum confinement, which has been shown experimentally[15–18] and by means of first principles and semiempirical electronic structure calculations.[19–21] In contrast, much less is known about the effects of dimensional reduction and the A-site cation on

the electronic and thermal properties of these materials. Ultraviolet (UV) and inverse photoemission spectroscopy combined with density functional theory (DFT) calculations have been reported for BA_2PbI_4 and BA_2PbBr_4, showing less band dispersion and a larger density of states (DOS) at the band edges than in their 3D counterparts.[22] DFT calculations by Gebhardt et al.[11] showed that the electronic structure of the layered bulk phase of PEA_2PbI_4 is almost unaffected by reducing the dimensionality to a monolayer, suggesting weak interactions between the molecular and perovskite sublattices along the stacking direction. Furthermore, the interaction between these sublattices was shown to be governed by steric effects.[23]

Thermal properties of 2D RP perovskites have come into focus only recently, with Giri et al.[12] reporting ultralow thermal conductivities in A_2PbX_4 (A= BA, PEA, X=I, Br) using thermoreflectance measurements combined with molecular dynamics simulations based on a classical force field. A theoretical study using a similar force field by Fridriksson et al. also showed that length and aromaticity of the A site molecule significantly affect the structural rigidity of the perovskite sublattice.[13] Temperature-dependent Raman measurements on A_2PbBr_4 further highlighted the role of the A site molecule, with PEA leading to strongly anisotropic vibrational modes related to the orientation of the phenethyl ring with respect to the perovskite sublattice.[24]

In this work we study the effects of dimensional reduction and A site cation on the electronic and thermal properties of 3D $CH_3NH_3PbI_3$ ($MAPbI_3$) and A_2PbI_4 (A=BA, PEA). We use ultraviolet photoelectron spectroscopy (UPS) and temperature-dependent Raman spectroscopy combined with first-principles density functional theory (DFT) calculations and molecular dynamics simulations based on machine-learned force fields with DFT accuracy to elucidate the contributions of the organic and inorganic sublattices to the electronic and vibrational DOS. The electronic valence band, DOS of all three materials close to the valence band maximum, is governed by the perovskite sublattice. The energetic position of the A-site-derived electronic states is inherited from the HOMO-LUMO gap of the isolated A-site cations. By systematically introducing structural distortions in 3D and 2D model systems, our DFT calculations demonstrate that the magnitude of the DOS close to the Fermi level is related to structural distortions rather than the dimensionality of the perovskite sublattice. The low-frequency vibrational DOS is governed by the inorganic sublattice and depends little on the choice of the organic cation. Anharmonic effects are more strongly pronounced in the RP perovskites as compared to $MAPbI_3$. Thermal transport is studied by Xenon-Flash Analysis, showing that the thermal properties in disordered pellets can be described by a volumetric mixture, where an increased size of the A-site cation leads to a reduced thermal conductivity.

9.3 Methods

9.3.1 Structures

Figure 9.1a and Figure 9.1b show the crystal structures of BA_2PbI_4 and PEA_2PbI_4 extracted from single crystal X-ray diffraction experiments under ambient conditions.[25,26] BA_2PbI_4 is orthorhombic with *Pbca* symmetry at room temperature. The out-of-plane lattice parameter is $c = 26.23\,\text{Å}$, whereas the in-plane lattice parameters are $a = 8.43\,\text{Å}$ and $b = 8.99\,\text{Å}$. PEA_2PbI_4 is triclinic with $P\bar{1}$ symmetry, with in-plane lattice parameters $a = b = 8.74\,\text{Å}$ and an out-of-plane lattice parameter of $c = 32.99\,\text{Å}$. $MAPbI_3$ undergoes a phase transition at $T = 327\,\text{K}$.[27] The high-temperature cubic ($Pm\bar{3}m$) and room temperature tetragonal ($I4/mcm$) phases are shown in Figure 9.1c and d.

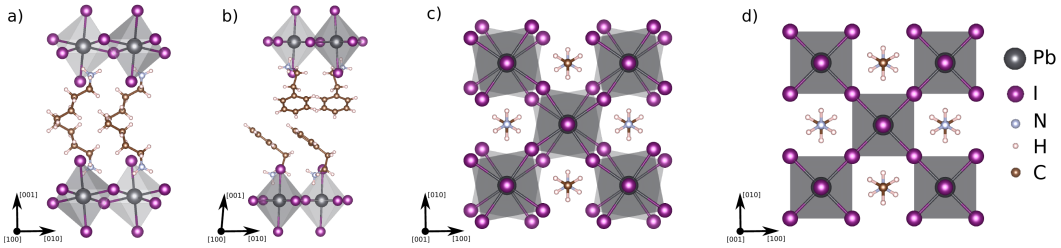

Figure 9.1: Schematic representation of the crystal structures used for all (static) DFT calculations. a) *Pbca* phase of BA_2PbI_4, b) $P\bar{1}$ phase of PEA_2PbI_4, c) $I4/mcm$ phase of $MAPbI_3$ and d) $Pm\bar{3}m$ phase of $MAPbI_3$. In the two $MAPbI_3$ phases, the MA molecules were oriented with the C-N axis pointing along the [001] direction and antiparallel such that their dipole moments cancel out.

9.3.2 UPS Measurements

UPS measurements were carried out on a PHI 5000 VersaProbe III system fitted with a He discharge light source providing stable and continuous He I and He II lines under ultrahigh vacuum ($\sim 10^{-10}$ mbar). Clean ITO substrates ($14 \times 14\,\text{mm}$) pre-treated with O_3/UV for 15 min at 50 °C were used as standard substrates for all UPS measurements. All samples were prepared via solution processing using the anti-solvent method. For $MAPbI_3$, 1 M PbI_2 and equimolar methyl-ammonium iodide (MAI) were dissolved in DMF. The solution was stirred at room temperature overnight and filtered using a $0.2\,\mu\text{m}$ PTFE filter. The obtained clear solution was spin-coated onto a clean ITO; while spinning, after 8 s from the start, $200\,\mu\text{L}$ of toluene was dripped over the substrate. Further, the substrate was annealed at 100 °C for 25 min to obtain uniform $MAPbI_3$ film. PEA_2PbI_4 and BA_2PbI_4 were also prepared following the same procedure, except that the stock solutions were

prepared by dissolving crystals of respective materials in DMF. The samples were directly transported to the UPS instrument by using a N_2 filled, sealed stainless steel transport vessel without exposing them to the ambient conditions. All measurements reported in this study were carried out with the He I (21.22 eV, 40 W) line with -5 V sample bias, and the corresponding photoemission with 90° take-off angle was collected at a multichannel analyzer. The Fermi level (E_F) and vacuum level (E_{vac}) were determined using a sputter cleaned gold foil. Work function and ionization potential values of the perovskites are calculated as the energy difference between E_{vac} and E_F, and E_{vac} and onset of the valence band, respectively. The resolution of the UPS measurements is ±0.15 eV, calculated using the Fermi edge full-width-half-maximum of the gold spectrum, and the presented work function and ionization potential values are reproducible within ±0.05 eV, consistent with the resolution limit.

9.3.3 Raman Measurements

The non-resonant Raman spectra were acquired using a micro-Raman spectrometer (WITec Alpha 300 RA+, Ulm, Germany) equipped with a UHTS 300 spectrometer and a back-illuminated Andor Newton 970 EMCCD camera. A frequency-doubled Nd-YAG laser with a wavelength of 785 nm was used as the excitation source. The laser beam was focused onto the sample by means of a 50× long working distance (numerical aperture NA=0.7, lateral resolution ca. 500 nm) Zeiss objective. The focal length of this spectrometer is 800 mm, and it is equipped with a diffraction grating having a groove density of 1200 lines per millimeter resulting in a spectral resolution of ~ 2 cm^{-1}. The samples were excited with ~ 10 mW laser power in in-plane polarization mode, and the spectra were collected after 50 accumulations with an integration time of 0.5 s. All spectra were processed using a Witec Suite Five (version 5.2) software that allowed compensating for cosmic radiation and other background signals.

9.3.4 Thermal Characterization

Thermogravimetric analysis was performed using a Netzsch PERSEUS STA 449 F3 Jupiter in platinum crucibles under nitrogen flow. A heating rate of 10 K min^{-1} was employed.

The heat capacity at constant pressure c_p was determined by differential scanning calorimetry measurements according to the ASTM E1269 standard. The measurements were performed on a TA instruments Discovery DSC 2500. The temperature profile ranged from -80 °C to 180 °C using a heating rate 20 K min^{-1} with a nitrogen flow of 50 mL min^{-1}. Two heating cycles were conducted and only the second cycle

was evaluated. Three samples for each material were prepared and averaged.
The density at room temperature was determined by helium pycnometry using an Ultrapyc 1200e (Quantachrome Instruments). Prior to each measurement, the volume of the empty cell was calibrated. Afterward, the samples were weighed into the cell and measured at 17 psi of helium after the cell was purged with helium for one hour. The sample volume and density were related to the pressure drop when opening the valve to a second known volume. One hundred runs were performed and averaged to extract the density at room temperature.
Thermal diffusivity was determined using a Netzsch LFA 467 HT. For this, pellets of 10 mm in diameter were pressed from each material and coated with graphite. The thickness of the samples was determined using the Olympus LEXT OLS5000 confocal microscope. Measurements were conducted under a nitrogen flow of 50 mL min^{-1} and each sample was measured three times at every temperature. The detector's field of view was adjusted using the build-in ZoomOptics system to only measure an area of 2.8 mm in diameter. In this way, a homogeneous sample thickness can be expected while, furthermore, signal falsifications due to the sample environment (e.g., masks or apertures) are excluded. Data analysis was performed using a single-layer Cape-Lehman model, taking into account heat losses on all sides.

9.3.5 Computational Details

All DFT calculations were performed within the generalized gradient approximation of Perdew−Burke−Ernzerhof (PBE)[28] as implemented in the Vienna Ab−initio Software Package (VASP),[29,30] using the projector augmented wave (PAW) potentials,[31] including the effect of spin-orbit coupling (SOC) self-consistently. The PAW pseudopotentials have the following atomic configurations: $2s^2 2p^3$ for N, $1s^1$ for H, $2s^2 2p^2$ for C, $6s^2 6p^2$ for Pb and $5s^2 5p^5$ for I. For RP perovskites BA_2PbI_4 and PEA_2PbI_4 we sampled the first Brillouin zone using Γ-centered **k**-point grids with $2 \times 2 \times 1$ points for the ground-state calculations and $6 \times 6 \times 2$ points for the DOS calculations, respectively, while for $MAPbI_3$ we employed a $6 \times 6 \times 6$ Γ-centered **k**-point grid. All calculations were performed using a cut-off energy for the plane-wave expansion of 500 eV and the experimental room-temperature crystal structures. To account for the on-average centrosymmetric structure of $MAPbI_3$ at room temperature and to avoid introducing artifacts related to the relative orientation of the MA molecules towards each other, we align the molecules such that they are antiparallel and their net dipole moment is zero, as would be expected on average at room temperature.[32] The structural models that were used in our static DFT calculations and as a starting point for our molecular dynamics simulations are depicted in Figure 9.1.
MLFFs were trained for BA_2PbI_4 and PEA_2PbI_4 during MD simulations with VASP, based on calculated total energies, forces, and stress tensors for automatically

(on-the-fly) selected structures in the isothermal–isobaric (NPT) ensemble. The coefficients of the MLFF are re-optimized after every DFT step. A variant of the GAP-SOAP[33,34] method is used as a descriptor of the local atomic configuration around each atom. Within a cut-off of 6 Å a two-body radial probability distribution $\rho_i^{(2)}$ is built, as well as three-body angular distribution $\rho_i^{(3)}$ within a cut-off of 5 Å. The atomic coordinates are smeared in the distributions by placing Gaussians with a width of 0.5 Å. The obtained distributions are projected on a finite basis set of spherical Bessel functions multiplied with spherical harmonics. The Bessel functions are of the order 6 and 7 for the radial and angular parts, respectively. Only the angular part has a maximal angular momentum of $l_{max} = 4$. The coefficients of the projections are gathered in the descriptor vector $\mathbf{X}_i$. A kernel-based regression method[35] is applied to map the descriptor to local atomic energy. The similarity between two local configurations is calculated by a polynomial kernel function of power 1 and 4 for the two- and three-body descriptors, respectively.
Training started from the relaxed structures corresponding to those represented in Figure 9.1 during 100 ps at 400 K with a timestep of 1.5 fs. The PBE functional, a 300 eV plane-wave cutoff, a $2 \times 2 \times 1$ Γ-centered **k**-point grid and a Langevin thermostat were applied. This was followed by constant temperature training at 300 K and 450 K, both for 100 ps. The training was concluded with cooling down from 350 to 150 K in 100 ps. In total 1245/1160 DFT calculations were done for BA_2PbI_4/PEA_2PbI_4, respectively. From these 424, 1265, 603, 165, 2004 / 144, 1200, 859, 134, 1769 (Pb, I, C, N, H), local atomic configurations were selected and constitute the basis of the fished MLFFs. These finished force fields were used to calculate the vibrational density of states (VDOS) of 300 K equilibrated $2 \times 2 \times 2$ supercells in the NVE ensemble. The open-source code: Dynamic Solids Large Ensemble Analysis Package (DS-LEAP) was used to calculate the VDOS from the 150 ps long trajectories.

9.4 Results and Discussion

9.4.1 Electronic Structure

We start by comparing the electronic structure of all three materials. Figure 9.2 shows the secondary electron cut-off (SECO) and valence band maximum (VBM) regions of 2D BA_2PbI_4 and PEA_2PbI_4 and 3D $MAPbI_3$ obtained from ultraviolet photoelectron spectroscopy (UPS), as well as the first principles DOS. The experimentally determined work function and ionization energies of the three perovskites are reported in Table 9.1, and are in close agreement with the previous reports.[22,36,37] It is worth noting that the ionization energy values of all three investigated perovskites are similar, emphasizing the fact that the frontier energy levels are

being dictated by PbI_2 irrespective of the organic cations constituting the perovskites.

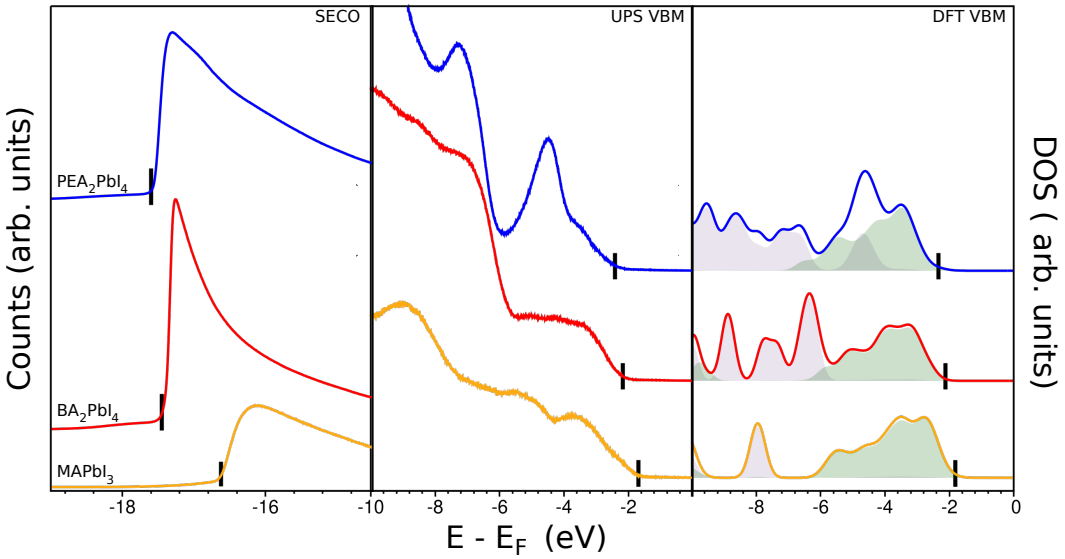

Figure 9.2: Ultraviolet photoelectron spectra (UPS) showing the secondary electron cut-off (SECO, left panel) and valence band maximum (VBM, middle panel) regions, as well as PBE total DOS (right panel) for $MAPbI_3$ (yellow), BA_2PbI_4 (red) and PEA_2PbI_4 (blue), scaled with respect to the Fermi energy level. The valence band onset is marked by a black dash line. The shaded areas in the computed DOS represent the projections onto molecular orbitals with states derived from the inorganic and organic sublattices in green and purple, respectively.

Table 9.1: Experimentally-determined work function and ionization energy of $MAPbI_3$, BA_2PbI_4 and PEA_2PbI_4.

	$\mathbf{MAPbI_3}$	$\mathbf{BA_2PbI_4}$	$\mathbf{PEA_2PbI_4}$
Work function (eV)	4.40	3.91	4.68
Ionization energy (eV)	6.09	6.08	6.10

The comparison of the DOS calculated with standard semilocal approximations of DFT with experimental photoelectron spectra is known to be complicated by several factors. First, the eigenvalue corresponding to the VBM, which should be equal to minus the ionization potential in exact Kohn-Sham DFT is typically overestimated by several electronvolts by standard semilocal approximations like PBE.[38] We, therefore, redshift our calculated DOS such that it matches the experimental VBM, i.e., the difference between the measured ionization energy and work function (see Table 9.1). Second, energetically high-lying valence bands have been shown to be in good approximations to the electron removal energies measured in a photoemission experiment, but only when calculated from very accurate electron densities.[39] Empirically one finds that the DOS calculated with PBE is compressed with respect to the experiment.[40,41] We, therefore, follow the approach by Tao[42]

and stretch our calculated DOS to match the measured spectra (corresponding to a stretch of $\sim 2.6\%$). A more rigorous approach would be the calculation of the electronic structure of all three materials within the GW approach, which allows for a more straightforward comparison with experimental photoemission spectra, but is challenging and computationally expensive for Pb-based halide perovskites and, therefore, outside the scope of this work.[43,44] Finally, it is worth mentioning that equating the electronic DOS with experimental photoemission also neglects other effects, such as those of the sample surface and the selection rules for a transition of the emitted electron from its initial to its final state.[45] However, perfect agreement with the experiment is not required for the peak assignment to the organic and the inorganic sublattices that we attempt in the following.

The right panel of Figure 9.2 shows the contributions of the inorganic and organic sublattices to the total DOS in green and purple, respectively. For all three materials, the DOS in the vicinity of the VBM is derived from electronic states associated with Pb s and I p states. For $MAPbI_3$, we find, in agreement with previous work, that MA-derived electronic states lie far below the VBM, at $\sim -8\,\text{eV}$ in our calculations. These states are well separated from the PbI-derived states at higher energies. This is different for the two RP compounds. While the DOS within $\sim 2\,\text{eV}$ below the VBM is dominated by Pb s- and I p-derived states for all three materials, the organic sublattice contributes already at $\sim -4\,\text{eV}$ for PEA_2PbI_4 and $\sim -6\,\text{eV}$ for BA_2PbI_4. In particular, our analysis allows us to assign the pronounced peak in the experimental spectrum of PEA_2PbI_4 at $\sim -4\,\text{eV}$ to the organic sublattice. The differences between the energetic positions of the electronic states derived from the organic sublattice can be explained by the HOMO-LUMO gaps of the isolated molecular cations. In Table 9.2, we compare the energy of the HOMO-LUMO gap of free-standing MA^+, BA^+, and PEA^+ with the energy difference of the energy bands derived from the organic sublattice. For all three A-site cations, the HOMO-LUMO gap is similar to the energy gap of the organic sublattice in the band structure. This analysis also shows that the differences in the energies of the molecular states arise primarily from the energetic position of the HOMO of the free-standing cations. The LUMO eigenvalues differ by $< 1\,\text{eV}$ from each other.

Table 9.2: Calculated HOMO and LUMO eigenvalues and HOMO-LUMO gaps of organic cations MA^+, BA^+ and PEA^+, the energy gap between the molecular states in the band structure of $MAPbI_3$, BA_2PbI_4 and PEA_2PbI_4.

	MA^+	**BA^+**	**PEA^+**
HOMO (eV)	-15.74	-11.56	-9.94
LUMO (eV)	-6.29	-5.79	-5.37
HOMO-LUMO gap (eV)	9.45	5.77	4.57
Energy gap (eV)	8.77	7.50	4.47

Despite the significant differences in the electronic DOS related to the different energies of the organic sublattices, the DOS of the inorganic sublattice is very similar for all three compounds. This observation is also sustained by the experimentally-determined ionization energies. As shown in Table 9.1, the ionization energies of all three materials are within 20 meV of each other, well within the resolution limit, irrespective of the dimensionality and the organic linker. Our DFT calculations allow us to track more subtle differences in the electronic structure of the three materials. The most striking difference between the three materials is that in the case of $MAPbI_3$, the DOS close to the VBM is primarily derived from the equatorial halides, i.e., the halide ions in the plane determined by the [100] and [010] directions in Figure 9.1, whereas in the case of BA_2PbI_4 and PEA_2PbI_4 it is derived from contributions of the axial halides, i.e., the halide ions along [001] direction in Figure 9.1. Furthermore, differing structural distortions of the inorganic sublattice as compared to perfect cubic symmetry lead to further changes in the electronic DOS in the vicinity of the VBM. The two RP perovskites feature an off-center displacement of the Pb ions, leading to alternating short and long Pb-I equatorial bond lengths. PEA_2PbI_4 further features distorted octahedra, which are compressed in the perovskite plane and elongated along the stacking direction, with alternating tilt angles. In contrast, the octahedra of BA_2PbI_4 are compressed in the stacking direction and elongated in the perovskite plane.

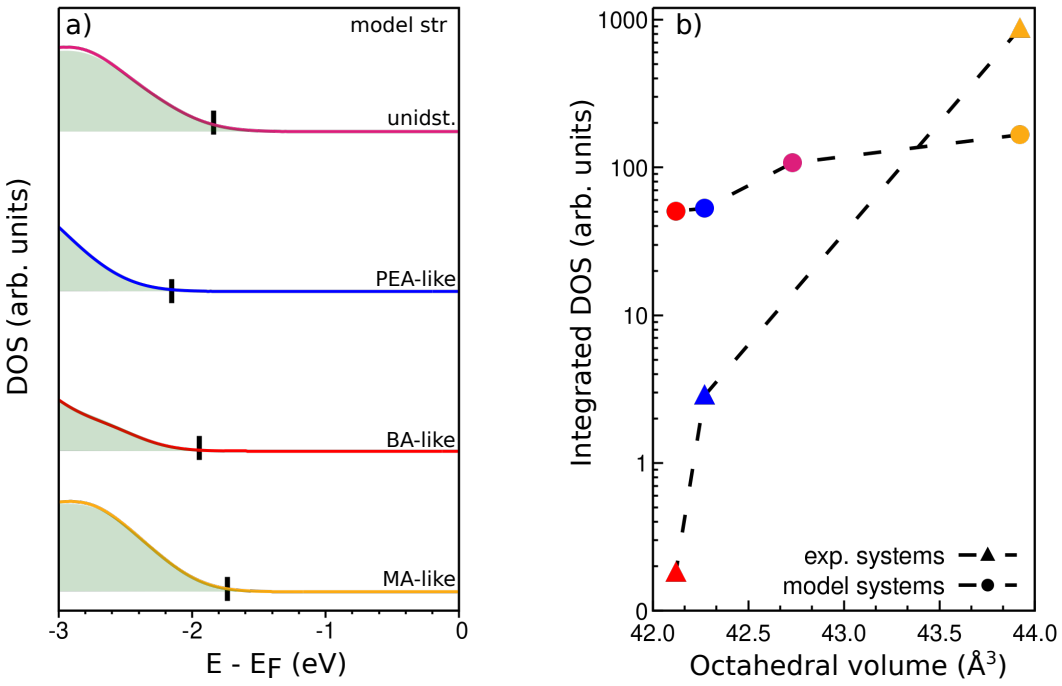

Figure 9.3: a) Calculated total DOS for distorted systems featuring MA-like (yellow), BA-like (red), PEA-like (blue) distortions as well as for the undistorted model (magenta). b) Integrated DOS for all experimental and model systems as a function of octahedral volume. The color of the points corresponds to the systems in panel a).

To differentiate between direct and indirect the effects of the organic sublattice on the electronic DOS, we constructed a set of model systems with layer thickness $n = 1$, in which we replaced the organic cation with Cs^+. First, we constructed an undistorted model system with untilted and undistorted metal-halide octahedra with Pb-I bond lengths of 3.15 Å as found in the cubic $Pm-3m$ phase of $MAPbI_3$. Second, we constructed model systems with distortions equivalent to those in the experimental structure of room temperature $MAPbI_3$, BA_2PbI_4, and PEA_2PbI_4. We refer to these structural models as MA-, BA- and PEA-like distorted systems in the following. Note that the experimental structures are RP phases with four octahedra per unit cell, two of which are in adjacent layers. Our model systems are monolayers with two octahedra per unit cell. Because interactions between adjacent layers are negligible in the experimental structures, this choice does not change our conclusions regarding the electronic DOS of our model systems. In order to avoid spurious interactions between periodic images in the model structures, a vacuum layer of at least 20 Å was introduced, and a dipole correction was applied in all calculations.

The electronic DOS of these systems is shown in Figure 9.3a. The comparison clearly shows that the different types of octahedral tilts and distortions in the four model systems lead to significant differences in the DOS close to the VBM. We quantify these differences by integrating the DOS from the VBM to ~ 30 meV below the VBM (corresponding to $E = k_BT$ at room temperature) for both the experimental structures and the model systems. As expected, we observe a stark dependence on the dimensionality, in agreement with previous reports.[46,47] Figure 9.3b shows that the integrated DOS is correlated with the octahedral volume; smaller volumes are correlated with larger distortions in these three systems, leading to fewer states within the analyzed energy range, a trend confirmed for both experimentally-determined structures and model systems.

9.4.2 Thermal Properties

We carried out low frequency (below 200 cm^{-1}) non-resonant Raman measurements in the temperature range of 298 K and 363 K. In Figure 9.4a, Raman spectra of BA_2PbI_4 and PEA_2PbI_4 pellets measured between 40 to 200 cm^{-1} at 298 K are shown. The deconvolution and unambiguous spectral assignment of Raman peaks from 2D perovskites are not straightforward as there is no consensus agreement among earlier reports on similar systems. For example, Dragomir[48] investigated both BA_2PbI_4 and PEA_2PbI_4 and assigned all peaks observed below 100 cm^{-1} exclusively to in- and out of phase Pb-I stretching vibrations and octahedral rotation; spectral features in the $100-200$ cm^{-1} range are attributed to convoluted torsional and libration modes of the organic cations, which is supported by a few other reports.[49–51]. On the other hand, Dhanabalan[24] and Maczka[52] identify the

peaks obtained from similar 2D perovskites located up to 150 cm^{-1} as originating from Pb-X stretching mode. In contrast, a detailed analysis of vibrational modes in tetragonal 3D methylammonium lead iodide by Leguy[53] attributes many Raman modes observed below 150 cm^{-1} to organic cation coupled lattice motions.

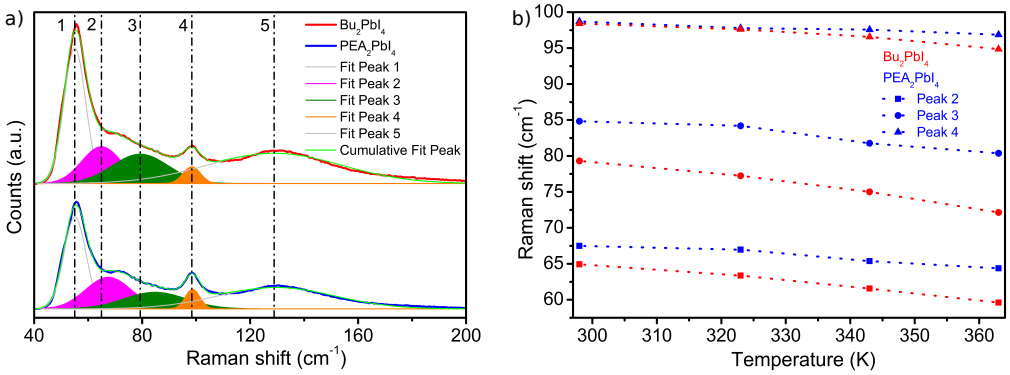

Figure 9.4: a) non-resonant Raman spectra of BA_2PbI_4 (red) and PEA_2PbI_4 (blue) pellets measured at room temperature (298 K) and the corresponding peak fits including the cumulative peak; the dash-dot lines are guide to eye, marking the fitted peaks maxima; b) Temperature dependent Raman shift of peak 2 (square), peak 3 (circle) and peak 4 (triangle) measured from BA_2PbI_4 (red) and PEA_2PbI_4 (blue) pellets.

Based on these reports, both spectra are deconvoluted into five individual components (peak 1, 2, 3, 4, and 5) as shown in Figure 9.4a.[48] Notably, satisfactory fits were obtained only through Gaussian functions, indicating an inhomogeneous broadening of the peaks arising from orientation and/or positional disorder of the organic cations in the Pb-I cages.[53] Due to the cut-off frequency of the optical filter used, spectral features below 50 cm^{-1} are not considered in the discussion. Given the broad nature of peak 5 and its inconclusive origin, only peaks 2, 3, and 4, which are attributed to the Pb-I stretching and octahedral rotational motions, are taken for further investigation on structural distortion in both systems.

The temperature-dependent Raman shifts of peaks 2, 3, and 4 are displayed in Figure 9.4b. At room temperature, peaks 2 and 3 of PEA_2PbI_4 are located slightly at higher frequency values compared to those of BA_2PbI_4, indicating a lower force constant for Pb-I bonds from the distorted octahedral core structure in the latter.[24] Interestingly, this is in good agreement with our calculated model structure described in Figure 9.3. Further, with increasing temperature, all three Raman peaks redshift with varying magnitude. Such observation is trivial as an increase in temperature softens the Pb-I octahedra framework and increases the dynamic disorder.[54] Interestingly, the relative shift of all three peaks from BA_2PbI_4 is greater than in PEA_2PbI_4, suggesting higher degrees of freedom for Pb-I and the octahedral framework, and structural distortions in the former.

In addition, the line widths of these peaks calculated from Gaussian fits show a

complex trend with increasing temperature. While peak 4 of both BA_2PbI_4 and PEA_2PbI_4 broadens with increasing temperature, the line width of peaks 2 and 3 are either decreasing or remain unchanged. Such inhomogeneous broadening of peak 4 is possibly due to the increased bond length distribution resulting from increased structural disorder, which is evidently high in BA_2PbI_4, corroborating the above results.[53] On the other hand, the anomalous behavior of peaks 2 and 3 could be due to two reasons: i) peaks 2 and 3 have a strong dependency on each other and peak 1 upon peak fitting. Hence, it may lead to over interpretation of the results; ii) motional narrowing effect that concerns the increased organic cation reorientation inside the Pb-I octahedral cages at higher temperatures that could result in rapid exchange among different orientational states.[54,55]

These observations suggest the existence of dynamic structural distortions in both BA_2PbI_4 and PEA_2PbI_4. However, it is prevalent in the former. This clearly indicates that the organic cations do play a role in controlling the vibrational motions of the Pb-halide framework and, consequently, the band edge structure.

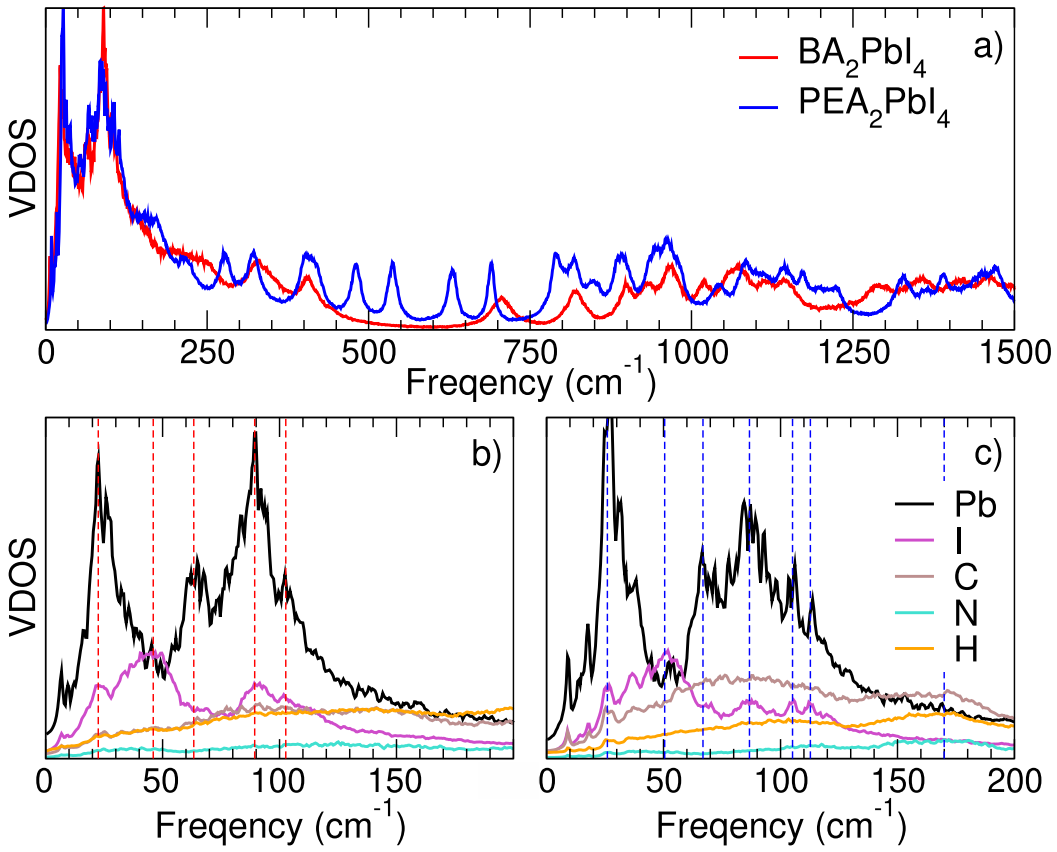

Figure 9.5: a) Vibrational density of states simulated at 300 K using molecular dynamics. The spectrum of b) BA_2PbI_4 and c) PAE_2PbI_4 are decomposed into atomic contributions on the low frequency range.

We have simulated the vibrational density of states (VDOS) of both crystals at 300 K by calculating the (mass-weighted) velocity auto-correlation functions from 150 ps long molecular dynamics simulations in the micro-canonical ensemble. The interaction potentials have been created using a state-of-the-art *on-the-fly* machine learning approach. This method has near DFT accuracy and has the clear advantage that it also captures the anharmonic effects related to the conformational changes of the molecules at elevated temperatures. The resulting VDOS spectra are shown in Figure 9.5.

Figure 9.5a shows the total VDOS of both perovskites on a large frequency domain. Above 200 cm^{-1} the spectra are quite different because they show the characteristic intra-molecular vibrations of the BA and PEA molecules. However, below 200 cm^{-1}, the spectra are remarkably similar, in agreement with our Raman spectroscopy experiments. Note that the Raman spectrum only shows dipole active modes, whereas the VDOS shows all atomic vibrations. In Figure 9.5b and c, we have decomposed the low-frequency part of the VDOS into its atomic contributions. We observe that the two large peaks are vibrations of the Pb atoms at ~ 25 cm^{-1} and ~ 88 cm^{-1}. Because these peaks are also visible in the I spectrum at the same frequencies, we can attribute these to Pb-I modes. Both I spectra show a dominant peak at ~ 48 cm^{-1}. However, a matching peak is not observed in the Pb spectrum. The inorganic components show a broad (relatively featureless) distribution in the low-frequency spectrum, indicative of weak coupling to the Pb-I framework.

To remove the fast oscillations above 100 cm^{-1} from the trajectory, a running average has been computed with a window size of 333 fs. The typical tilting and rotation pattern of the PbI octahedra in the 0 K structures of Figure 9.1a,b is retained at 300 K. The BA molecules allow for tilts of the octahedra away from the direction orthogonal to the 2D perovskite plane but show (on-time average) no rotations in this plane. The opposite occurs for the PEA molecules, with no tilts but alternating clockwise, counter-clockwise rotations of the octahedra in the plane. This behavior can be understood from the immobilized orientation of the ammonia group of the molecule relative to the PbI framework. In the 3D perovskite $MAPbI_3$ the ammonia group is able to attain different orientations depending on temperature. However, the longer tails of the PEA and BA molecules serve as anchors, keeping the ammonia group in its place. For PEA, the orientations are remarkably similar to in tetragonal $MAPbI_3$, i.e. the face-diagonals of the PbI cube. And for BA the close to cartesian axes orientation are similar to the orthorhombic phase. This results in PbI distortion modes very similar as the $a^0a^0c^+$ (in Glazer notation) tetragonal and $a^-b^+a^-$ orthorhombic structure.[56] The temperature for a phase transition involving a change in the PbI distortion modes is thereby much higher than in $MAPbI_3$, because of the barrier for an ammonia group to rotate with respect to the molecular backbone. Exploratory calculations at 400 K have shown that the ammonia group of the PEA molecule can rotate. However, these are rare events and not a 'propeller' type motion.

After the thermal properties were investigated on a molecular level, the thermal stability and conductivity were also analyzed. Initially, the thermal stability was verified by thermogravimetric analysis, shown in Figure 9.6a. In general, the 2D systems show a slightly earlier decomposition onset compared to the 3D $MAPbI_3$, while there are only minor differences between PEA_2PbI_4 and BA_2PbI_4. All systems show a stepwise decomposition where firstly, the organic components are decomposed between approximately 300 °C to 500 °C, while the inorganic components decompose above 500 °C. However, it should be noted that the 2D systems exhibit light-induced degradation, as Fang *et. al* have presented.[57]

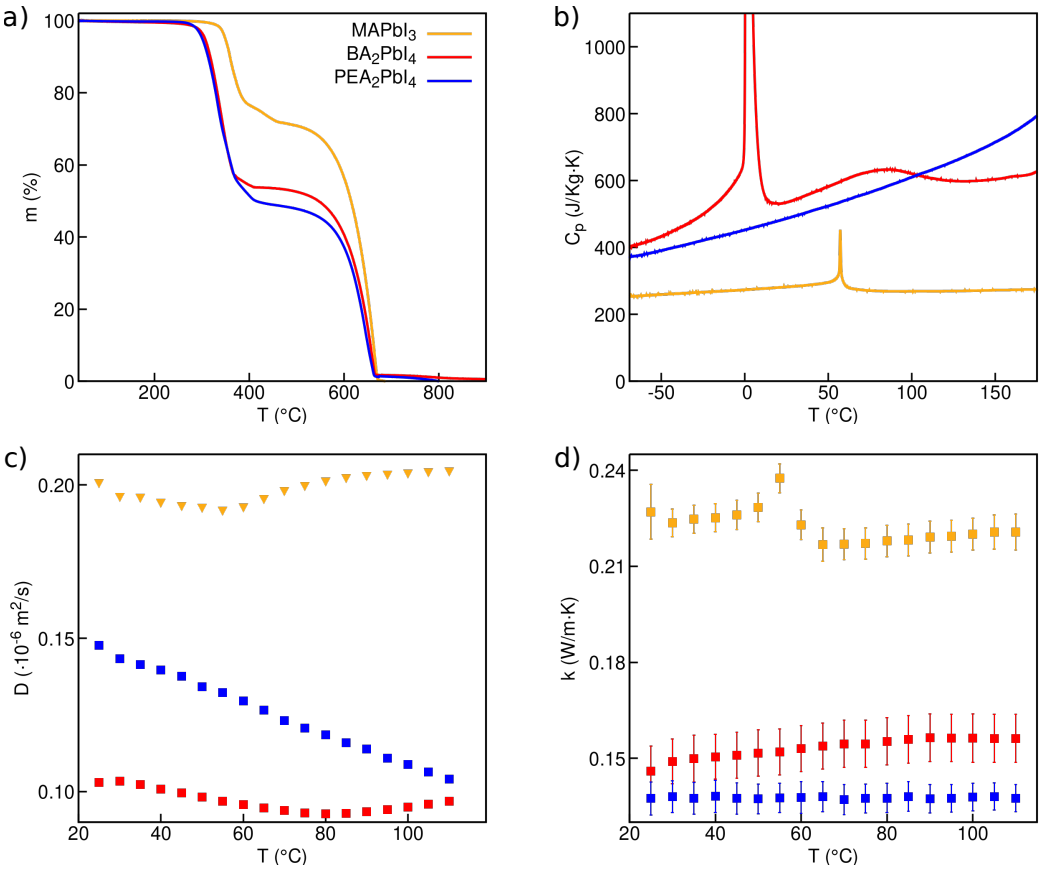

Figure 9.6: Thermal properties of $MAPbI_3$ (yellow), BA_2PbI_4 (red) and PEA_2PbI_4 (blue): a) thermogravimetric analysis, b) heat capacity, c) thermal diffusivity and d) resulting thermal conductivity.

Since thermal conductivity k is hard to access experimentally, thermal diffusivity D and volumetric heat capacity c_v, approximated as the product of specific heat at constant pressure c_p and density ρ, are measured to determine the thermal conductivity via $k = D \cdot c_v = D \cdot c_p \cdot \rho$. Peaks in the measured specific heat in Figure 9.6b can be attributed to phase transitions. While $MAPbI_3$ transitions from a tetragonal to a cubic symmetry at 54 °C, BA_2PbI_4 has an orthorhombic structure below and above 0 °C and the transition corresponds to a shift of the essentially

rigid butylammonium cations relative to the inorganic layers.[25,58,59] While the butylammonium cations are tilted with respect to the inorganic layers below 0 °C, they are almost perpendicularly arranged above the phase transition, accompanied by an increased interlayer spacing.[25]

As the dimensionality decreases, the heat capacity increases as it is a measure of how many vibrations can be excited inside the material. The order of the heat capacity matches the increasing degree of dynamic distortion as discussed above, with BA_2PbI_4 demonstrating the highest heat capacity. The heat capacity of PEA_2PbI_4 is monotonically increasing, characteristic for an organic material, while it levels off for BA_2PbI_4 at approximately 100 °C. When analyzing the density, a decrease by approximately a factor of 1.5 is observed when reducing incorporating larger organic cations. $MAPbI_3$ thereby exhibits a density of 4013 kg m^{-3}, while it reduces to 2651 kg m^{-3} for BA_2PbI_4. Further increasing the amount of organic components leads to a density of 2483 kg m^{-3} for PEA_2PbI_4. Even though hybrid halide perovskites are known to have large thermal expansion coefficients (order $10^{-3} - 10^{-4}$ K^{-1}), we consider the density to be constant. This is justified since we investigate only a small temperature range for our heat transport analysis.[60,61]

For determining the thermal diffusivity by employing XFA (Xenon-Flash Analysis) measurements, the respective materials were pressed into cylindrical pellets with 10 mm in diameter and approximately 1 mm in height. It has to be noted that thereby effective thermal properties are determined, as opposed to single crystallite measurements predominantly done in literature.[12,59–61] We, consequently, do not expect any anisotropic effects in these pellets.

PEA_2PbI_4 has a higher diffusivity than BA_2PbI_4, which might possibly be explained by π-stacking of the phenyl rings facilitating transport between neighboring cations. The different temperature dependencies of the thermal diffusivity are a measure of how fast a temperature change can propagate through the sample as a function of temperature. Here, $MAPbI_3$ and BA_2PbI_4 exhibit only a weak temperature dependency in the studied temperature regime, while for PEA_2PbI_4, a linear decrease with increasing temperature is apparent.

The resulting thermal conductivities show only minor temperature dependencies. This is known for $MAPbI_3$ in the investigated temperature regime, while it is reported for the first time for both 2D systems.[60] The two RP systems show a significantly lower thermal conductivity compared to $MAPbI_3$, while the thermal conductivity of PEA_2PbI_4 is yet lower than that of BA_2PbI_4. In this context, it seems to be the case that the increased organic layer thicknesses, or an increased amount of organic constituents, respectively, decreases the thermal conductivity slightly. This is in agreement with a recent study on the chain-length dependence of thermal conductivity in extended alkylammonium chains with the general formula $(C_nH_{2n+1}NH_3)_2PbI_4$.[59] The drop on thermal conductivity of the 2D hybrid perovskites is expected as an organic-inorganic interface is introduced that strongly hampers the thermal transport across this interface. Such behavior is known for

hybrid materials, e.g., nacre-mimetics.[62] The differentiation between PEA and BA provides some insights into the interplay between the vibrational properties of the molecular constituents and their volume phase relationship. As outlined in the discussion of the electronic properties, BA_2PbI_4 can be considered the softer specimen, exhibiting a higher degree of dynamic distortions of the inorganic framework and more degrees of freedom of the PbI bonds. Intuitively, this composite matrix should attenuate the thermal conductivity more strongly as compared to PEA_2PbI_4. These differences, however, seem to be counteracted by the presence of PEA as the interlayer cation. Even though there might be an enhanced interaction between adjacent PbI octahedral sheets due to π-stacking of the PEA moieties, this transfer channel is outweighed by the larger spacing between the sheets.

9.5 Conclusions

The influence of the organic cations on the electronic and thermal properties was investigated using first-principles calculations, ultraviolet photoelectron spectroscopy measurements, Raman measurements, and xenon flash measurements. Methylammonium lead iodide ($MAPbI_3$) was chosen as a well-studied model system, and butylammonium (BA_2PbI_4) and phenylethylammonium (PEA_2PbI_4) as large organic cations that lead to the formation of 2D structures due to their size. The ionization energies of all structures are similar, which can be assigned to lead iodide states that provide the highest energy levels for all systems. Even as the energy states originating from the organic cations lie below the valence band maximum, the distance to the valence band maximum is affected by varying the cation. Increasing the size from methylammonium to butylammonium to phenethylammonium, the energy states of the organic cation approach the valence band maximum. The energetic positions of the electronic states derived from the organic sublattice can be explained by the HOMO-LUMO gaps of the isolated molecular cations. It is furthermore shown that the differences in the energies of the molecular states arise primarily from the energetic position of the HOMO of the free-standing cations. In contrast, the LUMO shows only minor deviations between the cations. Furthermore, we demonstrate that the distortions of the PbI_6 octahedra mainly determine the shape of the density of states near the valence band maximum. The distortions increase from methylammonium over butylammonium to phenethylammonium leading to fewer states close to the valence band maximum, which is also observed experimentally.

Raman measurements and vibrational density of states, based on molecular dynamics simulations, revealed a satisfying agreement and were able to provide further insights into the molecular motions of these materials at room temperature. The temperature-dependent measurements further showed a stronger temperature de-

pendency for BA_2PbI_4, which was assigned to higher degrees of freedom for the inorganic lattice in this compound, while the inorganic lattice is more restricted in PEA_2PbI_4. The thermal conductivity of pressed pellets displays a decrease from $MAPbI_3$ (0.22 W m^{-1} K^{-1}) over BA_2PbI_4 (0.14 W m^{-1} K^{-1}) to PEA_2PbI_4 (0.13 W m^{-1} K^{-1}). The lower thermal conductivity of BA_2PbI_4 and PEA_2PbI_4 is mainly attributed to the reduced dimensionality, which significantly impedes thermal transport perpendicular to the inorganic sublattice. Additionally, the lower thermal conductivity of PEA_2PbI_4 compared to BA_2PbI_4 is attributed to an increased organic layer thickness or an increased amount of organic constituents, which counteracts the overall softer framework of BA_2PbI_4.
Overall, we developed an atomistic understanding of the effects of dimensional reduction and the interplay between the inorganic framework and the organic interlayers on the electronic and thermal properties of the selected RP perovskites. Whereas distortions by the organic interphase strongly influence the electronic properties, a much less pronounced effect was observed for the thermal transport properties. These are more strongly influenced by the introduction of interfaces and the interlayer distance.

9.6 Acknowledgement

This work was supported by the Bavarian State Ministry of Science and the Arts through the Collaborative Research Network Solar Technologies go Hybrid (SolTech), the Elite Network Bavaria, and the German Research Foundation (DFG) through SFB840 B7, and through computational resources provided by the Bavarian Polymer Institute (BPI). R.B. acknowledges support by the DFG program GRK1640.

9.7 References

[1] J. Jeong, M. Kim, J. Seo, et al., *Nature* **2021**, *592*, 381–385.

[2] S. Kumar, J. Jagielski, S. Yakunin, et al., *ACS Nano* **2016**, *10*, 9720.

[3] Y. Yuan, J. Huang, *Accounts of Chemical Research* **2016**, *49*, 286.

[4] T. Zhang, C. Hu, S. Yang, *Small Methods* **2020**, *4*, 1900552.

[5] C. C. Stoumpos, C. D. Malliakas, J. A. Peters, et al., *Crystal Growth and Design* **2013**, *13*, 2722.

[6] H. Wei, Y. Fang, P. Mulligan, et al., *Nature Photonics* **2016**, *10*, 333.

[7] I. C. Smith, E. T. Hoke, D. Solis-Ibarra, M. D. McGehee, H. I. Karunadasa, *Angewandte Chemie International Edition* **2014**, *53*, 11232–11235.

[8] L. N. Quan, M. Yuan, R. Comin, et al., *Journal of the American Chemical Society* **2016**, *138*, 2649–2655.

[9] D. H. Cao, C. C. Stoumpos, O. K. Farha, J. T. Hupp, M. G. Kanatzidis, *Journal of the American Chemical Society* **2015**, *137*, 7843.

[10] C. C. Stoumpos, D. H. Cao, D. J. Clark, et al., *Chemistry of Materials* **2016**, *28*, 2852.

[11] J. Gebhardt, Y. Kim, A. M. Rappe, *Journal of Physical Chemistry C* **2017**, *121*, 6569.

[12] A. Giri, A. Z. Chen, A. Mattoni, et al., *Nano Letters* **2020**, *20*, 3331.

[13] M. B. Fridriksson, S. Maheshwari, F. C. Grozema, *Journal of Physical Chemistry C* **2020**, *124*, 22096–22104.

[14] H. Tsai, W. Nie, J.-C. Blancon, et al., *Nature* **2016**, *536*, 312.

[15] T. Ishihara, J. Takahashi, T. Goto, *Solid State Communications* **1989**, *69*, 933–936.

[16] E. A. Muljarov, S. G. Tikhodeev, N. A. Gippius, T. Ishihara, *Physical Review B* **1989**, *51*, 14370.

[17] K. Gauthron, J.-S. Lauret, L. Doyennette, et al., *Optics Express* **2010**, *18*, 5912.

[18] K. Tanaka, T. Takahashi, T. Kondo, et al., *Physical Review B* **2005**, *71*, 045312.

[19] J. C. Blancon, A. V. Stier, H. Tsai, et al., *Nature Communications* **2018**, *9*, 2254.

[20] Y. Cho, T. C. Berkelbach, *Journal of Physical Chemistry Letters* **2019**, *10*, 6189–6196.

[21] M. Palummo, S. Postorino, C. Borghesi, G. Giorgi, *Applied Physics Letters* **2021**, *119*, 051103.

[22] S. Silver, J. Yin, H. Li, J.-L. Brédas, A. Kahn, *Advanced Energy Materials* **2018**, *8*, 1703468.

[23] H. Du, H. Hu, *IOP Conference Series: Earth and Environmental Science* **2017**, *69*, 012176.

[24] B. Dhanabalan, Y.-C. Leng, G. Biffi, et al., *ACS Nano* **2020**, *14*, 4689–4697.

[25] D. G. Billing, A. Lemmerer, *Acta Crystallographica Section B* **2007**, *63*, 735–747.

[26] K.-Z. Du, Q. Tu, X. Zhang, et al., *Inorganic Chemistry* **2017**, *56*, 9291–9302.

[27] A. Poglitsch, D. Weber, *Journal of Chemical Physics* **1987**, *87*, 6373–6378.

[28] J. P. Perdew, K. Burke, M. Ernzerhof, *Physical Review Letters* **1996**, *77*, 3865–3868.

[29] G. Kresse, J. Hafner, *Physical Review B* **1993**, *47*, 558–561.

[30] G. Kresse, J. Furthmüller, *Physical Review B* **1996**, *54*, 11169–11186.

[31] J. Klimes, M. Kaltak, G. Kresse, *Physical Review B* **2014**, *90*, 075125.

[32] L. Leppert, S. E. Reyes-Lillo, J. B. Neaton, *Journal of Physical Chemistry Letters* **2016**, *7*, 3683–3689.

[33] A. P. Bartók, M. C. Payne, R. Kondor, G. Csányi, *Physical Review Letters* **2010**, *104*, 136403.

[34] A. P. Bartók, R. Kondor, G. Csányi, *Physical Review B* **2013**, *87*, 184115.

[35] C. M. Bishop, *Pattern Recognition and Machine Learning*, Springer New York, **2011**.

[36] S. Olthof, K. Meerholz, *Scientific Reports* **2017**, *7*, 40267.

[37] J. Yang, S. Xiong, J. Song, et al., *Advanced Energy Materials* **2020**, *10*, 2000687.

[38] S. Kümmel, L. Kronik, *Reviews of Modern Physics* **2008**, *80*, 3.

[39] D. P. Chong, O. V. Gritsenko, E. J. Baerends, *Journal of Chemical Physics* **2002**, *116*, 1760.

[40] T. Körzdörfer, S. Kümmel, *Physical Review B* **2010**, *82*, 1–9.

[41] J. Endres, D. A. Egger, M. Kulbak, et al., *Journal of Physical Chemistry Letters* **2016**, *7*, 2722.

[42] S. Tao, I. Schmidt, G. Brocks, et al., *Nature Communications* **2019**, *10*, 2560.

[43] M. R. Filip, F. Giustino, *Physical Review B* **2014**, *90*, 245145.

[44] L. Leppert, T. Rangel, J. B. Neaton, *Physical Review Materials* **2019**, *3*, 103803.

[45] D. Golze, M. Dvorak, P. Rinke, *Frontiers in Chemistry* **2019**, *7*, 377.

[46] L. Zhang, W. Liang, *Journal of Physical Chemistry Letters* **2017**, *8*, 1517–1523.

[47] Y.-Q. Zhao, Q.-R. Ma, B. Liu, et al., *Nanoscale* **2018**, *10*, 8677–8688.

[48] V. A. Dragomir, S. Neutzner, C. Quarti, et al., Lattice vibrations and dynamic disorder in two-dimensional hybrid lead-halide perovskites, **2018**.

[49] D. Cortecchia, S. Neutzner, A. R. Srimath Kandada, et al., *Journal of the American Chemical Society* **2017**, *139*, 39–42.

[50] T. Ivanovska, C. Quarti, G. Grancini, et al., *ChemSusChem* **2016**, *9*, 2994–3004.

[51] C. Quarti, E. Mosconi, F. De Angelis, F. D. Angelis, *Chemistry of Materials* **2014**, *26*, 6557.

[52] M. Mcaczka, M. Ptak, A. Gagor, D. Stefanska, A. Sieradzki, *Chemistry of Materials* **2019**, *31*, 8563–8575.

[53] A. M. A. Leguy, A. R. Goñi, J. M. Frost, et al., *Physical Chemistry Chemical Physics* **2016**, *18*, 27051–27066.

[54] N. S. Dahod, A. France-Lanord, W. Paritmongkol, J. C. Grossman, W. A. Tisdale, *Journal of Chemical Physics* **2020**, *153*, 044710.

[55] K. Nakada, Y. Matsumoto, Y. Shimoi, K. Yamada, Y. Furukawa, *Molecules* **2019**, *24*, 626.

[56] P. S. Whitfield, N. Herron, W. E. Guise, et al., *Scientific Reports* **2016**, *6*, 35685.

[57] H.-H. Fang, J. Yang, S. Tao, et al., *Advanced Functional Materials* **2018**, *28*, 1800305.

[58] M. Wang, S. Lin, *Advanced Functional Materials* **2016**, *26*, 5297–5306.

[59] M. A. J. Rasel, A. Giri, D. H. Olson, et al., *ACS Applied Materials & Interfaces* **2020**, *12*, 53705–53711.

[60] C. Ge, M. Hu, P. Wu, et al., *Journal of Physical Chemistry C* **2018**, *122*, 15973–15978.

[61] R. Heiderhoff, T. Haeger, N. Pourdavoud, et al., *The Journal of Physical Chemistry C* **2017**, *121*, 28306–28311.

[62] T. Dörres, M. Bartkiewicz, K. Herrmann, et al., *ACS Applied Nano Materials* **2022**, *5*, 4119–4129.

10

High-Temperature Thermal Transport in Porous Silica Materials: Direct Observation of a Switch from Conduction to Radiation

Anna M. Neuhöfer,* Kai Herrmann,* Flora Lebeda,* Tobias Lauster,* Christoph Kathmann,§ Svend-Age Biehs,§ and Markus Retsch*

* Department of Chemistry, Physical Chemistry 1, University of Bayreuth, Universitätsstraße 30, 95447 Bayreuth, Germany.

§ Institute of Physics, Carl von Ossietzky Universität, 26111 Oldenburg, Germany.

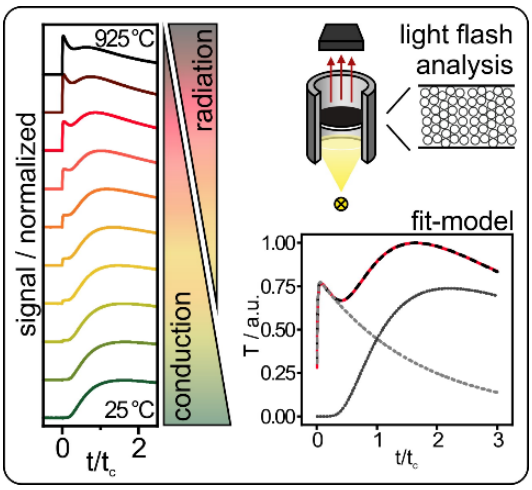

Published in *Advanced Functional Materials*, **2021**, *32*, 2108370.

10.1 Abstract

Efficient thermal insulation at high temperatures poses stringent requirements on suitable materials. Low density, porous inorganic structures with pore sizes in the sub-micrometer range are of particular interest for such materials to control heat conduction. Simultaneously, thermal radiation has to be suppressed, which depends on the optical properties of the constituents. Here, the authors demonstrate a direct observation of the transition from a conduction dominated to a radiation dominated thermal transport mechanism for the case of particulate silica materials at temperatures reaching up to 925 °C. A detailed analysis of the radiative transport through bulk silica as well as solid and hollow silica particles is provided. Optical transparency at high temperatures is the driving force, whereas surface wave modes barely contribute, particularly in case of the insulating particle packings. The existing analytical framework of laser flash analysis is extended to qualitatively describe the radiative and conductive heat transport by two independent diffusive transport models. The analysis provides a better understanding of the challenges to fabricate and analyze efficient thermal insulation materials at high operating temperatures, where multiple heat transport mechanisms need to be controlled.

10.2 Introduction

Thermal insulation plays an enormous role in various applications in everyday life, like buildings, automobiles, the oil and gas industry, and aerospace components. Aerogels - typically made from carbon or silica - are compelling materials for thermal insulation. Especially silica is suitable for thermal applications owing to its low thermal conductivity, high melting temperature, and chemical inertness. Furthermore, silica is naturally abundant and can be recycled after usage.

Colloidal structures based on hollow silica spheres can be regarded as high-density aerogels with a hierarchical pore structure. Aerogels have densities between 1 and 1000 kg/m^3,[1] while the density of hollow silica particle assemblies is in the range of 180 to 883 kg/m^3.[2] Colloidal assemblies have the advantage of easier fabrication due to the absence of a supercritical drying procedure. Furthermore, their well-defined pore sizes simplify the determination of structure-property relationships.

Most of the thermal insulation applications of aerogel materials have been considered at ambient temperatures. However, heat insulation at high operating temperatures is of great relevance for power plants, manufacturers, and aerospace. The thermal properties of insulating samples at high temperatures have been typically determined by the hot wire or hot plate techniques.[3–8] One drawback of these techniques is that relatively large samples with diameters up to 20 cm and several centimeter thicknesses are needed for the measurements. In case of the transient hot disc method

even two identical specimens are required. Therefore, high temperature (HT) laser flash analysis (LFA) would be an interesting alternative, because just one sample with a diameter of 1 cm and a few millimeters thickness is needed. The LFA method has been well-established for room temperature (RT) measurements on a wide range of samples, including composites, monoliths, polymers, to name a few. Ruckdeschel et al. performed LFA on colloidal crystals from hollow silica nanoparticles and examined the thermal transport mechanisms.[2,9] While Ruckdeschel et al. examined the size range of $250 - 500$ nm, Mofid et al. examined the thermal properties of the sub 100 nm region.[10] There are few cases where LFA was used for aerogel samples up to 1500 °C. They have been performed by Wiener et al.[11] and Feng et al.[12] However, the groups used carbon aerogels, which render them opaque across a wide spectral range.

The overall thermal conductivity of porous materials, like aerogels and colloidal structures, can be described by three contributions: solid and gaseous conduction and radiation. Solid conduction takes place in the amorphous silica matrix material. The microstructure of the materials dictates the thermal conductivity in the solid conduction case. Amorphous structures, inclusions of defects, or micropores reduce the thermal conductivity through the skeleton of the porous material.[13]

Gaseous conduction takes place in the pores in the aerogel or between and in the (hollow) nanoparticles. It is strongly influenced by the Knudsen effect when the mean free path of the gas equals or exceeds the pore size of the surrounding system.[14] For nitrogen gas, the mean free path is between 88 nm at 25 °C and 354 nm at 925 °C,[15] precisely in the region of colloidal crystals under investigation here. Therefore, the Knudsen effect plays a significant role in gaseous conduction, and is strongly reduced due to the strong confinement in pores smaller than 100 nm.

Radiation describes the effect that a surface emits electromagnetic waves due to its temperature. This energy is absorbed by another surface and reemitted, and so forth.[16] Every matter with temperatures above 0 K emits thermal radiation. An idealized object that absorbs all incident radiation and emits with an emissivity of unity is called a black body radiator. The emissive power of other surfaces is compared to this maximum performance and is a fraction of one. For highly insulating applications, the contribution of thermal radiation shall be suppressed as much as possible. This is achieved for polymer foams and aerogels by the addition of opacifiers,[17] like carbon,[4,6,18,19] or doping with materials such as Y_2O_3.[20] The group of Prof. Fricke has developed a thorough understanding of heat transport in aerogels.[4,6,7] They found that for high-density aerogels the solid conduction is the main transport path. Gaseous conduction and radiation become more critical with lower density. Heinemann et al. were able to show that there is a complex interaction of radiation and conduction inside the sample, while conduction predominates at the boundaries.[4,6] In the last ten years, the theoretical description of radiative heat transfer in many-body systems including the contribution of near-field effects has made great progress.[21] In particular, heat radiation in nanoparticle assemblies

Table 10.1: Density, ρ, thermal diffusivity, α, and thermal conductivity, κ, at 25 °C of the colloidal glasses from particles with diameter, d_p, and shell thickness, d_s.

Sample	d_p [nm]	d_s [nm]	ρ [g/cm^3]	α [mm^2/s]	κ [W/m K]
SiO_2 hollow small	287	29	0.594	0.251	0.111
SiO_2 hollow big	882	31	0.219	0.226	0.037
SiO_2 solid small	353		1.362	0.164	0.166
SiO_2 solid big	889		1.347	0.113	0.113
SiO_2 solid huge	8000		1.150	0.181	0.155

has been studied in a large numbers of works within the dipole approximation.[22] Within this approximation the radiative heat conductivity can be calculated in systems composed of several thousand or ten thousand nanoparticles.[23,24] However, this method is strictly speaking not applicable in dense colloids because higher multipole moments need to be included if the center-to-center distance between the nanoparticles is smaller than about three to four times the particle radius[25] which corresponds in a cubic lattice to a filling fraction of only 7% to 12%. Including these higher multipole makes the theoretical evaluation of the heat conductivity in many-body systems difficult. Since our samples are relatively large and dense we chose for the optical modelling an effective multilayer approach similar to Sakatani et al.[26] to calculate the radiative heat conductivity in powdered materials, but with the extension that we include near-field effects, i.e. the contribution of evanescent waves.

Our investigation uses the time resolution of high-temperature LFA measurements to unravel the gradual transition from solid conduction to radiative heat transport. We apply this unique advantage, which is not accessible by steady-state characterization methods, to colloidal glasses made from SiO_2 and TiO_2 solid and hollow particles. We work out the existence of these two transport processes in such porous materials and relate them to their optical properties.

10.3 Results and Discussion

We base our analysis on two types of porous silica materials, one comprising solid, the other comprising hollow spheres, owing to their high thermal insulation capability. We investigated for each type two samples of comparable size (*ca.* 300 nm and *ca.* 800 nm) and complement this data set with one batch of large *ca.* 8 μm sized solid silica beads. Owing to the filtration fabrication process, these particle assemblies can be considered colloidal glasses (Figure 10.9). The key geometries and resulting density data are summarized in Table 10.1. We measured LFA on these SiO_2 hollow and solid particles in a temperature range from $25 - 925$ °C (Figure 10.1). We represent the raw data of the time-dependent temperature evolution on the top surface of the samples in a normalized fashion. Precisely, we normalized the intensity

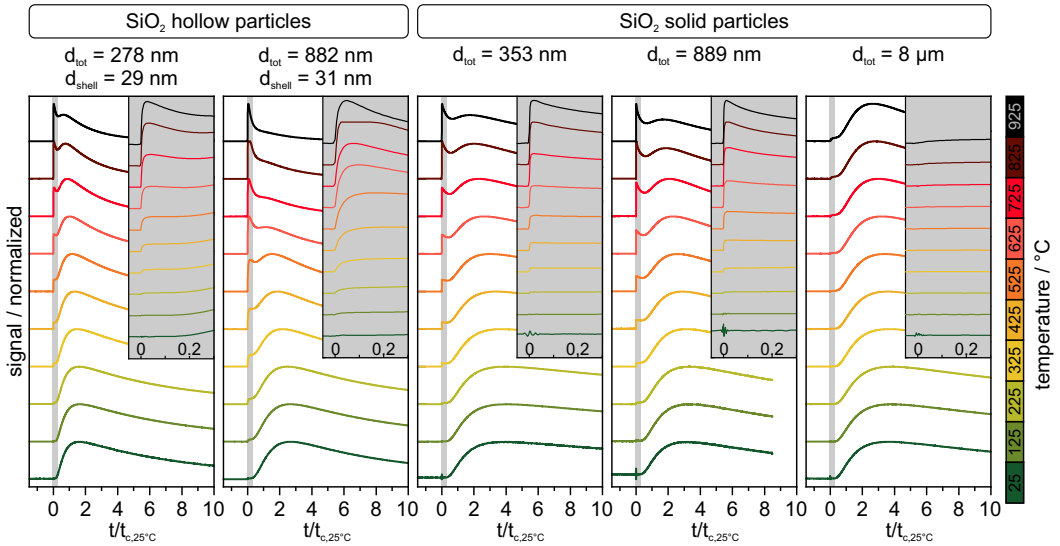

Figure 10.1: Temperature-dependent LFA measurement signal of SiO_2 hollow and solid particles. The grey insets show details of the radiation peak. The time data is normalized by the characteristic thermal response time t_c.

data by the maximum peak intensity since only the relative temperature change is relevant for our evaluation. We also normalized the timescale to better work out the two distinct transport mechanisms. Radiative and conductive heat transport occur at different characteristic time scales. By normalizing the time at 25 °C, $t_{c,25\ ^\circ\mathrm{C}} = L^2/(\pi^2 \cdot \alpha)$, with the sample thickness, L, and the thermal diffusivity at 25 °C, α, according to Cape and Lehmann, we remove any influence from the individual sample thickness.[27] This way of time-normalization, consequently, renders the time-dependent measurements more comparable to one another. At room temperature, we observe only the conductive heat transport contribution. This is represented by the broad maximum, which slowly decays due to thermal losses to the sample holder and environment. This shape of the time dependent temperature evolution is the classic case of an LFA experiment with solely conductive transport occurring through the sample. It can be well fitted for all cases based on established models, which include the one-dimensional heat diffusion equation in combination with certain loss mechanisms. For a detailed discussion and evaluation of the data fitting procedure in LFA experiments, we refer the reader to recent literature.[28] The results for thermal diffusivity and thermal conductivity at room temperature are summarized in Table 10.1 and confirm the thermal insulation properties of such particle packings. In particular, the hollow sphere structures are strongly insulating. With increasing temperature, a second, much faster contribution starts to become more and more prominent in case of the sub-μm sized silica samples. Only the case of the 8 μm beads is still dominated by the slow process described by conduction through the particles. All other samples have two maxima – one sharp at $t/t_{c,25\ ^\circ\mathrm{C}} < 0.2$, and one broad maximum at $1 < t/t_{c,25\ ^\circ\mathrm{C}} < 4$, which we interpret as radiative and conductive transport as outlined below, respectively. The

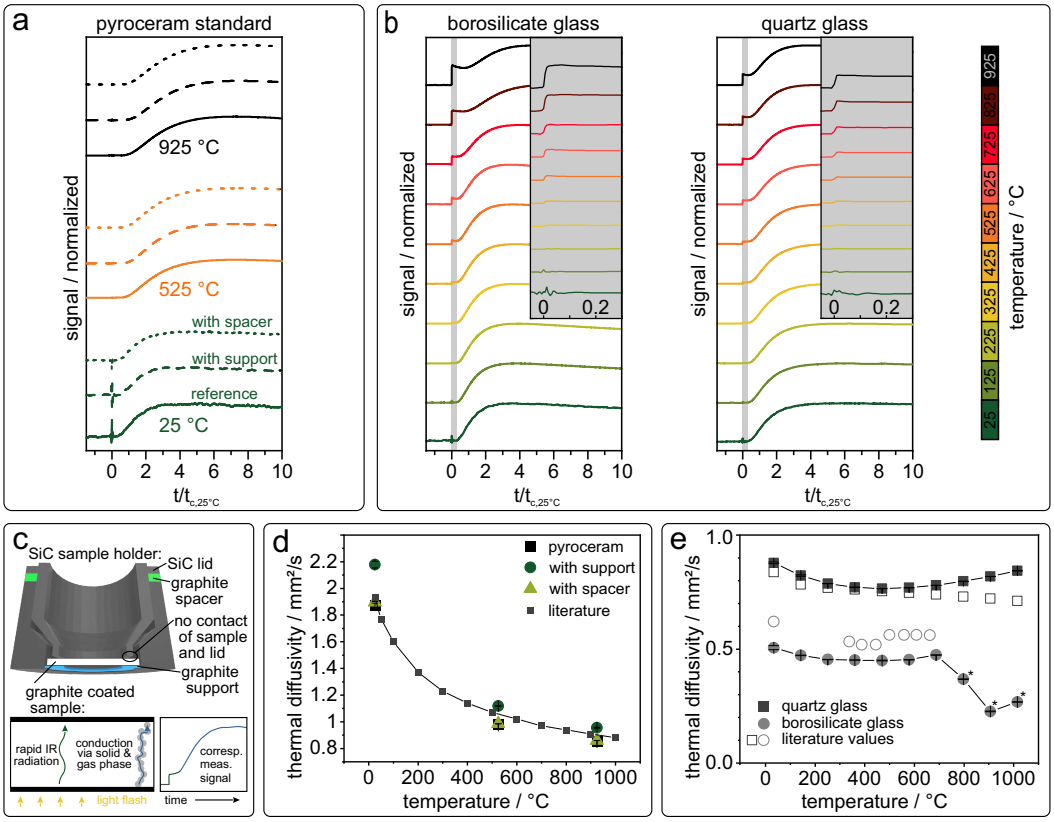

Figure 10.2: a) Temperature-dependent LFA signal of pyroceram standard, measured with modified LFA sample holder. b) Temperature-dependent LFA signal of bulk borosilicate glass and quartz glass measured with the modified sample holder. c) Illustration of modified LFA sample holder, and sketch of heat transfer processes with the corresponding measurement signal in a LFA measurement. d) The corresponding pyroceram thermal diffusivity, in comparison with literature values. e) The corresponding thermal diffusivity, in comparison to literature values.[29,30]

evolution of this fast temperature transport is most pronounced for the 882 nm hollow particles, where at 925 °C, no conduction peak is visible anymore. The time-dependent temperature profiles that we consistently observed in our sub-μm granular samples are highly unusual in the case of LFA experiments and cannot be described by the established models. Quite frankly, such data are typically coined "bad" measurements and are not considered any further. To prove the correctness of our measurements, we performed additional tests to exclude any other sources that could lead to this unique time-dependent temperature evolution at the sample surface (Figure 10.2). We, therefore, measured reference materials with known thermal diffusivities and ruled out a potential influence from our tailor-made sample holder (Figure 10.2c). This sample holder was equipped with a graphite support, which was necessary to carry the samples, which were smaller than the contact face of the original holder. Furthermore, a spacer between the holder and the lid was required to reduce the mechanical load of the lid onto the sample, which would have led to a breakage of the sample.

Figure 10.2a shows the normalized measurement data, at 25 °C, 525 °C, and 925 °C

for the original sample holder, with our graphite support, and with the graphite spacer in combination with pyroceram as standard material. The measurement data show an identical time-temperature evolution regardless of the sample holder configuration. There is no evolution of a second peak discernible. Fitting of the thermal diffusivity for this standard material provided slightly varying thermal diffusivity data, which we attribute to changes of thermal losses into the holder. Overall, a good agreement between the measured and literature data was observed for this opaque standard material (Figure 10.2d). As a second class of reference material, we measured the properties of optically transparent bulk borosilicate and quartz glass (Figure 10.2b). The corresponding thermal diffusivities and literature values are shown in Figure 10.2e. Literature values for quartz glass have been calculated according to Sergeev et al.[29] and match well with our measured data. Literature values for borosilicate glass were taken from Johnson et al.[30] and are systematically higher compared to our data. We note, however, that borosilicate glass may differ depending on the supplier, which can explain the deviations to our data. The thermal diffusivity of borosilicate glass above 625 °C decreased, because the glass softened and changed its shape.

The major difference between the pyroceram and the glass measurements is the appearance of an increasing step at $t/t_{c,25\ ^\circ\mathrm{C}} < 0.1$ for temperatures exceeding 425 °C. In contrast to the data of the hollow and solid particle samples, this radiation step is well-known and can be confidently fitted by the "transparent model" developed from the manufacturer, taking into account radiative and conductive contributions. As outlined in Figure 10.2c, this steplike increase in temperature can be associated with radiative heat transport between the sample bottom and top surface. Thermalization of the Xenon light flash, as well as mid-infrared emission and absorption, respectively, happen much faster compared to the ms time resolution of the XFA experiment. Therefore, the sample's top surface temperature is offset by a small amount, which is accounted for by the fitting procedure. When comparing the insets of Figure 10.2b and Figure 10.1, one recognizes a marked difference between the two early radiative events. A comparison of the radiation peak at $t/t_{c,25\ ^\circ\mathrm{C}} < 0.15$ is shown in Figure 10.11 in the Supporting Information. The granular samples demonstrate a marked loss in surface temperature after the initial increase, whereas the bulk material reaches a plateau. Even more important is the apparently slower temperature increase in particular in case of the hollow sphere samples. Since all bulk and particulate samples have been prepared in a comparable way, this slow temperature increase cannot be assigned to the heating dynamics of the graphitic coating layers that may vary from sample to sample in a small and non-systematic way. When looking at longer measurement times, the relative magnitude of the first steplike process to the slower broad temperature increase is vastly different between the bulk and the particulate samples. Whereas for bulk samples only a small temperature increase can be assigned to the early radiative transport, it becomes the dominant transport mechanism for solid and hollow spheres. However, owing to the

slow dynamics and high intensity the established models are not capable of fitting these two processes anymore. The fitting model becomes increasingly inaccurate for temperatures above 525 °C (Figure 10.12). Lunev et al. found a similar effect on alumina samples above 1000 °C and established a numerical model for their data.[31] For the hollow particles, the initial increase in temperature is reminiscent of the known temperature evolution of diffusive thermal transport. Even though radiative transport in non-scattering media is non-diffusive we, nevertheless, treated our measurement in a coarse approximation as a superposition of two diffusive transport processes based on the model of Cape and Lehman, which includes losses to the environment. Note that this simplified treatment uses the same diffusive thermal transport formalism for radiative and conductive transport. The temperature evolution was modeled as:

$$T(L,t) = A\sum_{m=0}^{\infty} C_{m,1}\xi_{m,1}e^{(\omega_{m,1}(t-\Delta t)/t_{c,1})} + \sum_{m=0}^{\infty} C_{m,2}\xi_{m,2}e^{(\omega_{m,2}t/t_{c,2})} \qquad (10.1)$$

where A is a parameter for the ratio between the maximum intensities of the two processes, and Δt is an initial time shift as the first process is not exclusively of diffusive nature.[27] $C_{m,i} = (-1)^m \frac{2\xi_{m,i}}{\xi_{m,i}^2+2H_i+H_i^2}$, where H_i represents the axial Biot number and $\xi_{m,i}$ is determined by $(\xi_{m,i}^2 - H_i^2)\tan(\xi_{m,i}^2) = 2\xi_{m,i}H_i$. Furthermore $\omega_{m,i} = -\frac{\xi_{m,i}^2}{\pi^2}$ and the characteristic time $t_{c,i} = \frac{L^2}{pi^2\alpha}$.

An example of this data evaluation is shown in Figure 10.3a for the small hollow spheres at 725 °C (the evaluation of the big hollow particles can be found in the Supporting Information, Figure 10.13), where both transport processes display a similar order of magnitude. There is a convincing agreement between the measured data and the applied model, which can separate the individual transport processes. This simplified model is robust for a wide temperature range, where both processes occur (Figure 10.3b) and it could also be applied to the large hollow sphere sample (Figure 10.13). Limitations of this model are conditions where one of the two processes strongly dominates, in the cases shown here at room temperature and > 900 °C. The intensity mismatch between the two processes is then too large and the fitting sensitivity insufficient for the weaker transport process. Another limitation is the timescale of the first diffusive process. The relatively slow temperature increase in case of the hollow sphere samples could be well-described. This was not possible for the solid particles anymore, where the radiative temperature increase is slightly faster, as shown in Figure 10.11. Nevertheless, we can extract from our simplified description semiquantitative information. The thermal diffusivity assigned to both processes should certainly only be taken as a rough estimate. The precondition of one-dimensional heat transport is not valid anymore in this system, where two temperature gradients on different timescales are present within the sample. The thermal diffusivity of both processes differs by two orders of magnitude and shows a negligible temperature dependence in case of the slow, conduction-based process,

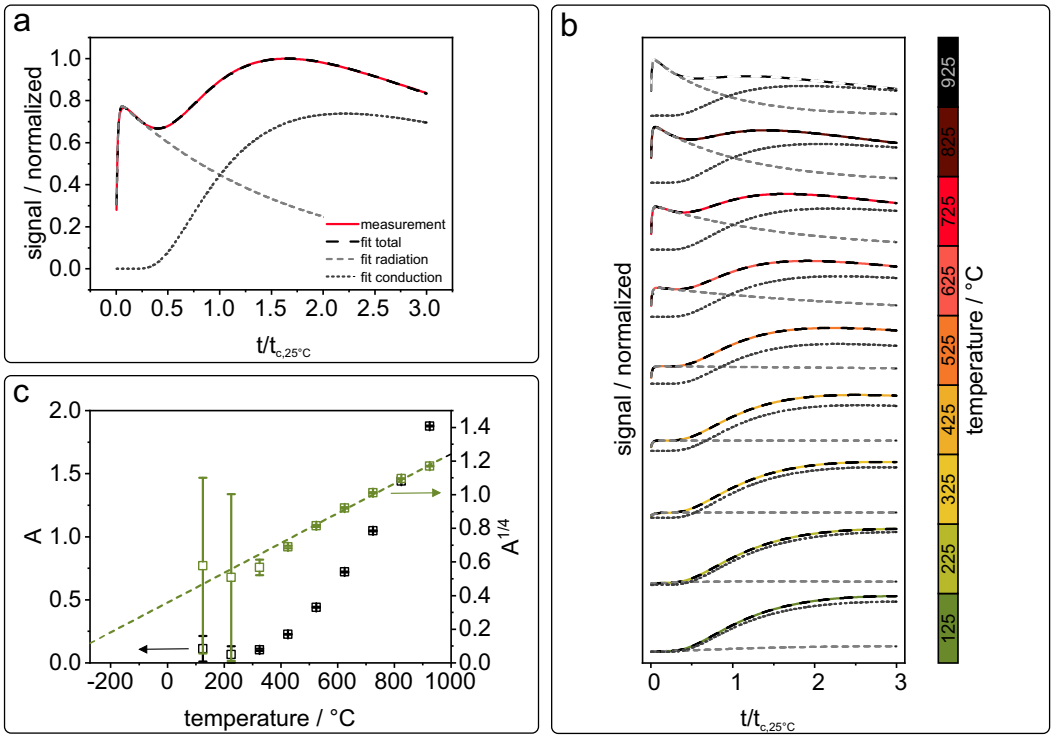

Figure 10.3: Double-diffusive model applied on 278 nm hollow particle measurements. a) Example of measurement at 725 °C. b) Application at all temperatures. c) Resulting ratio, A, of first and second diffusive process.

whereas the fast process becomes significantly faster with increasing temperature. This is commensurate with previous reports on radiative thermal transport at high temperatures, where a strongly increasing thermal conductivity has been reported.[32] Our model, furthermore, allows to quantify the temperature-dependent ratio, A, between the two processes, as shown in Figure 10.3c for the 278 nm hollow particle sample. This ratio follows a non-linear temperature dependency. It scales with T^4, owing to its radiative nature obeying Stefan-Boltzmann's law.[16]

Having outlined the direct observation of such two transport processes, we now want to turn the focus on the influence of the optical properties onto the radiative transport. The transmission spectra are shown in Figure 10.4. We find that all samples are transparent in the IR detector region between $3-5$ μm (yellow hatched area), except for the 8 μm solid silica particles. This correlates to the LFA results that did not show a distinct radiation peak for the 8 μm species. Optical transparency in this wavelength range is a precondition for radiative transport. Sub-micron sized TiO2 hollow spheres, for instance, have a comparable mesostructure to the SiO_2 hollow spheres, yet, they are fully opaque from the UV/Vis to the MIR range (Figure 10.14). Consequently, no radiative transport process could be observed (Figure 10.15). A slight reduction of the mid-infrared transmission can be achieved by inert calcination conditions of the hollow spheres, which retain a small fraction of carbon in the particles. Whereas the optical appearance changed strongly (Figure 10.16) and 10.17, the opacity in the $3-5$ μm range is not sufficient to suppress the radiative

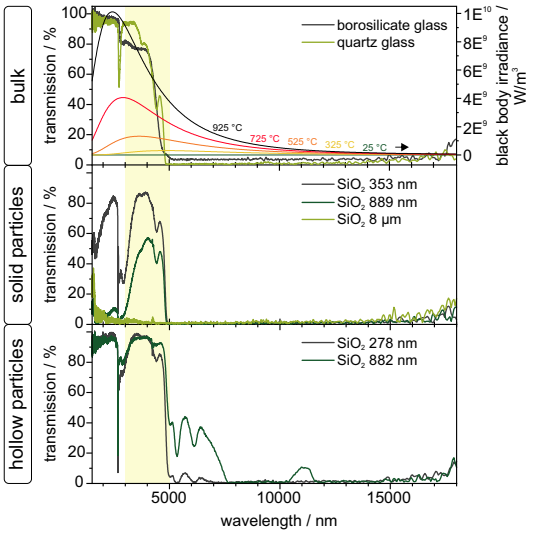

Figure 10.4: IR transmission data of bulk, solid particle, and hollow particle samples in comparison to black body irradiance. The LFA detection region between 3 and 5 μm is highlighted.

process (Figure 10.18).

To gain a deeper understanding of the radiative transport mechanism through such bulk and particulate materials, we used simulations based on the S-matrix method. These multibody calculations have been performed on a simplified two-dimensional multilayer model representing the most relevant structural parameters of our samples (Figure 10.5 left column). The model consists of top and bottom reservoirs representing the graphite coatings and in between one bulk SiO_2 layer or several SiO_2 layers with a thickness of 353 nm and 20 nm gaps, representing the small solid particle structures. Here, the assumption was made that the interparticle distance is 6% of the particle diameter, which was calculated with a 3D radial distribution function of an MD simulated particle structure (Figure 10.19). The big hollow particle structure is represented by 30 nm SiO_2 layers with 800 nm gaps, representing the hollow particle part, and 50 nm gaps, representing the interparticle distance. The calculated transmission spectra of the multilayer structure are in good agreement with the experimental data (Figure 10.5 middle column), and, therefore, can be considered a reasonable approximation to the particle structure. These models allow calculating $\tau_j^{12}(j = s, p)$, which mainly determine the modes contributing to the radiative heat flow between the two graphite layers. They contain the contributions of waves that are propagating($\kappa < k_0$) and waves that are evanescent ($\kappa > k_0$) in vacuum, where κ is the wave vector component parallel to the interface and k_0 is the wavenumber in vacuum.[33] Figure 10.5 (right column) shows the transmission τ_j^{12}, $\lambda - \kappa$ plane. In case of bulk SiO_2 radiative transport only occurs for wavelengths < 5 μm with a considerable contribution of evanescent waves. In the transparency window, the lateral wave vector κ which can propagate within SiO_2, is limited by $\sqrt{R(\epsilon_{SiO_2})}k_0 \approx 1.4k_0$. In case of the solid sphere analogous structure, we find a layer

dependence of the transmission coefficient. When increasing the number of layers from N = 9 to N = 3121 (Figure 10.20), only waves in the transparency window with $\lambda < 5$ μm can reach the second graphite layer. All other wavelengths are attenuated by the optical density of the SiO_2 particles. The solid spheres still show contributions of evanescent waves coupling to the graphitic reservoirs. It is interesting to note that there is no significant surface wave contribution in the reststrahlen band $\lambda = 8$ μm $- 9.3$ μm. We elaborated on the role of surface modes within the reststrahlen band more explicitly using a numerically exact boundary element method provided by SCUFF-EM based on 800 nm spheres (Figure 10.22). This method takes far- and near-field contributions to the transmission function into account. For two adjacent SiO_2 particles, the heat flux is indeed dominated by a surface mode at $\lambda = 9$ μm. This mode, however, quickly attenuates when including more particles. Furthermore, when considering the transmission between two graphitic objects, the major contribution originates from modes with $\lambda < 8$ μm. This is due to the fact that damping of the coupled surface modes is too strong to ensure an efficient coupling over long distances. Considering the radiative transport case through hollow silica spheres, one recognizes the absence of evanescent contributions in $\tau_p^{1,2}$. We attribute this to the increased distance between the silica surfaces. The major distance is governed by the hollow space (800 nm) inside of the silica capsules. The absence of evanescent waves is counteracted by a reduced optical density between 5 μm $< \lambda <$ 7.5 μm, where some transmission is also possible.

We used the transmission coefficients to calculate the heat transfer coefficients (htc), describing the radiative heat flow h^{12} from the graphite bottom at temperature T_1 and the heat flow h^{23} from the middle layer 2 at temperature T_2 towards the graphite top 3 at temperature T_3, where h^{12} is for small time scales the dominant contribution (see Supporting Information for details). The integrated htc of the multilayer models is shown in Figure 10.6 (left). The heat flow through the bulk silica film is larger than for the multilayer structure due to the larger contribution of the evanescent waves in the bulk film. Both particle structures feature comparable htc, which we rationalize by a compensation of the contributions of evanescent waves in case of the solid spheres and higher wavelength modes in case of the hollow spheres. Combining our double diffusive transport evaluation with the radiative transport analysis, we can draw several conclusions. Surface wave modes do not play a major role in the high temperature transport through particulate SiO_2 materials - the reststrahlen band is too far red-shifted. The optical density of the particle packing determines, which wavelengths can be transported through such structures, with a first window opening below 7.5 μm and the major contribution originating from < 5 μm. Evanescent waves are suppressed by the large porosity in the case of hollow silica beads.

We finally extended the multilayer model to also include thermal conduction through the individual layers (Figure 10.6, right, see Supporting Information for details). This calculation is based on a set of coupled differential equations, which include the

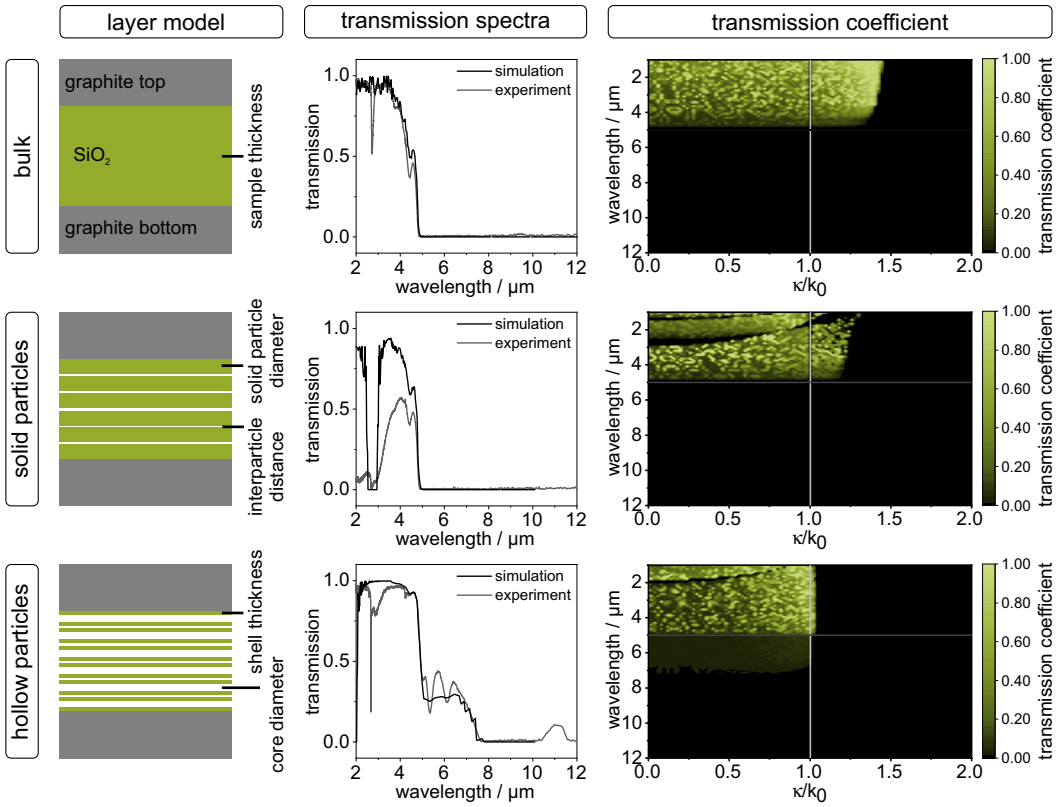

Figure 10.5: Left: Sketches of the layer model used for calculation of transmission spectra. Middle: Comparison between calculated and measured transmission spectra. Right: transmission coefficients of bulk, solid particle, and hollow particle structures.

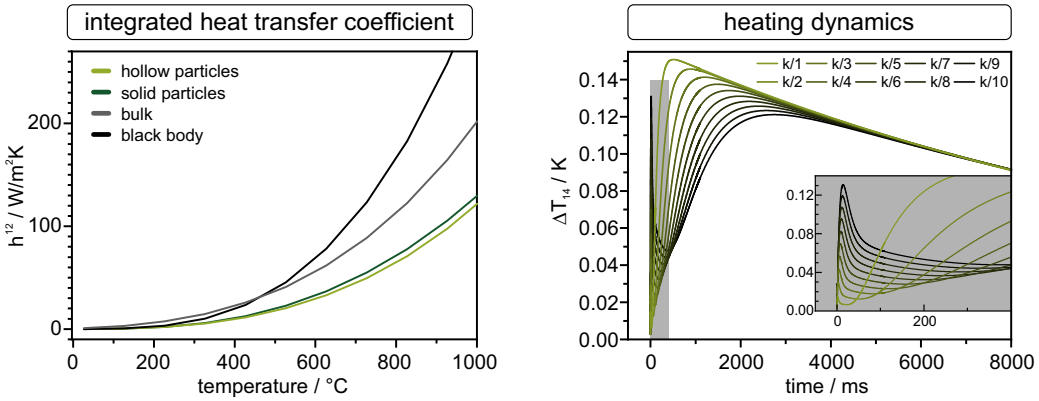

Figure 10.6: Integrated heat transfer coefficient h^{12} for hollow and solid SiO_2 particles, and bulk quartz glass, in comparison with black body radiation. The data was calculated using the multilayer model described in Figure 10.5 (left). Heating dynamics without lateral losses of the multilayer model from Figure 10.23, Supporting Information, at a temperature of 925 °C (right).

conductive and radiative heat flow between discrete layers. Two main conclusions can be drawn from this analysis. Firstly, the main features of the time-dependent temperature evolution observed in the LFA experiment are well captured by this analytic description. This corroborates our interpretation of the direct observation of a radiative and conductive heat transport process. Secondly, the systematic variation of the thermal conductivity of the solid skeleton stresses the importance of the relative heat transport capacity of these two channels. In case of a low conducting matrix, radiative transport becomes the dominant process. In case of a highly conducting matrix, radiative transport plays a subordinate role.

10.4 Summary and Conclusion

We demonstrated a direct observation of two distinct heat transport processes in mesostructured silica materials. We fabricated colloidal glasses comprising solid and hollow silica particles of 800 nm and 400 nm, respectively. The temperature evolution of the sample's top surface in an LFA experiment is dominated by a fast and a slow process. At room temperature heat conduction along the silica network dominates, rendering such silica particle packings efficient thermal insulators comparable to polymer foams. With increasing temperatures, however, thermal radiation becomes more important and finally dominant, owing to the T^4 increase in radiation power and the blue shift of the radiated wavelengths. Optical transparency in the mid-infrared range and good thermal emitters at the boundaries are preconditions to open this radiative heat transport pathway. Consequently, these silica materials lose their room-temperature insulating behavior with increasing temperature. Surface wave modes within the reststrahlen band do not contribute to this radiative transport process. Evanescent waves, on the contrary, do contribute to the overall heat transport, and are most prominent for bulk materials and ensembles of solid silica particles. The large intra-particle gaps caused by the hollow core in the case of silica capsules attenuates the contribution from evanescent waves. The radiative heat transport in hollow particle structures is slow enough to be described by a diffusive transport fit. Our results give a direct and detailed insight into the various transport mechanisms that govern high temperature heat transport. Controlling the optical properties in the mid-infrared range either by means of the composition, the structure or by adding additives is of paramount importance to maintain a strong thermal insulation behavior. The time-dependence of LFA measurements is a unique benefit to directly observe radiative and conductive thermal processes.

10.5 Experimental Section/Methods

Materials: Borosilicate glass (microscope slide, Menzel glass, Thermo Scientific) and quartz glass were cleaned with Hellmanex III (Hellma GmbH) and cut in pieces of 1x1 cm before the measurements. Sapphire discs ($d = 1$ cm, Edmund optics) were used as received.
SiO2 solid particles in three different sizes (353 nm, 889 nm, 8 μm) were purchased from microParticles GmbH and used as received. The synthesis of the SiO_2 and TiO_2 hollow particles is described in detail in the Supporting Information.
The particles were assembled using the vacuum filtration method described by Ruckdeschel et al.[34] A vacuum filtration system from Merck Millipore was used in combination with MF Millipore membrane filters with pore sizes of 0.2 μm and 0.45 μm. A Teflon funnel with a diameter of 1 cm has been used for the SiO_2 particles. A funnel with a diameter of 1.2 cm has been used for the TiO_2 particles because shrinkage of the samples during calcination has been considered. All samples have been dried at 40 °C in a vacuum overnight before calcination. The samples have been calcinated at 500 °C or 925 °C to remove organic components and avoid structural changes during the measurements.
Methods: UV-Vis measurements were conducted on a Cary 5000 (Agilent Technologies) in transmission mode with the Ulbricht sphere in the range of 250 and 2500 nm. A holder for the round-shaped samples was 3D printed for UV-Vis and IR measurements.
Infrared (IR) measurements were conducted on a VERTEX 70 spectrometer (Bruker) in the range of 1.5 and 18 μm. Transmission measurements have been made using a gold-coated integrating sphere with an MCT detector.
Laser scanning microscopy was performed using a LEXT OLS5000-SAF microscope (Olympus) to determine the sample thicknesses and volumes.
Laser Flash Analysis was conducted on a LFA 467 HT HyperFlash apparatus (Netzsch) in the range of 25 and 925 °C under a slight nitrogen stream (50 mL/min). The samples were coated with a thin layer of graphite on the top and bottom side and placed in the sample holder, equipped with self-made graphite support and spacer (Figure 10.2c).

Acknowledgements

We thank Stefan Rettinger and Tanja Feller for the help with STA and LEXT measurements, Thomas Tran for the determination of the mean particle distance and help with data evaluation, and Kishin Matsumori for some additional optical calculations. We also thank the Bavarian Polymer Institute, especially Ulrich Mansfeld and Markus Drechsler, for their help with SEM and TEM measurements.

This project was funded by the German Research Foundation (DFG RE3550/2–1). T.L. acknowledges funding by ERC Starting Grant VISIRday under Grant No. 714968, K.H acknowledges funding by SFB840, TP B7. S.-A. B. acknowledges support from the Heisenberg Programme of the German Research Foundation (DFG, project No. 404073166).

10.6 Supporting Information

10.6.1 Synthesis and Characterization of SiO_2 and TiO_2 Hollow Particles

Materials: Ammonium hydroxide solution (NH4OH, Sigma-Aldrich GmbH, 30-33%), 2,2'-azobis-(isobutyramidine) dihydrochloride (AIBA, Sigma-Aldrich GmbH, 97%), ethanol abs. (Sigma-Aldrich GmbH, $\geq$ 99.8%), 2-methacryloxyethyltrimethylammonium chloride (MTC, Sigma-Aldrich GmbH, 75% soln. in water), polyvinylpyrrolidone (PVP, Sigma-Aldrich GmbH), styrene (Sigma-Aldrich GmbH, $>$ 99%), tetraethyl orthosilicate (TEOS, Sigma-Aldrich GmbH, 98%) titanium butoxide (TBT, Sigma Aldrich GmbH, 97%) were used as received. Millipore water was taken from a Millipore Direct Q3UV unit (Merck Millipore).
2,2'-Azobis(2-methylpropionitril) (AIBN, Sigma-Aldrich GmbH) was recrystallized from ethanol before use.
Microscopy: Scanning electron microscopy (SEM) was performed using a Zeiss Ultraplus instrument using acceleration voltages of 3 kV. InLens and Everhard-Thornley detectors were used. A MATLAB circle detection function was used to evaluate the diameter of the particles. Transmission electron microscopy (TEM) measurements were performed with a JEOL JEM-2200FS field emission energy filtering transmission electron microscope (FE-EFTEM) operated at an acceleration voltage of 200 kV. Zero-loss filtered micrographs ($\Delta E \sim 0$ eV) were recorded with a bottom mounted CMOS camera system (OneView, Gatan) and processed with DM 3.3 image processing software (Gatan).
Polystyrene template particles: 217 nm particles (see Figure 10.7) were synthesized via emulsifier free emulsion polymerization.[35] For the synthesis, 1.8 g PVP (360 kg/mol), 235 mL Millipore water, 26 mL styrene, and 25 μL MTC were added to a 500 mL three-neck flask equipped with a gas inlet and reflux condenser. The emulsion was stirred at a stirring speed of 850 rpm using a large egg-shaped magnetic stirrer bar and heated to 70 °C under a slight argon flow. After 60 min 0.6 g AIBA, dissolved in 5 mL Millipore water, was added to initiate the polymerization. After the nucleation the stirring speed was reduced to 450 rpm and the reaction was allowed to continue over night. The polymerization was stopped by exposing the dispersion to ambient air and filtrated using a 125 μm nylon filter sieve. No further

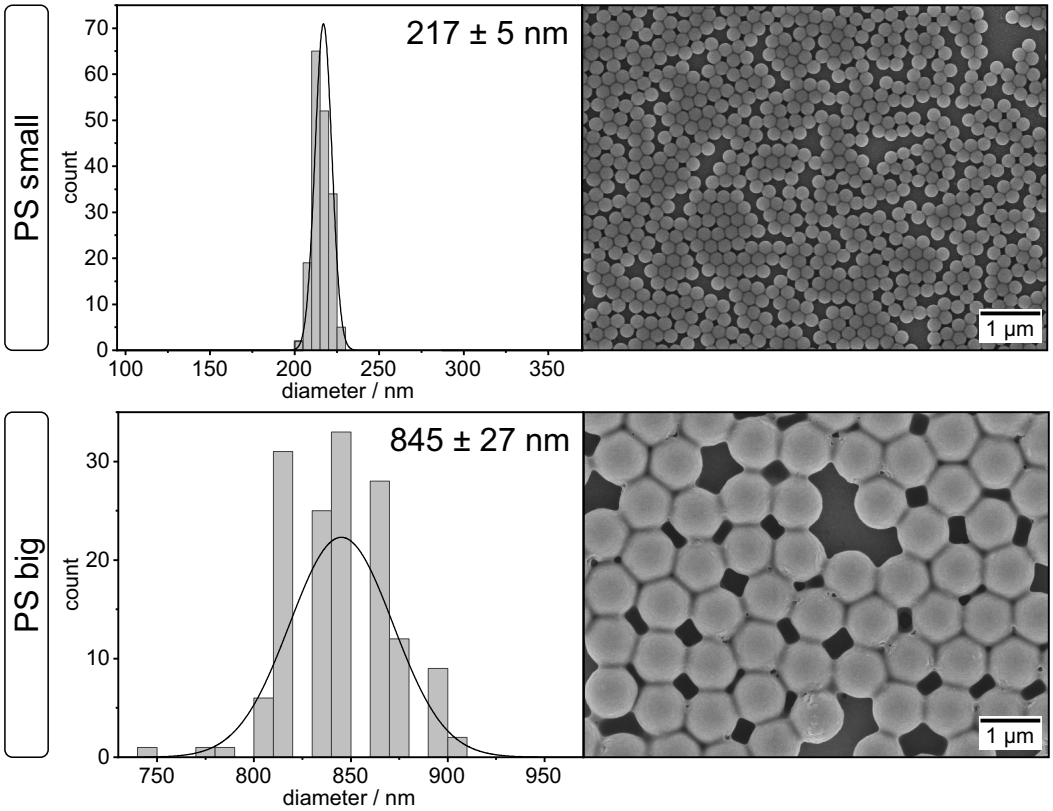

Figure 10.7: Histograms and SEM images of polystyrene particles that were used as template for the SiO_2 and TiO_2 hollow particles.

purification was required.

The 845 nm particles (Figure 10.7) were synthesized via dispersion polymerization.[36,37] 12 g PVP (40 kg/mol), 194 mL of ethanol, 40 mL Millipore water, 12 mL styrene and 1.2 g AIBN were added to a 1 L three-necked flask equipped with a reflux condenser and a gas inlet. The solution was degassed while stirring with an egg-shaped stirring bar with a speed of 150 rpm. After 30 min, the mixture was heated to the reaction temperature of 70 °C. After 90 min 194 mL ethanol, 12 mL styrene, and 450 μL MTC were premixed in an Erlenmeyer flask and added to the reaction. The reaction was carried out overnight under a slight argon flow. The polymerization was stopped by exposing the dispersion to ambient air and filtrated using a 125 μm nylon filter sieve. No further purification was required.

SiO_2 and TiO_2 hollow particles: A modified Stöber process was used for the synthesis of the silica shell to get PS@SiO2 core-shell particles.[38,39] For the synthesis, 40 mL (60 mL) dispersion of the 217 nm (845 nm) particles were diluted with 280 mL (450 mL) ethanol and 1/10 of 13.44 mL (1.8 mL) TEOS and stirred at 400 rpm at room temperature. After 20 min equilibration time, 20.8 mL (31 mL) NH_4OH solution was added. The remaining TEOS was added in nine more steps in time intervals bigger than 15 min and the reaction was stirred at room temperature over night. The particles were centrifuged and washed twice with ethanol and three times

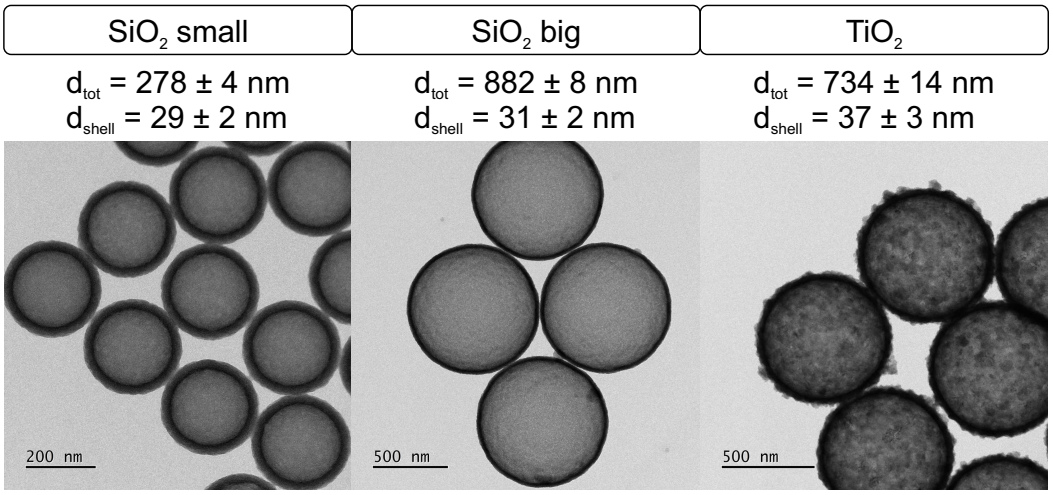

Figure 10.8: TEM images of SiO_2 and TiO_2 hollow particles after calcination at 500 °C.

with Millipore water for purification.

PS@TiO_2 core-shell particles were prepared using a method described by Cheng et al. and Lechner et al.[36,37] 40 mL dispersion of 845 nm particles and 234 mL ethanol were added to an Erlenmeyer flask equipped with a septum. The dispersion was stirred at 350 rpm with a magnetic stirrer bar. After 10 min of degassing, a solution of 4.8 mL TBT in 20 mL ethanol was added within 30 min using a syringe pump. After another 30 min the stirrer was stopped and the dispersion was allowed to age for 24 h. The core-shell particles were washed three times with ethanol for purification.

In order remove the PS core of the core-shell particles, the assembled samples were calcinated either in air or inert argon gas atmosphere using a modified temperature profile of Schroden et al.[37,40] A heating rate of 2 K/min was used for all heating steps. The samples were heated to 300 °C, followed by an isothermal step of 2 h. They were then heated to 400 °C, followed by an isothermal step of 5 h. After that the samples were heated to 500 °C or 925 °C, followed by an isothermal step of 5 h. Finally, the samples were cooled down to room temperature. The resulting hollow particles can be seen in Figure 10.8.

Figure 10.9 shows sideview SEM images of the calcinated colloidal glasslike structures. All structures stayed stable at calcination temperatures up to 925 °C. The broken shells of the TiO_2 particles came from cutting the sample in half with a knife.

10.6.2 X-Ray Powder Diffraction of TiO_2 Samples

X-ray powder diffraction was performed to investigate the titania phase of the hollow particles before and after LFA measurements at 925 °C. X-ray powder diffraction patterns for the TiO_2 samples were recorded on an Empyrean diffractometer in Bragg-

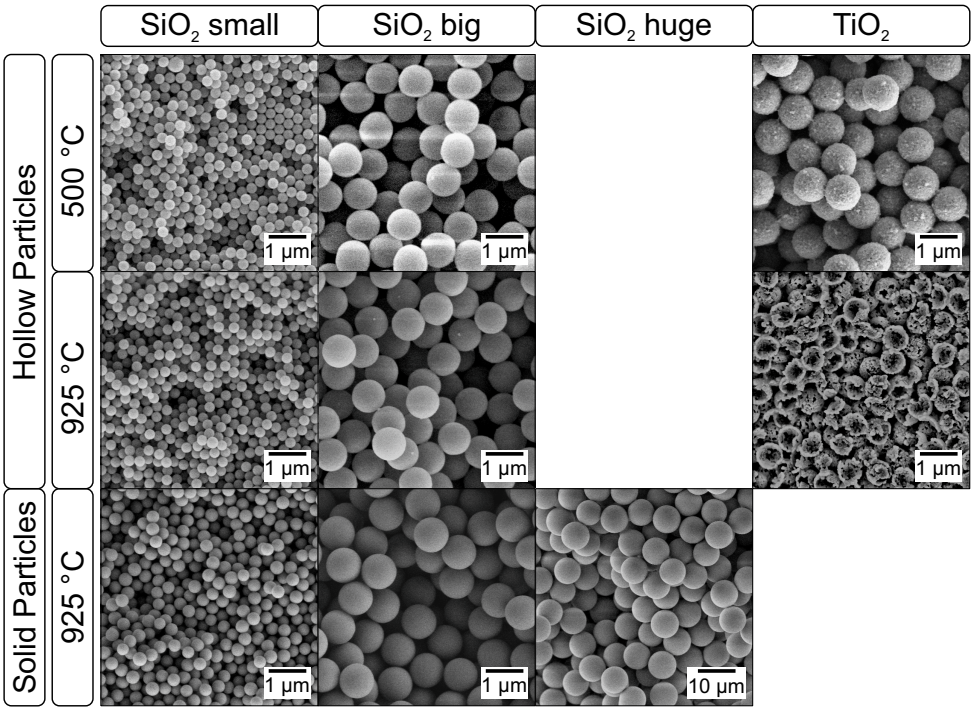

Figure 10.9: Sideview SEM images of all colloidal glasslike structures after calcination at 500 °C or 925 °C.

Brentano-geometry (PANalytical B.V.; the Netherlands) using Cu-Kα radiation ($\lambda = 1.54187$ Å). The samples were first calcinated in air atmosphere at 500 °C and then calcinated in inert gas atmosphere up to 925 °C. The results are shown in Figure 10.10. Both samples consist of 100% anatase.

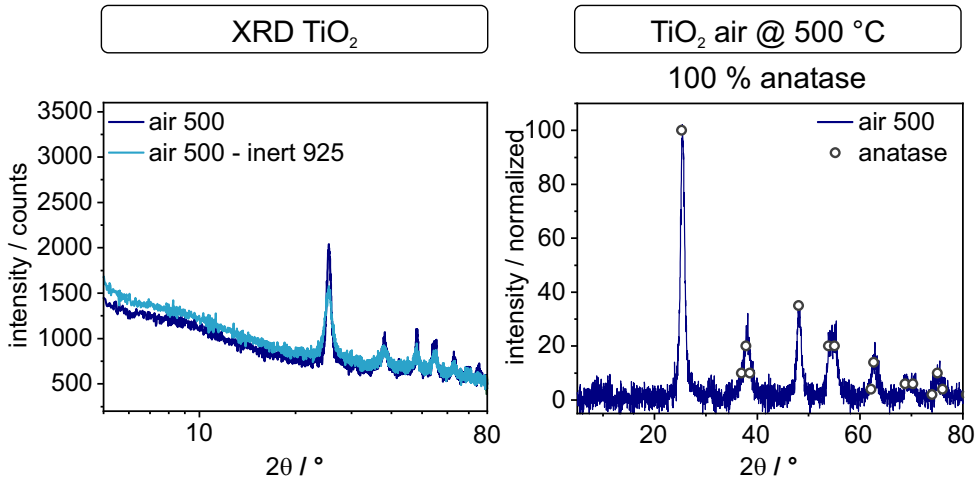

Figure 10.10: XRD spectra of TiO_2 hollow particles calcinated under different conditions, as well as peak evaluation for the 500 °C particles calcinated in air.

10.6.3 Transparent Fit of Radiation Data

Figure 10.12 shows measurement data with the transparent fit of the Protheus software (Netzsch) for hollow and solid particle and bulk quartz samples. It can be seen that the fit model was working perfectly for the bulk sample. However, it failed to fit the particle samples. The fit started getting inaccurate at 625 °C for the solid particle samples and 525 °C for the hollow particle samples. At 825 °C (solid) and 725 °C (hollow), the fit model could not fit the data anymore.This fit problem originated from the different peak shapes of the radiation peak, as shown in Figure 10.11. The bulk signal had a sharp initial temperature increase, followed by a decrease. The hollow particle signal had a diffusive-like shape. The solid particle signal is in between with a sharp initial increase, followed by a diffusive-like increase.

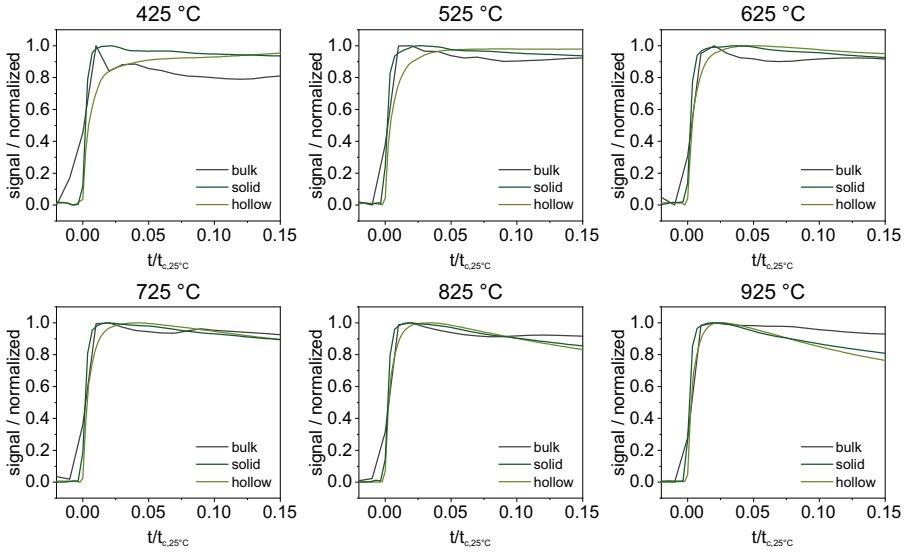

Figure 10.11: Peak shape of radiation peak of hollow and solid particles, and bulk quartz glass from 425 to 925 °C.

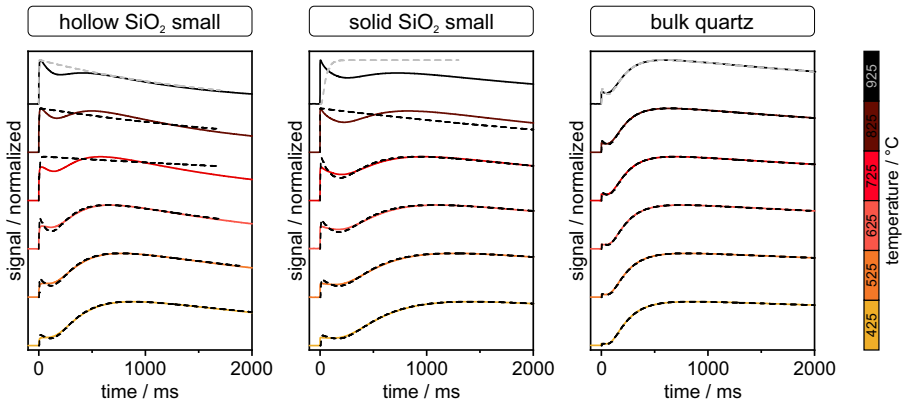

Figure 10.12: Transparent fit on LFA data of hollow and solid particles, and bulk quartz. The colored lines show the measurement signal at 425 to 925 °C, the dashed lines show the corresponding fit.

10.6.4 Double-Diffusive Model of LFA Data of Hollow Particle Samples

From the double-diffusive model, it was possible to determine the thermal diffusivity of the radiation and conduction process of the hollow particle samples. The results are shown in Figure 10.3 and Figure 10.13. The radiation diffusivity was increasing with increasing temperature. An increasing radiative thermal conductivity is known from the geophysical science and measurements and calculations on olivine samples, where the conductivity is calculated from high-temperature absorption data.[32] The conductive thermal diffusivity is almost constant in both samples. It has to be noted that the values do not represent the actual values because of two reasons. First, at higher temperatures, the conduction peak has almost vanished and the fit may be inaccurate. Second, the double-diffusive model is simplified and does not take into account reflection of heat at the sample-graphite-boundary. Therefore, an accurate evaluation of the conductive thermal diffusivity was not achieved with this fit.

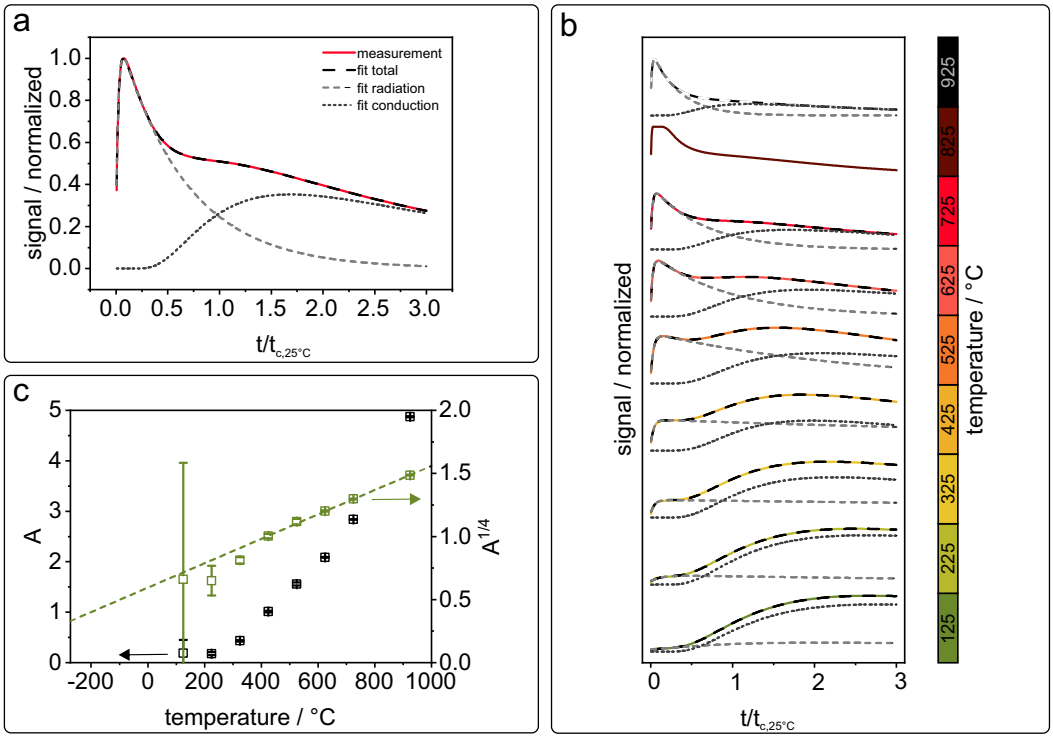

Figure 10.13: Double diffusive model applied to temperature-dependent measurements of big hollow particle samples.

10.6.5 TiO_2 Hollow Particle Sample

Similar to the 8 μm solid SiO_2 particles, the TiO_2 hollow particles have almost no transmission in the IR region (Figure 10.14). Because of the missing bandgap between 3 and 5 μm, radiation does not contribute to the thermal transport in the sample. Therefore, no radiation peak is visible in the measurements (Figure 10.15). The sample consisting of particles with a diameter of 734 nm and a shell thickness of 37 nm, has a density of 0.385 g/cm^3, a thermal diffusivity of 0.613 mm^2/s, and a thermal conductivity of 0.163 W/m·K at 25 °C.

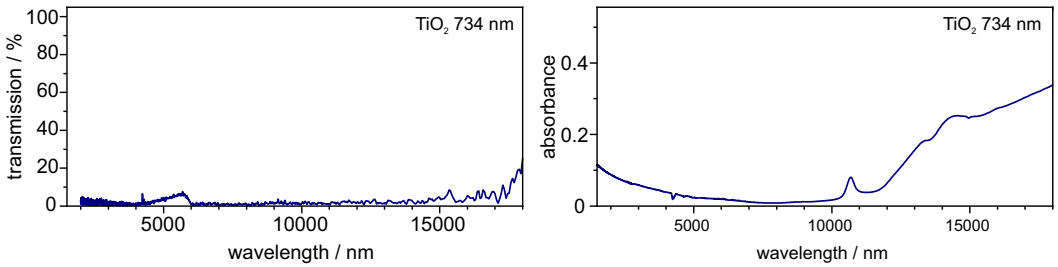

Figure 10.14: Transmission and absorbance spectra of TiO2 hollow particles in the IR region.

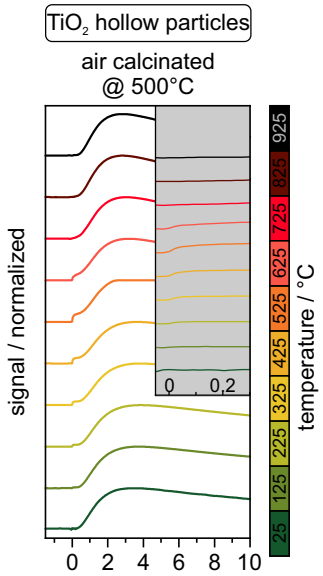

Figure 10.15: Temperature-dependent LFA measurement signals of TiO2 hollow particle samples that were calcinated at 500 °C in air or inert atmosphere before the measurement.

10.6.6 Inert Calcined SiO_2 Hollow Particle Samples

Figure 10.16 shows a picture of whole samples of SiO_2 hollow particles after calcination in air and inert atmosphere. The color of the inert calcinated samples comes from carbon residues in the hollow particles, as described by Wang et al.[41] The samples have totally different optical properties in the visible region, however in the IR region the transmission is barely reduced (Figure 10.17).Therefore, the thermal behavior, especially the intensity of the radiation peak, does not change, which can be seen in Figure 10.18.

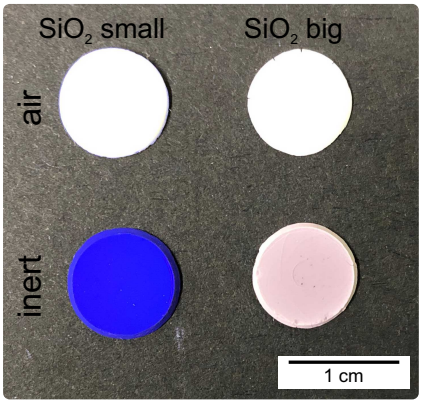

Figure 10.16: Picture of colloidal glasslike assemblies of SiO_2 hollow particles after calcination at 925 °C in air and inert atmosphere.

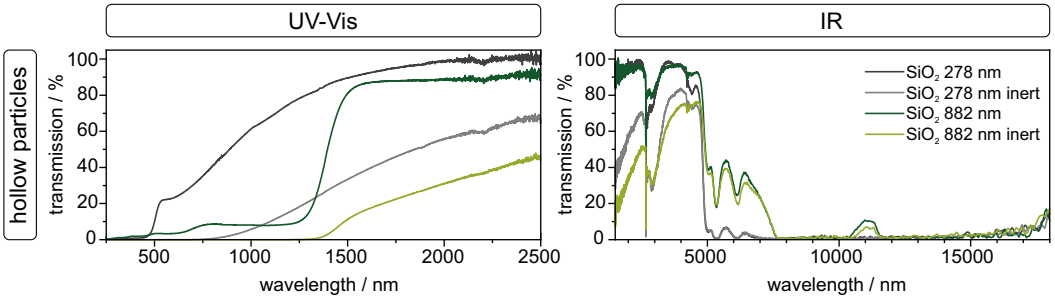

Figure 10.17: Optical properties of air and inert calcinated colloidal assemblies of hollow SiO_2 particles in the UV-Vis and IR region.

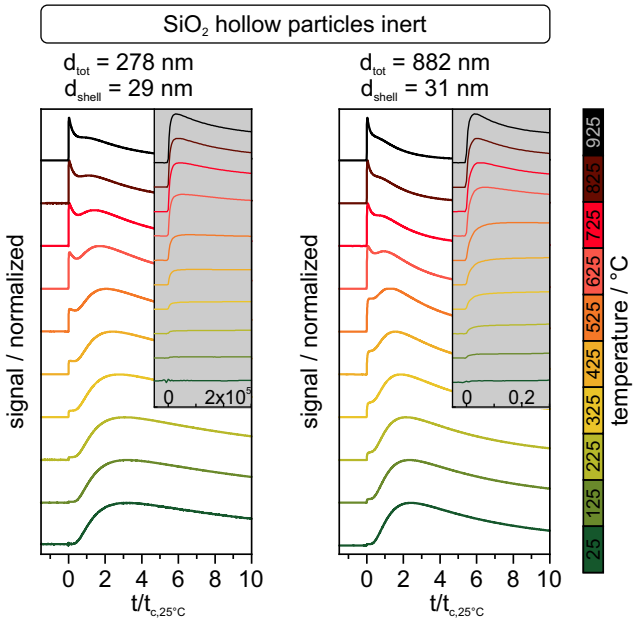

Figure 10.18: Temperature dependent LFA measurement signals of SiO_2 hollow particle samples that were calcinated in argon atmosphere at 925 °C before the measurement. The time is normalized by the characteristic thermal response time t_c.

10.6.7 Mean Particle Distance for Multilayer Model

To get the mean interparticle distance in colloidal glasses, an MD simulation of particles with a diameter of 1 μm with a compression rate of $1e^{-2}$ has been performed. The resulting packing density was 61.1%, which is comparable to the experimental data. The 3D radial distribution function of the simulated structure was calculated, according to Kopera et al.[42] An interparticle distance of 63 nm was determined. Thus, we assumed to have a mean distance of 6% of the total particle diameter for all samples.

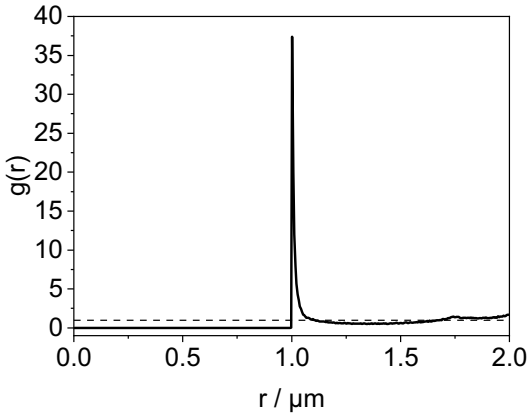

Figure 10.19: 3D radial distribution function of a colloidal glass with a packing density of 61.1% and particles with a diameter of 1 μm.

10.6.8 Transmission Coefficient: Influence of Number of Particle Layers

In Figure 10.20 we show the Transmission coefficient τ_p^{12} for the p-polarized waves (which include possible surface wave contributions) in the $\lambda - \kappa$ plane choosing $\delta = 20$ nm and the multilayer structure, which models the structure of solid 353 nm silica particles. It can be seen how the number of the Fabry-Pérot modes is increasing when increasing the number of layers from $N = 9$ ($d = 2.5$ μm) to $N = 3121$ ($d = 827$ μm) forming Bloch band structures[43] due to the periodicity of the structure. The same behavior can be expected for highly ordered nanoparticle structures. It can be further seen that when increasing the number of layers from $N = 9$ to $N = 3121$, only waves in the transparency window of glass for $\lambda < 5$ μm can reach the second graphite layer, and all the other waves are damped out due to the losses in the glassy part of the structure. The waves reaching the second graphite layer also include evanescent contributions because the wavevector in glass can be larger than in vacuum. In the transparency window, the lateral wave vector κ is limited by $\sqrt{R(\epsilon_{SiO_2})}k_0 \approx 1.4k_0$ due to the material and those waves which can tunnel between the layers of the multilayer structure will finally heat up the graphite layer. It is interesting to note that there is no significant surface wave contribution for h^{12} in the restrahlen band $\lambda \in [8$ μm : 9.3 μm$]$. This is due to the fact that damping of the coupled surface modes is too strong to ensure an efficient coupling over long distances.

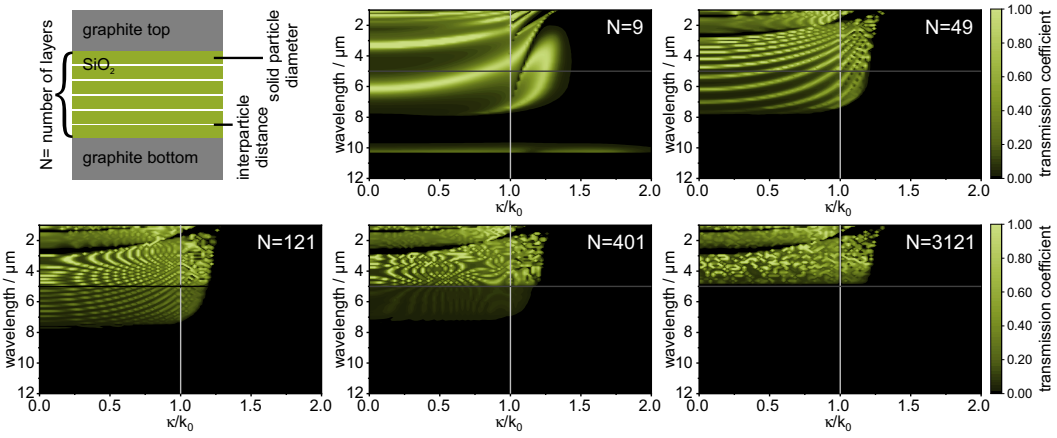

Figure 10.20: Transmission coefficients of a model representing solid SiO_2 particle glasses with an increasing number of layers, N, from 9 to 3121.

10.6.9 Heat Transfer Coefficient

The radiative heat flux in the multilayer systems was calculated by using the theory of fluctuational electrodynamics.

The heat transfer coefficient describing the radiative heat flow h^{12} from the graphite layer 1 at temperature T_1 and the heat flow h^{23} from the intermediate film 2 at temperature T_2 towards the second graphite layer 3 at temperature T_3 are given by the expressions[44–46]

$$h^{12/23} = \int_0^\infty \frac{d\omega}{2\pi} \sum_{\mathrm{j=s,p}} \int \frac{d\kappa}{(2\pi)^2} \frac{d\Theta(T)}{\partial T} \tau_j^{12/23}(\omega, \kappa) \tag{10.2}$$

Here $\Theta(T) = \hbar\omega/(\exp(\hbar\omega/k_bT) - 1)$ is the mean energy of a harmonic oscillator at temperature T; k_b is the Boltzmann and $\hbar$ the reduced Planck constant. The transmission coefficients $\tau_j^{12/23}$ (j = s,p) are the functions of the frequency ω and the lateral wavevector κ for s- and p-polarized waves and can have values between 0 and 1. They contain the contributions of propagating waves ($\kappa < k_0$) but also evanescent waves ($\kappa > k_0$) in vacuum introducing the vacuum wavevector$k_0 = \omega/c$ and the light velocity c. The complex expressions can be found in Messina et al.[33] However, they mainly depend on the distances δ and the layer thickness d as well as on the optical properties of the three layers. For example they depend on the corresponding amplitude transmission and reflection coefficients so that they can be evaluated as soon as the optical properties of the three layers are known. For the intermediate multilayer structure, we used the standard S-matrix method to calculate the needed reflection and transmission coefficients. The optical data for the permittivity of silica and graphite are taken from literature values in Ref.[44–46] The radiative heat flux Φ (W/m^2) to the graphite layer 3 is within this model simply

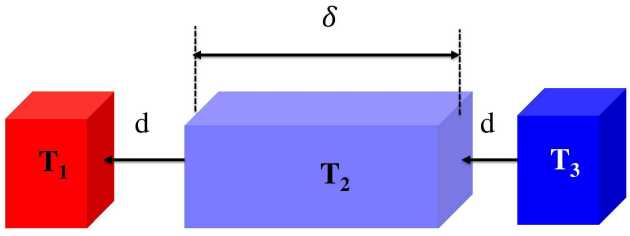

Figure 10.21: Sketch of the three-layer structure. Layer 1 and 3 are graphite sheets, and the intermediate layer 2 is the nanoparticle glass of thickness d.

given as:

$$\Phi = h^{12}(T_1 - T_2) + h^{23}(T_2 - T_3) \tag{10.3}$$

That means that in the first instance where the graphite layer 1 is heated by the laser flash, we have $T_1 > T_2 = T_3$ so that h^{12} describes the radiative coupling between the first and second graphite layers. Therefore the modes contributing to the radiative heat flow between the two graphite layers are mainly determined by τ_j^{12} (j = s,p).

10.6.10 Influence of Coupling Surface Modes on Transmission of Heat Radiation

To clarify the role of the surface mode contribution to the radiative heat flux, we have made exact numerical calculations using the open-source program SCUFF-EM developed by Homer Reid at MIT.[47] It uses a boundary element method to determine the transmission functions $F_{ij}(\omega)$ between two objects i and j so that the exchanged power P between these objects due to thermal radiation (far- and near-field) can then be determined by

$$P_{ij} = \int_0^\infty d\omega(\Theta(T_i) - \Theta(T_j))F_{ij}(\omega). \tag{10.4}$$

In Figure 10.22 we show the transmission functions for the heat flux between two, three, and four nanoparticles of diameter 800 nm and an interparticle distance of 50 nm. As can be expected, the heat flux between adjacent silica nanoparticles is dominated by the surface mode resonance at $\lambda \approx 9$ μm, and it becomes weaker and weaker when considering the coupling between nanoparticles with one or two nanoparticles in between them. When replacing the outer nanoparticles in the chain of 3 and 4 nanoparticles with a graphite particle, it can be nicely seen that the transmission of heat radiation will be mainly in the transparency region below 8 μm, i.e., below the reststrahlen band. The surface mode resonance contribution becomes already relatively weak for a chain of 4 nanoparticles, and it can be expected that it is negligible for chains of 3000 to 4000 nanoparticles.

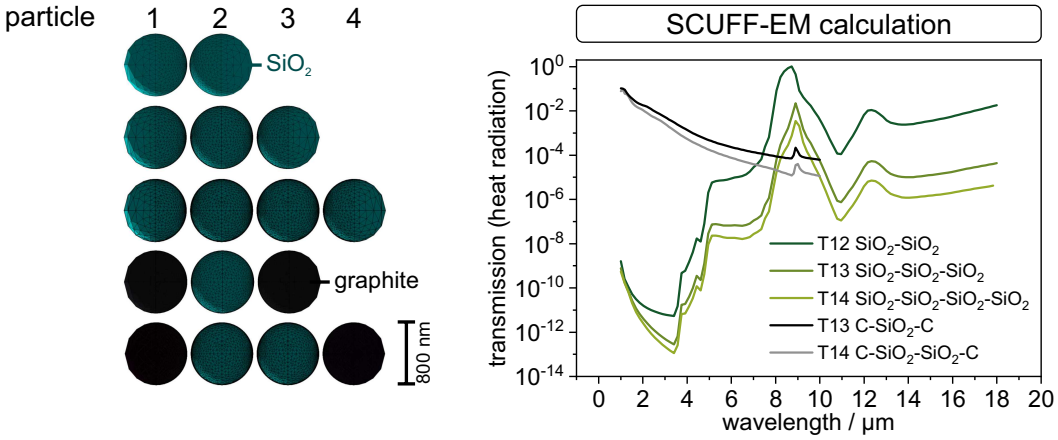

Figure 10.22: SCUFF-EM calculation of transmission functions for heat flux between first and last particle in a row of two to four particles.

10.6.11 Influence of Material Thermal Conductivity on Radiation

We have used a set of 14 coupled differential equations to describe the temperature evolution of the system. The first and last graphite layers are in this model split into a $d_{\mathrm{surf}} = 200$ nm thin surface layer (the skin depth of graphite for $\lambda = 1\ \mu$m – 10 μm is 100 nm – 200 nm) with temperatures T_1 and T_{14} standing for the surface temperatures of the laser flash heated first layer and the measured surface temperature of the last layer, and a layer of thickness d_c with temperatures T_2 and T_{13}. The glass film is divided into 10 layers of thickness $d_{\mathrm{SiO_2}}$ with temperatures T_3,T_4,...,T_{12}. In this model, we assume that the adjacent layers are coupled via thermal conduction and that the graphite layers are coupled to the 3 glass layers by h^{23} and between each other by h^{12}. Then using Newton's law of cooling, we have the set of equations

$$C_{\rho,\mathrm{C,surf}}\frac{dT_1}{dt} = h_{\mathrm{cond,C}}(T_2 - T_1) + h_{\mathrm{rad}}(T_m - T_1) + h_{\mathrm{cond,lat}}(T_m - T_1) \tag{10.5}$$

$$\begin{aligned} C_{\rho,\mathrm{C}}\frac{dT_2}{dt} = {} & h^{12}(T_{13} - T_{\mathrm{mean}}) + h^{23}(T_3 - T_2) + h_{\mathrm{cond,C-SiO_2}}(T_3 - T_2) \\ & + h_{\mathrm{cond,C}}(T_1 - T_2) + h_{\mathrm{cond,lat}}(T_{\mathrm{m}} - T_2) \end{aligned} \tag{10.6}$$

$$\begin{aligned} C_{\rho,\mathrm{SiO_2}}\frac{dT_3}{dt} = {} & h_{\mathrm{cond,C-SiO_2}}(T_2 - T_3) + h_{\mathrm{cond,C-SiO_2}}(T_4 - T_3) \\ & + h^{23}(T_2 - T_3) + h_{\mathrm{cond,lat}}(T_{\mathrm{m}} - T_3) \end{aligned} \tag{10.7}$$

$$C_{\rho,\mathrm{SiO_2}}\frac{dT_4}{dt} = h_{\mathrm{cond,SiO_2}}(T_3 - T_4) + h_{\mathrm{cond,SiO_2}}(T_5 - T_4) + h_{\mathrm{cond,lat}}(T_m - T_4) \tag{10.8}$$

$$... = ...$$

$$\begin{aligned} C_{\rho,\mathrm{C}}\frac{dT_{13}}{dt} = {} & h^{12}(T_2 - T_{\mathrm{mean}}) + h^{23}(T_{12} - T_{13}) + h_{\mathrm{cond,C-SiO_2}}(T_{12} - T_{13}) \\ & + h_{\mathrm{cond,C}}(T_{14} - T_{13}) + h_{\mathrm{cond,lat}}(T_m - T_{13}) \end{aligned} \tag{10.9}$$

$$C_{\rho,\mathrm{C,surf}}\frac{dT_{14}}{dt} = h_{\mathrm{rad}}(T_m - T_{14}) + h_{\mathrm{cond,C}}(T_{13} - T_{14}) + h_{\mathrm{cond,lat}}(T_m - T_{14}) \tag{10.10}$$

In these equations T_m is the ambient temperature, T_{mean} is the mean temperature in the glass medium, and

$$C_{\rho,\mathrm{C,surf}} = C_{\mathrm{C}}\rho_{\mathrm{C}}d_{\mathrm{surf}}, \quad C_{\rho,\mathrm{C}} = C_{\mathrm{C}}\rho_{\mathrm{C}}d_{\mathrm{C}}, \quad C_{\rho,\mathrm{SiO_2}} = C_{\mathrm{SiO_2}}\rho_{\mathrm{SiO_2}}d_{\mathrm{SiO_2}} \tag{10.11}$$

are the products of the heat capacities of graphite and silica, the corresponding mass densities (Table 10.2), and the layer thicknesses where $d_{\mathrm{SiO2}} = d/10$, $d_{\mathrm{surf}} = 200$ nm, and d_{C} can vary from 10 μm to 30 μm. The heat transfer coefficients h^{12} and h^{23} are defined above h_{rad} is the htc of the graphite layer into vacuum, and takes the radiative cooling of the surface layers into account. The heat transfer coefficients caused by thermal conduction in graphite, in silica, or between graphite and silica are defined as

$$h_{\mathrm{C}} = \frac{\kappa_{\mathrm{C}}}{d_{\mathrm{surf}} + d_{\mathrm{C}}}, \quad h_{\mathrm{SiO_2}} = \frac{\kappa_{\mathrm{SiO_2}}}{d_{\mathrm{SiO_2}}}, \quad h_{\mathrm{C,SiO_2}} = \frac{1}{\frac{1}{h_{\mathrm{SiO_2}}} + \frac{1}{h_{\mathrm{C}}}} \tag{10.12}$$

The values of the thermal conductivities κ_{C} and $\kappa_{\mathrm{SiO_2}}$ are taken from literature (Table 10.2). Since the Kapitza resistance between graphite and silica is extremely small, we have neglected it. $h_{\mathrm{cond,lat}}$ is a parameter which can be used to model lateral conductive losses in the sample.

This model neglects the thermal radiation channels within the graphite and silica media. That means it is assumed that within the materials conduction is more important than radiation. The numerical results also suggest that h^{23} has negligible impact for the used parameters underlining the assumption that the radiative coupling between adjacent layers by the surface mode interaction is small compared to the conductive one. Note that in this model, there are only three more or less unknown parameters: the conductivity of the glass medium $\kappa_{\mathrm{SiO_2}}$ which is actually measured by the LFA (i.e. by fitting the model to the data), the thickness of the graphite layers which are estimated to be 20 μm to 30 μm (dependent on the number of coated layers), and the lateral conductivity $h_{\mathrm{cond,lat}}$.

In Figure 10.23 we show the simulation of the LFA experiment by plotting the temporal temperature evolution $\Delta T_{14} = T_{14} - T_m$ of the second graphite surface temperature for $T_m = 925$ °C with initial conditions $T_1 = T_m + 10$ K and $T_2 = T_3 = ... = T_{14} = T_m$ at time $t = 0$ ms and $d_{\mathrm{C}} = 20$ μm. The values for h^{12} and h^{23} are calculated for the multilayer structure replacing the solid 353 nm nanoparticles with $N = 3121$ layers (so that $d = 827$ μm) and $\delta = 20$ nm. To show the impact of the conductivity of the intermediate glass layer, we have varied $\kappa_{\mathrm{SiO_2}}$. It can be seen that the relative strengths of the peaks, which are due to heating by thermal radiation or conduction, highly depend on the thermal conductivity of the glass layer.

Table 10.2: Specific heat capacity, C_p, and thermal conductivity, κ, of quartz glass and graphite. C_p of quartz glass was taken from Smyth et al.[48], κ was calculated using the thermal diffusivity from our measurements on bulk quartz (Figure 10.2) and a density of 2.201 g/cm^3. The C_p of graphite was calculated according to Butland et al.[49], κ was calculated according to McEligot et al.[50]

	Quartz		Graphite	
T / °C	C_p / J/g·K	κ / W/m·K	C_p / J/g·K	κ / W/m·K
25	0.744	1.439	0.713	131.338
125	0.879	1.593	0.980	121.156
225	0.981	1.700	1.193	111.718
325	1.057	1.793	1.360	103.023
425	1.110	1.870	1.491	95.072
525	1.153	1.952	1.596	87.865
625	1.189	2.041	1.681	81.402
725	1.217	2.137	1.751	75.683
825	1.242	2.238	1.809	70.707
925	1.263	2.345	1.857	66.476

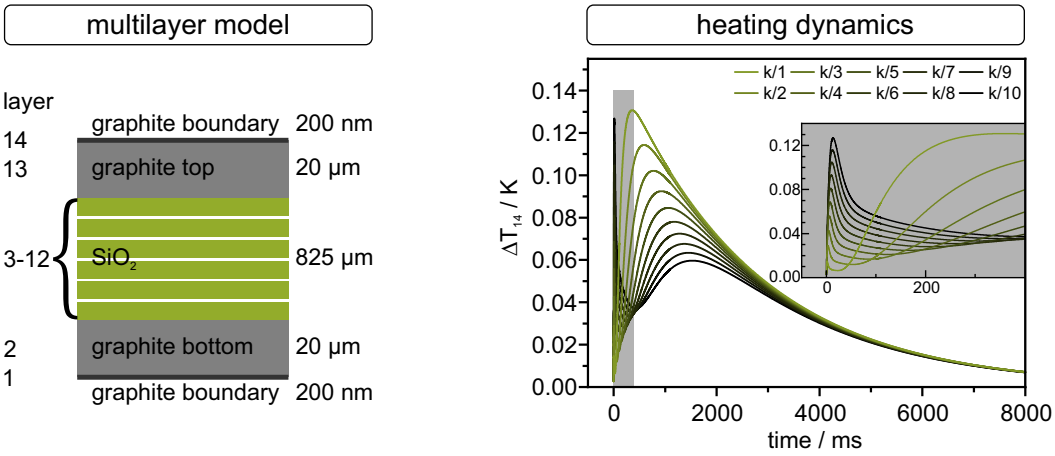

Figure 10.23: Multilayer model for heating dynamics calculations of a solid SiO_2 colloidal structure with a particle diameter of 353 nm (left). Heating dynamics with lateral losses of the multilayer model at a temperature of 925 °C (right).

10.7 References

[1] A. Du, B. Zhou, Z. Zhang, J. Shen, *Materials* **2013**, *6*, 941–968.

[2] P. Ruckdeschel, A. Philipp, M. Retsch, *Advanced Functional Materials* **2017**, *27*, 1702256.

[3] E. Cohen, L. Glicksman, *Journal of Heat Transfer* **2014**, *136*, 041301.

[4] J. Fricke, T. Tillotson, *Thin Solid Films* **1997**, *297*, 212–223.

[5] U. Gross, L.-T.-S. Tran, *International Journal of Heat and Mass Transfer* **2004**, *47*, 3279–3290.

[6] U. Heinemann, R. Caps, J. Fricke, *International Journal of Heat and Mass Transfer* **1996**, *39*, 2115–2130.

[7] X. Lu, R. Caps, J. Fricke, C. Alviso, R. Pekala, *Journal of Non-Crystalline Solids* **1995**, *188*, 226–234.

[8] G. Wei, Y. Liu, X. Zhang, F. Yu, X. Du, *International Journal of Heat and Mass Transfer* **2011**, *54*, 2355–2366.

[9] P. Ruckdeschel, M. Retsch, *Advanced Materials Interfaces* **2017**, *4*, 1700963.

[10] S. A. Mofid, B. P. Jelle, X. Zhao, et al., *Journal of Building Engineering* **2020**, *31*, 101336.

[11] M. Wiener, G. Reichenauer, S. Braxmeier, F. Hemberger, H.-P. Ebert, *International Journal of Thermophysics* **2009**, *30*, 1372–1385.

[12] J. Feng, J. Feng, C. Zhang, *Journal of Porous Materials* **2011**, *19*, 551–556.

[13] P. Ruckdeschel, T. W. Kemnitzer, F. A. Nutz, J. Senker, M. Retsch, *Nanoscale* **2015**, *7*, 10059–10070.

[14] S. N. Schiffres, K. H. Kim, L. Hu, et al., *Advanced Functional Materials* **2012**, *22*, 5251–5258.

[15] G. Wedler, *Lehrbuch der Physikalischen Chemie*, John Wiley & Sons, **2012**.

[16] T. L. Bergman, *Fundamentals of Heat and Mass Transfer*, John Wiley & Sons, **2011**.

[17] T. Xie, Y.-L. He, Z.-J. Hu, *International Journal of Heat and Mass Transfer* **2013**, *58*, 540–552.

[18] S. Zeng, A. Hunt, R. Greif, *Journal of Non-Crystalline Solids* **1995**, *186*, 271–277.

[19] H. Liu, T. Li, Y. Shi, X. Zhao, *Journal of Materials Engineering and Performance* **2015**, *24*, 4054–4059.

[20] V. G. Parale, H.-N.-R. Jung, W. Han, et al., *Journal of Alloys and Compounds* **2017**, *727*, 871–878.

[21] S.-A. Biehs, R. Messina, P. Venkataram, et al., *Reviews of Modern Physics* **2021**, *93*, 025009.

[22] P. Ben-Abdallah, S.-A. Biehs, K. Joulain, *Physical Review Letters* **2011**, *107*, 114301.

[23] R. Messina, M. Tschikin, S.-A. Biehs, P. Ben-Abdallah, *Physical Review B* **2013**, *88*, 104307.

[24] E. Tervo, M. Francoeur, B. Cola, Z. Zhang, *Physical Review B* **2019**, *100*, 205422.

[25] D. Becerril, C. Noguez, *Physical Review B* **2019**, *99*, 045418.

[26] N. Sakatani, K. Ogawa, Y. Iijima, et al., *AIP Advances* **2017**, *7*, 015310.

[27] J. A. Cape, G. W. Lehman, *Journal of Applied Physics* **1963**, *34*, 1909–1913.

[28] A. Philipp, J. F. Eichinger, R. C. Aydin, et al., *Heat and Mass Transfer* **2019**, *56*, 811–823.

[29] O. A. Sergeev, A. G. Shashkov, A. S. Umanskii, *Journal of Engineering Physics* **1982**, *43*, 1375–1383.

[30] L. F. Johnson, D. P. H. Hasselman, E. Minford, *Journal of Materials Science* **1987**, *22*, 3111–3117.

[31] A. Lunev, V. Zborovskii, T. Aliev, *International Journal of Thermal Sciences* **2021**, *160*, 106695.

[32] T. J. Shankland, U. Nitsan, A. G. Duba, *Journal of Geophysical Research: Solid Earth* **1979**, *84*, 1603.

[33] R. Messina, P. Ben-Abdallah, B. Guizal, M. Antezza, S.-A. Biehs, *Physical Review B* **2016**, *94*, 104301.

[34] P. Ruckdeschel, A. Philipp, B. A. F. Kopera, et al., *Physical Review E* **2018**, *97*, 022612.

[35] J. W. Goodwin, J. Hearn, C. C. Ho, R. H. Ottewill, *Colloid and Polymer Science* **1974**, *252*, 464–471.

[36] Z. Deng, M. Chen, S. Zhou, B. You, L. Wu, *Langmuir* **2006**, *22*, 6403–6407.

[37] A. M. Lechner, T. Feller, Q. Song, et al., *Colloid and Polymer Science* **2020**, *298*, 867–878.

[38] W. Stöber, A. Fink, E. Bohn, *Journal of Colloid and Interface Science* **1968**, *26*, 62–69.

[39] C. Graf, D. L. J. Vossen, A. Imhof, A. van Blaaderen, *Langmuir* **2003**, *19*, 6693–6700.

[40] R. C. Schroden, M. Al-Daous, C. F. Blanford, A. Stein, *Chemistry of Materials* **2002**, *14*, 3305–3315.

[41] M. Wang, S. Lin, *Advanced Functional Materials* **2016**, *26*, 5297–5306.

[42] B. A. F. Kopera, M. Retsch, *Analytical Chemistry* **2018**, *90*, 13909–13914.

[43] P. Yeh, M. Hendry, *Choice Reviews Online* **1989**, *26*, 6299.

[44] R. Kitamura, L. Pilon, M. Jonasz, *Applied Optics* **2007**, *46*, 8118.

[45] A. B. Djurišić, E. H. Li, *Journal of Applied Physics* **1999**, *85*, 7404–7410.

[46] I. H. Malitson, *Journal of the Optical Society of America* **1965**, *55*, 1205.

[47] M. T. H. Reid, S. G. Johnson, *IEEE Transactions on Antennas and Propagation* **2015**, *63*, 3588–3598.

[48] H. T. Smyth, H. S. Skigeb, W. B. Harsell, *Journal of the American Ceramic Society* **1953**, *36*, 327–328.

[49] A. Butland, R. Maddison, *Journal of Nuclear Materials* **1973**, *49*, 45–56.

[50] D. McEligot, W. D. Swank, D. L. Cottle, F. I. Valentin, *Technical Report: Office of Scientific and Technical Information (OSTI)* **2016**.

11

Homogeneous Polymer Films for Passive Daytime Cooling: Optimized Thickness for Maximized Cooling Performance

Kai Herrmann,* Tobias Lauster,* Qimeng Song,* and Markus Retsch*,§

* Department of Chemistry, Physical Chemistry 1, University of Bayreuth, Universitätsstraße 30, 95447 Bayreuth, Germany.

§ Bavarian Polymer Institute, Bayreuth Center for Colloids and Interfaces, and Bavarian Center for Battery Technology (BayBatt), University of Bayreuth, Universitätsstraße 30, 95447 Bayreuth, Germany.

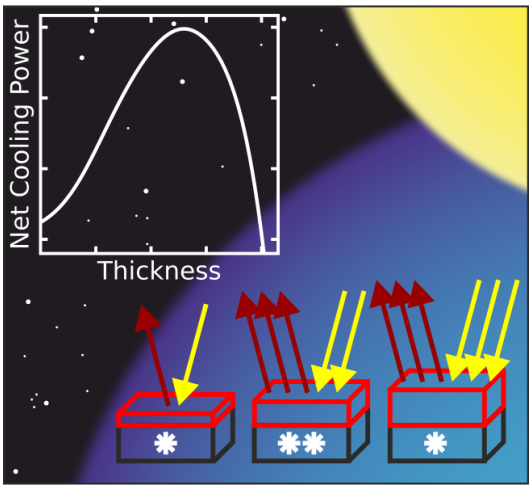

Published in *Advanced Energy and Sustainability Research*, **2021**, *3*, 2100166.

11.1 Abstract

Passive radiative cooling materials that spontaneously cool below ambient temperature can save tremendous amounts of energy used for cooling applications. A multitude of materials, structures, and fabrication strategies have been reported in recent years. Important material parameters like a tailored or broadband emissivity, angle selectivity, or the influence of nonradiative heat losses are discussed in detail. The material thickness has been far less researched and is typically chosen sufficiently thick to ensure high emission in the atmospheric transparency window between wavelengths of $8-13$ μm. However, no only the material emittance but also atmospheric and solar energy uptake depend on the material thickness. This broadband interplay has been less addressed so far. Herein, it is shown how an optimum thickness of a passive cooling material can be predicted when the optical properties of the material are known. Using complex refractive index data, the thickness-dependent cooling performance of polydimethylsiloxane (PDMS) in back-reflector geometry as exemplary material is calculated. For both day- and nighttime operation, an optimum emitter thickness is reported. The findings are verified experimentally by measuring the equilibrium temperatures of PDMS films with different thicknesses in a rooftop experiment. The presented analytical approach is directly transferable to other materials.

11.2 Introduction

The field of passive daytime radiative cooling materials has significantly developed in the last decade. Many new materials emerged that show a cooling effect below ambient temperature, even with direct sunlight illumination.[1,2] The key to achieving a net cooling power is minimizing energy absorption and maximizing energy emission. A multitude of approaches were proposed that lead to the desired optical properties, including photonic structures,[3,4] polymeric-,[5,6] and composite materials.[7,8]
A material is primarily a good candidate for passive radiative cooling if it exhibits a high emissivity in the wavelength range of thermal radiation at ambient temperature. This wavelength range is located in the mid to far IR region (approximately $3-50$ μm). Second, a low absorptivity in the solar region is required because any energy uptake from the sun directly reduces the cooling power. This energy absorption is prevented by including a reflective metal layer below the emitter material,[8–11] by the use of a solar filter approach[12,13] or by efficient scattering of solar wavelengths by the material itself.[5,14,15] Thirdly, and most complex is to avoid radiative energy uptake by the surrounding atmosphere. Since this radiance appears in a similar wavelength regime as the emitted thermal radiation, special care must be taken. The most common approach here is to focus emission on the first

$(8-13\ \mu\text{m})$ and second $(16-28\ \mu\text{m})$ atmospheric transmission window where low atmospheric radiation is present. With a confined emission in this spectral region, the lowest temperatures below ambient can be reached. However, the cooling power at ambient temperature is reduced in comparison to a blackbody emitter.[1,16]

The material thickness is an essential parameter for the applicability of passive cooling materials and was discussed by several groups in the literature.[10,17,18] For example, in the work of Zhou et al., a PDMS layer on an aluminum substrate is considered.[10] The authors chose a 150 μm thick layer and found that above 100 μm thickness, the emissivity in the $8-13\ \mu$m wavelength range was close to unity. In the work of Zhu et al., the thickness of a PDMS layer on a reflective silver layer was discussed, and a thickness of 200 μm was suggested.[18] The authors found that up to this thickness, the emissivity in the wavelength range from 2.5 to 25 μm was increasing, but for a higher thickness of 300 μm, there were only minor changes. Besides PDMS as emitting layer, the group of Zhu et al. investigated the thickness of a composite material consisting of In2O3 particles in a polymethyl methacrylate matrix.[19] They found the thickness of their composite needs to be larger than 25 μm to have high emissivity within the first and second atmospheric window. In the work of Tian et al. poly-4-methyl-1-pentene (PMP) films of different thicknesses are used to determine the complex refractive index of the material.[17] In this work, the investigated film with a thickness of 1283 μm was found to have the highest absorptance within the first and second atmospheric window. In all this previous work, the emitter thickness was optimized to maximize the emission within the first and/or second atmospheric window. However, the material thickness also affects the solar absorption and atmospheric energy uptake behavior of a material simultaneously. This interplay of thickness dependencies for the different energetic contributions has been barely addressed so far. The relevance of optical thickness in the solar range becomes even more relevant, considering emerging aesthetic passive cooling designs, where colored films are fabricated. As long as coloration is not based on Bragg diffraction,[15,20–23] a suitable tradeoff between color impression and thermal load based on the absorption and thermalization process[24] needs to be found.

This work focuses on PDMS as an often used and well-characterized passive cooling material to conceptually address the optimum thickness of an emitter material. Our study provides a theoretical approach based only on the fundamental optical constants for estimating the optimum emitter thickness. Experimental data subsequently verify the outlined theoretical framework. Therefore, PDMS thin films of several thicknesses on Ag mirrors were prepared to determine the equilibrium temperatures below ambient during day- and night-time. In conclusion, we point out how to optimize the sample thickness of a given emitter material for passive day- and night-time cooling applications in the back-reflector geometry.

11.3 Theoretical Approach

To determine the optimum thickness, we first derive how the individual energetic contributions of a passive cooling material depend on the emitter material thickness. Taking into account all the energy exchange processes, the net cooling power P_{cool} can be defined as[1]

$$P_{\text{cool}} = P_{\text{mat}} - P_{\text{sun}} - P_{\text{atm}} - P_{\text{nonrad}} \tag{11.1}$$

where P_{mat} represents the energy radiated by the material, P_{sun} the absorbed energy due to solar radiation, P_{atm} the absorbed energy due to atmospheric radiation and P_{nonrad} intrinsic losses due to convection and conduction. The considered energy exchange processes are schematically shown in Figure 11.1.

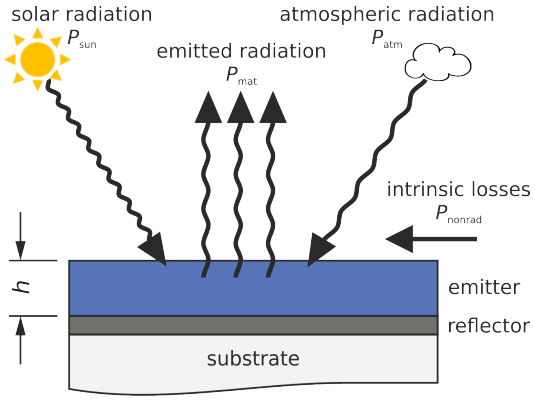

Figure 11.1: Schematics of the radiative cooler containing the considered energy exchange processes.

To calculate the different energetic contributions, the broadband optical constants of the emitter material, a solar radiation spectrum, an atmospheric transmission spectrum, and the non-radiative heat transfer coefficient are required. Typically, the AM1.5 spectrum is used to model solar radiation. An atmospheric transmission spectrum at the measuring location is modeled using Modtran to allow for the highest accuracy possible.[25,26] The data used for the calculations performed in this paper and a schematic for calculating the thickness dependent angular and spectral emissivity are shown in Figure 11.2.

The energy radiated by the emitter material can be calculated using the spectral

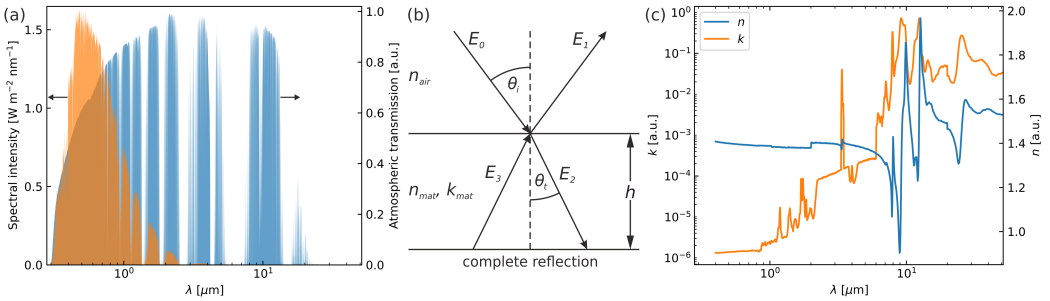

Figure 11.2: (a) Atmospheric transmittance spectrum generated using Modtran for the measurement location (Bayreuth), as well as the employed AM1.5 solar spectrum.[25,26] (b) Schematics for calculating the angular and spectral emittance based on the complex refractive index of the material and its thickness. (c) Utilized complex refractive index data for PDMS.[27,28]

radiance I_b described by Planck's law, which depends on the emitter material temperature T_mat and the emissivity of the emitter material $\varepsilon_\mathrm{mat}(\lambda, h, \theta)$, depending on wavelength λ, thickness h and polar angle θ, and the azimuthal angle ϕ.

$$P_\mathrm{mat} = \int_0^{2\pi} d\phi \int_0^{\pi/2} \sin\theta \cos\theta \, d\theta \int_0^{\infty} I_b(\lambda, T_{mat}) \cdot \varepsilon_\mathrm{mat}(\lambda, h, \theta) \, d\lambda \tag{11.2}$$

Azimuthal dependency is not considered in our spectral-dependent and directional-independent viewpoint and therefore reduces to a factor of 2π.

$$P_\mathrm{mat} = 2\pi \int_0^{\pi/2} \sin\theta \cos\theta \int_0^{\infty} I_b(\lambda, T_{mat}) \cdot \varepsilon_\mathrm{mat}(\lambda, h, \theta) \, d\lambda \, d\theta \tag{11.3}$$

Here, the thickness dependency becomes evident because the emittance of the film depends on the material thickness h. The angular and spectral emittance of the film $\varepsilon_\mathrm{mat}(\lambda, h, \theta)$ is defined as $1 - R(\lambda, h, \theta)$, where $R(\lambda, h, \theta) = \frac{|E_0|^2}{|E_1|^2}$ is the reflectance, as proposed by Zhu et al.[19] A schematic representation for calculating the angular and spectral emittance is shown in Figure 11.2b.

To calculate the emittance, the following parameters are introduced with the Fresnel equation for s- and p-polarized waves, respectively

$$r^\mathrm{s}_\mathrm{air,mat} = \frac{n_\mathrm{air} \cos\theta_i - n_\mathrm{mat} \cos\theta_t}{n_\mathrm{air} \cos\theta_i + n_\mathrm{mat} \cos\theta_t} \tag{11.4}$$

$$r^\mathrm{p}_\mathrm{air,mat} = \frac{n_\mathrm{mat} \cos\theta_i - n_\mathrm{air} \cos\theta_t}{n_\mathrm{mat} \cos\theta_i + n_\mathrm{air} \cos\theta_t} \tag{11.5}$$

$$\cos\theta_t = \sqrt{1 - \left(\frac{n_\mathrm{air}}{n_\mathrm{mat}}\right)^2 \sin^2\theta_i} \tag{11.6}$$

Perfect reflection at the material-silver interface results in

$$\frac{|E_3|^2}{|E_2|^2} = \exp(-2\alpha \cdot h_\mathrm{eff}) \tag{11.7}$$

With the absorption coefficient α and the angle-dependent effective thickness h_eff as

$$\alpha = \frac{4\pi \cdot k}{\lambda}, \quad h_\mathrm{eff} = h/\cos\theta_t \tag{11.8}$$

For an incoherent wave, one can calculate the reflectance for s- and p-polarization following the derivation of Zhu et al.[19] as

$$R^\mathrm{s,p} = |r^\mathrm{s,p}_\mathrm{air,mat}|^2 + \frac{\left|1 - (r^\mathrm{s,p}_\mathrm{air,mat})^2\right|^2 \exp(-2\alpha \cdot h_\mathrm{eff})}{1 - |r^\mathrm{s,p}_\mathrm{air,mat}|^2 \exp(-2\alpha \cdot h_\mathrm{eff})} \tag{11.9}$$

The spectral-, thickness-, and angular-dependent emittance is then finally calculated as

$$\varepsilon_{\mathrm{mat}}(\lambda, h, \theta) = 1 - \frac{R^{\mathrm{s}} + R^{\mathrm{p}}}{2} \tag{11.10}$$

The thickness dependency of the material's emittance is apparent in the energy radiated by the material and the energies absorbed due to solar and atmospheric radiation. As for the incoming radiation from the sun, a fixed position is used with $\theta_{\mathrm{sun}} = 48.2°$ for AM1.5 conditions, the angular integration vanishes, and only a spectral integration is performed.

$$P_{\mathrm{sun}} = \int_0^{\infty} I_{\mathrm{AM1.5}}(\lambda) \cdot \varepsilon_{\mathrm{mat}}(\lambda, h, \theta_{\mathrm{sun}})\, d\lambda \tag{11.11}$$

Here, $I_{\mathrm{AM1.5}}$ denotes the AM1.5 spectral distribution of solar radiation depicted in Figure 11.2a.[26] In contrast, for incoming radiation from the atmosphere, the angular intergration has to be performed.

$$P_{\mathrm{atm}} = 2\pi \int_0^{\pi/2} \sin\theta \cos\theta \int_0^{\infty} I_b(\lambda, T_{atm}) \cdot \varepsilon_{\mathrm{atm}}(\lambda, \theta) \cdot \varepsilon_{\mathrm{mat}}(\lambda, h, \theta)\, d\lambda\, d\theta \tag{11.12}$$

where $\varepsilon_{\mathrm{atm}}(\lambda, \theta) = 1 - \tau_{\mathrm{atm}}(\lambda, 0)^{1/\cos\theta}$ with $\tau_{\mathrm{atm}}(\lambda, 0)$ being the spectral transmittance of the atmosphere at zero zenith angle depicted in Figure 11.2a. Intrinsic losses due to convection and conduction are treated with a comprehensice heat transfer coefficient h_{nonrad}.

$$P_{\mathrm{nonrad}} = h_{\mathrm{nonrad}} \cdot (T_{\mathrm{atm}} - T_{\mathrm{mat}}) \tag{11.13}$$

This heat transfer coefficient is taken as an average of literature values with $h_{\mathrm{nonrad}} = 4.4\ \mathrm{W\ m^{-2}\ K^{-1}}$.[2,3,19,29,30] Instead of performing the spectral integration from zero to infinity, the upper boudary is set to 55 μm due to limited data availability. This limit if justified because approximately 97% of the emitted thermal energy at 298 K is confined to wavelengths below 55 μm. Furthermore, convergence of the upper integration boundary os shown in Figure 11.8, Supporting Information. Moreover, the influence of the comprehensive heat transfer coefficient h_{nonrad} is also shown in Figure 11.9, Supporting Information.

11.4 Results and Discussion

11.4.1 Calculations

To illustrate the concept of an optimum emitter thickness, we first examine the individual energetic contributions for PDMS at T_{amb}. At ambient temperature, the non-radiative contributions P_{nonrad} can be discarded, as no intrinsic losses due to conduction or convection are present, and emitter and atmospheric thermal

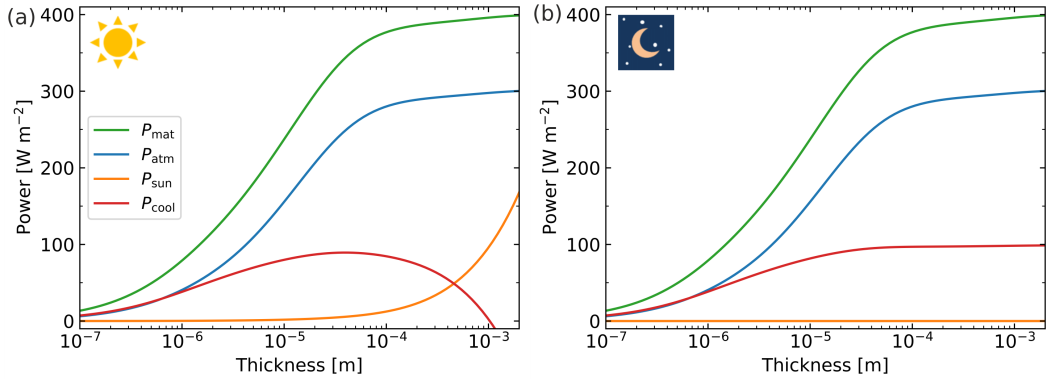

Figure 11.3: Individual energetic components contributing at ambient temperature as a function of thickness, as well as the resulting cooling power, during day- (a) and night-time (b).

radiation are modeled at the same temperature. The remaining contributions of equation (11.1) and the resulting cooling power at ambient temperature are depicted in Figure 11.3.

Figure 11.3a displays the daytime case, revealing an optimum emitter thickness where the resulting cooling power is maximized. At low thicknesses P_{mat} and P_{atm} exhibit an increase, as in the IR-regime where those contributions have their origin, the absorption coefficient of PDMS has the highest order of magnitude. At thicknesses above $1 \cdot 10^{-4}$ m, those contributions reach a quasi-plateau, where the difference between them remains approximately constant. At the same time, for emitter thicknesses above $1 \cdot 10^{-5}$ m, the absorption in the solar wavelength regime is no longer negligible. The absorbed energy due to solar radiation increases, with further increasing the emitter thickness. The counterbalance between the increasing emitted power below $1 \cdot 10^{-4}$ m and the increasing absorbed power due to solar radiation above $1 \cdot 10^{-5}$ m, therefore, leads to a maximum cooling power as a function of emitter thickness. For the night-time case in Figure 11.3b, the contribution of solar radiation is zero, leading to a plateau being reached at high emitter thicknesses. Even as the emitted power and the power absorbed due to atmospheric radiation both continue to increase with increasing emitter thickness, the resulting cooling power asymptotically approaches a constant value. Therefore, no optimum thickness is apparent, but a minimum thickness required to reach the highest cooling power can be estimated.

After the individual contributions have been treated as a function of thickness at ambient temperature, the resulting cooling power for PDMS as a function of emitter thickness and emitter temperature is shown in Figure 11.4. Here, the cooling power is color-coded and displayed as a function of thickness and temperature difference relative to the atmospheric temperature. Negative cooling powers, equivalent to a sample that heats up, are not shown for simplicity. The boundary of the color-coded area thus represents the achievable equilibrium temperatures below ambient for the respective thickness. Red dots highlight the thickness with the highest cooling power

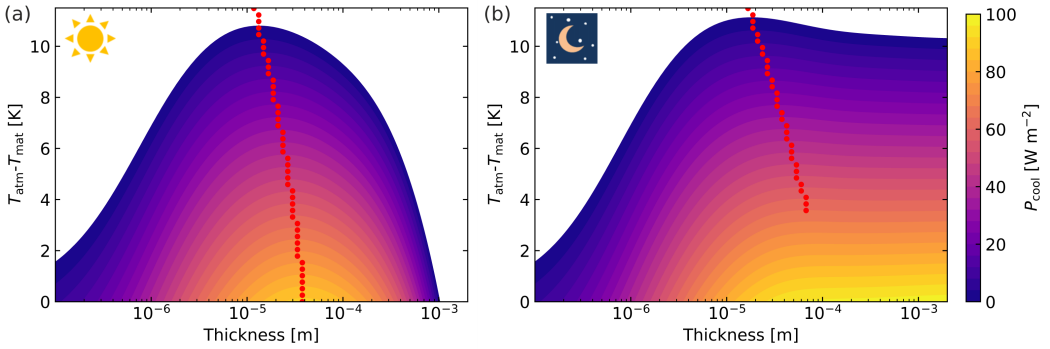

Figure 11.4: Resulting cooling power as a function of thickness and emitter temperature, as well as highlighted thickness (red dots) with the highest cooling power at the respective temperature, during day- (a) and night-time (b).

at the respective temperature below ambient.

In general, the cooling power decreases as the material cools below ambient temperature ($T_{atm} - T_{mat} > 0$), as the blackbody radiation is reduced, and non-radiative heat transfer is apparent. An optimum thickness effect can be recognized in both the maximum cooling power at ambient, as discussed above, as well as the minimum equilibrium temperature below ambient, and therefore the highest temperature difference, for the daytime case. A slight shift of the highest cooling power to lower thicknesses with increasing the temperature difference between material and ambient is apparent. This shift can be understood as the emitted power approximately scales with temperature to the fourth power. A lower emitted power due to a lower emitter temperature is then counterbalanced by the incoming solar and atmospheric radiation at lower thicknesses. Our result confirms that a cooler with a certain thickness can either reach the lowest possible equilibrium temperature or the highest cooling power at ambient temperature. Conceptually, both cannot be optimized simultaneously, even as the absolute thickness values only differ by half an order of magnitude. This distinction was also the subject of discussion by other researchers when comparing different artificial emitter materials, where a blackbody emitter has higher cooling power at ambient but selective emitters can reach lower equilibrium temperatures.[1,16]

The resulting cooling power as a function of thickness and temperature during night-time for PDMS is shown in Figure 11.4b. Close to ambient, as discussed in Figure 11.3b, the cooling power asymptotically approaches a maximum value, where an increase in thickness only incrementally increases the maximum cooling power due to the exponential nature of the material emissivity. Compared to the daytime case, higher cooling powers and lower equilibrium temperatures can be reached due to the absence of solar radiation. Only above a certain temperature difference threshold, an optimum thickness in a similar order of magnitude as for the daytime case becomes apparent. This effect is discussed in the Supporting Information (Figure 11.10), as the effect is significantly less pronounced than during daytime. In general, for

materials with different optical properties, an optimum thickness for the night-time cooling power may be more strongly pronounced and should, therefore, be separately verified.

The main difference between day- and night-time is a clearly defined optimum emitter thickness during daytime. In contrast, a plateau is reached at high emitter thicknesses during night-time, and only above a certain temperature difference threshold, an optimum thickness becomes apparent.

To point out that this is a general effect and not only applicable to PDMS, we performed similar calculations for other commercial polymeric materials, i.e., polystyrene (PS), polymethyl methacrylate (PMMA), and polyethylene terephthalate (PET), where broadband complex refractive index data are available in the literature.[29] There, the same basic principles of optimum emitter thickness apply and are shown in the Supporting Information (Figure 11.11).

11.4.2 Sample Characterization

To confirm our theoretical observations, we prepared a set of PDMS films with different thicknesses and characterized their absorption properties with UV-Vis- and FTIR-Spectroscopy. Further, we conducted rooftop experiments to determine the reached equilibrium temperatures (see experimental section).

The actual absorptance of PDMS films with different thicknesses on reflecting Ag films is displayed in Figure 11.5. For thinner PDMS layers, the emission is more confined within the first atmospheric window. We attribute this to the high absorption coefficient of the material in this spectral region. For higher thicknesses, the absorptance in the near-infrared region is substantially increasing, leading to an overall increase in emitted radiation. However, at the same time, the absorption of solar radiation is promoted. The silver mirror efficiently reflects all wavelengths larger than 400 nm and, therefore, prevents absorption of solar radiation by the underlying substrate. However, for shorter wavelengths, the absorptance increases. This loss in cooling power cannot be avoided in our sample geometry and leads to reduced cooling power in the daytime case.

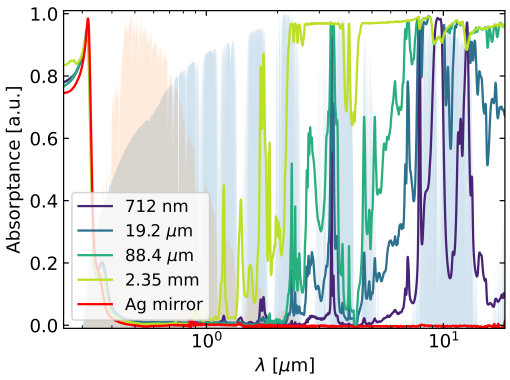

Figure 11.5: Absorptance of the respective PDMS samples with different thicknesses on Ag mirrors from UV-Vis to mid-IR range.

To compare if the used optical data can adequately describe our samples, we calculated the absorptance for the respective thicknesses based on the complex refractive index. The resulting absorptance spectra (Figure 11.12) capture the main features

in the mid-infrared region. However, in the solar region, larger deviations for the thickest sample are evident. Therefore, the exact determination of the complex refractive index is crucial for a prediction of the cooling performance. Substantial variations in the absorption coefficient can be expected for every material due to the large wavelength range relevant for passive cooling materials. The availability of precise theoretical data spanning several orders of magnitude is a limitation of our theoretical approach.

11.4.3 Rooftop Measurements

We experimentally determined the passive cooling performance of PDMS films with different thicknesses by a rooftop experiment to verify the theoretical expectation. PDMS films were prepared on Ag coated silicon wafers by spincoating or attachment (see experimental section). As shown in Figure 11.6, samples were placed individually in self-built setups for rooftop measurements.

Styrofoam insulation was applied to the outside to reduce conduction, and an LDPE cover was used to minimize convection, respectively. Additionally, the entire setup was covered with Al foil to reflect most of the solar irradiation. To ensure comparability between the different setups, the variety between each setup was first checked by tracking the temperature of five identical Al mirrors in daytime (Figure 11.13). A minor deviation of approximately 0.5 °C was observed during a 1.5 h rooftop measurement, under the average direct sunlight irradiation of 857 W m^{-2}. In the daytime experiment, since an LDPE foil is applied to prevent convection, a slight greenhouse effect is apparent in the measurement cell,[31,32] which results in a temperature elevation of all measured samples when exposed to the sunlight. As shown in Figure 11.6b, the temperature of the bare Ag mirror itself increased by approximately 7 °C at an average direct sunlight irradiation of 754 W m^{-2}, compared to air temperature. We attribute this greenhouse effect to a parasitic solar absorption of the sample holder and of the Ag mirror itself. Consistently, we do not observe this increase of the temperature baseline during night-time, where the Ag mirror exhibits a similar temperature to air. To have a precise comparison and to emphasize the impact of the layer thickness on the passive cooling performance of the emitter, the measured temperature of the PDMS films with different thicknesses are, therefore, compared to the bare Ag mirror. During the experiment, the Ag mirror is exposed to comparable measurement conditions as the samples (Figure 11.6c/e). We, therefore, use the Ag mirror temperature as reference instead of the air temperature, which is susceptible to measurement conditions, e.g., location or wind speed.

In the night-time experiment (Figure 11.6d), the passive cooling effect of the PDMS films is directly observable. All films cool down from their initial temperature (air temperature) after exposure to the clear sky until a steady state was approached.

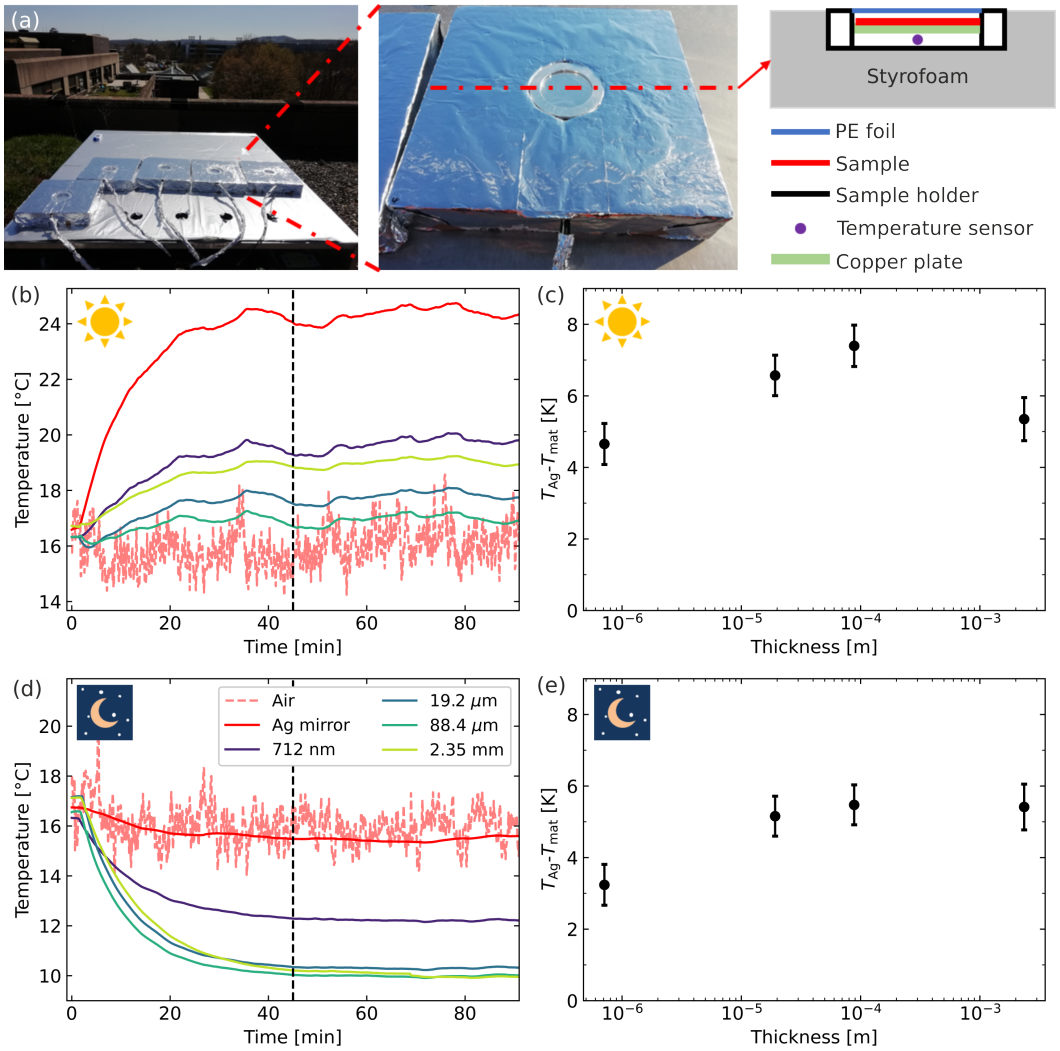

Figure 11.6: Rooftop measurement for PDMS films at day- and night-time. (a) Photographs and schematic of the setup for rooftop measurements. Temperature tracking of PDMS films on Ag mirror with different thicknesses, i.e., 712 nm, 19.2 μm, 88.4 μm, and 2.35 mm, and the bare Ag mirror, (b) day- and (d) night-time. The average solar irradiation during the entire daytime measurement was 754 W m^{-2}. The temperature difference between the bare Ag mirror and the PDMS films as a function of layer thickness at (c) day- and (e) night-time, respectively. The measurement was carried out under a clear sky on 23.04.2021, Bayreuth, Germany.

By contrast, the Ag mirror reference exhibited only an insignificant temperature reduction, which is likely attributed to the thin passivating layer of SiO_2.

To compare the cooling performance of the samples, we extracted the steady state temperature difference between PDMS films and the Ag mirror reference from the experiments. The average temperature difference data in the steady state regime (after 45 min) are displayed in Figure 11.6c/e. During daytime, the temperature difference increased from 4.7 K for the 712 nm thick film to 7.4 K for the 88.4 μm film. We attribute this increase in passive cooling performance to the increased overall emittance of the film. In contrast, the passive cooling performance is reduced for the much thicker 2.35 mm PDMS film. In this case, the temperature difference dropped to 5.3 K. We attribute this drop to the increased absorption of solar radiation, as discussed in section 11.4.1 (Figure 11.3a). For the night-time case, the observed temperature difference between films and reference increases with increasing film thickness, reaching a plateau at high thicknesses. For the larger thicknesses, the temperature difference is not significantly increased further.

Despite the differences in the assumptions made in the calculations and actual experimental conditions, the observations of thickness dependent passive cooling performance of PDMS films are in good agreement with the results obtained from our theoretical calculations. Sources of error having the most significant influence are deviations of the actual solar and atmospheric spectra to the environmental ones, as well as deviations of the sample's optical properties from those calculated by the optical constants. Also, the exact determination of the comprehensive heat transfer coefficient would increase the accuracy of the calculations but is a non-trivial task. Since many parameters influence the net cooling power in complex and entangled dependencies, the agreement of theory and experiment is nevertheless very convincing. All the mentioned sources of error affect the absolute values of the equilibrium temperature, but not the day and night-time dependence trend.

To ensure that the observed behavior of the samples with different thicknesses is also valid for a more extended measurement time, we performed continuous measurements (from 18:00, 25th to 18:00, 26th April 2021, University of Bayreuth, Bayreuth, Germany). The measured temperatures of the different samples and an Ag reference are presented in Figure 11.7a. All PDMS films with different thicknesses exhibit a lower temperature than the Ag mirror in the entire 24 h measurement. The overall temperatures are lower during night-time and increase with the onset of solar irradiance. To further reveal the thickness dependence on the cooling performance of PDMS films, the temperature difference ($T_{\mathrm{Ag}} - T_{\mathrm{mat}}$) is plotted in Figure 11.7b. A maximum temperature difference of 3.2 K, 4.4 K, 4.3 K, and 4.7 K was obtained for the 712 nm, 19.2 μm, 88.4 μm, and 2.35 mm PDMS films during night-time, respectively. In contrast, a maximum temperature difference of 5.8 K, 7.4 K, 8.1 K, and 6.7 K was observed from the 712 nm, 19.2 μm, 88.4 μm, and 2.35 mm PDMS films in daytime. The observed temperature difference is consistent with our previous observations in short-time rooftop measurements and

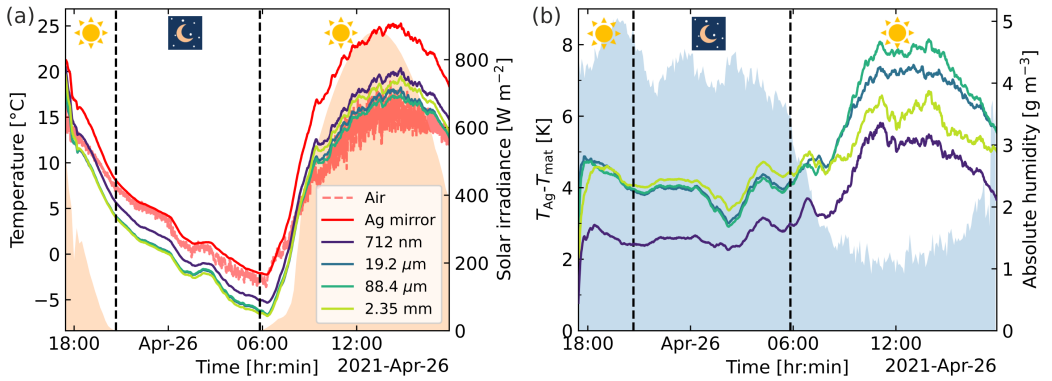

Figure 11.7: 24 h rooftop measurement of PDMS films with different thicknesses. a) Temperature tracking of different samples. Corresponding solar irradiation is plotted as the background. b) Temperature difference between Ag mirror and the PDMS films ($T_{\mathrm{Ag}} - T_{\mathrm{mat}}$) during the entire measurement, along with the absolute humidity. The measurement was carried out under a clear sky, on 25-26.04.2021, Bayreuth, Germany.

the simulation result. Again, for the night-time case, except for the thinnest sample, the different thicknesses reach similar temperature differences in accordance with the short time measurement. During daytime, the different thicknesses spread out, revealing the optimum thickness effect.

The absolute temperature difference is smaller for the night-time period of the experiment compared to the daytime. This observation is counter-intuitive because, during daytime, additional cooling power is lost by the absorption of solar radiation. However, the absolute sample temperature is lower at night-time, so a reduced cooling power is apparent. Besides the absolute temperature also the humidity in the atmosphere is affecting the cooling potential. We monitored the relative humidity next to the experimental setup and calculated the absolute humidity present to account for changes in temperature (Figure 11.7b). The atmosphere's higher water content during night-time decreases the atmospheric transparency, and hence, the atmospheric radiance increases, leading to a smaller equilibrium temperature difference.

11.5 Conclusion

In this work, we presented a complex refractive index-based method to determine the optimum thickness for passive-cooling emitter materials in a back-reflector configuration. We observed optimum thicknesses in both day- and night-time applications, depending on the optical properties of the material. The optimum thickness significantly influences the daytime application, while it is rather a factor in minimizing fabrication costs at maximum cooling capacity during night-time. Our calculations further confirmed that a cooler with the highest ambient temperature cooling power does not necessarily reach the lowest equilibrium temperature. Our

approach focuses on materials that use a back-reflector geometry to prevent solar heat uptake. The theoretical prediction can also be used for coolers that operate with a solar filter layer or rely on a scattering approach. For these calculations, the model needs to be adjusted to deal with the solar radiation term properly. Especially, proper complex refractive index characterization and theoretical description of a highly scattering material can be challenging. Overall, we emphasize that in addition to the passive cooling material and its nano/microstructure, the layer thicknesses of the passive cooling device need to be optimized as well.

11.6 Experimental Section

Calculations: An atmospheric temperature of 298.15 K was used for both day- and nighttime to calculate the cooling power. All integrations were done using the trapezoidal integration method in Matlab. As functions inside the integrals need to have the same energy spacing to perform numerical integration, the spectral radiative powers of the sun and atmosphere are adapted to the complex refractive index spacing of the material because they are available in higher resolution. This adaption was done using the 1D data interpolation method in Matlab.
Fabrication of PDMS Films on Ag Mirrors: PDMS films with different thicknesses were prepared on protected silver mirrors. For the mirrors, a 100 nm thick Ag layer was thermally evaporated on the wafer. Following, a 10 nm thick layer of Silicon oxide was deposited with a sputter coating step. This additional protection layer is used to prevent oxidation of the silver layer after PDMS deposition. A prepolymer mixture of PDMS (Sylgard 184, Dow Chemical) with a mixing ratio of prepolymer to crosslinker of 10:1 (by mass) was degassed in a desiccator with reduced pressure. The mixture was spincoated on the mirrors with 1000 rpm and 3000 rpm to obtain layers with approximately 100 μm and 20 μm thickness, respectively. For the approximately 1 μm thick PDMS layer, the prepolymer/crosslinker mixture was diluted to a 25 wt% solution with *n*-Hexane. The mixture was then spincoated onto the silver mirror with 4000 rpm. The layers were cured at room temperature over 48 h. For the sample with 2.35 mm thickness, the prepolymer mixture was filled in a mold and cured at 75 °C for 1.5 h. A circular piece with a diameter of approximately 5 cm was cut and gently placed on a silver mirror.
The sample thickness of the thinner samples (712 nm, 19.2 μm, and 88.4 μm) was determined with a 3D laser scanning microscope (LEXT OLS 5000, Olympus). A small incision was made to determine the actual height of the polymer layer. An area of 258 μm^2 around the incisions was imaged, and the height difference was determined by averaging the two major height fractions present in the image. The 2.35 mm high sample height was determined with a touch probe (Litematic VL-50, Mitutoyo). Different spots on the sample were measured, and the resulting height

values were averaged.

Optical characterization with UV-vis and FTIR-Spectroscopy: UV-Vis Reflectance R was measured with a UV-vis spectrometer (Cary 5000, Agilent Technologies) equipped with an Integrating sphere accessory (Labspheres). The measurements were conducted at the reflection port of the sphere with a fixed incident angle of 8°. As a reference, a Spectralon diffuse reflectance standard (Labspheres) was used. The FTIR-Spectroscopy measurements were conducted with an IR-spectrometer (Vertex 70, Bruker) combined with a gold coated integrating sphere accessory (A562, Bruker). The measurements were performed at the lower reflection port of the accessory (non-normal incidence). As a reference, a gold mirror was used. The absorptance (emittance) A was calculated considering the energy conservation with $A = 1 - R$ assuming, that transmission can be neglected due to the silver layer.

Rooftop performance experiment: All rooftop measurements were carried out on the roof of a four-floor building (University of Bayreuth, Bayreuth, Germany) under a clear sky. The emitter was placed in a homemade sample holder (3D printed with material of acrylonitrile butadiene styrene), which was thermally insulated by Styrofoam and covered with Mylar aluminum Foil. (Figure 11.6a). Low-density polyethylene (LDPE) foil with a thickness of approximately 10 μm was applied to the sample holder to prevent convection. The emitter temperatures were measured by PT100 temperature sensors and recorded by a digital multimeter (DAQ6510, Tektronix, Germany) every 5 s. Air temperature is measured with a thermal couple (T-type) which is placed in the ambient environment next to the setup. The solar irradiance data are obtained from the weather station University Bayreuth (Ecological-Botanical Garden, 400 m away from the rooftop measurement). During the rooftop measurement, all sample setups were first stored under the table to achieve a similar starting temperature. A few minutes after the start of data recording, the sample setups were placed on the table to face the sky. Short- and long-term measurements were conducted for 1.5 h and 24 h, respectively. During the measurements, the relative humidity RH was tracked with a temperature logger (LOG220, DOSTMANN electronic GmbH) next to the setup. The absolute humidity AH in g/m3 was calculated using RH in percent and the ambient temperature T_{amb} in °C by $AH = \frac{6.112 \cdot \exp(\frac{17.67 \cdot T_{\mathrm{amb}}}{T_{\mathrm{amb}}+243.15}) \cdot RH \cdot 2.1674}{273.15+T_{\mathrm{amb}}}$.

Acknowledgments

K.H. and T.L. contributed equally to this work. The authors gratefully acknowledge the contributions of M.Sc. Thomas Tran, Stefan Rettingerm for technical support and Klaus Müller for the metal evaporation. The solar radiance data were kindly provided by Prof. Christoph Thomas. This project has received funding from

the European Research Council (ERC) under the European Union's Horizon 2020 research and innovation program (grant agreement no. 714968).

11.7 Supporting Information

11.7.1 Convergence of the Resulting Calculated Cooling Power

To verify the convergence of the resulting cooling power as a function of the upper integration boundary, we map out the corner points of the thickness-temperature space shown in Figure 11.4.

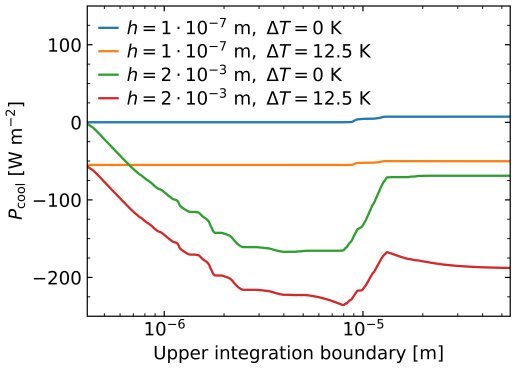

Figure 11.8: Convergence of the integrated total cooling power as a function of upper integration boundary for the points enclosing the analyzed temperature and thickness space.

Namely, those are thicknesses of $1 \cdot 10^{-7}$ m and $1 \cdot 10^{-3}$ m and temperatures differences of 0 K and 12.5 K relative to ambient.

Convergence of the resulting cooling power as a function of the upper integration can be seen. For high thickness and temperature differences, maybe higher integration boundaries might be needed, but for the calculations performed in this work, the upper integration boundary of 55 μm is sufficient.

11.7.2 Influence of the Non-Radiative Heat Transfer Coefficient

To analyze the influence of the comprehensive heat transfer coefficient due to convection and conduction, several coefficients are used spanning two orders of magnitude. Regardless of the absolute value, an optimum thickness is always apparent. As intrinsic losses increase, smaller temperature differences to ambient are apparent, as to be expected.

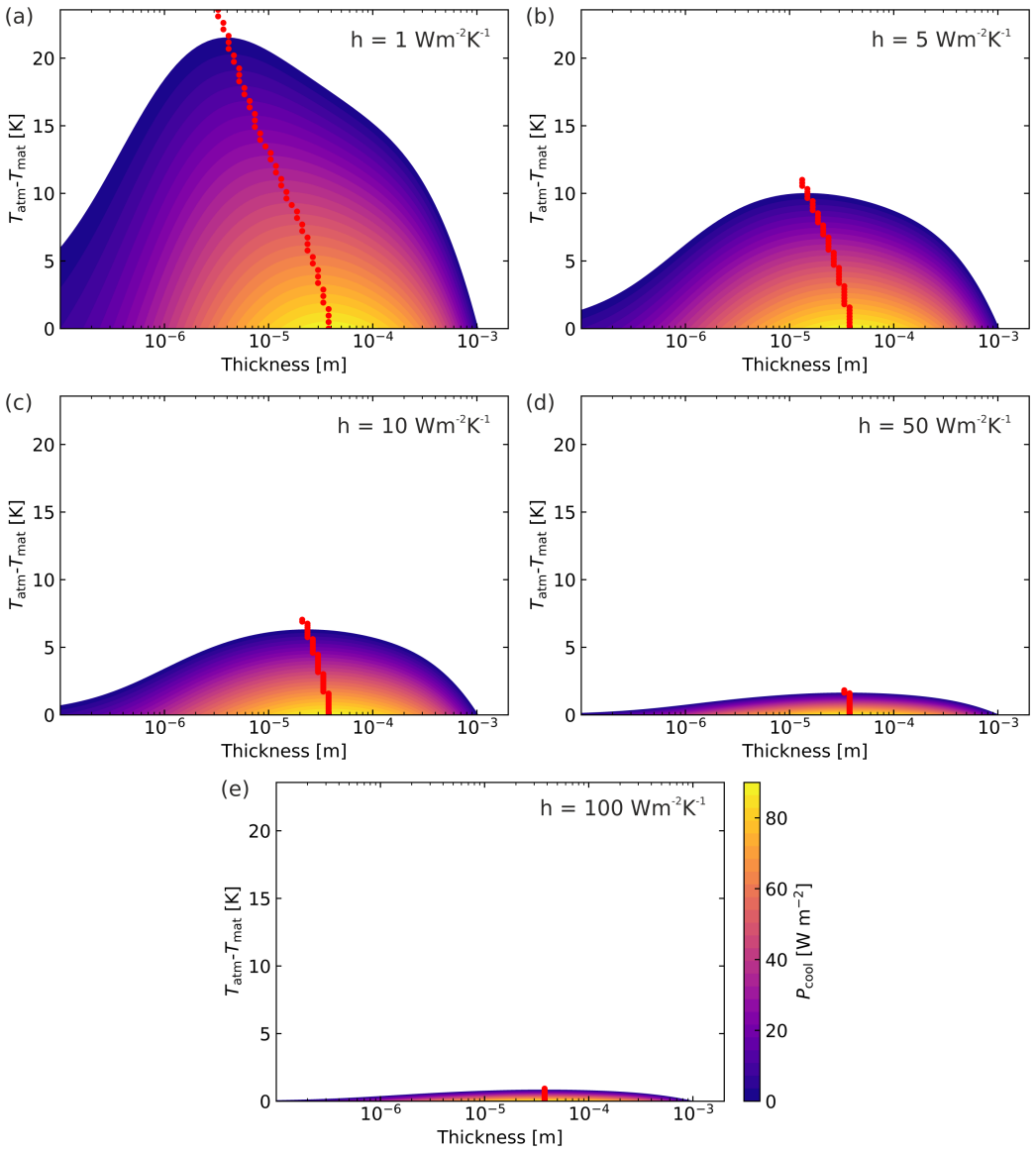

Figure 11.9: Influence of the non-radiative heat transfer coefficient on the net cooling power for PDMS.

11.7.3 Optimum Emitter Thickness During Night-Time

Only above a certain temperature difference threshold, an optimum thickness in a similar order of magnitude as for the daytime case becomes apparent. This maximum has a different origin compared to the daytime case. As the emitter temperature decreases, the power radiated decreases due to Planck's law of radiation. Above a certain threshold, for PDMS approximately 3 K below ambient, the derivatives regarding the thickness of the power absorbed and emitted have an intersection point. This intersection point represents a zero crossing in the derivative of the net cooling power, and in this case, a maximum cooling power. To better illustrate this effect, we focus on a temperature difference of 0 K and 10 K relative to ambient temperature.

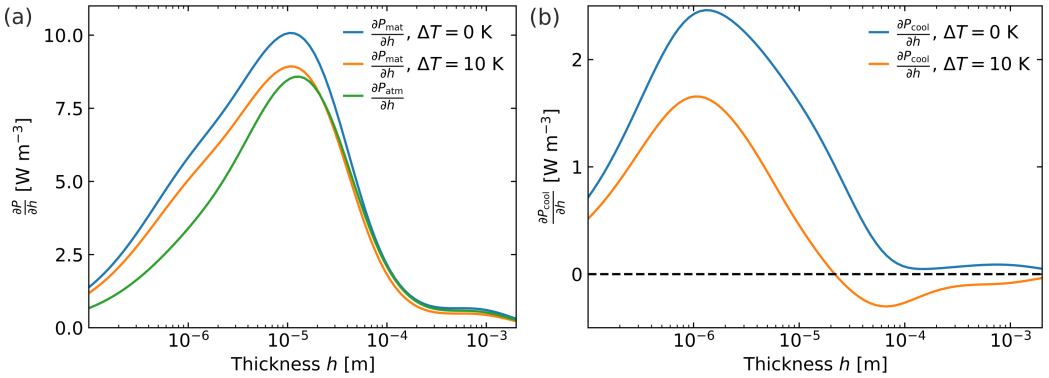

Figure 11.10: Numerical derivatives of the individual energetic contributions of material and atmosphere as a function of thickness during night-time (a), as well as the total cooling power (b) with respect to thickness. For $\Delta T = 10$ K, there is an optimum thickness apparent, while there is none for $\Delta T = 0$ K.

At ambient temperature, the derivative of the power emitted is continuously higher than the derivative of the power absorbed by the atmosphere. As the emitter temperature decreases, above a certain thickness, here approximately 20 μm, the derivative of the power absorbed by the atmosphere exceeds the derivative of the power emitted. This point represents a zero crossing of the total cooling power, depicted in Figure 11.10b, and in this case, a maximum cooling power that is not apparent at ambient temperature.

11.7.4 Verification of the Calculations by Means of Further Materials

We also performed calculations based on the complex refractive index of other polymeric materials to verify the optimum thickness effect for passive cooling in back-reflector geometry.[27,28] For polystyrene, polymethyl methacrylate, and polyethylene terephthalate, the cooling powers as a function of thickness and temperature are shown in Figure 11.11.

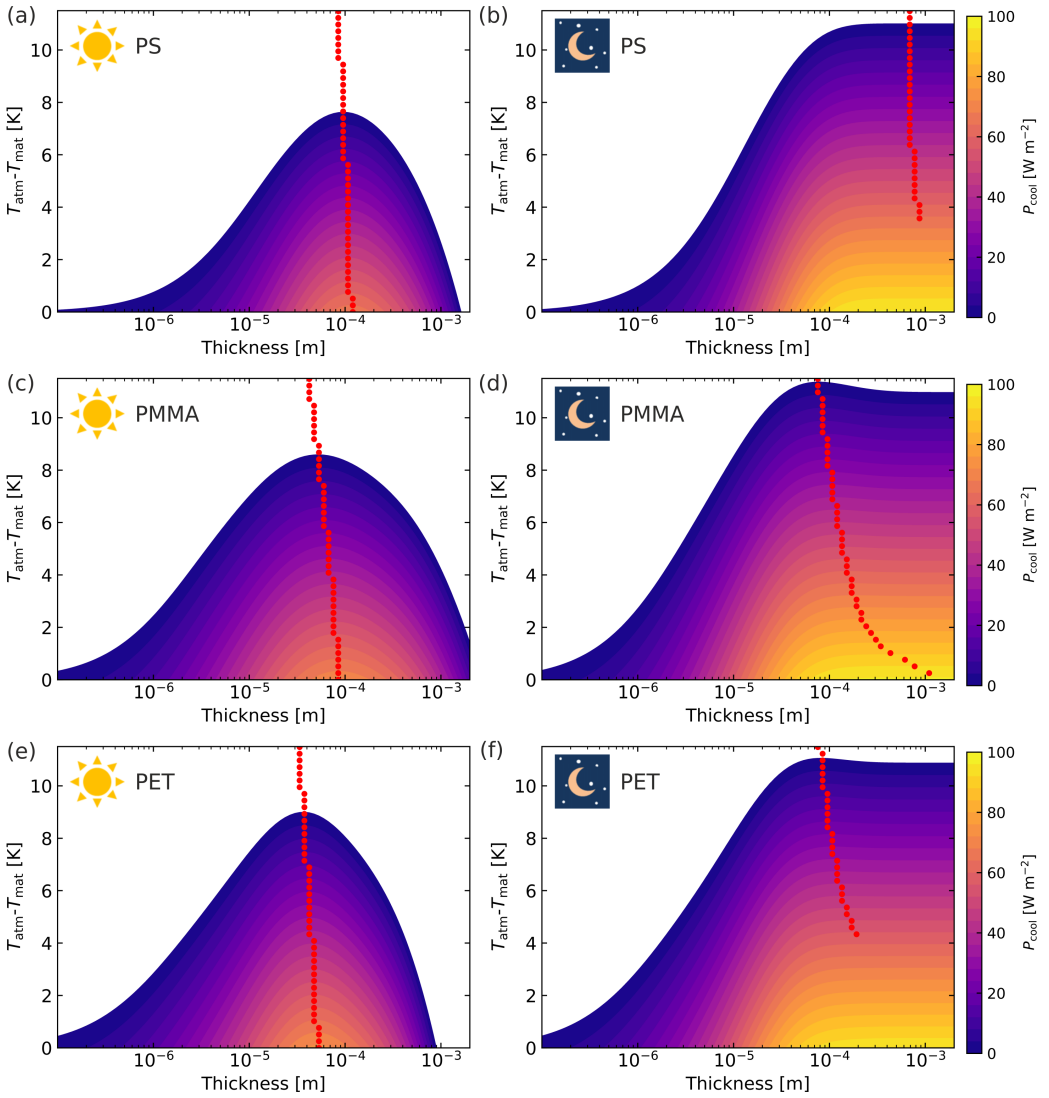

Figure 11.11: Resulting cooling power as a function of thickness and emitter temperature, as well as highlighted thickness (red dots) with the highest cooling power at the respective temperature, during daytime and night-time for polystyrene (a), (b) polymethyl methacrylate (c), (d) and polyethylene terephthalate (e), (f).

All materials investigated exhibit an optimum thickness during daytime, while the position, as well as the absolute cooling powers, vary. The same can be seen during

night-time, whereas the temperature threshold below which an optimum thickness becomes apparent is also dependent on the emitter material. In summary, this can be interpreted as a general confirmation of the effect.

11.7.5 Complex Refractive Index Data as a Source of Error

The primary source of error, in addition to the atmospheric and solar spectrum, are the complex refractive index data of the investigated emitter material. A comparison of the measured absorptance spectrum and the expected absorptance based on the measured thickness and the complex refractive index is shown in Figure 11.12.
A qualitative agreement between measured and estimated absorptance spectrum is apparent, while the absolute values exhibit clear deviations. The main drawback is the overestimation of the absorption in the solar regime, leading to an optimum cooling power at lower thicknesses. For further work based on this approach, accurate complex refractive index data are, therefore, crucial.

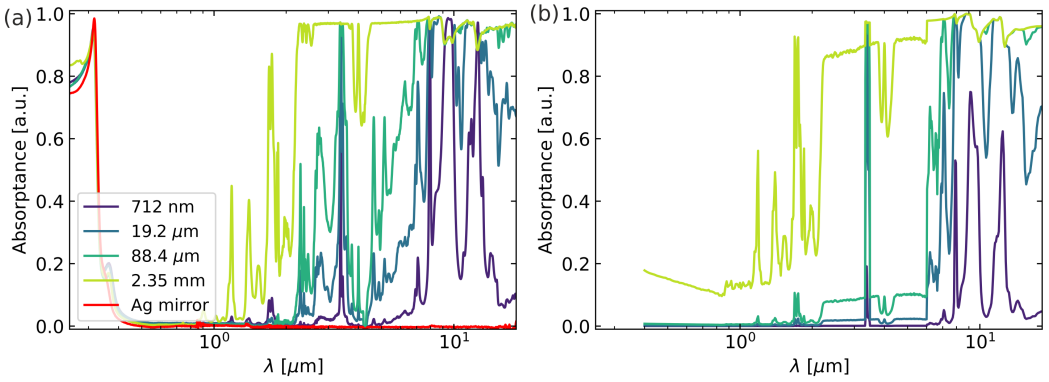

Figure 11.12: Measured absorptance (a) in comparison to the estimated absorptance based on the complex refractive index data and thickness (b) for an angle of incidence of 8°.

11.7.6 Verification of the Measurement Setup

To determine errors induced by the measurement setup, a measurement with five identical Al mirrors was performed. As the identical Al mirrors exhibit a maximum standard deviation of ±0.3 K, not to overstate our results an error of the measurement setup of ±0.5 K is assumed.

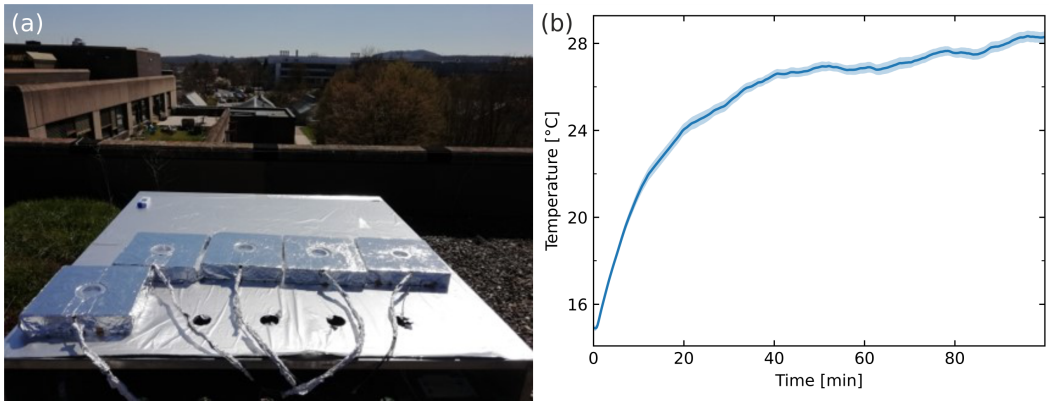

Figure 11.13: (a) photography of the setups used to measure the samples' daytime cooling performance. (b) Comparison of sample temperatures for the samples during the measurement time. Mean and standard deviation of five identical Al mirrors under the average solar irradiation of approximately 856 W m^{-2}. (Start at 12:20, 23rd April 2021, University of Bayreuth, Bayreuth, Germany)

11.8 References

[1] M. M. Hossain, M. Gu, *Advanced Science* **2016**, *3*, 1500360.

[2] B. Zhao, M. Hu, X. Ao, N. Chen, G. Pei, *Applied Energy* **2019**, *236*, 489–513.

[3] A. P. Raman, M. A. Anoma, L. Zhu, E. Rephaeli, S. Fan, *Nature* **2014**, *515*, 540–544.

[4] N. W. Pech-May, T. Lauster, M. Retsch, *ACS Applied Materials & Interfaces* **2021**, *13*, 1921–1929.

[5] J. Mandal, Y. Fu, A. C. Overvig, et al., *Science* **2018**, *362*, 315–319.

[6] T. Wang, Y. Wu, L. Shi, et al., *Nature Communications* **2021**, *12*, 365.

[7] A. R. Gentle, G. B. Smith, *Nano Letters* **2010**, *10*, 373–379.

[8] Y. Zhai, Y. Ma, S. N. David, et al., *Science* **2017**, *355*, 1062–1066.

[9] J.-l. Kou, Z. Jurado, Z. Chen, S. Fan, A. J. Minnich, *ACS Photonics* **2017**, *4*, 626–630.

[10] L. Zhou, H. Song, J. Liang, et al., *Nature Sustainability* **2019**, *2*, 718–724.

[11] U. Banik, A. Agrawal, H. Meddeb, et al., *ACS Applied Materials & Interfaces* **2021**, *13*, 24130–24137.

[12] E. Torgerson, J. Hellhake, *Solar Energy Materials and Solar Cells* **2020**, *206*, 110319.

[13] N. W. Pech-May, M. Retsch, *Nanoscale Advances* **2020**, *2*, 249–255.

[14] W. Huang, Y. Chen, Y. Luo, et al., *Advanced Functional Materials* **2021**, *31*, 2010334.

[15] H. Kim, S. McSherry, B. Brown, A. Lenert, *ACS Applied Materials & Interfaces* **2020**, *12*, 43553–43559.

[16] Y. Li, L. Li, L. Guo, B. An, *Optical Materials Express* **2020**, *10*, 1767.

[17] Y. Tian, L. Qian, X. Liu, et al., *Scientific Reports* **2019**, *9*, 19317.

[18] Y. Zhu, Y. Ye, D. Wang, Y. Cao, *OSA Continuum* **2021**, *4*, 416.

[19] R. Zhu, D. Hu, Z. Chen, et al., *Nano Letters* **2020**, *20*, 6974–6980.

[20] C. Sheng, Y. An, J. Du, X. Li, *ACS Photonics* **2019**, *6*, 2545–2552.

[21] L. Zhu, A. Raman, S. Fan, *Applied Physics Letters* **2013**, *103*, 223902.

[22] Y. Chen, J. Mandal, W. Li, et al., *Science Advances* **2020**, *6*, 5413.

[23] G. J. Lee, Y. J. Kim, H. M. Kim, Y. J. Yoo, Y. M. Song, *Advanced Optical Materials* **2018**, *6*, 1800707.

[24] R. A. Yalçın, E. Blandre, K. Joulain, J. Drévillon, *ACS Photonics* **2020**, *7*, 1312–1322.

[25] B. J. Park, J. P. Pantina, E. M. Furst, et al., *Langmuir* **2008**, *24*, 1686–1694.

[26] A. Berk, P. Conforti, R. Kennett, et al. in 6th Workshop on Hyperspectral Image and Signal Processing: Evolution in Remote Sensing (WHISPERS), IEEE, **2014**.

[27] X. Zhang, J. Qiu, X. Li, J. Zhao, L. Liu, *Applied Optics* **2020**, *59*, 2337.

[28] X. Zhang, J. Qiu, J. Zhao, X. Li, L. Liu, *Journal of Quantitative Spectroscopy and Radiative Transfer* **2020**, *252*, 107063.

[29] B. Bhatia, A. Leroy, Y. Shen, et al., *Nature Communications* **2018**, *9*, 5001.

[30] C. G. Granqvist, A. Hjortsberg, *Journal of Applied Physics* **1981**, *52*, 4205–4220.

[31] S. Y. Jeong, C. Y. Tso, J. Ha, et al., *Renewable Energy* **2020**, *146*, 44–55.

[32] D. Chae, M. Kim, P.-H. Jung, et al., *ACS Applied Materials & Interfaces* **2020**, *12*, 8073–8081.

12

A Tailored Indoor Setup for Reproducible Passive Daytime Cooling Characterization

Qimeng Song,* Thomas Tran,* Kai Herrmann,* Tobias Lauster,* Maximilian Breitenbach,* and Markus Retsch*,§

* Department of Chemistry, Physical Chemistry 1, University of Bayreuth, Universitätsstraße 30, 95447 Bayreuth, Germany.

§ Bavarian Polymer Institute, Bayreuth Center for Colloids and Interfaces, and Bavarian Center for Battery Technology (BayBatt), University of Bayreuth, Universitätsstraße 30, 95447 Bayreuth, Germany.

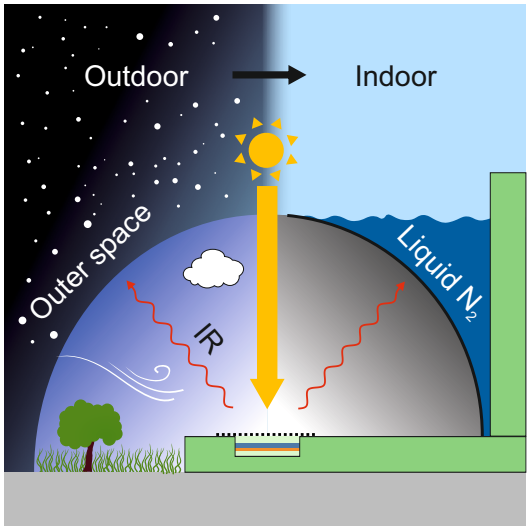

Published in *Cell Reports Physical Science*, **2022**, *3*, 100986.

12.1 Abstract

Passive daytime cooling materials can lower global energy consumption owing to their autonomous cooling capability. Although a significant number of passive cooling materials have been developed recently, their performance characterization is still challenging. Field tests experience high variability due to uncontrollable changes in environmental conditions. Here, we design an indoor setup to characterize the performance of passive cooling materials reproducibly and independently of weather and season. Outdoor measurement conditions are approximated using a liquid-nitrogen-cooled aluminum dome, a solar simulator, and a wavelength-selective inverse sky-window filter. In contrast to outdoor measurements, the results of various reference materials show remarkable precision and repeatability. Additionally, the impact of solar light intensity and temperature on the passive cooling performance can be experimentally investigated. Our setup is a first step in the development of a standardized test method to bring accuracy, reproducibility, and comparability to the emerging field of passive cooling materials.

12.2 Introduction

Passive daytime cooling has emerged as a strong candidate to alleviate the global energy demand for cooling.[1,2] It conveys heat from a material to outer space through the atmospheric window ($8 - 13\ \mu$m) without external energy consumption. For an ideal daytime passive cooling performance, low absorption in the solar range ($0.3 - 2.5\ \mu$m) and high emission over the mid-infrared (MIR) region is stringently required. In the last few years, advanced fabrication techniques have led to various novel materials, including photonically structured materials,[3–5] hybrid composites,[6–9] highly porous materials,[10–13] and hierarchically structured materials.[14–17] These classes of materials promote the development of devices for daytime passive cooling applications.

Two essential techniques are usually used to evaluate a material's passive cooling performance: optical spectroscopy and field testing.[2,18] The former determines the spectral absorption of a material in both the solar and MIR regions. Utilizing a theoretical model based on energy balance considerations, the net passive cooling power of a material can be calculated. Li et al. introduced a simple figure of merit to fairly assess the performance of distinct cooling materials based on their optical properties.[19] However, the comprehensive optical properties, including angle and temperature dependence, of a material, are rather hard to access, especially for complex materials, e.g. multilayer composites, self-adaptive metamaterials[20,21] and materials with irregular surface topography, making it difficult to achieve a precise comparison.

During field testing, the steady-state temperature of a sample and its cooling power at ambient temperature are obtained. However, outdoor measurements are impressionable and uncontrollable, and the outcome strongly depends on measurement conditions,[22,23] e.g., geographical location, solar intensity, ambient temperature, humidity, wind speed, and air pressure. The uncontrollable and unsteady atmospheric conditions limit the comprehensive characterization of passive cooling materials firstly, and replication of the measurement results secondly. Due to this challenge, different materials cannot be compared reasonably. Therefore, a comparable and standardized test method is urgently required to push the development of passive daytime cooling materials forward. In contrast to outdoor environments, an indoor setup is independent of weather conditions and provides a stable and controllable environment for passive cooling characterization. A simple indoor setup for passive cooling characterization was reported by Zhou et al.[24] By using liquid nitrogen-cooled black aluminum foil as a heat sink, the nighttime passive cooling behavior of a PDMS film was imitated. However, their indoor setup did not include a light source. The characterization was thus limited to nighttime conditions. A similar setup was also constructed by Park et al. in a glovebox.[25] With applying a solar simulator, the characterization can be performed in the presence of solar light. Very recently, a hybrid refrigerative thermoelectric cooling system was built by Wong et al. to simulate the radiative cooling effect artificially under controlled conditions.[26] Their sophisticated setup achieved a reasonable accuracy (deviation of $17\% - 33\%$). Still, a repeatable and comprehensive characterization method for passive daytime cooling materials remains an enormous challenge.

In this work, we present a tailored indoor setup for comprehensively characterizing the performance of daytime passive cooling materials. The setup allows measurements with and without illumination of the sample, analogous to daytime and nighttime field testing, respectively. It consists of a liquid nitrogen-cooled, hemispherical aluminum dome (Al) as a heat sink, and an air mass (AM) 1.5 solar simulator as a light source. To the best of our knowledge, our method is the first indoor setup for the experimental characterization of passive cooling materials in both nighttime and daytime, with outstanding repeatability showcased for three distinct materials, namely, a silver (Ag) mirror, a polydimethylsiloxane (PDMS) film, and a graphite coating. Furthermore, our setup can experimentally determine the impact of environmental changes such as the ambient temperature or solar irradiation intensity, on the material's cooling performance. Such a parametric investigation is unfeasible with field tests due to uncontrollable environmental conditions. Lastly, our indoor setup is robust and simple to build, opening a promising pathway to quantitatively compare passive cooling materials designed in different research groups.

12.3 Results and Discussion

12.3.1 Indoor Setup Design

The most important aspects of passive cooling field testing that a feasible indoor setup must capture are: (1) radiative heat transfer from the sample to outer space, (2) illumination of the sample by the sun, and (3) measurement at moderate temperatures. The realization of these key measurement aspects can each be attributed to distinct parts of the proposed setup.

Radiative heat transfer. The samples emit hemispherically to outer space, which acts as a heat sink, with a temperature of approximately 3 K. To imitate this behavior, we utilize a hemispherical Al dome with a diameter of 60 cm. The high thermal diffusivity of Al ensures a homogeneous temperature distribution across the entire surface. The inner surface of the dome was coated with graphite to enhance its broadband absorption, thus resembling space as a heat sink for radiative heat transport. A polyethylene (PE) container is imposed on the hemisphere creating a reservoir around the Al dome. Liquid nitrogen is filled inside this reservoir and cools the dome down to approximately 80 K. The entire setup is thermally insulated using extruded polystyrene foam (XPS, Styrodur, BASF) with a thickness of 8 cm to prevent cold loss. A schematic of the indoor setup is shown in Figure 12.1. Detailed dimensions and a photograph are in Figure 12.6. During the measurement, a small steady influx of liquid nitrogen compensates for all remaining heat losses to the environment. The sample is placed in a homemade measurement cell constructed by XPS under the center of the dome. Low-density polyethylene (LDPE) foils were applied above the sample to prevent convection.

Solar illumination. The average solar irradiation is generally presented by the AM 1.5 spectrum with a power of approximately 1000 W m^{-2}, which is well-established in the characterization of photovoltaic devices.18 In the laboratory environment, a solar simulator was placed directly on the top of the dome to provide AM 1.5 solar light with an illumination area of 5×5 cm^2. The hole in the dome accounts for 0.8% of the total area seen by the sample and is thus negligible. The similarity between the light of the solar simulator and the sun is shown in Figure 12.7. The light hits the sample at an angle of 8° to prevent back reflection into the solar simulator.

Sample temperature. The most challenging part of the indoor setup is to keep the sample at moderate temperatures while cooling the dome down to liquid nitrogen temperatures. The significant temperature difference across the short distance between the cooled dome and the sample holder naturally leads not only to the desired radiative heat transfer, but also to undesired convection and conduction. Conduction is minimized by employing XPS insulation in combination with air gaps between the sample and the dome. Several LDPE foils (thickness approximately 15 μm), possessing a high solar and IR transparency (Figure 12.8), act as a convection

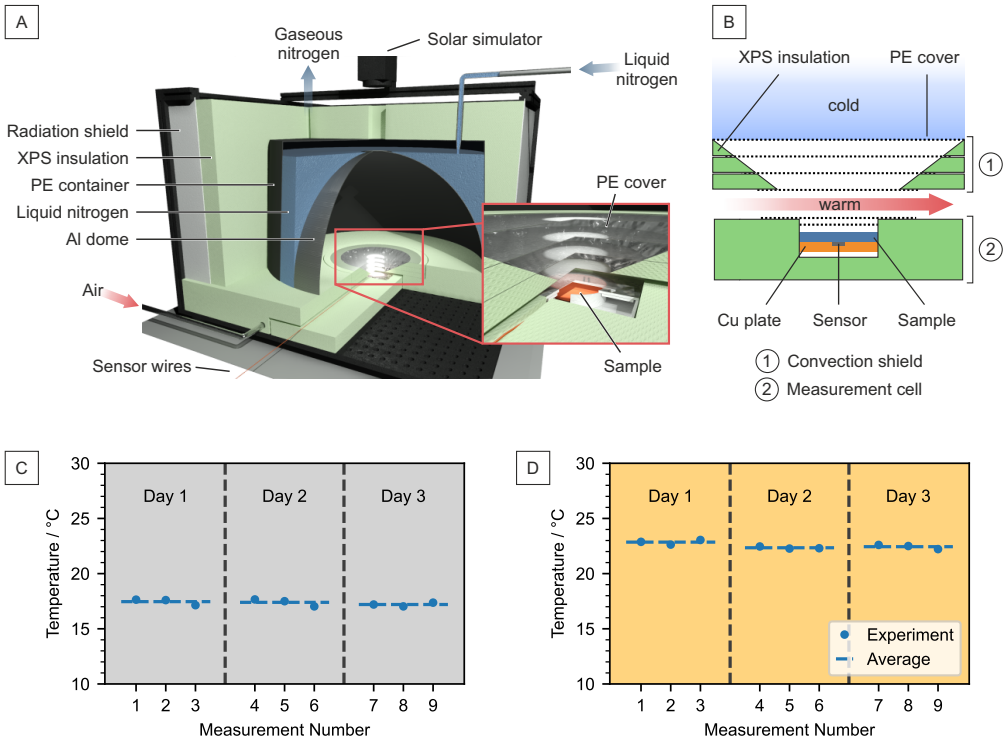

Figure 12.1: (A and B) Schematic of the indoor setup for characterizing passive daytime cooling. A liquid-nitrogen-cooled aluminum dome imitates outer space, while a solar simulator illuminates the sample. A convection shield in combination with XPS minimizes non-radiative heat transfer between the dome and sample. Detailed schematic of the sample holder (B). A warm gas flow between the convection shield and the sample holder allows controlling the temperature inside the measurement cell. (C and D) The steady-state temperature of an Ag mirror measured (C) w/o and (D) w/ solar light. Results show outstanding precision that cannot be achieved with outdoor measurements.

barrier between the sample and the cold air inside the dome. These PE layers reduce the solar radiation intensity in the sample by 25%, due to absorption, reflection, and scattering. Furthermore, the reduction of the transmittance is angle dependent. Previous reports showed that angles $< 60°$ have a dominant contribution to the emission of passive cooling materials.[4,27,28] Therefore, the convection shield made from XPS and LDPE has a cone-shaped inner part, with a zenith angle of 60° to reduce the thermal loss (conduction and convection) area while marginally blocking the pathway of thermal radiation from the sample. Conductive heat transport from each gas compartment to the next would eventually cool the air below the convection shield. A heated flow of dry air offsets this effect. The constant airflow and the stable laboratory environment (Figure 12.9) ensure highly stable and reproducible experiments. Moreover, controlling the temperature by tuning the airflow temperature allows for experimentally setting the ambient temperature and elaborating the temperature-dependent performance of passive cooling materials.

12.3.2 Performance Assessment

We investigated the repeatability of the indoor setup without (w/o) and with (w/) solar light. Multiple measurements of the steady-state temperature of an Ag mirror on different days are shown in Figure 12.1c and d. A standard deviation of ±0.24 K and ±0.26 K was obtained from nine measurements over three consecutive days w/o and w/ light, respectively. This minor deviation shows that our indoor setup possesses an outstanding repeatability in both nighttime and daytime-like measurements. When shining solar light with one sun power on the Ag mirror, the temperature increased by about 6 K. Since a LDPE foil is applied to the measurement cell to prevent convection, we thus attribute the temperature increase to the greenhouse effect caused by the parasitic solar light absorption of the Ag mirror and sample holder. This phenomenon has also been observed in outdoor measurements.[29,30]
For outdoor measurements, an intuitive definition of the ambient temperature is the air temperature, which can be measured simultaneously with the sample temperature. For indoor measurements, however, the environment temperature results from the interplay between the cold dome and the warm gas flow. The large temperature gradient between the sample holder and the dome surface prevents a meaningful ambient temperature measurement in the vicinity of the actual sample. Therefore, an alternative way to define the ambient temperature is needed. Ag possesses a low emissivity in both the solar and IR region and therefore closely resembles the ambient temperature inside of the measurement cell without any major radiative heat losses or gains. We confirm this assumption by comparing the Ag mirror temperature with the ambient temperature in a field test (Figure 12.2a and b), where both temperatures almost overlap. The ambient temperature for the indoor setup is thus defined as the temperature obtained with an Ag mirror.

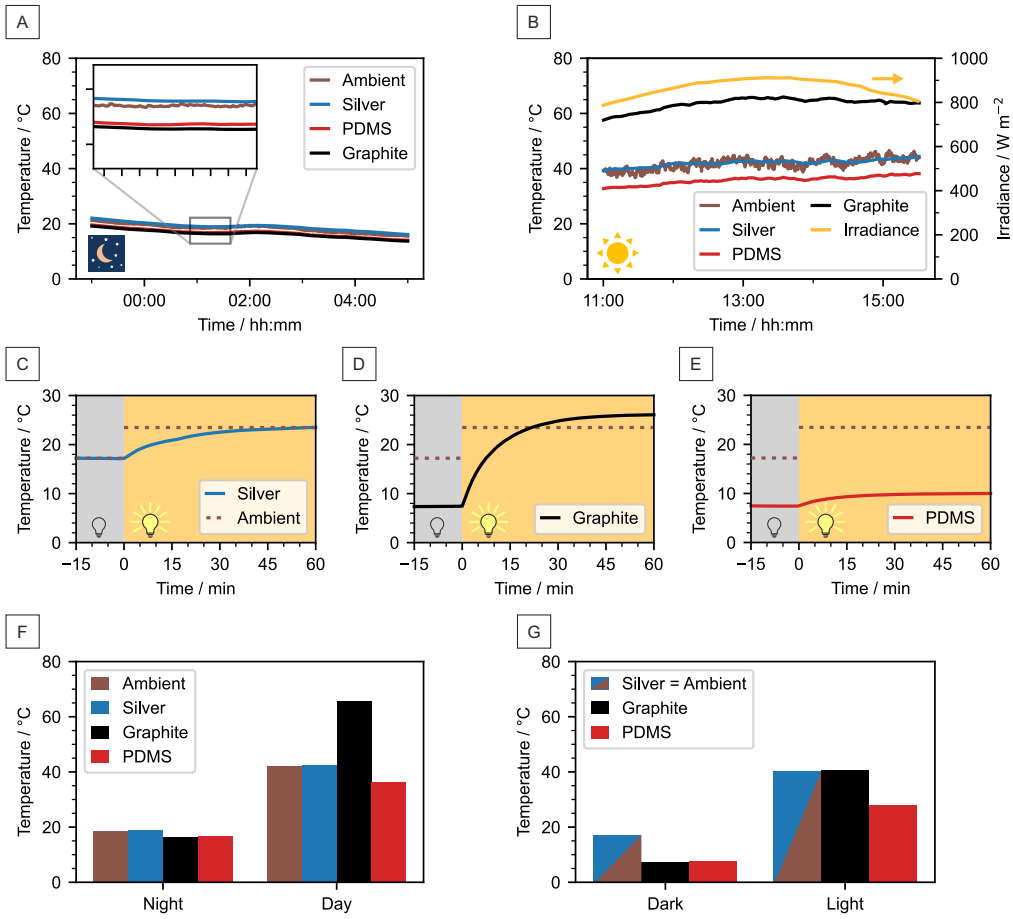

Figure 12.2: (A and B) Outdoor rooftop measurement for the reference materials at (A) nighttime and (B) daytime. The measurement was carried out under a clear sky, on June 17–18, 2021 in Bayreuth, Germany. (C–E) Indoor measurements of the (C) Ag mirror, (D) PDMS film, and (E) graphite coating. The turn-on point of the solar simulator was defined as 0 min. The dashed lines indicate the respective ambient temperatures for measurements w/o and w/ light. (F and G) The steady-state temperature of the reference materials in the (F) outdoor and (G) indoor measurements, respectively.

To verify the reliability of the indoor setup, we analyzed three reference materials: an Ag mirror, a PDMS film on an Ag mirror, and a graphite coated silicon wafer. The chosen materials possess very different optical properties. Ag has a very low emissivity in both the visible and MIR regions, as outlined above. Furthermore, it has been widely applied to the backside of daytime passive cooling devices to minimize solar absorption.[6,31] PDMS is a good passive cooling material due to its inherent selective emissivity in the MIR region. By combining the PDMS film and an Ag mirror, a practical daytime passive cooler is easily constructed.[24,32] As the last sample, we use a graphite coating exhibiting broadband absorption in the solar and MIR regions. The spectral emissivity of all reference materials is shown in Figure 12.10.

Measurements of the reference materials were carried out w/o and w/ light irradiation (Figure 12.2c-e). For measurements w/o light, a steady-state temperature of

17.2 °C, 7.5 °C, and 7.4 °C was observed for the Ag mirror, the PDMS film, and the graphite coating, respectively. The PDMS film and graphite coating show a steady-state temperature approximately 10 K lower than the Ag mirror. This is caused by the emissivity dependence of the radiative heat transfer. In contrast to the PDMS film and graphite coating, the Ag mirror shows negligible emissivity in the MIR region.

Subsequently, the solar simulator was used to simulate daytime measurements. After the reference materials reached a steady-state temperature in the dark, the solar simulator with one sun power was switched on. The temperature of all reference samples increased, and a new steady-state temperature was reached within 1 h. Compared with the Ag mirror (+6.3 K) and the PDMS film (+2.6 K), the temperature increase of the graphite coating was substantial (+18.8 K). The temperature increase of the Ag mirror can be explained by the absorption of the sample holder and the greenhouse effect. The different light response of the reference materials occurs because graphite has a significantly higher absorption in the solar regime. In addition, more than a 10 K difference in the steady-state temperature was observed between the Ag mirror and the PDMS film. The much lower final temperature of PDMS film demonstrates the good passive daytime cooling performance of the PDMS film agreeing with field testing in the literature.[24,29]

To compare the results of the indoor experiment with the conventionally used field testing, outdoor measurements of the reference materials (Figure 12.2a and b) were conducted in both nighttime (23:00−05:00) and daytime (11:00–15:30). The setup for the outdoor measurements is shown in Figure 12.11. The PDMS film and graphite coating show similar steady-state temperatures at nighttime, approximately 2.5 K lower than the Ag mirror (Figure 12.2f). During the daytime, the Ag back mirror of the PDMS sample reflected most solar irradiation, while the PDMS transferred heat to outer space via IR radiation. Therefore, the PDMS film keeps its sub-ambient temperature even with an average solar intensity of around 850 W m^{-2}. In contrast, the graphite coating absorbed considerable solar energy and warmed up to approximately 60 °C.

Indoor measurements were performed with the respective ambient outdoor temperatures, 17 °C and 40 °C (Figure 12.2g). We observe that the absolute values of steady-state temperature for the reference materials obtained from indoor and outdoor measurements do not agree with each other. A daytime sub-ambient cooling by 6.2 K was observed from an outdoor measurement of a PDMS film, while 12.1 K was obtained from the indoor setup. We attribute this difference to two main contributions. First, the black coated Al dome represents a broadband black body. More radiative heat can be transferred to it compared with the higher selectivity of the atmospheric window in outdoor measurements. Hence, the sub-ambient cooling power is increased. Second, the irradiance in the outdoor measurement is 900 W m^{-2}, while the irradiance in the indoor measurement is only 750 W m^{-2}. Consequently, the absorbance in the visible spectrum leads to a higher heat input for the outdoor case.

Considering these effects, the values agree reasonably well. The reproducible values of the indoor setup allow for better comparison between different measurements as displayed in the literature. PDMS samples measured at different locations and times show an even larger range of temperature reductions. For instance, Zhou et al. observed a sub-ambient cooling of 11 K at Buffalo, NY, USA (February 2018).[24] Zhu et al. reported 3.3 K at Nanjing, China (November 2019)[33], and our previous study showed 7.4 K at Bayreuth, Germany (April 2020).[29] The disparity in the investigation of similar PDMS films from different groups is attributed to the distinct measurement conditions, e.g., ambient air temperature, humidity, solar irradiation. Even subsequent measurements with the same setup from one group at a fixed location are prone to fluctuations, due to the equilibration time and the natural changes in temperature, humidity, and solar radiation. Consequently, multiple tests are typically run simultaneously to allow for comparability among different samples. In contrast, the proposed indoor setup enables measurements with a predetermined condition and, thus, allows a quantitative comparison of measurements from different days.

12.3.3 Cooling Power Characterization

Besides the sub-ambient temperature that a passive cooling material can reach, its net cooling power is another important parameter for quantifying the cooling performance. The standard technique to measure the net cooling power is using a feedback-controlled electrical heater underneath the sample to maintain the ambient temperature. As a result, the recorded input heating power is equivalent to the net cooling power.4 However, the cooling power obtained from outdoor measurements, in most cases, fluctuates over time due to the unstable conditions, mainly solar intensity, wind speed, and cloud coverage. Hence, such outdoor measurements are typically carried out for many hours and merely reach a temporary steady state condition, making a quantification of the cooling power difficult.[7,11,34] By contrast, a steady net cooling power can be measured with the presented indoor setup in a matter of minutes. The ambient temperature is set to the Ag mirror temperature determined under the same measurement condition. We assume that at this temperature, no non-radiative losses, i.e., convection and conduction, occur. As shown in Figure 12.3a and b, the net cooling power of a PDMS film (approximately 88.4 μm) was obtained within 30 min. The PDMS film exhibits a net cooling power of about 200 W m^{-2} at an ambient temperature of 19.5 °C, w/o solar light. Compared to the net cooling power of the PDMS-based passive cooling devices reported in the literature, i.e., up to approximately 130 W m^{-2},[31] the value obtained from the indoor setup is relatively high. This is attributed to the absence of atmospheric thermal radiation outside of the sky window range in the indoor setup.[35] Nevertheless, characterizing the passive cooling power with the indoor setup allows for a precise and defined

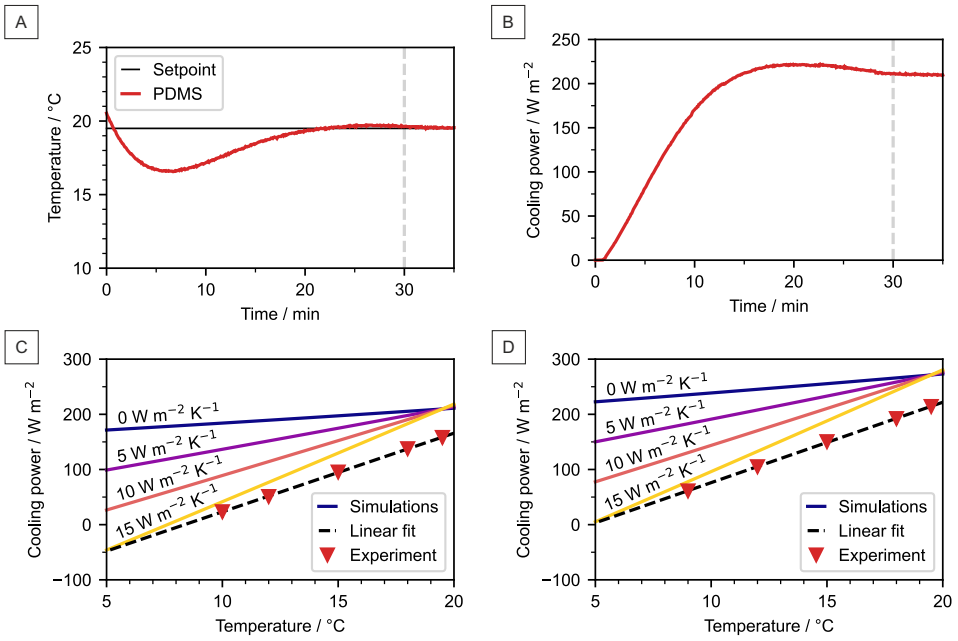

Figure 12.3: (A and B) Temperature tracking (A) and net cooling power measurement (B) of a PDMS film (88.4 μm) via the indoor setup. (C and D) A steady net cooling power could be obtained within 30 min. Numerically calculated net cooling power as a function of emitter temperature with different non-radiative heat transfer coefficients (h_c) for (C) a thin PDMS film (19.2 μm) and (D) a thick PDMS film (88.4 μm), based on the configuration of the indoor setup. The respective experimental values are measured and plotted to estimate hc for our setup. Values of 11.6 and 11.2 W m^{-2} K^{-1} were obtained for the thin and thick PDMS samples, respectively. For the experiments, the setpoint was 19.5 °C and solar light was excluded

measurement with a reasonably fast equilibration time.

For materials exposed to the clear sky, the net cooling power can be calculated with the radiative model, $P_{\text{cool}} = P_{\text{mat}} - P_{\text{sun}} - P_{\text{atm}} - P_{\text{nonrad}}$. Here, P_{mat} is the thermal irradiation power of the emitter, P_{sun} is the solar power absorbed by the material, P_{atm} is the absorbed power from the atmosphere, and P_{nonrad} is the absorbed power due to conduction and convection. P_{nonrad} can be expressed as $P_{\text{nonrad}} = h_c \cdot (T_{\text{atm}} - T_{\text{mat}})$, where h_c is the non-radiative heat transfer coefficient. For the indoor setup, the inner space is filled with nitrogen and the path between the sample and the dome is short. Thus, P_{atm} can be omitted and the equation can be simplified to $P_{\text{cool}} = P_{\text{mat}} - P_{\text{sun}} - P_{\text{nonrad}}$ and $P_{\text{cool}} = P_{\text{mat}} - P_{\text{nonrad}}$ for daytime and nighttime, respectively. It needs to be noted that h_c varies from measurement to measurement because of the distinct measurement conditions, and the estimation of h_c has been widely conducted, whereas, it should not depend on the material optical properties.[4,36]

To better understand our indoor setup and verify that h_c is indeed independent of the optical properties for all indoor setup measurements, we calculated the theoretical net cooling powers of PDMS films with various optical properties and compared them with the actual indoor measurements. The h_c dependent net cooling

power of PDMS films with two different thicknesses, 88.4 μm and 19.2 μm, was calculated via the radiative cooling model based on the indoor setup configuration. The model was thoroughly discussed in our previous work, which demonstrated the thickness dependence on optical properties and passive cooling performance.[29] The complex refractive index of PDMS films used in the calculation was obtained from the literature.[37,38] To determine h_c of our indoor setup measurements, the net cooling powers of the PDMS samples were measured at five different temperatures. We observed a linear relationship between the sample temperature and the cooling power, that agreed with the expected trend obtained from the numerical calculations (Figure 12.3c and d). Based on the linear fitting of the measurement points, we estimate h_c of the indoor measurements to be 11.6 W m^{-2} K^{-1} and 11.2 W m^{-2} K^{-1} for the measurements of thin and thick PDMS films, respectively (Figure 12.12). The consistent h_c value obtained from the indoor measurements with different samples proves the stability and reliability of the indoor setup. In addition, we observed a slight offset between the measured and calculated net cooling power. We attribute this to the approximations in the theoretical model, the adopted complex refractive index value from the literature,[29] and the uncertainty of the measurement.

12.3.4 Variation of Environmental Parameters

Solar irradiance and ambient temperature vary with time and location. They strongly influence the cooling capacity of passive daytime cooling devices. As shown in Figure 12.4a and b, solar irradiance changes from 0 to approximately 950 W m^{-2} during a summer day, and ambient air temperature changes between about -10 °C to about 35 °C over a year in Bayreuth, Germany. How do temperature and solar radiance influence the cooling performance? In our indoor setup, the solar irradiance can be changed between 0% and 100% of one sun via the solar simulator. We, therefore, examined the sub-ambient cooling as well as the net cooling power of a graphite coating at various solar intensities, from 0% to 100%. As illustrated in Figure 12.4c, the temperature difference ($T_{\text{graphite}} - T_{\text{amv}}$) increased from about -10 K to +10 K with increasing solar intensity from 0% to 100%. Concomitantly, the net cooling power declined gradually. Moreover, the temperature difference and the net cooling power showed a linear trend with respect to the solar intensity.

The temperature controllable gas flow allows tuning of the ambient temperature in the measurement cell between 10 °C and 35 °C (Figure 12.13). The temperature dependence of blackbody radiation is well-known. An increasing emitter temperature enhances the thermal irradiation, and, therefore, the cooling performance. We measured the steady-state temperature of a PDMS film (88.4 μm) at various ambient temperatures. We found that with increasing the ambient temperature, the cooling performance was also enhanced as indicated by the increased sub-ambient cooling (Figure 12.4d). The sub-ambient cooling rose from 8.7 K to 11.0 K with

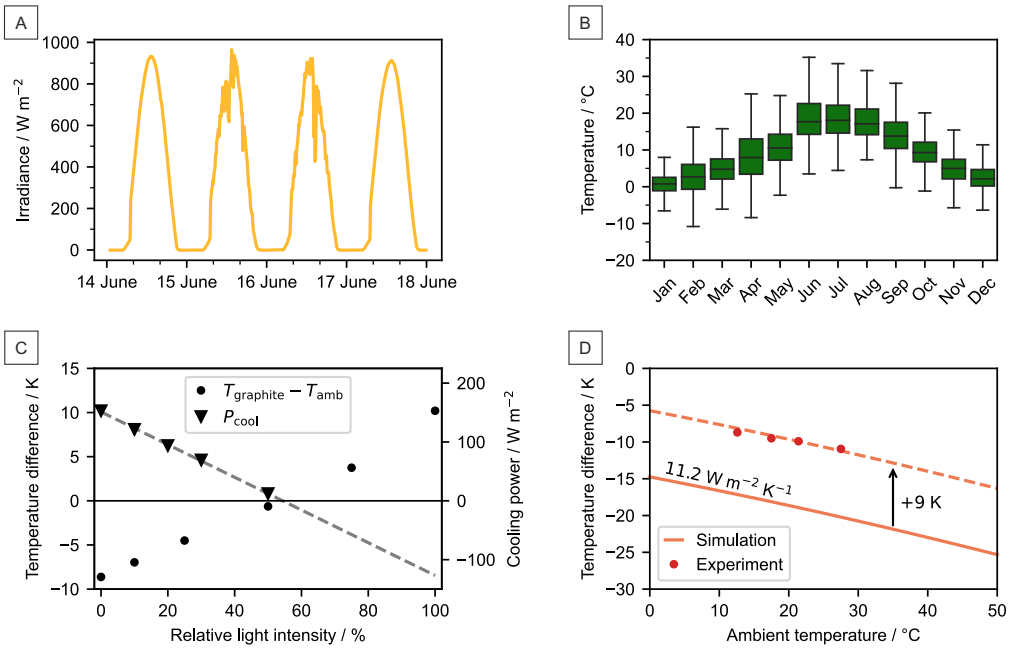

Figure 12.4: (A) Solar irradiance over four days in Bayreuth, Germany. (B) Ambient air temperature of different months in Bayreuth, Germany, over the last three years. (C) Impact of solar intensity on the passive cooling performance of a graphite coating. The temperature difference ($T_{\text{graphite}} - T_{\text{amb}}$) and net cooling power (P_{cool}) show a linear trend when increasing the solar light intensity from 0% to 100% of one sun (1000 W m^{-2}). (D) The impact of ambient temperature (T_{amb}) on the cooling performance of a PDMS film. Both the simulation and experiment show that T_{amb} enhances the cooling performance leading to a decrease of the temperature difference ($T_{\text{PDMS}} - T_{\text{amb}}$).

increasing the ambient temperature from 12.6 °C to 27.5 °C. We confirmed this temperature dependence by a numerical calculation with $h_c = 11.2$ W m^{-2} K^{-1}. Despite the offset between the experimental and theoretical values (approximately 9 K), the trends agree well.

In general, passive cooling materials can be divided into two groups. The first group are selective emitters, which emit only at the atmospheric window ($8 - 13$ μm). These emitters transfer heat directly to outer space without interference from the atmosphere. The second one is broadband emitters. Broadband emitters emit not only at the atmospheric window but also outside, resulting in heat exchange with the atmosphere itself.[39] It is controversial which kind of emitter is better suited for passive cooling applications.[31,40] In its current form, our setup is best suited to compare emitters of the same type, i.e., compare broadband with broadband and selective with selective emitters. However, the discrimination between broadband and selective emitters is limited due to the lack of an atmospheric window. Directly simulating the atmosphere within the indoor setup is rather challenging.

Instead of equipping the indoor setup with a direct MIR filter with a transmission similar to the atmosphere to further imitate the field testing, an inverse MIR filter that emits only in the atmosphere window regime can be introduced. By placing the inverse MIR filter, which possesses ambient temperature, between the sample and the cold dome during the measurement, only the spectral radiation outside the atmosphere window regime can reach the cold dome (Figure 12.5a). The filter will block the rest. Selective emitters can thus be distinguished from broadband emitters by comparing the proportion of cooling power loss in a two-step measurement without and with the inverse MIR filter installed. The radiation in the atmosphere window regime contributes distinctly to the radiative cooling ability of broadband emitters and selective emitters.

We demonstrate such an inverse MIR filter by coating a LDPE foil with a thin layer of PDMS. A thin PDMS film with the desired thickness on a LDPE foil ensures a high absorption in the regime of $8 - 13$ μm and simultaneously high transmission in the remaining spectral range (Figure 12.5b). The cooling power of PDMS films with different thicknesses, i.e., 712 nm, 8.6 μm, 13.1 μm, and 88.4 μm, is determined w/o and w/ the PDMS-PE filter to prove the concept (Figure 12.5c and Figure 12.14). The optical properties of the PDMS films show that with increasing film thickness, they gradually transition from a selective to a broadband emitter (Figure 12.15). Consequently, the cooling power without the MIR filter increased gradually. This is in good agreement with our previous work based on outdoor measurements.[29]28 The cooling power reduces dramatically when applying the PDMS-PE filter. The decrease varies for the differently thick PDMS films. To highlight the cooling power difference caused by the PDMS-PE filter, the relative power loss was calculated as power loss $= (P_{\mathrm{w/o}} - P_{\mathrm{w/}})/P_{\mathrm{w/o}}$ and is shown in Figure 12.5d. The increasing thickness of the PDMS films reduces the cooling power loss, which indicates that the PDMS-PE filter affects selective emitters more importantly than broadband emitters.

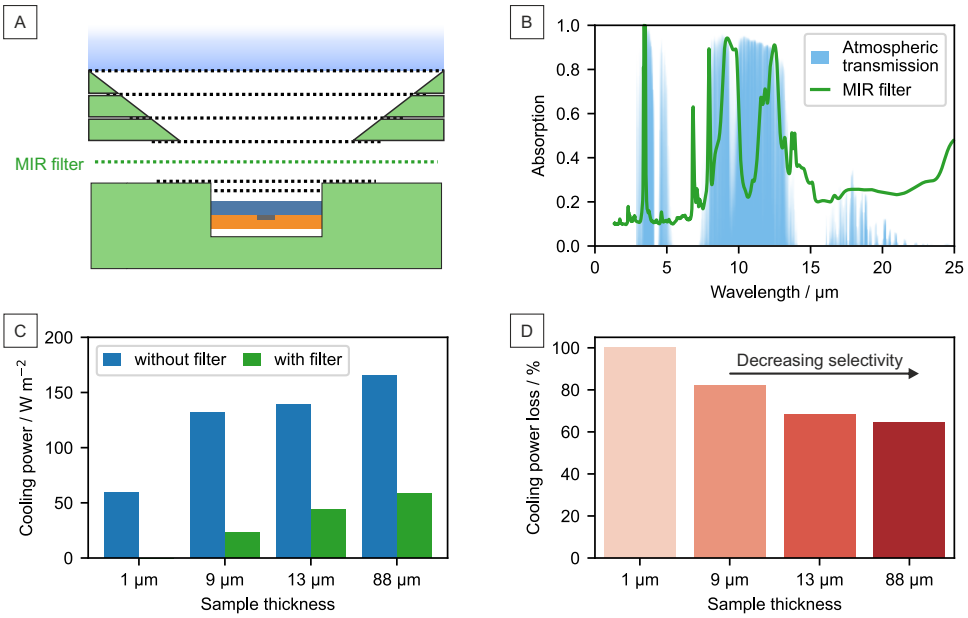

Figure 12.5: (A) An MIR filter consisting of PDMS on PE is inserted between the sample and the convection shield. (B) The absorption spectrum of the PDMS-PE filter is comparable with the transmission of the atmosphere. (C) Cooling power measurements of differently thick PDMS samples with and without the filter. With increasing thickness, the cooling power rises. The introduction of the MIR filter results in a significant reduction of cooling power. (D) The relative cooling power loss decreases with increasing PDMS film thickness. The loss correlates with the emission selectivity of the samples.

Besides, we also calculated the cooling power loss of the PDMS films w/ and w/o atmosphere with outdoor conditions (Figure 12.16). Despite the deviation of the absolute value between the experiment and the simulation, the trend agrees well. The deviation is mainly attributed to the imperfect match between the PDMS-PE filter and the atmosphere. The inverse MIR filter design can assess the influence of the sky-window transmission on the cooling power but is not suitable to compare the temperature reduction with outdoor measurements. A direct temperature comparison required a filter matching the sky-window properties.

Although it is hard to imitate the atmosphere in the indoor setup, with the inverse MIR filter, the indoor setup can distinguish between selective and broadband emitters. The possibility to add a tailor-made filter to our setup further expands the scope for its applicability to characterize passive daytime cooling materials close to field testing conditions. Further additions may include filters that account for a specific relative humidity or cloud coverage. Another class of filters may address the angular dependence of the thermal emission of a given material by controlling the view factor of the dome in dependence on the polar angle. Such a measurement capability is highly demanded to characterize emissive materials with diffusive reflectance properties. For instance, the heat management properties of smart textiles can be investigated with such a sample-dome layout, when operated at body heat and room temperature, respectively.[41]

In summary, we constructed a versatile indoor setup to thoroughly characterize the performance of passive cooling materials for both daytime and nighttime. Our setup combines a liquid-nitrogen-cooled Al dome with a solar simulator. Unlike conventional outdoor measurements, our setup allows controlling the measurement conditions, leading to outstanding reproducibility and time-saving measurements. Characterizing materials in a laboratory environment makes measuring and comparing materials independent of weather, time, and location. Additionally, the impact of solar intensity and ambient temperature on the cooling performance can be practically studied. Such comprehensive investigations are impossible for outdoor measurements due to the uncontrollable atmospheric conditions. We are convinced that our test setup is a first step toward a standardized passive cooling test routine. A standardized method to practically compare the cooling performance of various innovative materials from research groups all over the world is, however, a gatekeeper to turning passive cooling into a widespread and applied technology.

Acknowledgements

The authors gratefully thank Stefan Rettinger and the mechanical workshop (University Bayreuth) for technical support and Klaus Müller for the metal evaporation. We are indebted to Prof. Christoph Thomas for kindly providing the solar radiance and air temperature data. T.T. and T.L. acknowledge support from the Elite Network Bavaria (ENB). The authors acknowledge financial support from the European Research Council (ERC) under the European Union's Horizon 2020 research and innovation program (grant agreement no. 714968).

12.4 Supplemental Figures

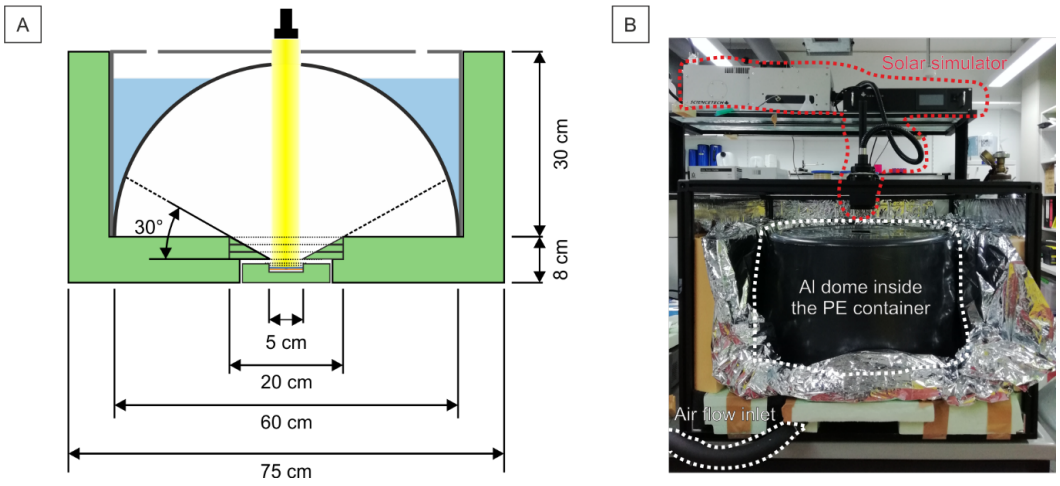

Figure 12.6: Indoor setup design. (A) Detailed dimensions and (B) photograph of the indoor setup. Related to Figure 12.1 and Indoor Setup Design.

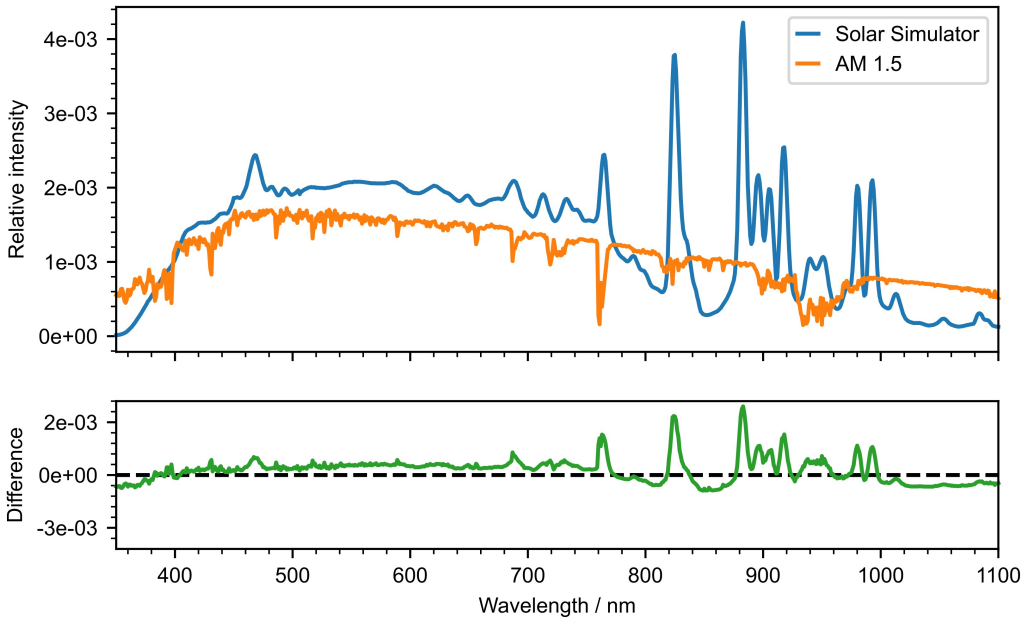

Figure 12.7: Comparison between the solar light from the sun (AM 1.5) and the solar simulator. The intensity shown is relative to the total intensity of the light source, i.e., the integral from 0 to infinity is 1 for each individual curve. Related to Indoor Setup Design.

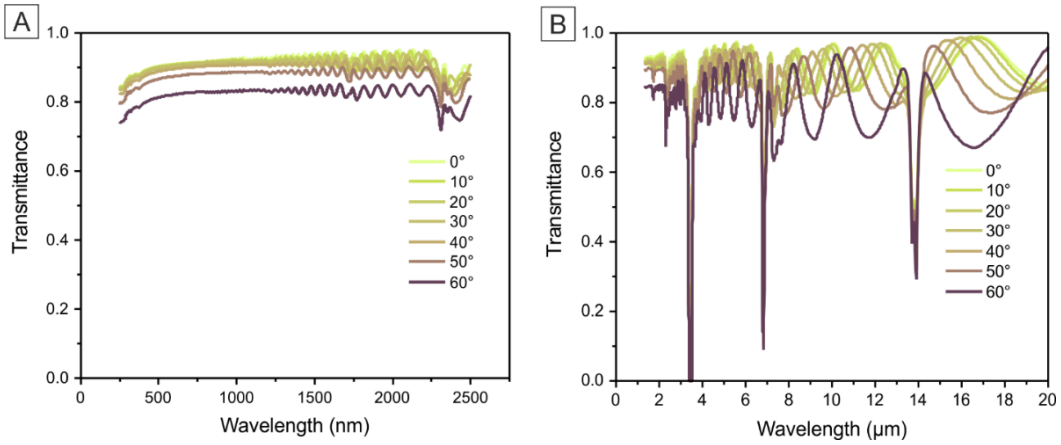

Figure 12.8: Angle-dependent optical properties in (A) UV/Vis and (B) IR regime for a single, 15 μm thick PE window used in the convection shield. Related to Indoor Setup Design.

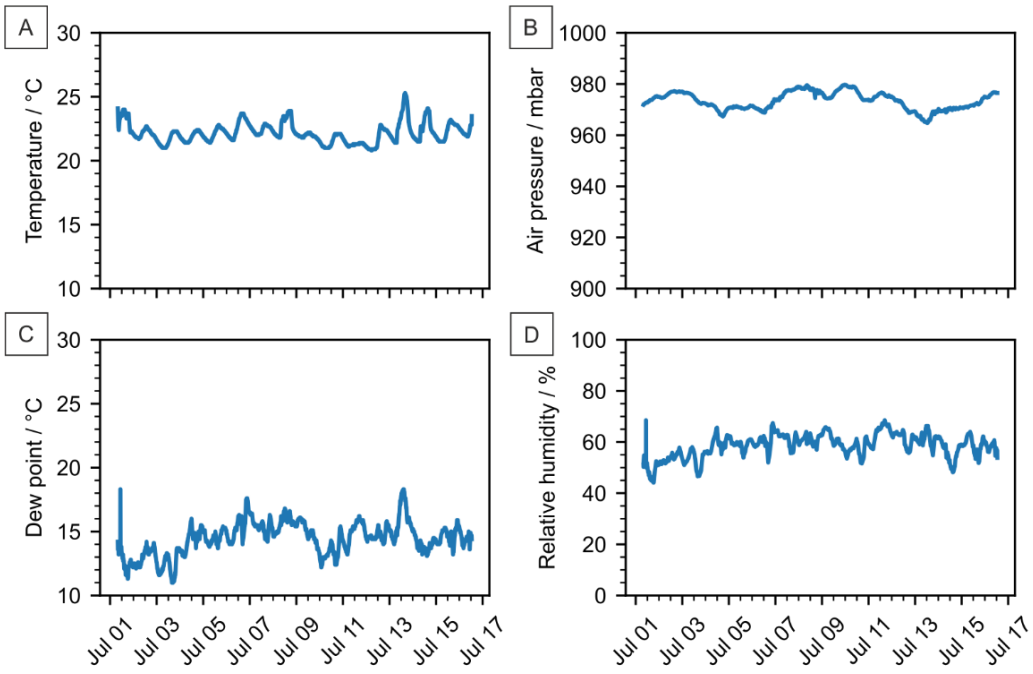

Figure 12.9: Laboratory conditions. (A) Ambient temperature, (B) air pressure, (C) dew point, and (D) relative humidity in the laboratory over a week. Related to Indoor Setup Design.

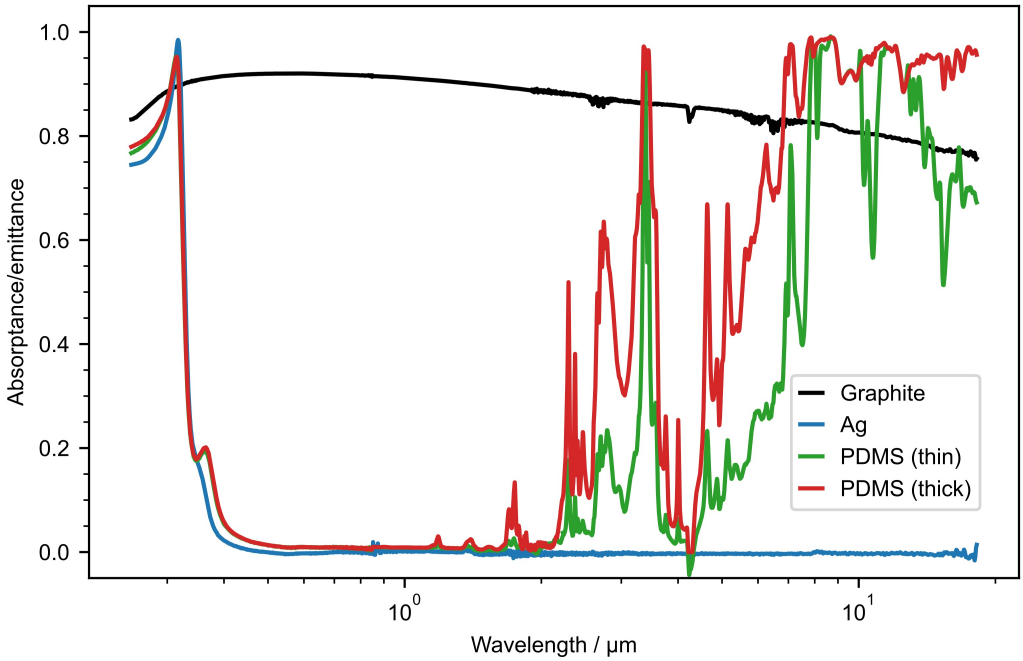

Figure 12.10: Optical properties of the reference materials used in this work, i.e., PDMS, Ag, and graphite, in the UV/Vis and MIR region. Related to Figure 12.2 and Performance Assessment.

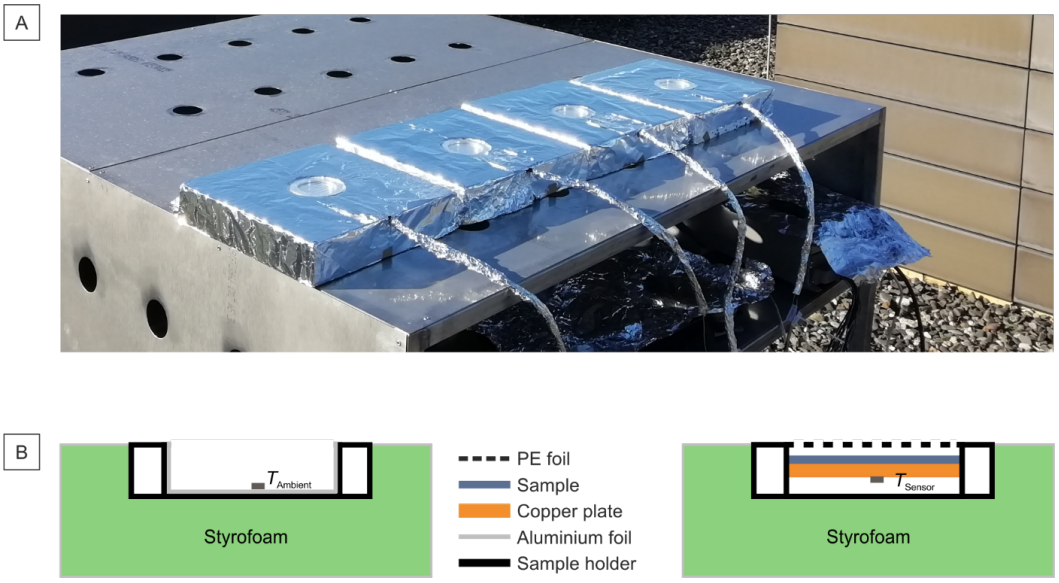

Figure 12.11: Outdoor setup design. (A) Photograph and (B) schematic of the setup for outdoor measurements. Related to Figure 12.2 and Performance Assessment.

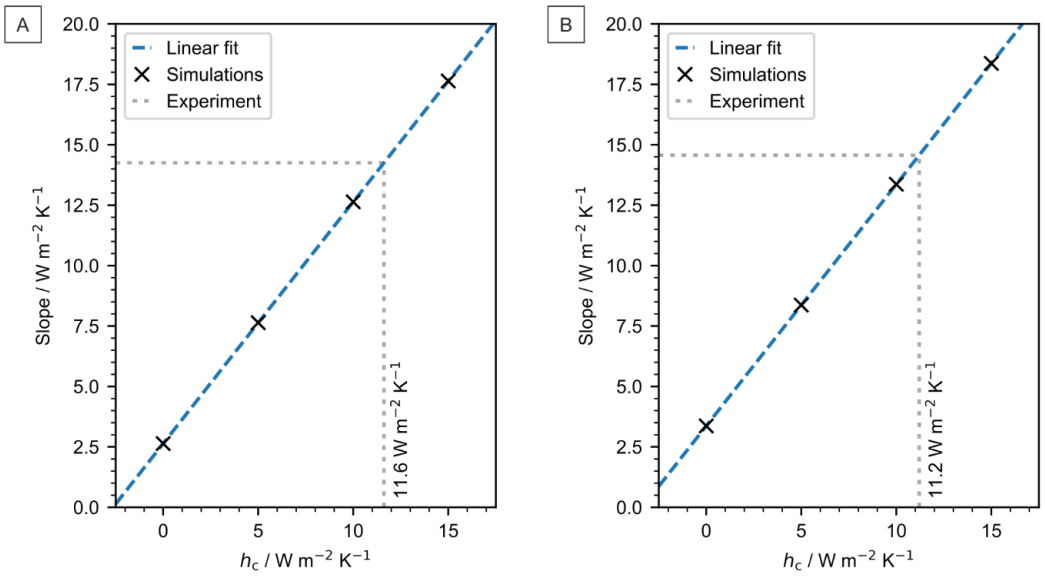

Figure 12.12: Determination of h_c for the thin (A) and thick (B) PDMS samples in the indoor setup measurement. The linear fit shows how the slope of the simulated cooling power behaves for different values of h_c. Calculating the slope of the experimental cooling powers leads to h_c values of 11.6 and 11.2 W m^{-2} K^{-1} for the thin and thick PDMS samples, respectively. Related to Figure 12.3 and Cooling Power Characterization.

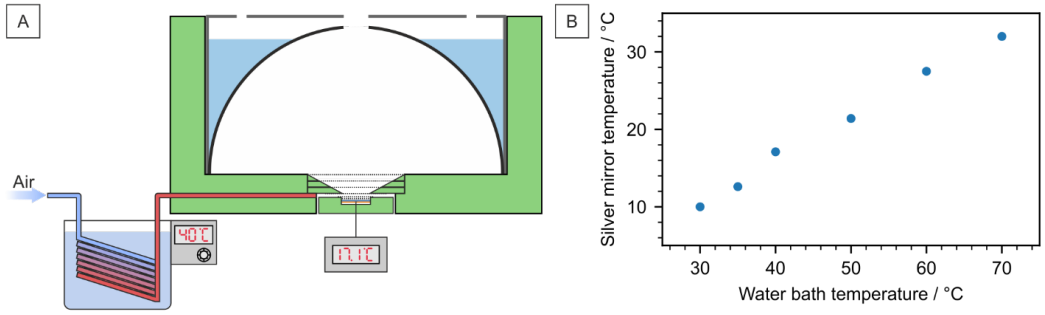

Figure 12.13: Tunable ambient temperature of the indoor setup. (A) Schematic of a part of the indoor setup. (B) Ambient temperature of the indoor setup as a function of water bath temperature. Related to Figure 12.4 and Variation of Environmental Parameters.

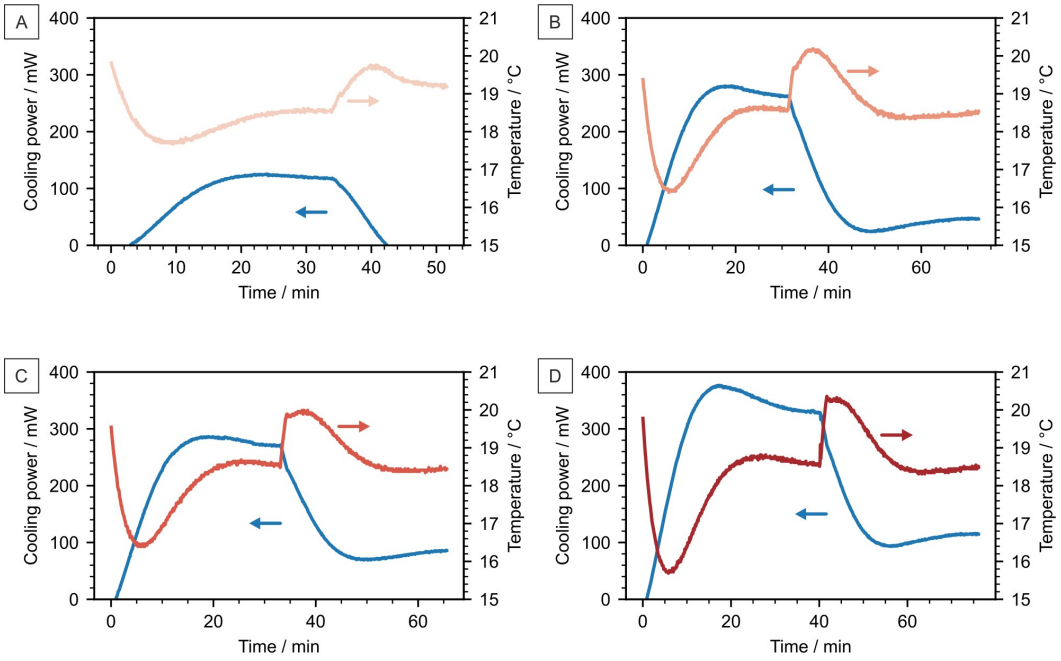

Figure 12.14: Cooling power measurements with and without a MIR filter for PDMS samples with a thickness of (A) 712 nm, (B) 8.6 μm, (C) 13.1 μm, and (D) 88.4 μm. The MIR filter is inserted into the indoor setup after temperature and cooling power reach a steady state. The insertion of the MIR filter leads to a significant decrease in cooling power for all samples.

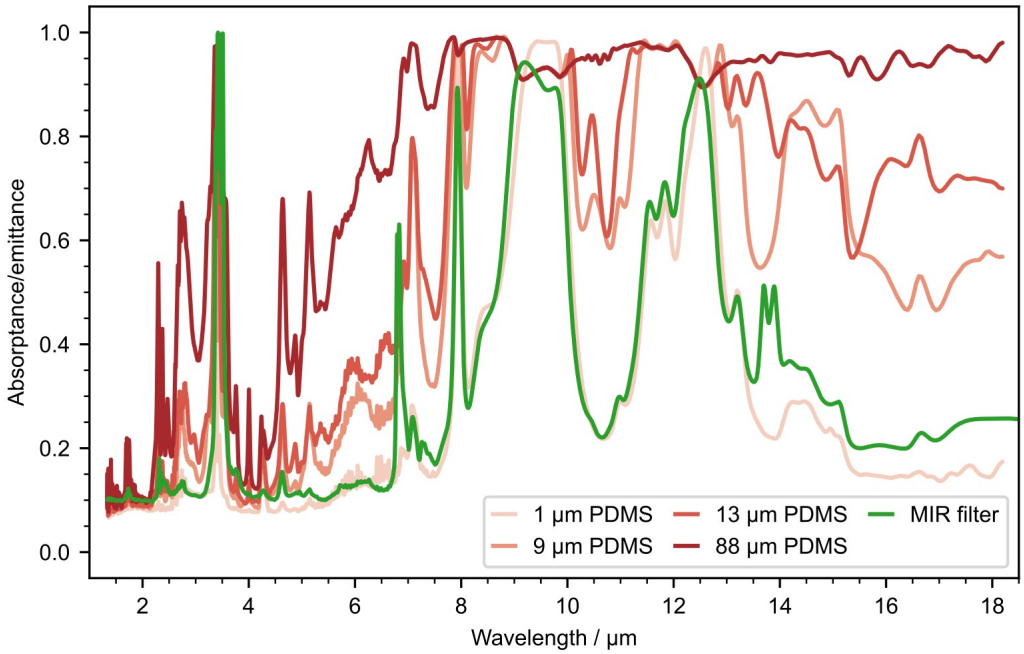

Figure 12.15: Absorption spectra for PDMS films of different thicknesses and the MIR filter. Decreasing thickness leads to higher emission selectivity.

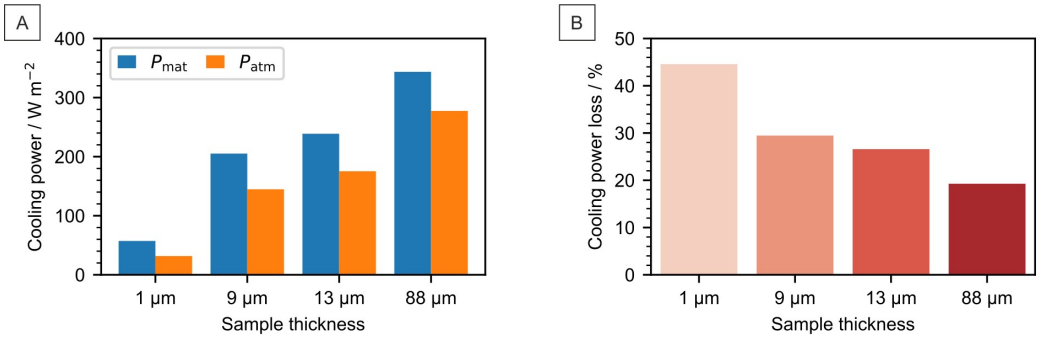

Figure 12.16: Simulation results for PDMS samples with different thicknesses in outdoor conditions. (A) Absolute contributions to the cooling power. (B) Cooling power loss. The loss is calculated as $(P_{\mathrm{mat}} - P_{\mathrm{atm}})/P_{\mathrm{mat}}$.

12.5 Supplemental Experimental Procedures

12.5.1 Preparation of Reference Materials

Ag mirrors. Ag with a thickness of 100 nm was thermally evaporated on a silicon wafer ($r = 2.5$ cm), followed by a deposition of 10 nm silicon oxide (SiO_2) with a sputter coating step.

PDMS films. PDMS films with different thicknesses (88.4 μm, 13.1 μm, 8.6 μm and 712 nm) were prepared on top of the Ag mirrors. For this, a prepolymer of PDMS (Sylgard 184, Dow Chemical) was mixed with a curing agent in a ratio of 10:1 (by weight) and degassed in a desiccator under vacuum. Subsequently, films with a thickness of 88.4 μm and 13.1 μm were prepared via spin-coating (1000 rpm and 3000 rpm) on the Ag mirror. For films with a thickness of 8.6 μm and 13.1 μm, the prepolymer/cross-linker mixture was diluted to a 75 wt% and 25 wt% solution, respectively, with n-hexane. The films were then prepared via spin-coating (3000 rpm and 4000 rpm) on the Ag mirror. The PDMS layers were cured at room temperature for 48 h.

Graphite coating. The graphite coating is prepared by spray coating graphite (Cramolin, Germany) onto a precleaned silicon wafer ($r = 2.5$ cm), followed by evaporation of the solvent at ambient temperature.

Thickness determination. The layer thickness of the reference samples, namely PDMS films and graphite, was determined by using a 3D laser scanning microscope (LEXT OLS 5000, Olympus). A thickness of 88.4 μm, 13.1 μm, 8.6 μm, 712 nm, and 3.2 μm was obtained for the four PDMS films and the graphite coating, respectively.

PDMS-PE window. A prepolymer of PDMS (Sylgard 184, Dow Chemical) was mixed with a curing agent in a ratio of 10:1 (by weight) and degassed in a desiccator under a vacuum. The resulting mixture was diluted to a 50 wt% solution with n-hexane. A PDMS thin film was spin-coated (3500 rpm) on a LDPE foil (thickness of around 15 μm), which was evenly attached to a silicon wafer ($r = 7.5$ cm). A PDMS-PE window was obtained by detaching the PDME-PE foil from the silicon wafer.

12.5.2 Optical Characterization with UV-Vis and FTIR Spectroscopy

Broadband optical properties of the reference materials were characterized by UV-Vis and FTIR spectroscopy. UV-Vis reflectance of the reference materials was measured with a UV-Vis spectrometer (Cary 5000, Agilent Technologies) equipped with an integrating sphere accessory (Labspheres). A Spectralon diffuse reflectance standard (Labspheres) was used as a reference. The FTIR spectroscopy measurements were

carried out on an IR-spectrometer (Vertex 70, Bruker) coupled with a gold-coated integrating sphere accessory (A562, Bruker). A gold mirror was used as a reference. The absorptance (emittance) was calculated as absorptance (emittance) = 1 – reflectance. We assume that the transmission can be neglected because of the silver layer at the back.

12.5.3 Transmittance Characterization of the Convection Shield

We used a pyroelectric sensor (Coherent FieldMaxII) to measure the power of the solar simulator irradiation. Triplicate measurements were performed with and without the convection shield between the simulator and the sensor. The transmittance was calculated as $1 - P_{\text{w/ shield}}/P_{\text{w/o shield}}$.

12.5.4 Indoor Measurements

Daytime measurements are imitated by applying solar light provided by a solar simulator (AX-LAN400, SCIENCETECH, CANADA) with an illumination area of 5×5 cm^2. For nighttime measurements, the solar simulator was turned off. For all indoor measurements, dried air was warmed up by a water bath with a controlled temperature and flushed the area between the convection shield and measurement cell. Liquid nitrogen was filled into the setup to cool down the Al dome. Prior to filling the liquid nitrogen into the setup, the inner space of the dome is flushed with N_2 to remove air. Thus, no pronounced water condensation was observed on the convection shield. The temperature of the dome is maintained during the entire measurement by continuously filling liquid nitrogen into the setup. The sample temperature is measured with a thermocouple (type T) and collected by a digital multimeter (DAQ6510, Tektronix, Germany) every 5 s. To determine the steady-state temperature, data from the last 5 min of the measurement were averaged.

For the indoor measurements with the PDMS-PE window, the prepared PDMS-PE foil was placed above the sample holder at a distance of around 5 mm.

Repeatability test. A Ag mirror was used to check the repeatability of the setup. The temperature of the air flow was controlled by setting the water bath to 40 °C. The steady-state temperature of the Ag mirror was measured three times per day on three different days w/ and w/o one sun power of solar light (approximately 1000 W m^{-2}).

Solar intensity dependence test. The graphite coating was measured to highlight the influence of solar intensity on the cooling performance. The temperature of the airflow was set to 40 °C. The intensity of the solar light was varied from 0% to 100% of one sun power (approximately 1000 W m^{-2}). The steady-state temperature and

the cooling power of the graphite coating were then obtained under each condition. The net cooling power was measured by actively heating the graphite coating to keep it at the same temperature as a Ag mirror under the same conditions (water bath temperature and solar irradiance).

Ambient temperature dependence test. A PDMS film (88.4 μm) was applied to proof the temperature dependence of the thermal irradiation. The temperature of the air ow was set to 35 °C, 40 °C, 50 °C, and 60 °C. Subsequently, the steady-state temperature of the Ag mirror and the PDMS film was measured w/o the solar light.

12.5.5 Rooftop Measurements

Rooftop measurements for daytime and nighttime were carried out on the roof of a four-floor building (17.–18.06.2021, University of Bayreuth, Bayreuth, Germany) under a clear sky. The reference samples were each placed in identical homemade sample holders. The holders were thermally insulated by Styrofoam and covered with Mylar aluminum foil. Convective heat transfer was prevented by applying a low-density polyethylene (LDPE) foil with a thickness of approximately 15 μm. The emitter temperatures were measured by Pt-100 temperature sensors and recorded with a digital multimeter (DAQ6510, Tektronix, Germany) every 5 s. Temperatures between 1:00−1:30 and 13:00−13:30 were averaged to obtain steady-state temperatures. One sample holder covered with Al foil but without LDPE foil was used to obtain the ambient temperature. The solar irradiance data were collected from the weather station at the University Bayreuth (Ecological-Botanical Garden, 400 m away from the rooftop measurement).

12.5.6 Numerical Calculations

The numerical calculations for theoretically estimating the steady-state temperature and cooling power of the PDMS films are based on a model that is described in our previous study.[29] The broadband optical properties of the PDMS film are obtained from the literature.[37,38] The sample was tilted 8° to avoid direct reflection of the solar light. For simplicity, this has been neglected in the numerical calculations. A polar angle θ of 60° and an azimuthal angle of 360° was applied to the calculation based on the configuration of the indoor setup. We assume that no thermal radiation was emitted by the liquid nitrogen-cooled dome.

To calculate the cooling powers of PDMS films with different thicknesses, i.e. 88.4 μm, 13.1 μm, 8.6 μm, 712 nm, with the outdoor condition, a polar angle θ of 90° and an azimuthal angle of 360° was applied. Ambient temperature of the emitter is set to 18.5 °C, which is the preset temperature of PDMS films for indoor cooling power

measurement. For emitters with a temperature as same as ambient temperature, the nighttime cooling power is calculated as $P_{\text{mat}} - P_{\text{atm}}$. P_{mat} is the total power emitted by the sample. P_{atm} is the absorbed power from the atmosphere. The cooling power loss is calculated as $(P_{\text{mat}}–P_{\text{atm}})/P_{\text{mat}}$.

12.6 References

[1] M. Santamouris, J. Feng, *Buildings* **2018**, *8*, 168.

[2] Z. Li, Q. Chen, Y. Song, B. Zhu, J. Zhu, *Advanced Materials Technologies* **2020**, *5*, 1901007.

[3] E. Rephaeli, A. Raman, S. Fan, *Nano Letters* **2013**, *13*, 1457–1461.

[4] A. P. Raman, M. A. Anoma, L. Zhu, E. Rephaeli, S. Fan, *Nature* **2014**, *515*, 540–544.

[5] D. Chae, M. Kim, P.-H. Jung, et al., *ACS Applied Materials & Interfaces* **2020**, *12*, 8073–8081.

[6] Y. Zhai, Y. Ma, S. N. David, et al., *Science* **2017**, *355*, 1062–1066.

[7] X. Wang, X. Liu, Z. Li, et al., *Advanced Functional Materials* **2019**, *30*, 1907562.

[8] B. Zhu, W. Li, Q. Zhang, et al., *Nature Nanotechnology* **2021**, *16*, 1342–1348.

[9] S. Zeng, S. Pian, M. Su, et al., *Science* **2021**, *373*, 692–696.

[10] A. Leroy, B. Bhatia, C. C. Kelsall, et al., *Science Advances* **2019**, *5*, eaat9480.

[11] J. Mandal, Y. Fu, A. C. Overvig, et al., *Science* **2018**, *362*, 315–319.

[12] J. Wang, J. Sun, T. Guo, et al., *Advanced Materials Technologies* **2021**, *7*, 2100528.

[13] H. Zhong, P. Zhang, Y. Li, et al., *ACS Applied Materials & Interfaces* **2020**, *12*, 51409–51417.

[14] N. N. Shi, C.-C. Tsai, F. Camino, et al., *Science* **2015**, *349*, 298–301.

[15] H. Zhang, K. C. S. Ly, X. Liu, et al., *Proceedings of the National Academy of Sciences* **2020**, *117*, 14657–14666.

[16] T. Wang, Y. Wu, L. Shi, et al., *Nature Communications* **2021**, *12*, 365.

[17] S. Wang, Y. Wang, Y. Zou, et al., *ACS Applied Materials & Interfaces* **2021**, *13*, 21888–21897.

[18] B. Zhao, M. Hu, X. Ao, N. Chen, G. Pei, *Applied Energy* **2019**, *236*, 489–513.

[19] X. Li, J. Peoples, Z. Huang, et al., *Cell Reports Physical Science* **2020**, *1*, 100221.

[20] S. Wang, T. Jiang, Y. Meng, et al., *Science* **2021**, *374*, 1501–1504.

[21] K. Tang, K. Dong, J. Li, et al., *Science* **2021**, *374*, 1504–1509.

[22] M. M. Hossain, M. Gu, *Advanced Science* **2016**, *3*, 1500360.

[23] M. Dong, N. Chen, X. Zhao, S. Fan, Z. Chen, *Optics Express* **2019**, *27*, 31587.

[24] L. Zhou, H. Song, J. Liang, et al., *Nature Sustainability* **2019**, *2*, 718–724.

[25] G. Park, K. Roh, H. Kim, et al., *Advanced Materials Technologies* **2021**, *7*, 2101205.

[26] R. Y. Wong, C. Tso, C. Y. Chao, *International Journal of Heat and Mass Transfer* **2021**, *174*, 121341.

[27] Z. Huang, X. Ruan, *International Journal of Heat and Mass Transfer* **2017**, *104*, 890–896.

[28] U. Banik, A. Agrawal, H. Meddeb, et al., *ACS Applied Materials & Interfaces* **2021**, *13*, 24130–24137.

[29] K. Herrmann, T. Lauster, Q. Song, M. Retsch, *Advanced Energy and Sustainability Research* **2021**, *3*, 2100166.

[30] S. Y. Jeong, C. Y. Tso, J. Ha, et al., *Renewable Energy* **2020**, *146*, 44–55.

[31] J.-l. Kou, Z. Jurado, Z. Chen, S. Fan, A. J. Minnich, *ACS Photonics* **2017**, *4*, 626–630.

[32] I. Haechler, H. Park, G. Schnoering, et al., *Science Advances* **2021**, *7*, eabf3978.

[33] Y. Zhu, Y. Ye, D. Wang, Y. Cao, *OSA Continuum* **2021**, *4*, 416.

[34] T. Li, Y. Zhai, S. He, et al., *Science* **2019**, *364*, 760–763.

[35] M. Chen, D. Pang, X. Chen, H. Yan, *Journal of Physics D: Applied Physics* **2021**, *54*, 295501.

[36] T. M. Nilsson, G. A. Niklasson, *Solar Energy Materials and Solar Cells* **1995**, *37*, 93–118.

[37] X. Zhang, J. Qiu, X. Li, J. Zhao, L. Liu, *Applied Optics* **2020**, *59*, 2337.

[38] X. Zhang, J. Qiu, J. Zhao, X. Li, L. Liu, *Journal of Quantitative Spectroscopy and Radiative Transfer* **2020**, *252*, 107063.

[39] D. Zhao, A. Aili, Y. Zhai, et al., *Applied Physics Reviews* **2019**, *6*, 021306.

[40] Y. Li, L. Li, L. Guo, B. An, *Optical Materials Express* **2020**, *10*, 1767.

[41] Q. Gao, T. Lauster, B. A. F. Kopera, et al., *Advanced Functional Materials* **2021**, *32*, 2108808.

Eidesstattliche Versicherungen und Erklärungen

§ 8 Satz 2 Nr. 3 PromO Fakultät für Biologie, Chemie & Geowissenschaften

Hiermit versichere ich eidesstattlich, dass ich die Arbeit selbstständig verfasst und keine anderen als die von mir angegebenen Quellen und Hilfsmittel benutzt habe (vgl. Art. 64 Abs. 1 Satz 6 BayHSchG).

§ 8 Satz 2 Nr. 3 PromO Fakultät für Biologie, Chemie & Geowissenschaften

Hiermit erkläre ich, dass ich die Dissertation nicht bereits zur Erlangung eines akademischen Grades eingereicht habe und dass ich nicht bereits diese oder eine gleichartige Doktorprüfung endgültig nicht bestanden habe.

§ 8 Satz 2 Nr. 4 PromO Fakultät für Biologie, Chemie & Geowissenschaften

Hiermit erkläre ich, dass ich Hilfe von gewerblichen Promotionsberatern bzw. –vermittlern oder ähnlichen Dienstleistern weder bisher in Anspruch genommen habe noch künftig in Anspruch nehmen werde.

§ 8 Satz 2 Nr. 7 PromO Fakultät für Biologie, Chemie & Geowissenschaften

Hiermit erkläre ich mein Einverständnis, dass die elektronische Fassung der Dissertation unter Wahrung meiner Urheberrechte und des Datenschutzes einer gesonderten Überprüfung unterzogen werden kann.

§ 8 Satz 2 Nr. 8 PromO Fakultät für Biologie, Chemie & Geowissenschaften

Hiermit erkläre ich mein Einverständnis, dass bei Verdacht wissenschaftlichen Fehlverhaltens Ermittlungen durch universitätsinterne Organe der wissenschaftlichen Selbstkontrolle stattfinden können.

Bayreuth, 16.12.2022

Kai Herrmann

Conductive and Radiative Heat Transport:
Contributions from Experimental and Theoretical Methods
Dissertation, 2022

University of Bayreuth
Physical Chemistry 1
Faculty of Biology, Chemistry & Earth Sciences
Universitätsstraße 30
95447 Bayreuth